

# ENERGY FLUXES AT THE AIR-SNOW INTERFACE

A Thesis Submitted to the  
College of Graduate Studies and Research  
in Partial Fulfillment of the Requirements  
for the degree of Doctor of Philosophy  
in the Department of Geography & Planning (Centre for Hydrology)  
University of Saskatchewan  
Saskatoon

By

Warren D. Helgason

©Warren D. Helgason, October/2009. All rights reserved.

# PERMISSION TO USE

In presenting this thesis in partial fulfilment of the requirements for a Postgraduate degree from the University of Saskatchewan, I agree that the Libraries of this University may make it freely available for inspection. I further agree that permission for copying of this thesis in any manner, in whole or in part, for scholarly purposes may be granted by the professor or professors who supervised my thesis work or, in their absence, by the Head of the Department or the Dean of the College in which my thesis work was done. It is understood that any copying or publication or use of this thesis or parts thereof for financial gain shall not be allowed without my written permission. It is also understood that due recognition shall be given to me and to the University of Saskatchewan in any scholarly use which may be made of any material in my thesis.

Requests for permission to copy or to make other use of material in this thesis in whole or part should be addressed to:

Head of the Department of Geography and Planning  
117 Science Place  
University of Saskatchewan  
Saskatoon, Saskatchewan  
Canada  
S7N 5C8

# ABSTRACT

Modelling the energy exchange between the snowpack and the atmosphere is critical for many hydrological applications. Of the terms present in the snow energy balance, the turbulent fluxes of sensible and latent heat are the most challenging to estimate, particularly within mountain environments where the hydrological importance is great. Many of the flux estimation techniques, such as the bulk transfer method, are poorly adapted for use in complex terrain. In order to characterize the turbulence and to assess the suitability of flux estimation techniques, eddy covariance flux measurements and supporting meteorological data were collected from two mountain valley forest openings in Kananaskis Country, AB. These sites were generally calm, however wind gusts were frequently observed which markedly affected the turbulence characteristics and increased the rates of momentum and heat transfer. In order to successfully apply the bulk transfer technique at these sites, it was necessary to use environment-specific transfer coefficients to account for the effect of the surrounding complex terrain. These observations were compared with data collected on a treeless alpine ridge near Whitehorse, YT, where it was found that many of the turbulence characteristics were similar to flat sites. However, the boundary layer formed over the alpine ridge was very thin and the site was poorly suited for estimating surface fluxes. The mountain results were further contrasted with data collected over a homogeneous and flat prairie site located near Saskatoon, SK. This site included measurement of all of the snow energy terms, permitting an estimate of the energy balance closure obtainable over snow surfaces. The observed energy balance residual was very large, indicating that the eddy covariance technique was unable to capture all of the turbulent energy. It was concluded that an unmeasured transfer of sensible heat was occurring which was strongly correlated with the long-wave radiation balance. Mechanisms for this relationship were hypothesized. Two snow energy balance models were used to investigate the energy imbalance, where it was observed that the flux terms could be suitably simulated if effective parameters were used to augment the sensible heat transfer rate. The results from this thesis contribute to the understanding of heat transfer processes over snow surfaces during mid-winter conditions and improve the ability to model turbulent heat and mass fluxes from snow surfaces in complex environments.

# ACKNOWLEDGEMENTS

Completion of this dissertation would not have been possible without the support and encouragement received from my colleagues, friends, and family.

I am extremely grateful to my supervisor, Prof. John Pomeroy for providing me this opportunity and for being a patient teacher and mentor. I would also like to extend a special thanks to my advisory committee members: Dr. Alan Barr, Prof. David Sumner, and Dr. Alain Pietroniro, whose guidance and conscientious review of my work has been invaluable. Sincere gratitude is extended to my external examiner, Dr. William Massman, for his careful evaluation of this work and for the welcome insight that he provided.

I would like to recognize the staff of the Centre for Hydrology, Joni Onclin and Mike Solohub for their help in the office, lab, and field and for their friendship throughout.

Thanks to my current colleagues in Agricultural and Bioresource Engineering for their tremendous support and patience while I was ‘distracted’ by an unfinished thesis.

My experience as a student was greatly enriched by all of the other students around me. I would especially like to acknowledge my original office mates Gro Lilbaek and Pablo Dornes, who were always available to have a discussion and made for short enjoyable days.

Much love and thanks are owed to my wife Bobbi for her selfless support and sacrifice during my studies and for her patient understanding through the peaks and valleys encountered along the journey. And of course, thanks to Kaitlyn for reminding me not to take it too seriously.

Finally, I would like to thank my father, Bob Helgason, whose understated guidance and unconditional support throughout my life has brought me to this point.

This thesis is dedicated to the memory of my mother, Vibeke Helgason, for instilling in me the desire to continue learning.

# CONTENTS

<b>Permission to Use</b>	<b>i</b>
<b>Abstract</b>	<b>ii</b>
<b>Acknowledgements</b>	<b>iii</b>
<b>Contents</b>	<b>v</b>
<b>List of Tables</b>	<b>viii</b>
<b>List of Figures</b>	<b>ix</b>
<b>List of Abbreviations</b>	<b>xii</b>
<b>1 Introduction</b>	<b>1</b>
1.1 Background . . . . .	1
1.1.1 Estimating Turbulent Fluxes over Snow Surfaces . . . . .	2
1.2 Scope . . . . .	4
1.3 Specific Objectives . . . . .	4
1.4 Organization of the Thesis . . . . .	4
<b>2 Review of Theory and Literature</b>	<b>6</b>
2.1 Some Physical Properties of Snow . . . . .	6
2.2 Snow Energy Balance . . . . .	6
2.2.1 Energy Transport Mechanisms . . . . .	7
2.3 Turbulent Transport Equations . . . . .	10
2.4 Atmospheric Boundary Layers . . . . .	14
2.5 Parameterization of Turbulent Fluxes over Snow Surfaces . . . . .	17
2.6 Numerical Snow Models . . . . .	21
2.7 Energy Fluxes over Snow . . . . .	22
<b>3 Methods</b>	<b>25</b>
3.1 Study Sites . . . . .	25
3.1.1 Hay Meadow, Kananaskis, Alberta . . . . .	25
3.1.2 Mud Lake, Kananaskis, Alberta . . . . .	33
3.1.3 Kernen Farm, Saskatoon, Saskatchewan . . . . .	35
3.1.4 Wolf Creek Alpine, Whitehorse, Yukon . . . . .	38
3.2 Experimental Methodology . . . . .	41
3.2.1 Eddy Covariance . . . . .	41
3.2.2 Snow Energy Balance Measurements . . . . .	45
3.3 Modelling and Parameterization of Turbulent Flux Processes . . . . .	51

3.3.1	Bulk Transfer Calculation . . . . .	51
3.3.2	Modeling . . . . .	52
<b>4</b>	<b>Observations of the Turbulent Boundary Layer over Snow</b>	<b>54</b>
4.1	Chapter Overview . . . . .	54
4.2	Site Characterization . . . . .	55
4.2.1	Wind Flow Characteristics . . . . .	55
4.2.2	Typical Latent and Sensible Heat Flux Values . . . . .	57
4.3	Characteristics of the Surface Boundary Layer During Well-Developed Flow Conditions . . . . .	58
4.3.1	Meteorological Conditions of Selected Events . . . . .	58
4.3.2	Boundary Layer Structure . . . . .	64
4.3.3	Turbulence Spectra and Cospectra . . . . .	66
4.4	Turbulent Flux Characterization . . . . .	71
4.4.1	Turbulence Scales and Flux Calculation . . . . .	71
4.4.2	Turbulent Transfer Processes . . . . .	78
4.5	Summary of Turbulence Generation Mechanisms . . . . .	83
<b>5</b>	<b>The Snow Energy Balance</b>	<b>87</b>
5.1	Chapter Overview . . . . .	87
5.2	Energy Balance Closure . . . . .	88
5.2.1	Energy Partitioning for Selected Events . . . . .	90
5.2.2	Snow Temperature Profiles . . . . .	93
5.3	Causes of the Energy Imbalance . . . . .	99
5.3.1	Consideration of Missing Energy Terms . . . . .	103
5.4	Summary and Conclusions . . . . .	107
<b>6</b>	<b>Heat Transfer to Permeable Snow Surfaces</b>	<b>108</b>
6.1	Chapter Overview . . . . .	108
6.2	Conceptual Processes of Heat Exchange with Snow Surfaces . . . . .	109
6.2.1	Transfer Mechanisms . . . . .	109
6.2.2	Exchange Area . . . . .	113
6.2.3	Energy Gradient . . . . .	114
6.3	Discussion . . . . .	117
6.4	Chapter Summary . . . . .	118
<b>7</b>	<b>Parameterizing Turbulent Fluxes over Snow Surfaces</b>	<b>119</b>
7.1	Chapter Overview . . . . .	119
7.2	Homogeneous Prairie - Kernen Farm . . . . .	119
7.2.1	Measured Turbulent Exchange Coefficients . . . . .	120
7.2.2	Strategies for Parameterization . . . . .	122
7.2.3	Numerical Snow Modelling . . . . .	126
7.3	Mountain Valley (Hay Meadow) . . . . .	131

7.3.1	Measured Turbulent Exchange Coefficients . . . . .	131
7.3.2	Strategies for Parameterization . . . . .	132
7.4	Summary and Conclusions . . . . .	138
7.4.1	Summary and Recommendations for the Prairie Environment . . . . .	138
7.4.2	Recommendations for Mountain Valleys . . . . .	139
<b>8</b>	<b>Summary and Conclusions</b>	<b>140</b>
<b>A</b>	<b>Background Meteorological Conditions</b>	<b>161</b>
<b>B</b>	<b>Spectra and Cospectra</b>	<b>167</b>

# LIST OF TABLES

2.1	Roughness length values for snow and ice surfaces selected from literature. . . . .	20
3.1	Hay Meadow A (2005) instrumentation details. . . . .	28
3.2	Hay Meadow B (2006) instrumentation details. . . . .	32
3.3	Mud Lake (2006) instrumentation details. . . . .	34
3.4	Kernen Farm (2007) instrumentation details. . . . .	37
3.5	Wolf Creek Alpine (2007) instrumentation details. . . . .	40
3.6	Critical values of non-dimensional frequency. . . . .	43
4.1	Mean turbulence characteristics observed during selected events. . . . .	61
4.2	Example values of the normalized standard deviation of velocity components collected in various environments. . . . .	64
4.3	Total contribution to flux from scales beyond the turbulence gap. . . . .	72
4.4	Percentage of records that are classified as non-stationary. . . . .	77
5.1	Summary of conditions pertaining to temperature profiles in Figure 5.6. . . . .	97
7.1	Performance of bulk transfer parameterization schemes. . . . .	124
7.2	Performance of simulated turbulent fluxes. . . . .	127
7.3	Accumulated turbulent fluxes (Hay Meadow 2005). . . . .	138

# LIST OF FIGURES

2.1	Conceptual snow energy balance approaches. . . . .	7
2.2	Depiction of atmospheric boundary layer structure. . . . .	12
2.3	Roughness length ratios as described by the Andreas (1987b) model. . . . .	19
3.1	Contour map of Hay Meadow clearing, showing location of measurement towers. . . . .	27
3.2	Photograph of Hay Meadow tower at location A (2005). . . . .	30
3.3	Photograph of Hay Meadow clearing. . . . .	31
3.4	Photograph of Mud Lake. . . . .	35
3.5	Photograph of Kernen Farm. . . . .	36
3.6	Photograph of Wolf Creek Alpine site. . . . .	39
3.7	Schematic of snow thermocouple array. . . . .	47
4.1	Frequency distribution of mean 30 min. wind speeds. . . . .	56
4.2	Variation of mean turbulence intensity with wind speed: (a) longitudinal, (b) vertical. . . . .	57
4.3	Variation of the turbulent kinetic energy with mean horizontal wind speed. . . . .	58
4.4	Heat flux frequency distribution: (a) sensible heat flux; (b) latent heat flux. . . . .	59
4.5	Comparison of winds at HM valley bottom and upwind ridge top for 26 February, 2006: (a) mean wind speed; (b) mean wind direction. . . . .	62
4.6	Selected wind speed profiles measured at HM on 26 February, 2006. . . . .	63
4.7	Frequency weighted, normalized longitudinal velocity spectra. . . . .	67
4.8	Frequency weighted, normalized lateral velocity spectra. . . . .	68
4.9	Frequency weighted, normalized vertical velocity spectra. . . . .	68
4.10	Frequency weighted, normalized momentum cospectra. . . . .	69
4.11	Frequency weighted, normalized kinematic heat flux cospectra. . . . .	70
4.12	Frequency weighted, normalized kinematic water vapour flux cospectra. . . . .	70
4.13	Example of MRFD applied to Kernen Farm (wind speed $\approx 7 \text{ m s}^{-1}$ ). . . . .	73
4.14	Example of MRFD applied to Kernen Farm (wind speed $\approx 1 \text{ m s}^{-1}$ ). . . . .	74
4.15	Example of MRFD applied to HM (wind speed $\approx 4.5 \text{ m s}^{-1}$ ). . . . .	75
4.16	Ratio of vector averaged wind speed to the average instantaneous wind speed. . . . .	76
4.17	Offset angle between horizontal wind speed vector and kinematic momentum flux vector. . . . .	77
4.18	Momentum non-stationarity vs. mean wind speed (bin averaged). . . . .	78
4.19	Friction velocity as a function of wind speed for near-neutral conditions ( $\bar{u} > 1.0 \text{ m s}^{-1}$ ). . . . .	79
4.20	Linear correlation coefficients for u-w velocity components. . . . .	80
4.21	Friction velocity vs. mean wind speed . . . . .	81
4.22	Temperature scale as a function of the bulk temperature gradient for near-neutral conditions ( $U > 1.0 \text{ m s}^{-1}$ ). . . . .	82
4.23	Linear correlation coefficients of kinematic heat flux components (w-T). . . . .	82

4.24	Vapour density scale as a function of the bulk specific humidity gradient for neutral conditions ( $U > 1.0 \text{ m s}^{-1}$ ). . . . .	83
5.1	Energy balance closure. . . . .	89
5.2	Cumulative energy fluxes measured over the month of February. . . . .	90
5.3	4-5 Feb. event: (a) wind speed (1.75 m); (b) air and snow temperatures; (c) measured surface fluxes; (d) comparison of surface fluxes with internal energy changes. . . . .	94
5.4	7-8 Feb. event: (a) wind speed (1.75 m); (b) air and snow temperatures; (c) measured surface fluxes; (d) comparison of surface fluxes with internal energy changes. . . . .	95
5.5	13-15 Feb. event: (a) wind speed (1.75 m); (b) air and snow temperatures; (c) measured surface fluxes; (d) comparison of surface fluxes with internal energy changes. . . . .	96
5.6	Snow temperature profiles. . . . .	98
5.7	Internal energy change of near surface snowpack vs. air temperature measured at 1.58 m. . . . .	105
5.8	The limiting Bowen ratio value as a function of surface temperature. . . . .	106
6.1	Conceptual wind velocity profile over a permeable snow surface. . . . .	111
6.2	Slip velocities estimated for the snow-air interface. . . . .	112
6.3	Conceptual temperature profile at the air-snow interface. . . . .	114
6.4	Surface temperature depression dependency on $Q_{LW}$ and $\bar{u}$ . . . . .	116
7.1	Inferred drag coefficient ( $C_d$ ) for KF filtered data: (a) stable conditions; (b) unstable conditions. . . . .	120
7.2	Inferred bulk heat transfer coefficient ( $C_h$ ) for KF filtered data: (a) stable conditions; (b) unstable conditions. . . . .	121
7.3	Ratio of turbulent transfer coefficients for KF ( $C_d C_h^{-1}$ ) for KF filtered data. . . . .	121
7.4	Inferred bulk vapour transfer coefficient ( $C_v$ ) for KF filtered data. . . . .	122
7.5	Cumulative daily turbulent heat fluxes as measured as the energy balance residual and calculated by various bulk transfer parameterization scenarios. . . . .	124
7.6	The ratio of transfer coefficients, $C_d C_h^{-1}$ , predicted by Andreas (1987b) at increasing wind speeds under neutral conditions for various $z_{0m}$ values. . . . .	126
7.7	KF numerical modelling - energy partitioning. . . . .	129
7.8	KF numerical modelling - energy flux comparison. . . . .	130
7.9	Comparison of off-line modelling approach (surface renewal model; $z_{0m} = 1.0 \times 10^{-3}$ ) with SNTHERM-1. . . . .	131
7.10	HM bulk transfer drag coefficient $C_d$ , as it varies with stability. . . . .	132
7.11	HM bulk transfer (a) heat coefficient ( $C_h$ ), and (b) vapour transfer coefficient ( $C_v$ ), as they vary with stability. . . . .	133
7.12	HM bulk transfer coefficient ratios as they vary with stability. . . . .	133
7.13	Estimation of sensible heat fluxes using bulk transfer formulae, Hay Meadow 2005. . . . .	135
7.14	Estimation of latent heat fluxes using bulk transfer formulae, Hay Meadow 2005. . . . .	136
7.15	Sum of the estimated turbulent heat fluxes, Hay Meadow 2005. . . . .	137

A.1	Background meteorological conditions of data collection period of HM site A.	162
A.2	Background meteorological conditions of data collection period of HM site B.	163
A.3	Background meteorological conditions of data collection period of ML. . . . .	164
A.4	Background meteorological conditions of data collection period of KF. . . . .	165
A.5	Background meteorological conditions of data collection period of WCA. . . . .	166
B.1	Composite $w$ spectra for sites and events considered in Chapter 4. . . . .	168
B.2	Composite $u$ spectra for sites and events considered in Chapter 4. . . . .	168
B.3	Composite $v$ spectra for sites and events considered in Chapter 4. . . . .	169
B.4	Composite $T_s$ spectra for sites and events considered in Chapter 4. . . . .	169
B.5	Composite $\rho_v$ spectra for sites and events considered in Chapter 4. . . . .	170
B.6	Composite $uw$ cospectra for sites and events considered in Chapter 4. . . . .	170
B.7	Composite $wT$ cospectra for sites and events considered in Chapter 4. . . . .	171
B.8	Composite $w\rho_v$ cospectra for sites and events considered in Chapter 4. . . . .	171

# LIST OF ABBREVIATIONS

CLASS	Canadian Land Atmosphere Surface Scheme
HM	Hay Meadow
KF	Kernen Farm
ML	Mud Lake
M-O	Monin Obukhov [similarity theory]
MRFD	multi resolution flux decomposition
RMSE	root mean squared error
SSA	specific surface area
TKE	turbulent kinetic energy
UEB	Utah Energy Balance
WCA	Wolf Creek Alpine
$A$	surface area
$a$	ratio of eddy diffusivities
$Bo$	Bowen ratio
$Bo^*$	Bowen limit
$C_d$	bulk drag coefficient
$C_h$	bulk heat transfer coefficient
$C_v$	bulk vapour transfer coefficient
$CO_{AB}$	cospectral intensity of variables A and B
$c_p$	specific heat (at constant pressure)
$D_p$	particle diameter
$d$	snow layer thickness
$E$	evaporation mass flux
$E_A$	discrete spectral intensity of variable A
$e$	kinetic energy per unit mass
$e_{ref}$	vapour pressure of air at a reference height
$e_{surf}$	vapour pressure of air at the surface
$f$	coriolis parameter
$f$	function of variables
$f$	frequency
$g$	acceleration due to gravity
$H$	height of the snowpack
$H_R$	radiation flux divergence
$h_{a \rightarrow i}$	interfacial heat transfer coefficient (between air and ice)
$h_o$	height of roughness elements
$h_v$	volumetric interfacial heat transfer coefficient
$\mathbf{i}$	stream-wise unit vector
$\mathbf{j}$	span-wise unit vector
$K$	permeability
$K_m$	eddy diffusivity for momentum
$K_h$	eddy diffusivity for heat

$K_v$	eddy diffusivity for vapour
$k$	thermal conductivity
$\mathbf{k}$	wall-normal unit vector
$L$	Obukhov length
$L_{fus}$	latent heat of fusion
$L_{sub}$	latent heat of sublimation
$L_{vap}$	latent heat of evaporation
$N$	number of samples
$Nu$	Nusselt number
$n$	porosity (Ch. 6)
$n$	non-dimensional frequency (Ch. 3 & 4)
$P$	pressure
$Pe$	Peclet number
$Pr$	Prandtl number
$Q^*$	net all-wave radiation flux
$Q_A$	advected energy flux
$Q_E$	latent heat flux
$Q_G$	ground heat flux
$Q_H$	sensible heat flux
$Q_{L^*}$	long-wave radiation flux
$Q_{Li}$	incoming long-wave radiation flux
$Q_{Lo}$	outgoing long-wave radiation flux
$Q_K$	energy flux to the snowpack
$Q_{S^*}$	net short-wave radiation flux
$Q_{Si}$	incoming short-wave radiation flux
$Q_{So}$	outgoing short-wave radiation flux
$q$	specific humidity
$q_r'''$	rate of volumetric energy conversion due to radiation
$q_{ref}$	specific humidity at reference height
$q_{surf}$	specific humidity at surface
$R_F$	rate of freezing
$R_M$	rate of melting
$Re^*$	roughness Reynold's number
$Re_D$	particle diameter Reynold's number
$Re_K$	permeability Reynold's number
$Ri_b$	bulk Richardson number
$r$	linear correlation coefficient
$S$	sublimation mass flux
$S_A$	spectral intensity of variable A
$S_q$	source or sink of vapour
$Sc$	Schmidt number
$T$	temperature
$T$	period length
$T_{ref}$	air temperature at reference height
$T_s$	sonic temperature

$T_{surf}$	surface temperature
$T^*$	non-dimensional temperature scale
$t$	time
$U$	internal energy content of the snowpack
$u$	longitudinal horizontal (stream-wise) wind velocity component
$u_p$	filter velocity within snowpack
$u_s$	slip velocity
$u_*$	friction velocity
$V$	volume
$v$	latitudinal horizontal (span-wise) wind velocity component
$\mathbf{v}$	wind vector
$w$	vertical (wall-normal) wind velocity component
$z$	vertical distance above some datum
$z_{0m}$	roughness length for momentum transfer
$z_{0q}$	roughness length for vapour transfer
$z_{0s}$	roughness length for arbitrary scalar transfer
$z_{0T}$	roughness length for heat transfer
$\alpha$	structure coefficient for Beavers and Joseph (1967) boundary condition.
$\epsilon$	emissivity
$\epsilon_{diss}$	rate of energy dissipation
$\zeta$	dimensionless M-O stability parameter
$\theta$	potential temperature
$\kappa$	von Kármán constant
$\kappa_h$	molecular diffusivity of heat
$\kappa_v$	molecular diffusivity of water vapour
$\lambda$	wavelength
$\nu$	kinematic fluid viscosity
$\rho$	density
$\rho_{vs}$	saturation vapour pressure
$\sigma$	standard deviation
$\sigma$	Stefan-Boltzman constant
$\tau$	momentum flux
$\Phi$	latitude
$\phi$	volume fraction
$\phi_h$	dimensionless temperature gradient
$\phi_m$	dimensionless wind shear
$\phi_v$	dimensionless vapour gradient
$\psi_h$	M-O similarity function for heat
$\psi_m$	M-O similarity function for momentum
$\psi_v$	M-O similarity function for vapor
$\Omega$	angular frequency
$\nabla$	vector differential operator

# CHAPTER 1

## INTRODUCTION

### 1.1 Background

A large portion of the earth's land surface is covered by snow and ice; either in a quasi-permanent state as polar ice-sheets and alpine glaciers, or in a temporary state as in seasonal snow-covers. The importance of the snow-cover spans many physical and temporal scales. Locally, the snow-cover provides critical ground insulation for many winter ecological processes (Campbell et al. (2005); Jones and Pomeroy (1998)); replenishes soil moisture reserves through snow melt infiltration (*e.g.* Grace 1990); and refills surface water bodies from snowmelt runoff, sustaining aquatic ecosystems. On a regional scale, snowmelt is responsible for the bulk of the flow in many rivers (Armstrong and Brown 2008) and contributes towards recharging groundwater supplies (Hayashi et al. 2003). On scales ranging from local to global, the snow surface interacts with the atmosphere by lowering temperatures through a reduced surface albedo and through sublimating and melting snow. Melting ice sheets affect sea surface temperatures, ocean currents, and ultimately the jet stream patterns (Barry 2002). In many cases, even those areas that never directly receive precipitation in its solid form are in some manner impacted by the snow cover.

Given the vast impact that the snow cover has on human activities and comfort, there is considerable interest in being able to model the interactions between the snow cover and the atmosphere; chiefly concerning the flow of energy between the two media. A few of the primary application areas include: (1) prediction of snowmelt rates for hydrological purposes; (2) determination of land surface - atmosphere interactions for climate modeling and weather prediction; and (3) prediction of avalanche hazard for for the transportation and recreation industries.

A general energy balance, defined for the snow-atmosphere interface is presented in (1.1), where the sum of the net radiation heat transfer ( $Q^*$ ) to the snow surface and the turbulent sensible heat ( $Q_H$ ) transfer due to forced convection imposed by the wind, and the latent energy ( $Q_E$ ) required for a convective mass transfer involving a phase change from solid to

vapour state, is balanced by the energy transfer to the snowpack ( $Q_K$ ).

$$Q^* + Q_H + Q_E = Q_K \quad (1.1)$$

The goal of the work described in this thesis is to improve the understanding of the surface energy balance, and to further develop the techniques used to model the physical processes concerning snow melt and atmospheric energy exchange. The focus is specifically on the turbulent transfer of heat and mass over snow surfaces.

### 1.1.1 Estimating Turbulent Fluxes over Snow Surfaces

Methods for calculating turbulent fluxes typically employ a simplified set of turbulent transport equations, along with some variation of a first order turbulence closure scheme (flux-gradient, K-theory, bulk transfer method, etc.) and then utilize Monin Obukhov similarity theory (hereafter referred to as M-O theory) to account for the effect of density stratification upon the flow. These techniques will be presented in detail in Chapter 2, however an introduction to the technique is provided here using the bulk transfer method as an example. Using equations (1.2)-(1.4), the friction velocity  $u_*$ , the sensible heat flux  $Q_H$ , and the latent heat flux  $Q_E$  can be calculated from the gradients of wind speed  $u$ , temperature  $T$ , and specific humidity  $q$  between the reference height (subscript  $z$ ), and the snow surface (subscript  $s$ ). The transfer coefficients, usually termed the roughness lengths, for momentum, heat, and water vapour are given as  $z_{0m}$ ,  $z_{0T}$ , and  $z_{0q}$ , respectively. The profile correction factors, which use M-O theory to account for the effect of thermal stratification on turbulence, are given as  $\psi_m$ ,  $\psi_h$ , and  $\psi_v$  for momentum, heat and water vapour respectively.

$$u_* = \kappa \bar{u} \left[ \ln \left( \frac{z}{z_{0m}} \right) - \psi_m \right]^{-1} \quad (1.2)$$

$$Q_H = \kappa \rho c_p u_* (T_z - T_s) \left[ \ln \left( \frac{z}{z_{0T}} \right) - \psi_h \right]^{-1} \quad (1.3)$$

$$Q_E = \kappa \rho L_{sub} u_* (q_z - q_s) \left[ \ln \left( \frac{z}{z_{0q}} \right) - \psi_v \right]^{-1} \quad (1.4)$$

The resulting equations (1.2)-(1.4) are based on the simplifying argument that the turbulent fluxes are proportional to the mean gradients, along with an empirical correction for the effects of atmospheric stability. The use of these equations, and their appropriate parameter values, has been the subject of much experimental and theoretical research, which will be reviewed in Chapter 2. However, the majority of the development work has been conducted

in flat, homogeneous terrain, and is often based upon highly selective datasets. The research has necessarily been implemented in this manner; forced by the motivation to find a tractable way to represent the incredibly complex turbulent flow that occurs over the heterogeneous earth surface.

At the present time, there is considerable interest in applying snowmelt and atmospheric models in mountainous areas. From a hydrological perspective, these areas are very significant as they are commonly snow-covered and are often the primary hydrological contributors to rivers that supply water to vast surrounding areas. In addition to hydrological modeling results that could forecast stream flow, it is also desirable to model the interactions between the snow- or ice-covered mountains and the overlying atmosphere, which is of great significance for accurate weather prediction, and understanding the effects of climate change. Prediction of avalanche hazard exclusively concerns mountainous terrain, with a stringent requirement to estimate the climatic forcing and the resulting metamorphism of the snowpack that could create avalanche-prone stratigraphy. To date, most modeling efforts have used these simplified calculation techniques just described.

From both the modeling and measurement perspectives, heterogeneous, snow-covered mountain terrain presents some serious challenges. The most significant obstacle is to model the effect of turbulence due to complex wind flow patterns in such an environment. At present, our understanding of atmospheric boundary layers in complex environments is incomplete. The mountain environment has received relatively little study by micrometeorologists, resulting in considerable uncertainty about turbulent transfer processes in these environments. Furthermore, the stable boundary layer which often develops over snow surfaces, is less studied than its neutral or unstable counterparts. The effect of this is that there is very little existing information that could be used to assess the suitability of existing flux estimation techniques and parameterizations in complex mountain terrain.

The limitations of the basic flux-gradient approach and the semi-empirical parameterizations need to be reassessed. At the very least, the existing practices must be critically examined considering that flux-gradient approaches were developed from the theory of horizontally homogeneous, equilibrium boundary layers, and M-O theory and its empirical formulations has been developed and validated from experiments over large flat, homogeneous regions. Thus it is expected that these techniques will yield uncertain results for highly complex mountain regions. However, despite this limitation, these techniques are still commonly employed in these areas; largely because this approach is computationally tractable. More complicated efforts that consider full three-dimensional, unsteady flows and make use of higher order turbulence schemes greatly increase the computational requirement. When the additional requirement of handling stratified flow is included, the current state of model

development is exceeded.

In this thesis, the turbulence structure of complex mountainous areas was investigated by making direct measurements of the turbulent fluxes in two mountain valleys in Kananaskis Country, AB, and at a mountain ridge top site near Whitehorse, YT. In order to contrast the mountain sites with a more simple environment, and also to investigate measurement and modeling difficulties that are specific to cold snow-covered surfaces, detailed energy balance measurements were made at a near-ideal homogeneous site located near Saskatoon, SK. The data collected from these contrasting environments were then used to evaluate the flux-gradient approach.

## 1.2 Scope

This work specifically examines turbulent fluxes from static snow surfaces (not actively being transported by the wind), and in open areas where the vegetation is buried by snow. The immediate area is considered open and is relatively homogeneous, however surrounding areas may not be. The mountain environments included in this assessment of surface turbulence processes in complex terrain are limited to include two mountain valleys and a broad alpine ridge. The complex environments are contrasted with an open and level prairie environment. For this thesis, only point scale processes are considered as the spatial distribution of turbulence and energy were not measured.

## 1.3 Specific Objectives

The specific objectives of this thesis are to:

1. Describe the processes affecting turbulent transfer over snow surfaces in open environments of differing topographic complexity;
2. Develop a better understanding of the energy exchange mechanisms operating between the snowpack and the atmosphere;
3. Assess the limitations of the currently employed flux-gradient estimation techniques in open environments.

## 1.4 Organization of the Thesis

Chapter 2 presents the relevant theory of estimating the energy transfer to snow surfaces and reviews recent literature pertaining to this topic. Chapter 3 details the study sites, their

instrumentation, as well as describes the approach taken to evaluate each specific objective. Chapter 4 addresses the 1st objective, Chapters 5-6 the 2nd objective, and Chapter 7 the final objective. Last, the findings are summarized and recommendations are provided in Chapter 8.

# CHAPTER 2

## REVIEW OF THEORY AND LITERATURE

### 2.1 Some Physical Properties of Snow

Snow on the ground is a porous medium, made up of an ice matrix with the interstitial space occupied by air and liquid water. Recently fallen snow has an average density of 50-120 kg m<sup>-3</sup> (Pomeroy and Gray 1995). Individual snow crystals falling to the ground quickly undergo metamorphism, where temperature and vapour gradients within the snowpack cause the shape of individual crystals and the properties of the ice matrix to change (Colbeck 1982). The density of snow increases with age where it is affected by metamorphism and by redistribution processes such as wind transport, resulting in typical densities ranging from 200-350 kg m<sup>-3</sup> (Pomeroy and Gray 1995). Low density layers are formed when large snow crystals form under strong vapour gradients such as depth hoar (Sturm and Benson 1997) or surface hoar (Colbeck 1988). Conversely, when rain or melt water freezes within the snowpack dense ice layers are formed. The porous nature of snow, and the variable micro-structure permits a very large specific surface area (measurements by Legagneaux et al. (2002) report values ranging from 100 to 1580 cm<sup>2</sup> g<sup>-1</sup>) over which potential heat and mass exchange can occur.

### 2.2 Snow Energy Balance

Determination of the amount of energy available for snowmelt relies on a conceptual energy balance of a control volume which may be defined for the entire snowpack, or for a single layer of snow, or alternatively a control surface placed at the air-snow interface (Figure 2.1). For the general case of a one-dimensional energy balance the sum of all of the vertical energy fluxes through the upper and lower faces of the control volume is equal to the rate of change in the internal energy content of the volume.

In the case of selecting a control volume for the entire snowpack, such as in Male and Gray (1981), the energy balance can be written as (2.1), where  $Q^*$  is the net radiation flux,  $Q_H$  is

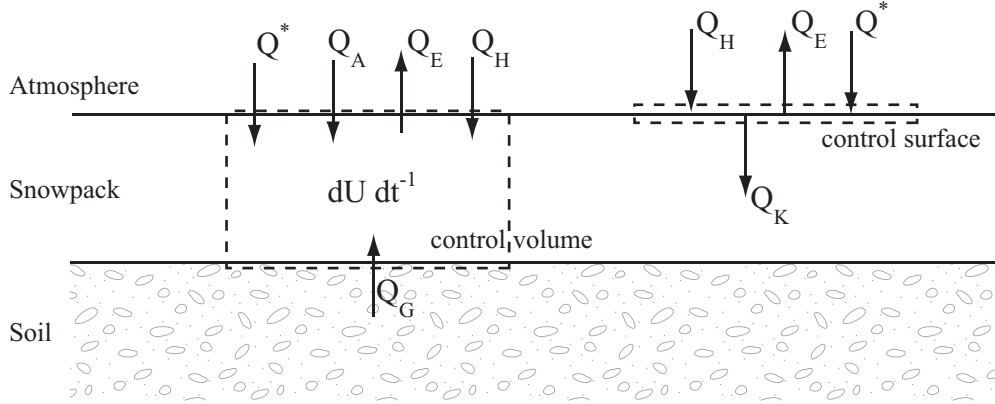


**Figure 2.1:** Conceptual snow energy balance approaches.

the sensible heat flux,  $Q_E$  is the latent heat flux,  $Q_A$  is the heat flux that is due to advected energy, such as that contained in liquid precipitation falling on snow,  $Q_G$  is the ground heat flux, and  $U$  is the internal energy content of the snowpack. If the energy balance is adopted for a single layer of snow, the individual terms present depend on the vertical position of the layer within the snowpack.

$$\frac{dU}{dt} = Q^* + Q_H + Q_E + Q_A + Q_G \quad (2.1)$$

Alternatively, an energy balance can be drawn around the snow-air interface as in (2.2), where  $Q_A$  has been omitted. This formulation is for an infinitesimally-thin volume with negligible mass so changes in internal energy can be neglected, and heat fluxes directed towards the snowpack are denoted as  $Q_K$ . One potential shortcoming of this approach is that not all of the energy conversions occur exactly at the surface. For example, the incoming shortwave radiation flux penetrates the semi-transparent snowpack (*e.g.* Warren 1982), requiring that  $Q_K$  be an effective parameter that may include radiation, conduction, and convection heat transfer modes, as will be discussed in the following section.

$$Q_H + Q_E + Q^* = Q_K \quad (2.2)$$

### 2.2.1 Energy Transport Mechanisms

The net all-wave radiation flux,  $Q^*$  consists of the sum of the net shortwave, or solar radiation fluxes (with wavelengths,  $\lambda$ , ranging from 0.3 to 5  $\mu\text{m}$ ), and the net long wave, or thermal infrared radiation fluxes ( $5 < \lambda < 40 \mu\text{m}$ ) (Warren 1982). This relationship is presented in (2.3) where  $Q_{Si}$  and  $Q_{So}$  are the incoming and outgoing shortwave radiation fluxes, and  $Q_{Li}$  and  $Q_{Lo}$  are the incoming and outgoing long wave radiation fluxes.

$$Q^* = Q_{Si} + Q_{So} + Q_{Li} + Q_{Lo} \quad (2.3)$$

With respect to shortwave radiation, the important properties are reflectance and transmission. The ratio of reflected radiation to that received is often termed the shortwave albedo, which varies as a function of wavelength. The albedo is largely dependent on snow grain size (Wiscombe and Warren 1980), causing a decrease in reflectance as snow ages and undergoes metamorphism, and it also depends on impurities present in the snow (Warren and Wiscombe 1980). The spectrally integrated albedo of snow ranges from about 90% for fresh snow to less than 60% for melting snow (Warren 1982). Due to the translucent nature of snow, transmission of solar radiation is quite important. The downward flux of solar radiation extinguishes approximately exponentially with depth due to adsorption and scattering (Male and Gray 1981).

At longer wavelengths, most of the radiation is adsorbed within a few particle diameters (Berger 1979). Very little thermal radiation is reflected, resulting in snow acting as a near-blackbody in the thermal infrared range with an emissivity of 0.985-0.99 (Dozier and Warren 1982, Warren 1982).

The sensible heat flux,  $Q_H$ , represents the energy that is transferred by means of convection (may be forced, free, or mixed modes) between the snowpack and the overlying air. The latent heat flux,  $Q_E$ , is the energy required to sublimate snow particles. By definition,  $Q_E$  is coupled with the mass flux of evaporation (sublimation) by  $Q_E = L_{sub}S$ , where  $L_{sub}$  is the latent heat of sublimation, and  $S$  is the mass flux of sublimation. Together  $Q_H$  and  $Q_E$  are collectively referred to as the turbulent heat fluxes. These transport mechanism are the focus of this thesis and will be elaborated on in §2.3.

Advected energy,  $Q_A$ , may be transported to the snowpack or between layers in the forms of liquid precipitation (*e.g.* Marks et al. 1998) or melt water (*cf.* Albert and Krajieski 1998), which change phase within the specified control volume thereby releasing latent heat. It may also occur when mass is horizontally advected into the control volume by blowing snow (Pomeroy 1988), or when energy (sensible heat) is advected into the control volume by upwind snow-free patches (Shook and Gray 1997, Granger et al. 2002).

The ground heat flux term,  $Q_G$ , represents the energy transfer between the bottom of the snowpack and the underlying medium (*e.g.* soil, peat, or rock). For seasonal snow-covers,  $Q_G$  is usually a source of energy to the snowpack as the ground cools. This energy term, although it is often of minor significance, plays a large role in controlling the thermal regime of the bottom of the snowpack and can sometimes play a role in snowmelt (Male and Gray 1981).

As suggested in the preceding section, the flow of energy within the snowpack is very

complex and many mechanisms are responsible. Energy transfers due to thermal conduction, free and forced convection, penetration of solar radiation, and latent heat transfer due to vapour diffusion and phase change may all be occurring simultaneously within the snowpack.

With respect to thermal conduction, the conductivity values for snow reported in the literature are commonly reported as ‘effective’ thermal conductivity values that generally contain three transport processes lumped into a single value (Sturm et al. 1997). The processes included are: (1) conduction through the ice lattice; (2) conduction through the pore space; and (3) latent heat transport across pore spaces due to vapour sublimation and condensation. Arons and Colbeck (1998) suggest that the latent contribution may be responsible for 50% of the heat transfer in snow. The thermal conductivity can be described from snow micro-structure (*e.g.* Arons and Colbeck 1998) or it can be estimated from snow density.

Forced convection within the pore space can occur where the permeability is large enough and there is a forcing pressure gradient. Albert and Hardy (1995) artificially induced a surface pressure of 2.5 Pa in a shallow (28 cm) snowpack using a fan. Within minutes, a response in the snowpack temperature was noted. Albert and Schultz (2002) made direct measurement of naturally occurring ventilation by measuring the downwind concentration of SF<sub>6</sub> that was injected into a hoar layer at depth of 15 cm and timing the arrival of the plume of gas. Under light winds (3 m s<sup>-1</sup>), the measured interstitial velocity was 0.2 cm s<sup>-1</sup>, just slightly higher than what would be expected for diffusion alone. However, when the test was conducted at a wind speed of 9 m s<sup>-1</sup> the interstitial velocity was 1.3 cm s<sup>-1</sup>, providing evidence that ventilation was occurring.

Large temperature gradients within the snowpack can also cause free convection to occur. In a snowpack, this may occur due to differential heating at the soil-snow interface, such as differences in soil temperature due to uneven soil moisture. Sturm (1991) observed the effects of convection in a highly permeable seasonal snowpack in Alaska, and calculated the average convective velocity to be around 0.2 mm s<sup>-1</sup>.

The internal energy content of the snow,  $U$ , depends on the snow density, the temperature and the amount of liquid water in the snowpack, and can be calculated for a layer of snow with thickness  $d$  as (2.4) where  $\rho$  is the density,  $c_p$  is the heat capacity, and  $\phi$  is the fraction of volume occupied by a particular constituent. The formulation presented here assumes that the porous medium is at thermal equilibrium, *i.e.*  $T_s = T_i = T_w = T_a$  where the subscripts  $s$ ,  $i$ ,  $w$ , and  $a$  denotes snow, ice, liquid water, and air, respectively.

$$U = d(\rho_i c_{p,i} \phi_i + \rho_a c_{p,a} \phi_a + \rho_w c_{p,w} \phi_w) T_s \quad (2.4)$$

## 2.3 Turbulent Transport Equations

The following section describes how the equations for estimating the turbulent fluxes are derived, and summarizes the more detailed presentations in Brutsaert (1982), Jensen and Busch (1982) and Stull (1988). In modeling the transfer of heat and vapour between the surface and the atmosphere, the vapour and temperature fields are considered to be transported by the wind field. The necessary set of equations includes a statement about the conservation of mass, the Navier-Stokes equations to represent the wind field, as well as conservation equations for energy and water vapour. A Cartesian coordinate system is used, where the wind velocity vector  $\mathbf{v} = \mathbf{i}u + \mathbf{j}v + \mathbf{k}w$  is the sum of its components in the stream-wise, span-wise and wall-normal directions, respectively. In the adopted vector notation, the del operator  $\nabla = \mathbf{i}\frac{\partial}{\partial x} + \mathbf{j}\frac{\partial}{\partial y} + \mathbf{k}\frac{\partial}{\partial z}$  is used to represent the 3-D nature of the transport equations.

To adequately describe the flow, the continuity equation (2.5) and the Navier-Stokes equations (2.6), for an incompressible fluid with constant viscosity, under the Boussinesq approximations (which state that density variations are negligible except where included in the gravitational body force), are used along with a term for the effect of the earth's rotation on the coordinate system. The terms included in (2.6), from left to right, are the (i) inertial and (ii) advective rates of change in the wind vector,  $\mathbf{v}$ , which are balanced by the forces acting per unit mass of fluid: (iii) due to the pressure gradient,  $\nabla P$ , (iv) due to gravity,  $g$ , with a correction for temperature-induced fluid density variations, (v) internal stresses due to viscosity,  $\nu$ , and (vi) and due to Coriolis acceleration which is caused because the coordinate system is rotating with an angular frequency,  $\Omega$ . The pressure, density,  $\rho$ , and virtual temperature,  $T_V$ , are considered to have a static part (subscript S) and a dynamic part (subscript D) which varies slightly with elevation (Brutsaert 1982).

$$\nabla \cdot \mathbf{v} = 0 \quad (2.5)$$

$$\frac{\partial \mathbf{v}}{\partial t} + (\mathbf{v} \cdot \nabla) \mathbf{v} = -\frac{1}{\rho_s} \nabla P_D + g \left( \frac{T_{VD}}{T_{VS}} \right) \mathbf{k} + \nu \nabla^2 \mathbf{v} - 2\Omega \times \mathbf{v} \quad (2.6)$$

The energy and moisture conservation equations (2.7-2.8) both assume that the potential temperature,  $\theta$ , and specific humidity,  $q$ , can be considered as conservative properties of the air. The potential temperature is defined as the temperature which an air parcel would be at if it were transported adiabatically from its reference state to a reference pressure of 100 kPa, and is related to the actual temperature,  $T$ , by  $\theta = T(1000/P)^{R/c_p}$ . The changes in concentration of  $\theta$  and  $q$  with time are then modeled as advection-diffusion problems, where  $\kappa_h$  and  $\kappa_v$  are the molecular diffusivities for heat and vapour, respectively. In the case of the

energy equation (2.7), the last two terms on the right hand side represent the radiative flux divergence, where  $H_R$  is the local radiative heat flux, and the energy change associated with phase change, where  $L_{vap}$  is the latent heat of vaporization and  $E$  is the rate of evaporation. In the conservation of water vapour equation (2.8)  $S_q$  is a body source term representing additional vapour sources.

$$\frac{\partial \theta}{\partial t} + (\mathbf{v} \cdot \nabla) \theta = k_h \nabla^2 \theta - \frac{1}{\rho c_p} \nabla \cdot H_R - \frac{1}{\rho c_p} L_{vap} E \quad (2.7)$$

$$\frac{\partial q}{\partial t} + (\mathbf{v} \cdot \nabla) q = k_v \nabla^2 q + \frac{S_q}{\rho} \quad (2.8)$$

Since the flow in the atmosphere near the earth surface is usually turbulent, Reynolds decomposition is applied to separate each instantaneous variable into a mean and fluctuating part, i.e.  $T = \bar{T} + T'$ ,  $w = \bar{w} + w'$ , etc., where the over-bar indicates the mean part and prime denotes the fluctuating part. After applying the decomposition method to the conservation equations, new equations for the mean and fluctuating parts are obtained. Only the equations for the mean parts are further presented in this thesis as (2.9) - (2.12), where in equations (2.10) to (2.12), the third term from the left is the introduced transport term due to turbulent motions. This term causes considerable difficulty because of the fluctuating product. Since this term is not often measured, it must be modeled. However, modeling it using higher order terms introduces even higher order terms, thus creating the so-called turbulence closure problem

$$\nabla \cdot \bar{\mathbf{v}} = 0 \quad (2.9)$$

$$\frac{\partial \bar{\mathbf{v}}}{\partial t} + (\bar{\mathbf{v}} \cdot \nabla) \bar{\mathbf{v}} + (\nabla \cdot \overline{\mathbf{v}'\mathbf{v}'}) = -\frac{1}{\rho_s} \nabla \bar{P}_D + g \left( \frac{\bar{T}_{VD}}{\bar{T}_{VS}} \right) \mathbf{k} + \nu \nabla^2 \bar{\mathbf{v}} - 2\Omega \times \bar{\mathbf{v}} \quad (2.10)$$

$$\frac{\partial \bar{\theta}}{\partial t} + (\bar{\mathbf{v}} \cdot \nabla) \bar{\theta} + (\nabla \cdot \overline{\mathbf{v}'\theta'}) = \kappa_h \nabla^2 \bar{\theta} - \frac{1}{\rho c_p} \nabla \cdot H_R - \frac{1}{\rho c_p} L_{vap} E \quad (2.11)$$

$$\frac{\partial \bar{q}}{\partial t} + (\bar{\mathbf{v}} \cdot \nabla) \bar{q} + (\nabla \cdot \overline{\mathbf{v}'q'}) = \kappa_v \nabla^2 \bar{q} + \frac{S_q}{\rho} \quad (2.12)$$

The equations (2.9) - (2.12) are not trivial to solve due to the aforementioned closure problem, the complexity of the physical situation, and the onerous requirements to measure all of the necessary variables. Fortunately, it is possible to simplify these equations considerably by considering the earth's surface as a uniform flat plate of infinite length over

which a boundary layer develops. Analogous to the well studied boundary layer processes in engineering sciences (such as those measured in a wind tunnel), the atmospheric boundary layer can be considered to have an inner layer, in which the effects of surface roughness are felt, and an outer layer that is removed from surface effects and is controlled by the free stream velocity. The terminology is depicted in Figure 2.2. Within the outer layer, often referred to as the Ekman layer, Coriolis effects are present. Within the inner layer, hereafter termed the surface sublayer, the Reynolds shear stress is approximately constant, and the Coriolis effect can be ignored. In this region the transfer of momentum is affected by the transfer of heat and water vapour (non-neutral atmospheric conditions). The bottom region of this layer, where temperature and vapour effects are negligible, is occasionally referred to as the dynamic sublayer. However, the dynamic sublayer does not extend right to the ground surface, rather an interfacial sublayer is defined where the flow is affected by the viscosity of the fluid and by the nature of the individual roughness elements. This layer may also be referred to as the viscous sublayer for smooth flows or the roughness sublayer for rough flows. The height of the interfacial sublayer is on the order of the roughness elements. For snow surfaces, which typically have small roughness elements, turbulence is minimal within the interfacial sublayer and diffusion prevails.

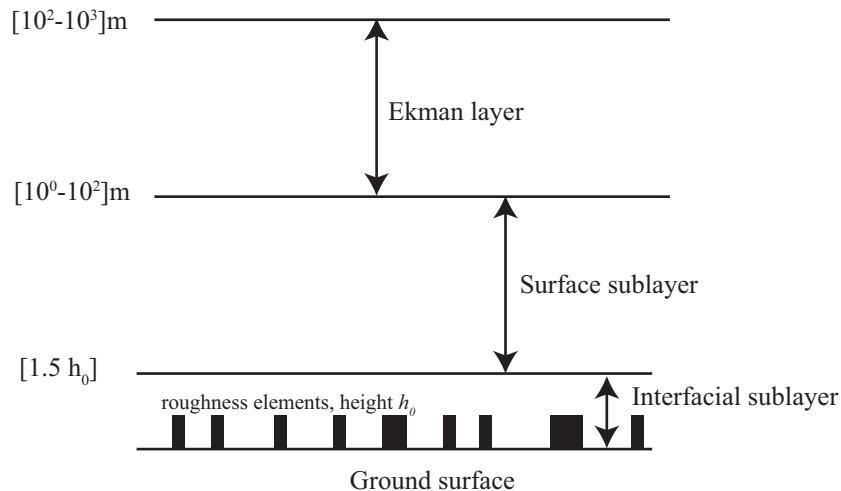


**Figure 2.2:** Depiction of atmospheric boundary layer structure. Note: the height range of each layer is adapted from Brutsaert (1982, p.54).

Within the context of the atmospheric boundary layer, the equations of motion can be reduced by the following simplifications: (1) boundary layer approximations (horizontal gradients and vertical velocities are negligible compared to the vertical gradients and horizontal velocities); (2) viscous forces are small except very close to the wall and can be neglected; and (3) horizontal homogeneity. The resulting set of equations are summarized below for the

horizontal (stream-wise) velocity (2.13), the span-wise velocity (2.14), the vertical velocity (2.15), the potential temperature (2.16), and water vapour (2.17). Within the horizontal motion equations (2.13)-(2.14), the variable  $f = 2\Omega \sin \Phi$  is the Coriolis parameter, where  $\Phi$  is the latitude.

$$\frac{d\bar{u}}{dt} = f\bar{v} - \frac{1}{\rho} \frac{\partial \bar{P}}{\partial x} - \frac{\partial \overline{u'w'}}{\partial z} \quad (2.13)$$

$$\frac{d\bar{v}}{dt} = -f\bar{u} - \frac{1}{\rho} \frac{\partial \bar{P}}{\partial y} - \frac{\partial \overline{v'w'}}{\partial z} \quad (2.14)$$

$$\frac{d\bar{w}}{dt} = -g - \frac{1}{\rho} \frac{\partial \bar{P}}{\partial z} \quad (2.15)$$

$$\frac{d\bar{\theta}}{dt} = -\frac{\partial \overline{w'\theta'}}{\partial z} + \frac{1}{\rho c_p} \left[ \frac{dH_R}{dz} + L_{vap} E \right] \quad (2.16)$$

$$\frac{d\bar{q}}{dt} = -\frac{\partial \overline{w'q'}}{\partial z} + \frac{S_q}{\rho} \quad (2.17)$$

Even though the situation has been greatly simplified, the fluctuating terms, or the Reynolds stress terms, still need to be modeled. The approach most commonly adopted for hydro-meteorological applications is the so-called K-theory, where by analogy to diffusive processes, the turbulent kinematic fluxes of momentum, heat, and water vapour are proportional to the local gradients of wind speed, temperature, and specific humidity (equations (2.18)-(2.20)). The proportionality factors  $K_m$ ,  $K_h$ , and  $K_v$  are known as the eddy diffusivities.

$$\overline{u'w'} = -K_m \frac{d\bar{u}}{dz} \quad (2.18)$$

$$\overline{\theta'w'} = -K_h \frac{d\bar{\theta}}{dz} \quad (2.19)$$

$$\overline{q'w'} = -K_v \frac{d\bar{q}}{dz} \quad (2.20)$$

Dimensional analysis is used by Jensen and Busch (1982) to illustrate the physical relationship between the eddy diffusivities and the flow parameters and the geometry. For example, in the neutral surface layer, where  $\overline{u'w'} = u_*^2$ , the wind speed gradient only depends on the friction velocity,  $u_*$ , and the height above the ground,  $z$ , such that  $f\left(\frac{d\bar{u}}{dz}, u_*, z\right) = 0$ .

Accordingly,

$$\frac{u_*}{z} \frac{d\bar{u}}{dz} = \kappa$$

where  $\kappa$  is known as von Kármán's constant, which has an experimentally determined value of 0.40 to 0.41. After rearranging and integrating between two heights,  $z_1$  and  $z_2$ , the logarithmic wind profile results (2.21).

$$\bar{u}_2 - \bar{u}_1 = \frac{u_*}{\kappa} \ln \left( \frac{z_2}{z_1} \right) \quad (2.21)$$

In most practical applications, only a single measurement is available and the lower height is taken as the surface, in which case the lower constant of integration becomes  $z_{0m}$ , which is also known as the roughness length for momentum. In this case the logarithmic wind equation becomes (2.22). The roughness length depends on the surface roughness, and is a description of the ability of the surface to absorb momentum.

$$\bar{u} = \frac{u_*}{\kappa} \ln \left( \frac{z}{z_{0m}} \right) \quad (2.22)$$

Similar dimensional arguments can be made for temperature and water vapour, which also result in logarithmic profile form as in (2.23)-(2.24). In these expressions, the terms  $a_h$  and  $a_v$  represent the ratio of the eddy diffusivities, *i.e.*  $a_h = K_h/K_m$  and  $a_v = K_v/K_m$ , respectively.

$$\bar{\theta}_s - \bar{\theta} = \frac{Q_H}{a_h \kappa u_* \rho c_p} \ln \left( \frac{z}{z_{0T}} \right) \quad (2.23)$$

$$\bar{q}_s - \bar{q} = \frac{Q_E}{a_v \kappa u_* \rho L_{sub}} \ln \left( \frac{z}{z_{0v}} \right) \quad (2.24)$$

## 2.4 Atmospheric Boundary Layers

Atmospheric boundary layers are made up of fluid motions on an extremely wide range of scales, ranging from synoptic and meso-scale motions where eddies could be on the order of kilometres down to the Kolmogorov scale (sub-millimetre) which are small enough to be affected by viscous forces. The spectra of these motions can be divided into three ranges (Kaimal and Finnigan 1994): (i) the energy containing subrange which is made up of length scales from tens of metres to kilometres (Panofsky and Dutton 1984) and contain most of the turbulent energy which is generated by shear and buoyancy; (2) the inertial subrange, where energy is neither produced nor dissipated but rather it is passed down from larger

scales towards finer and finer scales, and (3) the dissipation subrange where kinetic energy is converted to heat by viscosity, at wavelengths smaller than the Kolmogorov scale.

The spectral characteristics of atmospheric wind motions and the fluctuations of temperature, water vapour and other scalars are well documented. The quintessential spectral dataset collected to date has been Kaimal et al. (1972) which are commonly considered to be representative of the atmospheric boundary layer over homogeneous flat terrain. There are only a few examples of turbulence spectra over snow surfaces. Andreas (1987a) present a comprehensive set of spectra and cospectra collected over an extensive snow-covered surface that display an inertial subrange similar to those collected over other surfaces. Other examples of spectra collected on glaciers include Smeets et al. (1998), Smeets et al. (2000), and Cava et al. (2001).

The kinetic energy per unit mass of the turbulent motions,  $e = \frac{u'^2+v'^2+w'^2}{2}$ , provides a measure of the intensity of the turbulence. The budget of the turbulent kinetic energy (TKE) within the boundary layer reveals a great deal of information on the turbulent processes that are occurring. Equation 2.25 presents the budget of TKE for a homogeneous boundary layer aligned with the mean wind (Stull 1988), where the terms on the right hand side of (2.25) from left to right are: (I) shear production; (II) buoyancy production; (III) pressure transport; (IV) turbulent transport; and (V) the viscous dissipation (where  $\epsilon_{diss}$  is the rate of energy dissipation) .

$$\frac{\partial \bar{e}}{\partial t} = \underbrace{-(\overline{u'w'}) \left( \frac{\partial \bar{u}}{\partial z} \right)}_{\text{I}} + \underbrace{\frac{g}{\theta} (\overline{w'\theta'})}_{\text{II}} - \underbrace{\frac{1}{\rho} \frac{\partial}{\partial z} (\overline{w'p'})}_{\text{III}} - \underbrace{\frac{\partial}{\partial z} (\overline{ew'})}_{\text{IV}} - \underbrace{\epsilon_{diss}}_{\text{V}} \quad (2.25)$$

A key concept that underlies much of the micro-meteorological success at scaling the surface layer is that of the equilibrium layer, as originally proposed by Townsend (1961). This is essentially a layer near the surface, in which turbulence production (term I above) and turbulence dissipation (term V) are so large that aspects of the turbulent motion concerned with these processes are independent of conditions elsewhere in the flow. The conditions necessary for presence of an equilibrium boundary layer are presented by Townsend (1976) (*cf.* Raupach et al. 1991):

1. Turbulence transport terms are negligible in comparison with the local rates of shear production and dissipation, which reduces (2.25) to:

$$-(\overline{u'w'}) \left( \frac{\partial \bar{u}}{\partial z} \right) + \frac{g}{\theta} = \epsilon_{diss} \quad (2.26)$$

2. The equilibrium layer must be thin relative to the thickness of the entire boundary layer. This is necessary to ensure that the rates of turbulence production and dissipation are independent of the largest eddies, allowing the turbulence within the equilibrium layer to be independent of flow geometry.
3. The variation of shear stress across the layer must be small. This condition is consistent with a constant flux layer.

As an example of the importance of this concept, the above conditions permit the dimensional analysis required to derive the logarithmic velocity profile (Raupach et al. 1991).

As suggested by (2.25), the presence of a vertical heat flux affects the structure of the turbulence through the buoyancy of the air. This causes the wind profiles to deviate from their expected logarithmic behaviour. To account for this, Monin (1970) developed a semi-empirical solution based on dimensional analysis, which essentially states that in thermally stratified flow the turbulence can only depend on height above the surface,  $z$ , friction velocity,  $u_*$ , the surface kinematic heat flux,  $\overline{\theta'w'}$ , and the buoyancy parameter,  $g/\theta_0$ , where  $\theta_0$  is the average potential temperature of the surface layer. The dimensionless scaling variable is  $\zeta = z/L$ , where:

$$L = \frac{-u_*^3 \theta_0}{\kappa g \overline{\theta'w'}} \quad (2.27)$$

Negative values indicate unstable conditions, where buoyant forces are increasing vertical motions, and positive values indicate that the density stratification is suppressing turbulence. The latter is the common situation for the near-surface atmosphere over snow. Through application of this theory, dimensionless scaling variables for the flux gradient relationships can be found for wind shear, temperature and water vapour:

$$\frac{\kappa z}{u_*} \frac{d\bar{u}}{dz} = \phi_m \quad (2.28)$$

$$-\frac{\kappa z u_* \rho c_p}{Q_H} \frac{d\bar{\theta}}{dz} = \phi_h \quad (2.29)$$

$$-\frac{\kappa z u_* L_{sub} \rho}{Q_E} \frac{d\bar{q}}{dz} = \phi_v. \quad (2.30)$$

The correction for the wind, temperature, or humidity profile can be found by integrating:

$$\psi_m = \int_{z_{0m}/L}^{\zeta} [1 - \phi_m] \frac{d\zeta}{\zeta} \quad (2.31)$$

$$\psi_h = \int_{z_{0t}/L}^{\zeta} [1 - a_h \phi_h] \frac{d\zeta}{\zeta} \quad (2.32)$$

$$\psi_v = \int_{z_{0v}/L}^{\zeta} [1 - a_v \phi_v] \frac{d\zeta}{\zeta}, \quad (2.33)$$

which results in the corrections to (2.22)-(2.24):

$$u_* = \bar{u} \kappa \left[ \ln \left( \frac{z}{z_{0m}} \right) - \psi_m \right]^{-1} \quad (2.34)$$

$$Q_H = a_h \kappa u_* \rho c_p (\bar{\theta}_s - \bar{\theta}) \left[ \ln \left( \frac{z}{z_{0t}} \right) - \psi_h \right]^{-1} \quad (2.35)$$

$$Q_E = a_v \kappa u_* \rho \lambda_{sub} (\bar{q}_s - \bar{q}) \left[ \ln \left( \frac{z}{z_{0v}} \right) - \psi_v \right]^{-1}. \quad (2.36)$$

The stable boundary layer is a nearly constant feature of the atmosphere over snow, but can occur over most land surfaces when nocturnal thermal radiation losses result in surface cooling. The mildly stable boundary layer is still well described by M-O theory (Mahrt 1999, Grachev et al. 2005), however at increasing stability levels, turbulence near the ground can become greatly reduced due to suppression of vertical motions, and may become turbulent only intermittently (Nakamura and Mahrt 2005, Mahrt 2007). Suppressed turbulence near the surface may result in a low level jet forming which can result in elevated turbulence above the surface (*e.g.* Smedman 1988), resulting in a top-down turbulence structure (Mahrt 1999). Furthermore, meso-scale motions such as waves (Finnigan 1999), and meandering motions (Mahrt 2007) have a more prevalent interaction with turbulence-scale motions leading to non-stationarity conditions. Under these very stable conditions, similarity theories usually fail, posing a serious challenge to model development (Mahrt 1998).

## 2.5 Parameterization of Turbulent Fluxes over Snow Surfaces

In order to utilize bulk transfer estimation techniques, parameterization is required in two areas: (1) the turbulent transfer coefficients, and (2) the stability corrections.

The proper selection of the roughness lengths for momentum, heat, and water vapour are key to parameterizing turbulent transport. The starting point for discussion of the theory for heat transfer coefficients is that of Andreas (1987b), as it is one of the few theories that have been developed specifically for application to snow and ice surfaces. It is similar to the theory

of Brutsaert (1975b), both of which are based upon the surface renewal theory of Danckwerts (1951). Essentially these approaches model the scalar transfer processes that occur within the interfacial sublayer, where turbulent effects are absent and heat transfer is due to molecular diffusion (*i.e.* conduction). Turbulent energy is supplied from the surface sublayer to the interfacial sublayer by small eddies (Kolmogorov scale) that sweep the surface and remain in contact for some time before being ejected. In this sense, the eddies that are responsible for heat transfer are continuously ‘renewed’. A distinction is made between smooth and rough surfaces: for smooth surfaces, eddies sweep across the surface and then heat transfer occurs into the short-lived eddies; while for rough surfaces, individual eddies get trapped behind roughness elements and are considered to be temporarily stagnant. For smooth surfaces the heat transfer can be modeled as an advection-diffusion problem, whereas for rough surfaces the heat transfer is modeled as strictly diffusion problem. The theory of Andreas (1987b) predicts  $z_{0s}/z_{0m}$  as a function of the roughness Reynolds number, as seen in Figure 2.3. Here,  $z_{0s}$  is the roughness length for scalar transfer. In the smooth regime,  $z_{0s} > z_{0m}$  and their ratio takes on constant values, which is consistent with Prandtl number,  $Pr$ , of 0.71 and Schmidt number,  $Sc$ , of 0.63. In the rough regime, *i.e.*  $Re^* > 2.5$ ,  $z_{0s} < z_{0m}$  which is due to the fact that pressure differences across roughness elements transport momentum but not heat. Although Andreas initially presented this theory with little support from measurements, he has since provided more support in Andreas (2002) where he re-examined a number of previously published datasets from the literature. Denby and Snellen (2002) also evaluated the surface renewal model approach and found the theory to be consistent with their measurements over a melting glacier in Iceland. Andreas et al. (2005) provides additional support from measurements over the frozen Weddell Sea. However, the large degree of scatter (orders of magnitude) within these authors’ log-log plots of  $z_{0s}/z_{0m}$  vs.  $Re^*$  suggests that plenty of uncertainty remains. Other authors have noted dissimilar findings. For example, King and Anderson (1994) found that  $z_{0T}$  was significantly larger than  $z_{0m}$  for measurements over an ice shelf in Antarctica. Similarly, Calanca (2001) observed erratic  $z_{0T}$  values that were much larger than  $z_{0m}$  as measured on the Greenland ice sheet for melting conditions. Smeets and van den Broeke (2008) evaluated the Andreas (1987b) model on two glaciers (one in Iceland; one in Greenland) and found that it was adequate for  $z_{0m}$  values  $< 10^{-3}$  m, however it under-predicted  $Q_H$  for large hummocky roughness elements that are common to ablation zones of glaciers, so they adapted the scalar transport model of Brutsaert (1979) for permeable roughness elements to handle these conditions.

A few examples of measurements of the roughness lengths of momentum and heat are provided in Table 2.1. In general, the data do support that the roughness lengths for heat are usually smaller than that of momentum. The exception is King and Anderson (1994)

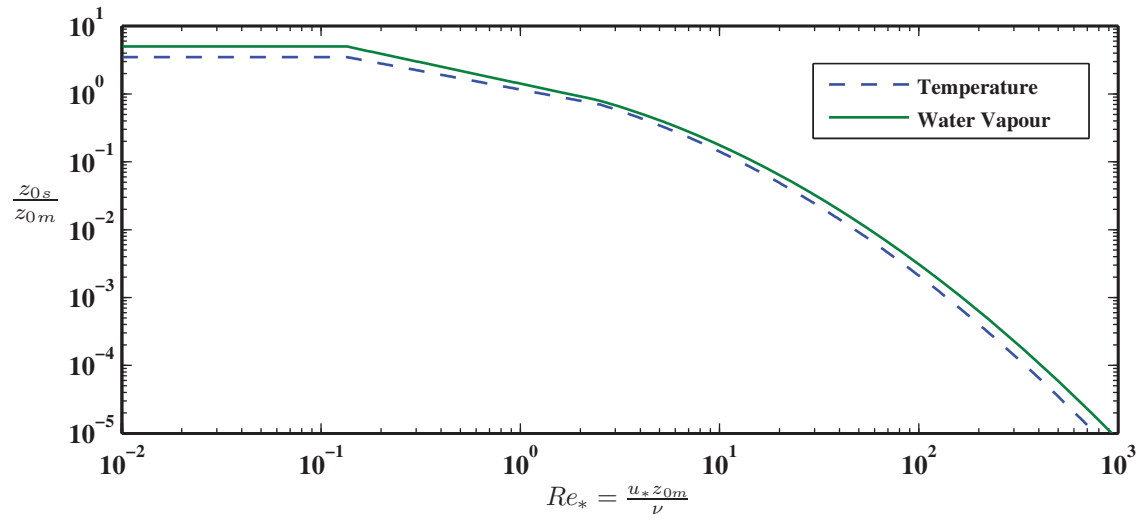


**Figure 2.3:** Roughness length ratios as described by the Andreas (1987b) model.

where the opposite was found.

**Table 2.1:** Roughness length values for snow and ice surfaces selected from literature.

Investigator(s)	$z_{0m}$ (m)	$z_{0r}$ (m)	Location
King and Anderson (1994)	$5.6 \times 10^{-5}$	$2.7 \times 10^{-2}$	Halley Research Station - Antarctica
Bintanja and van den Broeke (1995a)	$2.8 \times 10^{-6}$	$1.2 \times 10^{-6}$	Antarctic (blue ice)
	$7.5 \times 10^{-4}$		Antarctic (rough snow)
Smeets et al. (1998)	$1.0 \times 10^{-3}$	$6.0 \times 10^{-5}$	Pasterze Glacier (Austria) - melting ice
Munro and Davies (1977)	$1.0 \times 10^{-3}$		Vatnajökull ice cap (Iceland) - melting ice

With respect to the profile corrections, there are no unique concerns related to application over snow surfaces *per se*, however under increasingly stable conditions there is considerable uncertainty as to the accuracy of the existing profile functions (Mahrt 1998). The review of Andreas (2002), suggests that the equations of Holtslag and De Bruin (1988) are the most appropriate, as they permit flux under very stable conditions.

## 2.6 Numerical Snow Models

There are many different numerical approaches to modeling snowmelt. Initial efforts often featured temperature-index models, as suggested by their exclusive representation within an early snowmelt model inter-comparison study (World Meteorological Organization 1986). These simple empirical techniques are still commonly used (*e.g.* Ohmura 2001, Hock 2003, Sicart et al. 2008). At the other end of the modeling spectrum, physically based energy-balance models that estimate the terms in (2.1) have been around for more than four decades (*e.g.* Anderson 1968). Since then, numerous examples of snowmelt and snow-physics models based on the energy balance have been developed. These models differ in their complexity, such as the number of discretized elements used to represent the snow pack, and also in their parameterization schemes for estimating the various energy fluxes. With respect to modeling the turbulent fluxes, some models rely on empirical relations for  $Q_H$  and  $Q_E$  (*e.g.* Gray and Landine 1988). However, the majority of recent models employ some variation of the bulk transfer method *e.g.* SNTHERM (Jordan 1991), CROCUS (Brun et al. 1989), SNOBAL (Marks and Dozier 1992), UEB (Tarbotan and Luce 1996), and SNOWPACK (Bartelt and Lehning 2002). To the author’s knowledge, there are no models currently used for operational hydrology that employ a higher order turbulence model than the first order flux-gradient procedures previously described.

Models developed for the purpose of climate prediction usually rely on a land-surface scheme, such as the Canadian Land Surface Scheme (CLASS) (Verseghy 1991, 2000), to provide the boundary conditions at the earth surface. CLASS has a more simple description of the snow cover (as described in Brown et al. (2006)) than the energy balance models previously listed. However, usually these schemes also rely on the bulk transfer formulae to estimate the turbulent heat fluxes.

Inter-comparison studies have been conducted to evaluate and compare the performance of the various snow melt models (Slater et al. 2001, Etchevers et al. 2004, Rutter et al. 2009). The results of these inter-comparisons suggest that parameterization techniques for the turbulent fluxes vary widely, and the uncertainty in the estimates are on the same order as the fluxes (Etchevers et al. 2004). Difficulties in measuring the turbulent fluxes in winter

conditions have largely precluded a proper evaluation of the estimation techniques.

## 2.7 Energy Fluxes over Snow

Although mountain environments have inspired many researchers to investigate certain aspects of mountain climatology and the effect large scale topography on the planetary boundary layer, there have been relatively few studies of how the wind flow patterns in the complex terrain influence the turbulent fluxes of heat and water vapour from the various surfaces. In mountainous areas, meso-scale motions such as gravity waves, katabatic flows (drainage winds), and or other topographically induced motions due to flow separation can appear. In order to resolve the complex features of the flow, fine scale modeling of the wind flow is required. However, there are few models capable of doing this (Lehning et al. 2006). Computational fluid dynamics (CFD) models employed in the engineering sciences are sufficient to operate at small scales over irregular terrain, however they require modification in order to handle thermal stratification (Hug et al. 2005). Large eddy simulation (LES) techniques have been demonstrated to work in mountainous regions (Raderschall et al. 2002), however these models are limited by relatively small domains and are sensitive to the sub-grid modeling approach.

Observational datasets of near surface turbulence within mountain environments are not very common. Surface fluxes within a mountain valley have been measured using the eddy covariance technique by Doran et al. (1989), and Hiller et al. (2008). Turnipseed et al. (2002, 2003, 2004) report measurements of turbulence and energy balance over a forested site at Niwot Ridge, CO. Pomeroy et al. (2003) report energy balance and turbulent fluxes during snowmelt at Wolf Creek basin, near Whitehorse, YT. A large multi-agency effort, called the Mesoscale Alpine Programme (Bougeault et al. 2001), was recently conducted in the Alps and has contributed information regarding how large-scale flows influence flux generation processes (Rotach and Zardi 2007, Rotach et al. 2008). Turbulence measurements have also been reported over numerous glacier surfaces which have similar flow attributes as other mountain environments (*e.g.* Smeets et al. 1998, 1999, 2000, Denby and Snellen 2002).

Although direct measurements of the turbulent fluxes in mountainous areas are scarce, there have been numerous attempts to estimate the energy balance terms, with much of the work directed at quantifying losses due to sublimation. Golding (1978) calculated snow sublimation during chinooks at sites along the eastern Rocky Mountains, and found that mean daily evaporation during chinook events was 1-2 mm d<sup>-1</sup>, with maximum calculated rate of 10 mm d<sup>-1</sup>. Hood et al. (1999), who used the aerodynamic profile method in an alpine area of Colorado, reported that sublimation was highest during mid-winter (non-melt)

periods, and was dominated by episodic chinook events. Seasonal sublimation was 195 mm or 15% of snow accumulation. Observations and calculations by Marks and Dozier (1992) at an alpine site in the Sierra Nevada mountain range during mid-winter show that the turbulent fluxes (calculated with the bulk transfer method) were the largest input to the snow energy balance. However, during melt periods, net radiation dominated the energy balance. Bernier and Swanson (1993), using pan lysimeters, measured mean evaporative fluxes of  $1.07 \text{ mm d}^{-1}$  in a large (800 m dia.) forest clearing in the Alberta foothills, and found that evaporation rates were reduced as the size of the clearing was decreased. These measurements compared favourably to bulk transfer calculations. Cline (1995) made measurements of the surface energy balance of an alpine snowpack in the Colorado front ranges during snowmelt and found that net radiation accounted for 75% of the melt energy. The ablation due to sublimation during the snowmelt period was less than 4%. However, the cumulative sublimation was only slightly smaller than the sensible heat, suggesting that the effect on the energy balance is quite important.

The magnitude of the fluxes in equation (2.1) exhibit great temporal and spatial variability, so it is valuable to consider how these fluxes vary between different environments. Some examples are summarized below.

There has been a considerable amount of effort put into quantifying the energy balance over polar ice sheets. King et al. (2001), using bulk transfer formulae, calculated mean daily evaporation rates of  $0.15 - 0.20 \text{ mm d}^{-1}$  during the summer period at Halley, Antarctica. These amounts, when combined with a similar amount of evaporation from blowing snow, accounted for 25% of snowfall during the period. Bintanja and van den Broeke (1995b) calculated the latent heat flux from Antarctic snow and blue ice surfaces to be larger than both the sensible heat flux and the net radiation flux. Ablation due to sublimation was  $0.94 \text{ mm d}^{-1}$  on blue ice as measured with ablation stakes. Box and Steffen (2001) calculated annual sublimation rates to be as high as  $87 \text{ mm yr}^{-1}$  in the Jakobshavn ablation region of Greenland, ranging to seasonal condensation of  $18 \text{ mm yr}^{-1}$  on an ice sheet plateau above 2200 m. These were calculated using aerodynamic measurements (which were compared to eddy correlation measurements).

The most simple environment to make energy balance measurements is within continental areas. Measurements by Bengtsson (1980) in Sweden showed that average springtime sublimation from a snowpack was  $0.36 \text{ mm d}^{-1}$ , as measured with lysimeters. Based on these measurements and other theoretical considerations, the author states that seasonal sublimation rarely exceeds 10 to 20 mm in northern regions, however the latent heat flux is still of considerable importance because it limits the input of sensible heat available for snowmelt. Granger et al. (1977), based on energy balance measurements in the Canadian Prairies, for

two years of study, found that sublimation consumed about 14-22% of the available energy, and that sensible heat supplied 8-41% of the total energy. Hayashi et al. (2005), based on eddy covariance measurements in a snow-covered agricultural field in Japan, show that  $Q^*$  supplied about 75% of the melt energy, while  $Q_G$  and  $Q_H$  supplied the remaining 4% and 21% respectively. Twenty percent of the incoming energy was consumed by sublimation while 80% went to snowmelt. Sublimation fluxes were generally low, however during episodic Foehn events, rates as high as  $2.2 \text{ mm d}^{-1}$  were measured.

There has also been a considerable amount of research conducted on glacier surfaces, with the intent of better understanding their mass balances. Sicart et al. (2005) calculated the turbulent fluxes using the bulk transfer method for Zongo glacier, a high elevation tropical zone glacier, and report an average daily evaporation rate of  $2 \text{ mm d}^{-1}$  with maximum daily rates of  $6 \text{ mm d}^{-1}$ . Bintanja (1995) simulated the terms of the energy balance for Ecology Glacier in Antarctica and found that the combined turbulent heat fluxes supplied 36% of the energy for melt during a 1-month period during the summer ablation period.

# CHAPTER 3

## METHODS

### 3.1 Study Sites

The specific objectives addressed in this thesis rely on data collected from a number of different environments during non-overlapping periods between January 2005 and April 2007. Each study site is discussed individually below with details on the instrumentation and site characteristics. Specific details on the methodologies that were used in each experiment will be subsequently presented.

#### 3.1.1 Hay Meadow, Kananaskis, Alberta

##### Site Description

The ‘Hay Meadow’ mountain valley site is located at the Marmot Creek Research Basin ( $50^{\circ} 56'N$ ,  $115^{\circ} 08' W$ ) in the Kananaskis River valley, in the eastern slopes of the Rocky Mountains. It is a relatively large ( $\approx 7.3$  ha) grass covered clearing (Figure 3.1), that is bordered by the Kananaskis River to the East, by mixed aspen and pine forest to the North and South (in which the trees are approximately 13 m tall), and by sloping coniferous forest to the West. The vegetation in the clearing is mainly grass. The local terrain gently slopes at an average grade of 2.5% southeast, but is flanked by steep mountains on both sides of the valley.

The site was originally established in the fall of 2004 at location A (see Figure 3.1). Complete energy balance instrumentation was installed during January 2005 and data were collected through April 2005. Concerns that the aspen bluff to the south were affecting the turbulence measurements prompted the establishment of a new site at location B during summer 2005.

This site was selected because of its locally flat terrain and homogeneous land cover. Within the Kananaskis region of the Rocky Mountains, there are very few examples of such simple terrain, with the possible exceptions of frozen lakes, golf courses and some clear-

cuts. This site was a compromise between attempting to fulfill micro-meteorological siting guidelines while still capturing relevant processes that are occurring in the mountain valley environment.

Additional wind speed and direction data were also obtained from a station ( $50^{\circ}56.6'N$ ,  $115^{\circ} 11.4W$ , elev. 2543 m), operated by Environment Canada, which is located on the southern flank of Mt. Allan.

## **Instrumentation**

The instrumentation details for the 2 Hay Meadow sites can be found in Tables 3.1-3.2. With respect to location A, all of the instruments were mounted on a 5 m tower (Figure 3.2). The data were collected using a Campbell Scientific 23x data logger. Eddy covariance instrumentations were sampled at 10 Hz, while the other slow response instrumentation were sampled at 0.2 Hz. Mean data and turbulence statistics were output at 15 minute intervals. High frequency data were not stored for post-processing.

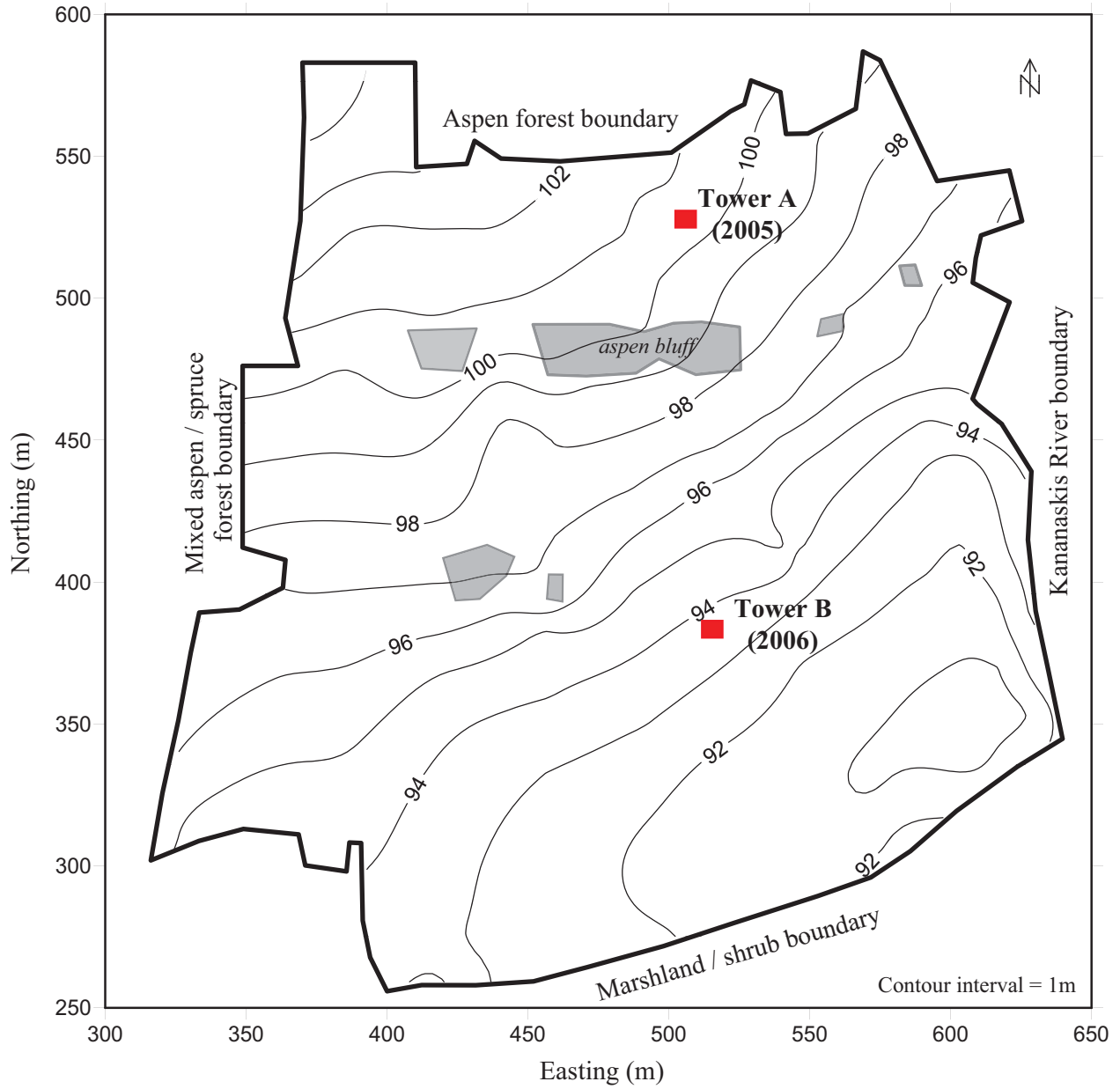


**Figure 3.1:** Contour map of Hay Meadow clearing, showing location of measurement towers. Note: Eastings, Northings, and contour elevations are relative to an arbitrary datum.

**Table 3.1:** Hay Meadow A (2005) instrumentation details.

Variable	Model	Instrument Height(s)*	Comments
Barometric Pressure	R.M. Young 61205V	n/a	
Snow Depth	Campbell Scientific SR50	1.27 m	
Wind speed (reference)	Met One 50.5	2.34 m	2d ultrasonic anemometer
Temperature / RH (reference)	Campbell Scientific HMP45C212	2.34 m	
Radiative surface temperature	Exergen IRTC	1.85 m	
Radiation flux	Kipp and Zonen CNR1	1.62 m	4-component radiometer
Wind fluctuations	Campbell Scientific CSAT3	1.95 m, 3.80 m	3d ultrasonic anemometer
Water vapour fluctuation	Campbell Scientific KH20	1.95 m, 3.80 m	Krypton hygrometer
Data logger	Campbell Scientific CR23X	n/a	

Note: Only instrumentation that were used in thesis are mentioned

\* Instrument heights are measured relative to ground surface

In summer 2005 a 10 m tower was established at location B (noted in Figure 3.3). The slow response instrumentation was sampled every 5 seconds, processed and recorded at 30 minute intervals by a Campbell Scientific CR23x data logger. A Campbell Scientific CR5000 data logger was used to poll the eddy covariance instrumentation at a frequency of 20 Hz. Data were processed and recorded at 30 minute intervals. Raw high frequency data were stored for later use.

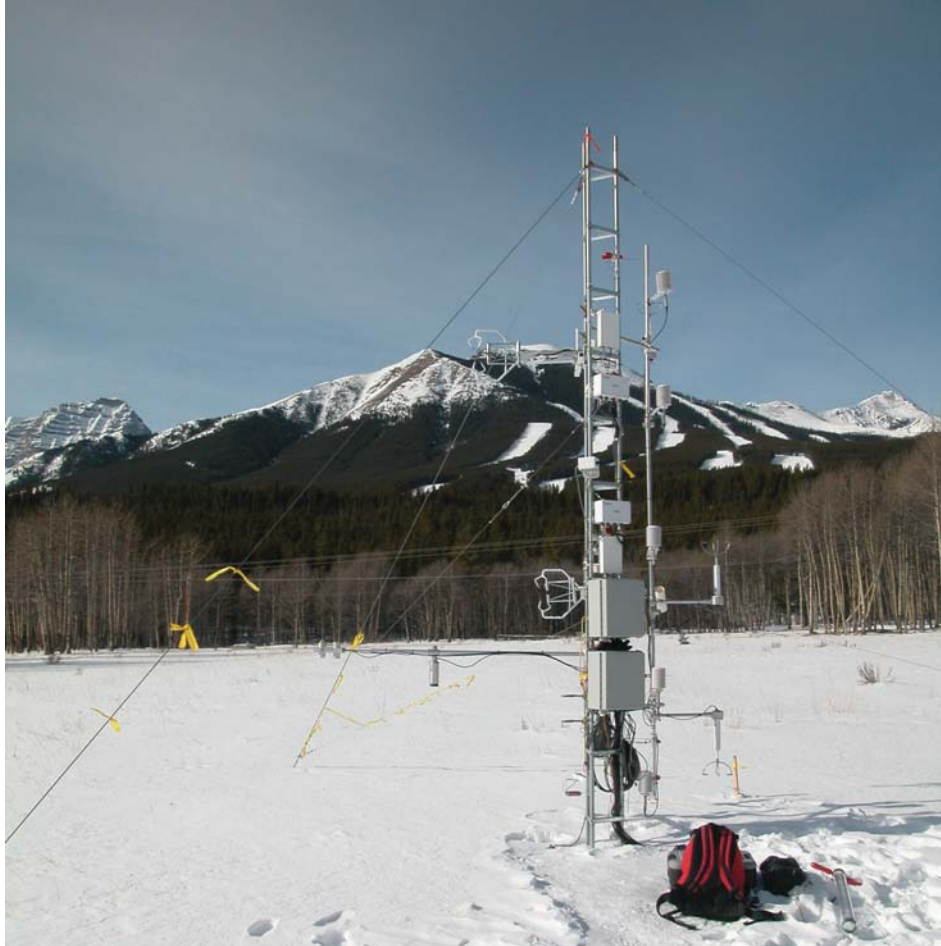


**Figure 3.2:** Photograph of Hay Meadow tower at location A (2005).



**Figure 3.3:** Photograph of Hay Meadow clearing.

**Table 3.2:** Hay Meadow B (2006) instrumentation details.

Variable	Model	Instrument Height(s)*	Comments
Barometric Pressure	R.M. Young 61205V	n/a	
Snow Depth	Campbell Scientific SR50	1.40 m	
Wind speed profile	Met One 50.5	0.35 m, 0.70 m, 1.70 m, 3.40 m	2d ultrasonic anemometer
Temperature / RH (reference)	Campbell Scientific HMP45C212	1.80 m	
Radiative surface temperature	Exergen IRTC	1.70 m	
Radiation flux	Kipp and Zonen CNR1	1.67 m	4-component radiometer
Wind fluctuations	Campbell Scientific CSAT3	1.80 m	3d ultrasonic anemometer
Water vapour fluctuation	Campbell Scientific KH20	1.80 m	Krypton hygrometer
Data logger	Campbell Scientific CR23X / CR5000	n/a	

Note: Only instrumentation that were used in thesis are mentioned

\* Instrument heights are measured relative to ground surface

## Measurement Conditions

The data selected from HM site A for use in this thesis were collected between 24 February through 3 March 2005. The days and evenings were mainly clear, and air temperatures ranged from  $-10^{\circ}\text{C}$  during the evening to  $+10^{\circ}\text{C}$  during the day. The snow cover was initially uniform, with a depth of approximately 10 cm, but then developed small bare patches during the last few days of the period. The evenings were usually calm with increased wind speeds during the day, although mean values always remained below  $4\text{ m s}^{-1}$ . The unobstructed fetch was approximately 50-150 m depending on wind direction. These data were used as a modeling dataset in Chapter 7.

The data used from HM site B were collected from 23 February through 27 February 2006. Snowfall was very limited at this site, and this dataset represents the extent of the data which were collected over a completely snow-covered ground. The depth of snow was approximately 0.07 m. The snow surface that developed in this environment was relatively flat with the exception of some exposed stems of grass. Wind blown features (drifting and sastrugi) were not present here. The fetch at this site was approximately 100-200 m. The dataset collected at this location was used to characterize the turbulence structure of this clearing in Chapter 4.

Plots of the mean wind speed, temperature, and bulk Richardson number for both of the HM sites are available in Appendix A.

### 3.1.2 Mud Lake, Kananaskis, Alberta

#### Site Description

Mud Lake is a small lake ( $50^{\circ} 47'\text{N}$ ,  $115^{\circ} 18'\text{W}$ ) located in the Smith-Dorien valley near Canmore, Alberta. This valley, located adjacent to the Kananaskis River valley (in which HM was located), is a higher elevation (approximately 1800 m). This site was established in January 2006 in order to supplement the Hay Meadow site as a “plan b” when snowfall events were small.

#### Instrumentation

Instrumentation details can be found in Table 3.3. The eddy covariance system was mounted on a roving system developed by the Centre for Hydrology. This was essentially a mast that was supported by a sled which was dug into the snowpack such that minimal obstruction of the wind flow would result from the sled body. The CNR1 was mounted on a separate stand that was built on a plastic sled which was buried in the snow to provide a stable platform.

**Table 3.3:** Mud Lake (2006) instrumentation details.

Variable	Model	Instrument Height*	Comments
Radiative surface temperature	Exergen IRTC	< 0.5 m	
Radiation flux	Kipp and Zonen CNR1	< 1 m	4-component radiometer
Wind fluctuations	Campbell Scientific CSAT3	1.95 m	3d ultrasonic anemometer
Water vapour fluctuation	Campbell Scientific KH20	1.95 m	Krypton hygrometer
Data logger	Campbell Scientific CR23X	n/a	

Note: Only instrumentation that were used in thesis are mentioned

\* Instrument heights are measured relative to snow surface



**Figure 3.4:** Photograph of Mud Lake.

### Measurement Conditions

Data were collected at ML from 21 January through 17 February 2006. The snow-covered lake is shown in Figure 3.4. New snow fell quite often during the data collection period which resulted in a very smooth snow surface. Although snow was frequently observed to blow (primarily due to wind gusts), wind-blown surface features were essentially absent. Along the axis of the valley, the unobstructed fetch could be up to 1 km, whereas for cross valley flows the fetch was approximately 100-200 m. This dataset was used to describe the turbulence structure in mountain valleys in Chapter 4.

### 3.1.3 Kernen Farm, Saskatoon, Saskatchewan

#### Site Description

Kernen Farm (Figure 3.5) is an agricultural research site owned by the University of Saskatchewan, located approximately 1.5 km E of Saskatoon, Saskatchewan. The site is located on a gently undulating (slopes less than 2%) lacustrine plain which is surrounded by rolling terrain to the south and east at distances greater than 4 km (Acton and Ellis 1978).



**Figure 3.5:** Photograph of Kernen Farm.

The city of Saskatoon lies to the West and agricultural farmland to the North. This site was chosen because, for all practical applications of micrometeorological techniques to hydrology, this site would be considered to be an ideal location to evaluate the snow energy balance. It is relatively flat, has a very homogeneous land cover and has no nearby obstacles which could interfere with boundary layer development and affect the turbulent flux processes.

### **Instrumentation**

Details regarding the instrumentation installed at this location are presented in Table 3.4. The setup consisted of a main tripod, which the eddy covariance systems, reference temperature and relative humidity, and the data loggers were mounted on, and an auxiliary mast which supported the radiometer and a 3-cup anemometer. The snow thermocouples, ground interface temperature and heat flux measurements were installed at a nearby location. A blowing snow particle detector (Brown and Pomeroy 1989) was installed approximately 10 cm above the ground, and was used to identify blowing snow conditions.

**Table 3.4:** Kernnen Farm (2007) instrumentation details.

Variable	Model	Instrument Height(s)*	Instrument Height(s)*	Comments
1	Instrument	Instrument Height(s)*	Instrument Height(s)*	Comments
Wind speed (reference)	Met One 014A		2.10 m	3-cup anemometer
Temperature / RH (reference)	Campbell Scientific HMP45C212		2.10 m	
Temperature (gradient)	E-type thermocouple		1.63 m, 3.26 m	diameter = $7.62 \times 10^{-5}$ m
Radiation flux	Kipp and Zonen CNR1		$\approx 1.5$ m	4-component radiometer
Ground heat flux	Hukseflux HFP01		0 m	installed at snow-soil interface
Snow temperature profile	E-type thermocouple		***	diameter = $2.55 \times 10^{-4}$ m
Wind fluctuations	Campbell Scientific CSAT3		1.90 m, 3.55 m	3d ultrasonic anemometer
Water vapour fluctuation	Campbell Scientific KH20		1.90 m, 3.55 m	Krypton hygrometer
Data logger	Campbell Scientific CR23X / CR5000		n/a	

Note: Only instrumentation that were used in thesis are mentioned

\* Instrument heights are measured relative to ground surface

\*\*\* Snow thermocouple heights are provided in Figure TC

## Measurement Conditions

The site at KF was established in late November 2006 and data were collected through March 2007. During this period, a snowpack developed that was approximately 42.5 cm deep near the instrument towers. This site was typical of prairie snowpacks in that the snow surface was gently undulating due to wind distribution with sastrugi developing at shorter scales. The dataset used for this thesis was limited to data collected between 19 January through 17 March 2007. This period was used to characterize the turbulence structure of this environment in Chapter 5. However, for the purposes of calculating the energy balance (Chapter 6), and for evaluating flux estimation techniques (Chapter 8), only the data collected in February were used since the air temperature was below freezing and no snow melt occurred. Background meteorological conditions for the record of data presented can be found in Appendix A.

### 3.1.4 Wolf Creek Alpine, Whitehorse, Yukon

#### Site Description

The Wolf Creek Alpine (WCA) site ( $60^{\circ} 34'N$ ,  $135^{\circ} 08' W$ ) is located within the Wolf Creek Research Basin, near Whitehorse, YT. The site is located on top of a broad windswept ridge, at an elevation of 1560 m.a.s.l. The top of the ridge is locally level for a distance of approximately 200 m. The site is well above the local tree line. Minor flow obstacles include a few exposed rocks.

#### Instrumentation

The instrumentation at this site (Table 3.5) consisted of two levels of eddy covariance along with HMP45C212 installed within 12-plate Gill-type radiation shields and exposed, non-ventilated fine wire thermocouples for gradient estimation. The instruments were mounted on a portable mast that was transported to the site and then erected for the study.



**Figure 3.6:** Photograph of Wolf Creek Alpine site.

**Table 3.5:** Wolf Creek Alpine (2007) instrumentation details.

Variable	Model	Instrument Height(s)*	Comments
Temperature / RH (reference)	Campbell Scientific HMP45C212	1.63 m, 3.26 m	
Temperature (gradient)	E-type thermocouple	1.63 m, 3.26 m	diameter = $7.62 \times 10^{-5}$ m
Wind fluctuations	Campbell Scientific CSAT3	1.63 m, 3.26 m	3d ultrasonic anemometer
Water vapour fluctuation	Campbell Scientific KH20	1.63 m, 3.26 m	Krypton hygrometer
Data logger	Campbell Scientific CR5000	n/a	

Note: Only instrumentation that were used in thesis are mentioned

\* Instrument heights are measured relative to ground surface

## Measurement Conditions

The data collected at this site were part of a short measurement campaign which occurred between 11-18 April 2007. The predominant wind direction during the period was from the South. It is believed that the flow remains attached at the point of the tower. However, a zone of separation is evident from a large snow drift that forms on the lee side of the ridge, immediately downwind of the tower. During the measurement campaign, the site was mostly snow covered (approximate depth of 0.30 m), but had a few exposed rocks and shrubs. This dataset was used to evaluate the turbulence processes occurring at an alpine ridge in Chapter 4. Background meteorological conditions can be found in Appendix A.

## 3.2 Experimental Methodology

### 3.2.1 Eddy Covariance

In employing the eddy covariance technique, the covariance between the vertical wind and the horizontal wind or a scalar field measured at a point above the surface are taken as being representative of the fluxes at the ground surface (the lower boundary condition) within the flux measurement footprint. The main conditions necessary for applying the eddy covariance technique are that the flow is homogeneous and steady. In obtaining the necessary statistics to describe the turbulent flow, investigators of atmospheric boundary layers are forced to invoke the ergodic hypothesis which states that time averages are equivalent to ensemble averages. In order for this hypothesis to be valid, all of the statistical moments must be considered as stationary, or that they do not vary with time (Katul et al. 2004). If these conditions are met, Reynolds averaging rules can be applied (Kaimal and Finnigan 1994), and the statistical moments (fluxes) can be linked to the Navier-Stokes equations (Katul et al. 2004), and upon satisfaction of the homogeneity conditions and after imposing certain simplifying assumptions, the eddy covariance technique can be used to relate the measured statistics at a point to fluxes at the bounding surface.

The eddy covariance technique used in this experiment employed a fast response sonic anemometer (Campbell Scientific CSAT3) to measure the wind velocity components,  $u_i$ ,  $v_i$ , and  $w_i$  (which are expressed in the right handed coordinate system of the anemometer, as indicated by subscript  $i$ ), and the sonic air temperature  $T_s$ , as well as a Krypton Hygrometer (Campbell Scientific KH20) which measures water vapour density  $\rho_v$ .

Where the data logger storage capacity permitted, the raw high frequency data were kept for post-processing. This was done at HM (location B only), KF, and WCA. For these sites, prior to calculating fluxes, the raw data were de-spiked. The despiking routine for all

sonic anemometer data ( $u$ ,  $v$ ,  $w$ , and  $T_s$ ) was based upon an examination of the vertical wind speed  $w$  in 100-point non-overlapping windows. If the instantaneous velocity  $w$  was  $> \pm 5.5$  standard deviations of the 100-point mean value, the outlying value was replaced with the mean value and a diagnostic flag was set high. Four consecutive outliers were not considered to be spikes (Vickers and Mahrt 1997). This routine makes the assumption that a spike detected in the vertical wind speed would suggest that all other sonic anemometer data for the same time step would be similarly affected, so consequently all other variables were replaced with their 100-point mean values. The KH20 data were subjected to a separate despiking routine, following the same algorithm. This routine differs slightly from the one described by Vickers and Mahrt (1997) as it represents a compromise between processing time and data quality. Spikes were typically only present in the data during poor meteorological conditions such as snowfall or condensation events. These periods would likely be excluded based on other data selection criteria.

Following de-spiking, the data processing procedures were similar for all of the data collection systems. The data were separated into 30-minute blocks and then all of the required moments were calculated. The eddy covariance products were rotated using the Planar-Fit method (Wilczak et al. 2001) into a new coordinate system defined as having its z-axis oriented perpendicular to the long-term mean stream line and having the y-axis perpendicular to the 30-minute streamline (and also perpendicular to the newly defined z-axis), and the x-axis oriented parallel to the 30 minute streamline. At Kernan farm, the upper sonic anemometer data were rotated into the coordinate system defined by the lower anemometer, thus ensuring that the output from both anemometers were in the same coordinate system. The sensible heat flux was calculated as the covariance between the vertical velocity fluctuations (from the mean) and the fluctuations in sonic temperature, both of which are obtained from the sonic anemometer. Although the true sensible heat flux  $\overline{w'T'}$  can differ from the heat flux calculated using the sonic temperature  $\overline{w'T_s}$ , given the cold temperatures and very low specific humidities typical of mid winter periods, the difference was found to be negligible, therefore:

$$Q_H = \rho c_p \overline{w'T'} \approx \rho c_p \overline{w'T_{sonic}'} \quad (3.1)$$

The latent heat flux was calculated as the covariance between the fluctuations of the vertical velocity and the water vapour density (3.2), which is directly measured using the Krypton Hygrometer. Under the measurement conditions encountered in this thesis, the effects of O<sub>2</sub> attenuation of the krypton radiation source, and the effects of the density variation due to the vapour flux (*i.e.* WPL corrections) (Webb et al. 1980) were negligible and were not applied.

**Table 3.6:** Critical values of non-dimensional frequency where attenuation due to path length averaging exceeds 5%.

Site	meas. ht.* (m)	u**	v**	w**	T <sub>s</sub> ***	wT <sub>s</sub> ****
Hay Meadow (2006)	1.80	1.0	2.5	1.7	1.0	3.0
Kernen Farm	1.58	0.9	2.2	1.5	0.9	2.6
	3.24	1.8	4.5	3.1	1.8	5.4
Wolf Creek Alpine	1.34	0.7	1.8	1.3	0.7	2.2
	2.97	1.6	4.1	2.9	1.6	4.9
<i>k<sub>1</sub>p<sub>crit</sub></i>		0.4	1.0	0.7	0.4	1.2

\* Instrument heights are relative to snow surface

\*\* *k<sub>1</sub>p* values obtained from Horst and Oncley (2006), Table B1

\*\*\* *k<sub>1</sub>p* values obtained from Horst and Oncley (2006), Table B3

\*\*\*\* *k<sub>1</sub>p* values obtained from van Dijk (2002), Table 1

$$Q_E = L_{sub} \overline{w' \rho_v'} \quad (3.2)$$

Due to the fixed path length of the sonic anemometer, it is impossible to sample eddies that are smaller than the distance between the transducers. The attenuation of the flux due to path length averaging is therefore dependent on the instrument path length, the height above the ground, the sampling frequency and the wind speed. Horst and Oncley (2006) calculate the transfer function required to correct for these losses which are expressed as a function of the product of the stream wise wavenumber  $k_1$  and the instrument path length  $p$ . Similarly, van Dijk (2002) provides the transfer function for the sensible heat flux using the CSAT anemometer. Table 3.6 provides the non-dimensional frequency  $n = fz/u$  at which the flux is attenuated by more than 5%. For a Nyquist frequency of 10 Hz (sampling frequency of 20 Hz), the flux attenuation of the velocity components only exceeds this value for wind speeds  $> 10 \text{ m s}^{-1}$ , while  $> 5\%$  attenuation of the scalar flux occurs at wind speeds greater than  $6 \text{ m s}^{-1}$ . The wind speeds were generally lower than these critical values, except occasionally at WCA, however the sonic anemometer was oversampled at 60 Hz. to avoid frequency limitations associated with the low measurement height. The fluxes reported within this thesis were not corrected for path length averaging.

The CSAT3 anemometer has a diagnostic feature where a flag is set high if something is preventing the instrument from making a good measurement. This was noticed to occur when one of the transducers was coated with rime or snowfall was blocking the signal. Any data with flags set high were excluded from the calculated statistic.

Data were only selected for use if they were from good wind directions that were not affected by the tower or other instruments, or in the case of the mountain sites, directions that maximized the unobstructed fetch lengths. Furthermore, fluxes or variances that involved data from the KH20 Krypton Hygrometer were rejected if the signal strength dropped signif-

icantly (as occurred when condensation was forming on the lenses). Data that were filtered will be identified throughout the text where applicable.

## Spectra and Cospectra

In calculating the spectra and cospectra, the data from each 30 minute period of interest were truncated to form  $N=2^{15}=32,768$  point blocks. The velocity components were then rotated into the mean wind direction using the Planar-Fit coordinate rotation (Wilczak et al. 2001), and were linearly detrended. After applying the discrete Fourier transform to variable  $A$  using Matlab, the discrete spectral intensity  $E_A$  was calculated following Stull (1988, p. 313). The spectral density,  $S_A$ , was then calculated by dividing  $E_A$  by  $1/T$ , where  $T$  is the length (s) of the data block. In order to prepare the spectral density estimates for graphical presentation, they were frequency weighted by multiplying  $S_A$  by the frequency  $f$  and were then smoothed by averaging to form 7 logarithmically spaced intervals per decade. Finally, the frequency scale was non-dimensionalized by normalizing by the product of the wind speed and the frequency, *e.g.*  $n = fz/U$ . Similar procedures were used to find the Cospectral densities  $Co_{AB}$  for variables  $A$  and  $B$ .

The calculated spectra and cospectra for selected events were averaged to form composite curves, and were compared to the spectra/cospectra collected by Kaimal et al. (1972), which are approximated by the following expressions (Kaimal and Finnigan 1994).

$$\frac{fS_u(f)}{u_*^2} = \frac{102n}{(1 + 33n)^{5/3}} \quad (3.3)$$

$$\frac{fS_v(f)}{u_*^2} = \frac{17n}{(1 + 9.5n)^{5/3}} \quad (3.4)$$

$$\frac{fS_w(f)}{u_*^2} = \frac{2.1n}{(1 + 5.3n)^{5/3}} \quad (3.5)$$

$$\frac{fCo_{ww}(f)}{u_*^2} = \frac{-12n}{(1 + 9.6n)^{7/3}} \quad (3.6)$$

$$\frac{fCo_{wT}(f)}{w'T'} = \frac{fCo_{w\rho_v}(f)}{w'\rho'_v} = \begin{cases} \frac{11n}{(1+13.3n)^{7/3}} & \text{for } n \leq 1.0 \\ \frac{4n}{(1+3.8n)^{7/3}} & \text{for } n > 1.0 \end{cases} \quad (3.7)$$

## Multi-Resolution Flux Decomposition

The multi-resolution flux decomposition (MRFD) (Howell and Mahrt 1997) was applied to the data to determine the appropriate flux averaging period and to determine the effect of non-

turbulent motions on the 30-minute turbulence statistics. Datasets of  $N = 2^{15} = 32,768$  points from each 30-minute period of interest were then rotated into the mean wind direction and were linearly de-trended. The data were then decomposed using the Haar wavelet transform in Matlab, which provided an array of coefficients at different scales  $p = 1 : 15$ . The energy at each scale was found by taking the square of the Haar coefficients and dividing by  $N$ . The scale dependent variance was then found by summing the energy at each scale. The cospectral gap identification routine of Vickers and Mahrt (2003) was then applied to the data to separate the energy that occurred on turbulent time scales vs. that occurring on longer time scales. This involved using a 1-2-1 filter on the MRFD coefficients to decrease the influence of any spurious values, so that a smooth cospectral shape could be examined. The scale at which the turbulent peak occurred at was then identified at the first decreasing cospectra value. The cumulative flux was then determined by summing the coefficients across all scales. Using the smoothed cospectra and cumulative flux plots the gap scale was identified by the first of three conditions: (1) a change in the sign of the cospectral coefficients; (2) the cumulative flux stops changing with scale; or (3) the cumulative flux begins to increase again. The smoothed cospectral values were only used to identify the gap scale, whereas the flux occurring before and after the gap scale was determined from the non-filtered MRFD coefficients.

### 3.2.2 Snow Energy Balance Measurements

The procedures described in this section relate to the energy balance investigation described in Chapter 5. The data for this experiment were collected from Kernen Farm, this site being an ideal location to evaluate the snow energy balance: it is relatively flat, has a very homogeneous land cover and has no nearby obstacles which would be expected to interfere with boundary layer development and affect the turbulent flux processes.

All of the relevant terms in (2.1) were directly measured in this experiment and average values were calculated at 30-minute intervals. The advection term,  $Q_A$ , was not included in the energy balance since there was no rain falling on the snowpack nor melt-water leaving the snowpack during the selected data periods. The amount of snowfall received in any 30-minute period was minimal, and could not be expected to contribute much energy at these short timescales. A similar rationale was applied to blowing snow where it was generally observed that the amount of blowing snow entering the control volume was equal to the amount leaving, and did not affect the energy status of the snowpack. Due to the extensive, uniform snowpack, the assumption of horizontal homogeneity was made and horizontal energy fluxes were not considered. The sign convention followed throughout the thesis is that fluxes directed towards the snowpack are considered positive, and those directed away from the

snowpack are considered to be negative.

## Internal Energy

The rate of internal energy change (3.8) depends on the rate that energy is required or liberated during melting,  $R_M$ , and re-freezing,  $R_F$ , and the internal energy change associated with each snow constituent: ice (subscript  $i$ ); liquid water (subscript  $w$ ); and air (subscript  $a$ ) as the temperature of the snowpack varies from a reference state (usually taken as  $0^\circ$  C). The constituents are considered on a fractional volumetric basis, and  $\phi_i + \phi_w + \phi_a = 1$ . The formulation presented here assumes that the porous medium is at thermal equilibrium, i.e.  $T_s = T_i = T_w = T_a$ , where the subscript  $s$  denotes snow (encompassing all of the aforementioned constituents). In (3.8)  $L_{fus}$  is the latent heat of fusion,  $\rho$  is the density and  $c_p$  is the heat capacity. The limits of integration for the 2nd term on the right are between the ground-snow interface ( $z = 0$ ) and the upper boundary of the snowpack ( $z = H$ ).

$$\frac{dU}{dt} = L_{fus}(R_F - R_M) - \int_0^H \left[ \frac{(\phi_i \rho_i c_{p,i} + \phi_w \rho_w c_{p,w} + \phi_a \rho_a c_{p,a})_z dT_s}{dt} \right] dz \quad (3.8)$$

Direct measurement of the rate of internal energy change is notoriously difficult, which is why it is rarely measured but rather taken as the residual after measuring the terms on the right hand side of (2.1). This is because the snow density, liquid water content, the snow temperature must all be measured. Particularly problematic is the liquid water content, which does not lend itself to continuous measurement. Point measurements can be obtained by onerous calorimetric approaches (Jones et al. 1983), by dilution techniques (Davis et al. 1985), or by more indirect dielectric techniques (eg. Denoth et al. 1984). However, during cold mid-winter periods where the liquid water content of the snowpack is negligible, the situation can be simplified greatly to (3.9) since melting and refreezing are not occurring.

$$\frac{dU}{dt} = \int_0^H \left[ \frac{(\theta_i \rho_i c_{p,i} + \theta_a \rho_a c_{p,a})_z dT_s}{dt} \right] dz \quad (3.9)$$

As the data selected in this experiment are only from periods where the air and snow temperatures are below freezing, the internal energy was determined from the depth and density of the snowpack and the measured internal temperature changes.

Snow densities were obtained from a snow pit nearby the snow thermocouple array on 21 January 2007 in which the average density was  $310 \text{ g cm}^{-3}$  but ranged from  $265 \text{ g cm}^{-3}$  for a depth hoar layer to  $390 \text{ g cm}^{-3}$  for an ice layer. In order to minimize disturbance around the measurement site, no further snow pit surveys were conducted. However, bulk snow densities along a nearby transect were sampled using a snow tube (30 cm<sup>2</sup> dia.) on 6

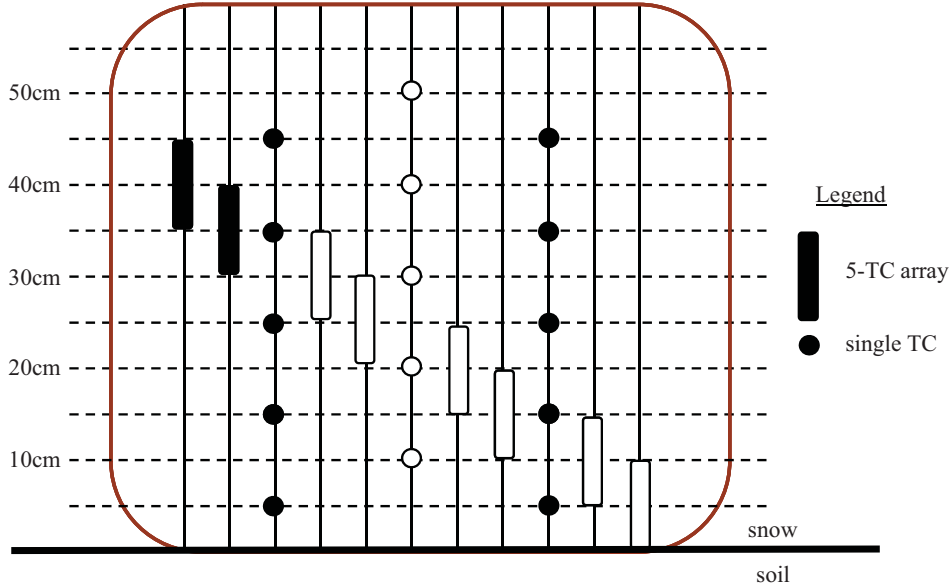


**Figure 3.7:** Schematic of snow thermocouple array. Thermocouple locations marked in solid black are those used within this thesis.

February ( $305 \pm 70 \text{ g cm}^{-3}$ ) and again on 22 February ( $265 \pm 35 \text{ g cm}^{-3}$ ). In order to account for changes in density that would affect the calculation of internal energy, SNTHERM (Jordan 1991) was used to model the snow metamorphism and associated density changes throughout the remaining winter period. The details of this model are discussed in §3.3.2.

Snow temperature measurements were made using 30 ga. type-E thermocouples that were attached to thin support wire which was strung between a frame made of copper tubing (Figure 3.7). The thermocouple wires were routed from the data logger along the ground to the bottom of the frame (at the snow-ground interface), and then up the appropriate support wire to the measurement height. Each support wire contained only 5 thermocouple wires in an effort to reduce the mass which could absorb solar radiation and melt the snow. The thermocouple array was installed at the beginning of December 2006, when there was only  $\approx 10 \text{ cm}$  of snow on the ground. Natural snowfall and redistribution processes then formed the snowpack around the thermocouples, providing an in-situ undisturbed measurement of the snow temperature profile. Melt-out around the support wires due to solar heating was not observed during the data collection period.

The snow surface temperature  $T_s$  was measured using the outgoing long-wave radiation measurement, and rearranging the long-wave radiation balance (3.10) where the emissivity  $\epsilon$  is taken as 0.99 (Warren 1982), and  $\sigma$  is the Stefan-Boltzman constant.

$$Q_{Lo} = \epsilon \sigma T_{surf}^4 + (1 - \epsilon) Q_{Li} \quad (3.10)$$

In order to apply (3.9), the snowpack was discretized into vertical segments that were specified while taking into consideration the spacing of the thermocouples, the snow density stratification observed in the 21 January snow pit, and the expected temperature fluctuation for that particular depth of snow. The segments used were 0(soil surface)-10 cm; 10-20 cm; 20-25 cm; 25-30 cm; 30-32 cm; 32-34 cm; 34-36 cm; 36-38 cm; 38-40 cm; 40-42 cm; and 42-42.5 cm (snow surface).

The accuracy of the snow thermocouple array depends on the errors introduced by the reference temperature measurement, the manufacturing tolerances of thermocouple wire, the measurement errors of the datalogger, and the linearization errors associated with converting the measured voltage to temperature. In this case, the largest uncertainty is introduced by the reference temperature measurement of the dataloggers (Campbell Scientific CR23x and CR5000), which both use a thermistor, with stated accuracy under cold conditions of better than  $\pm 0.5$  °C, to measure the temperature of the terminal block. According to the manufacturer, the expected accuracy in the field should be better than  $\pm 0.2$  °, if temperature gradients at the terminal block are minimal. To ensure this, additional insulation was placed within the data logger enclosure to ensure that the junction temperature measured was representative of the entire terminal block. The type-E thermocouple wire used in this study is specified to have an absolute accuracy of  $\pm 1.7$ °C, or a 1% slope error. Since the temperature differences between the thermocouple measurement and the reference (junction) temperature were always less than 15 °C the slope error can be used, implying that the error should be  $\pm 0.15$  °C. In order to minimize the effect of this error all of the thermocouples were made from the same spool of wire. Relative to the aforementioned error sources, the voltage measurement and temperature conversion errors are expected to be less than 0.002 °C. If all of these errors were random, the temperature measurement would have a total uncertainty of approximately  $\pm 0.25$  °C. However, it is more likely that the larger error terms are systematic which will have minimal influence upon the calculation of relative changes (both temporally and spatially). Furthermore, the random error is reduced substantially by making measurements at 5 sec. intervals, and calculating a 30 min. average. Finally, it is anticipated that the uncertainty of  $\Delta T$  was  $\pm 0.05$  °C.

Under the cold conditions of this study, it is believed that the changes in internal energy of the snow can be calculated with reasonable certainty. For estimating the uncertainty in eqn. (3.9), it was assumed that the snow density had an uncertainty of  $\pm 50$  kg m<sup>-3</sup>, which affected the accuracy to which the specific heat could be determined. It was also assumed that the thickness of the layer of snow (which was determined by the thermocouple spacing) was known to within 0.002 m. For the typical  $\Delta T$  values that were observed, the total uncertainty in calculation of the total change of internal energy for the 11 snow layers was

approximately  $\pm 10\%$ .

## Ground Heat Flux

Two Hukseflux HFP01 ground heat flux plates (Hukseflux Thermal Sensors, Delft, The Netherlands) were installed near the base of the snow temperature array by inserting the plate directly between the snowpack and the soil. The ground heat flux term,  $Q_G$ , was obtained directly from the average of the two heat flux plates. Two thermocouples were also installed at the soil-snow interface which served to validate the direction and the approximate magnitude of the ground heat flux (according to the temperature gradient between the interface and the snowpack).

The ground heat flux sensors were not specifically calibrated for this application. The manufacturers stated accuracy for uncalibrated use in soils was  $-5\%$  to  $+15\%$  (for 12-hour totals). Errors arising are largest when the thermal properties of the heat flux plate differ greatly from the measurement medium. Based on the measured densities, the thermal conductivity of the bottom layer of the snow pack was likely on the order of  $0.15\text{--}0.30 \text{ W m}^{-1} \text{ K}^{-1}$  (Sturm et al. 1997), while the frozen soil was likely between  $0.5\text{--}1.5 \text{ W m}^{-1} \text{ K}^{-1}$  depending on antecedent moisture conditions. Since the range of thermal conductivities for the soil compares favourably to the thermal conductivity for the heat flux plate, which was  $0.8 \text{ W m}^{-1} \text{ K}^{-1}$ , the technique is expected to give a reasonable measurement of the soil heat flux. However, considering the uncertainty in these estimates, it is possible that the systematic errors may be greater than the manufacturers stated accuracy. Fortunately, during the periods of interest the soil heat flux was nearly steady so that any measurement errors would appear as a consistent bias.

## Radiation Flux

The Kipp & Zonen CNR1 radiometer provides both downwelling and upwelling measurements of the short-wave ( $0.3$  to  $3.0 \lambda \text{ m}$ ) radiation flux  $Q_S$  and the long-wave ( $5.0$  to  $50.0 \lambda \text{ m}$ ) radiation flux  $Q_L$ . The net radiation  $Q^*$  flux was obtained from the sum of all 4 sensors.

During cold winter periods the largest source of radiation error is due to the formation of rime on the sensors. In order to minimize rime growth on the sensors, the CRN1 body was conditionally heated using the on-board  $12 \text{ V}$  heater whenever the battery had sufficient charge and the relative humidity of the air was greater than  $95\%$  with respect to ice. A similar error can occur when snow that falls during light winds blocks the upwards-facing sensors. In order to identify erroneous readings when the incoming short-wave dome was covered with snow, the outgoing radiation was used to provide an estimate of the incoming

radiation by dividing  $Q_{Si}$  by the albedo, which was calculated for all zenith angles greater than  $80^\circ$ . For the midwinter period presented, the typical albedo calculated in this manner was 0.92. The long-wave radiation, when affected by snow or rime, is much harder to detect. The incoming long-wave reading (prior to being corrected for the temperature of the body) will go to 0 if the sensor is covered suggesting that the temperature of the object it is looking at is at the same temperature as the sensor. This would have the same effect as cloud cover. Conditions where rime or snowfall errors were suspected were rare and are not believed to affect this dataset to any great extent. This error, when present, will over-estimate the incoming long-wave radiation flux (assuming that the upper sensor is most susceptible).

Other known errors of this sensor occur due to heating, and also under conditions of strong insolation, where a differential temperature can develop between the sensor and the aluminum body that contains the platinum resistance thermometer that the radiation flux is being referenced to. In any case, this effect would cancel out when calculating the net long-wave radiation. The effect of heating would affect the measured surface temperature making it seem slightly warmer than it should be.

Turnipseed et al. (2002) compared the CNR1 to a REBS Q\*7.1 instrument and found that during nocturnal periods, the CNR1 net long-wave flux measured by the CNR1 was 25% smaller (more negative), which resulted in a larger surface energy imbalance. Contrastingly, Kohsiek et al. (2007) reports that the REBS Q\*7 over-estimates the long-wave radiation at night as compared to the CNR1 (which compared well with other 4-component sensors in the study). van den Broeke et al. (2004) evaluated the CNR1 for unattended radiation observations in Antarctica and report that the long-wave sensors (CG3) operate within the manufacturers' specification ( $< 10\%$  error for daily totals). The conditions in the study of van den Broeke et al. (2004) are not very different from those experienced in the present study. Unfortunately, a nearby long-wave radiation measurement was not available to compare with the observations.

## **Turbulent Flux**

The two eddy covariance systems were mounted on arms extending from the tripod with the sonic anemometers oriented to the southwest ( $220^\circ$ ) such that the two prevailing wind directions of NW and SE would not be obstructed by the sensor arms. The Krypton Hygrometers were mounted at the same height and were offset by 15 cm from the center of the sonic anemometer sampling volume. The data from both eddy covariance systems were sampled and recorded at 20 Hz and were analyzed using the procedures described in §3.2.1.

### 3.3 Modelling and Parameterization of Turbulent Flux Processes

The methods described in this section primarily relate to the observations and modelling strategies reported in Chapter 7.

#### 3.3.1 Bulk Transfer Calculation

The bulk transfer equations (2.34)-(2.36), are commonly expressed in a more compact form using a transfer coefficient,  $C_d$ ,  $C_h$ , or  $C_v$ , for momentum, sensible heat, and water vapour, respectively which depend on the measurement height and the stability.

$$\tau = C_d U^2 \quad (3.11)$$

$$Q_H = \rho c_p C_h U (T_{surf} - T_{ref}) \quad (3.12)$$

$$Q_E = \rho \lambda_{sub} C_v U (q_{surf} - q_{ref}) \quad (3.13)$$

The bulk transfer coefficients are related to the roughness lengths by the expressions (3.14)-(3.16).

$$C_d = \kappa^2 \left[ \ln \left( \frac{z}{z_{0m}} \right) - \psi_m \right]^{-2} \quad (3.14)$$

$$C_h = \kappa^2 \left[ \ln \left( \frac{z}{z_{0m}} \right) - \psi_m \right]^{-1} \left[ \ln \left( \frac{z}{z_{0T}} \right) - \psi_h \right]^{-1} \quad (3.15)$$

$$C_v = \kappa^2 \left[ \ln \left( \frac{z}{z_{0m}} \right) - \psi_m \right]^{-1} \left[ \ln \left( \frac{z}{z_{0q}} \right) - \psi_h \right]^{-1} \quad (3.16)$$

For stable conditions, the profile functions of Holtslag and De Bruin (1988) were used:

$$\psi_m = \psi_h = \psi_v = -0.7 \zeta - 0.75 (\zeta - 14.29) \exp(-0.35 \zeta) - 10.72. \quad (3.17)$$

For unstable conditions, the functions of Paulson (1970) were used:

$$\psi_m = 2 \ln \left[ \frac{(1+x)}{2} \right] + \ln \left[ \frac{(1+x^2)}{2} \right] - 2 \arctan(x) + \frac{\pi}{2}; \quad (3.18)$$

$$\psi_h = \psi_v = 2 \ln \left[ \frac{(1 + x^2)}{2} \right], \quad (3.19)$$

where  $x = (1 - 16\zeta)^{0.25}$ .

The equations described above were used in two different ways. In order to compare the effective turbulence characteristics of each site, the transfer coefficients were backed out of equations (3.11)-(3.13) using measured flux values, along with measured values of the wind speed, temperature, and relative humidity at a reference height, and the temperature at the surface inferred from the thermal radiation balance (3.10). It was assumed that the air in contact with the surface was saturated with water vapour at the surface temperature. Alternatively, if the objective was to use equations (3.11)-(3.13) for calculating fluxes, the roughness lengths were obtained using the theory of Andreas (1987b) along with the profile functions described above.

### Empirical Transfer Coefficients

Within Chapter 7, the bulk transfer approaches described above are compared to the empirical Kuz'min method described in Kuchment and Gelfan (1996). The expressions for the sensible and latent heat fluxes are:

$$Q_H = 18.85(T_{ref} - T_{surf})(0.18 + 0.098\bar{u}) \quad (3.20)$$

$$Q_E = 32.82(e_{surf} - e_{ref})(0.18 + 0.098\bar{u}) \quad (3.21)$$

These equations predict the fluxes in  $[\text{W m}^{-2}]$ , when the temperature is provided in  $[\text{°C}]$ , the vapour pressure in  $[\text{mbar}]$  and the wind-speed in  $[\text{m s}^{-1}]$ . In (3.20),  $T_{surf}$  is replaced with  $0^\circ\text{C}$  if  $T_{ref} > 0^\circ\text{C}$ . In (3.20), the vapour pressure at the surface,  $e_{surf}$ , is assumed to be the vapour pressure over ice at the surface temperature,  $T_{surf}$ .

### 3.3.2 Modeling

The numerical snow energy balance models described in the following paragraphs were applied to KF for dates 7 February through 15 February 2007. In order to compare the output of the two models, the physical set up was kept as similar as possible.

#### SNTHERM

The one-dimensional snow heat and mass balance model SNTHERM.89.rev4 (Jordan 1991) was used to model the snow energetics. The modeling domain was discretized into eleven thin

control volumes for the snow which were made as small as could be adequately represented by the available thermocouples. These were the same layers as used to calculate the internal energy content, which were described in §3.2.2. The snow layers ranged from 0.10 m at the bottom of the snowpack to 0.02 m near the top of the snowpack, and the surface layer was specified as a 0.005 m layer. The soil zone consisted of a single 0.10 m layer.

The model was driven with measurements of incoming long-wave and short-wave radiation as well as wind speed (3-cup anemometer), air temperature, and relative humidity all measured at 1.75 m above the snow surface. The short-wave albedo was set to a fixed value of 0.92, which was based on measurements. SNTHERM models the turbulent fluxes using the bulk transfer method, for which the adopted parameterizations are described in Jordan et al. (1999). For the two modeling runs presented, all of the parameters were identical except for the momentum roughness length  $z_{0m}$  which was varied from  $1 \times 10^{-4}$  m to  $1 \times 10^{-3}$  m. The ratio of the sensible and latent heat transfer coefficients ( $C_h$  and  $C_e$  respectively) relative to the drag coefficient  $C_d$  were both set to 1.0.

## CLASS

The land surface scheme CLASS (version 3.4) (Verseghy 1991, 2000) was compared to the results obtained by the more detailed SNTHERM. The handling of snow by CLASS is relatively simple, and does not permit specification of the physical properties of the snow surface. The model only considers a single snow layer which was specified to be 0.425 m thick. The model was driven with the same input data as SNTHERM: incoming long-wave radiation, incoming short-wave radiation, wind speed, air temperature, and relative humidity. An initial value for the short-wave albedo was set to 0.90 (the maximum value allowed), however CLASS then models the change in albedo with time. The  $z_{0m}$  value of this model could not be set, and was maintained at its fixed value of 0.001 m. The default soil thicknesses were maintained, which consisted of three layers: 0-0.10 m; 0.10 m - 0.35 m; and 0.35-4.10 m.

# CHAPTER 4

## OBSERVATIONS OF THE TURBULENT BOUNDARY LAYER OVER SNOW

### 4.1 Chapter Overview

Operational approaches to calculating turbulent heat and water vapour fluxes typically employ the bulk transfer formulae (equations (2.34)-(2.36)), which are based on a simplified set of turbulent transport equations (as described in §2.3). Most energy balance snowmelt models use these simplified methods for estimating the turbulent fluxes (*e.g.* SNOWPACK (Bartelt and Lehning 2002), Crocus (Brun et al. 1989), Utah Energy Balance model (Tarbotan and Luce 1996), SNOWBAL (Marks and Dozier 1992, Marks et al. 1999), SNTHERM (Jordan 1991), etc.). Application of the flux-gradient approach along with M-O theory requires empirical parameterizations that have been developed at homogeneous measurement sites under very ideal conditions (*e.g.* the Kansas and Minnesota Experiments as described in Kaimal and Wyngaard (1990)). This is simply a reflection of what was considered necessary by the micro-meteorological community to simplify the complex physical problems of atmospheric flow (Kaimal and Finnigan 1994). Remarkably, despite their simplistic origins, these methods have been applied successfully in a number of more complex conditions (Munro 1989, Cullen et al. 2007, Marks et al. 2008). However, problems with this approach have also been documented (*e.g.* Arck and Scherer 2002, Pomeroy et al. 1998).

From a hydrological perspective, there is considerable interest in estimating turbulent fluxes in more complicated areas such as mountains, which are often the primary hydrological contributors to rivers that supply water to vast surrounding areas. Mountain environments are extremely complex, and the heterogeneous terrain presents some serious challenges to both measurement and modeling approaches and consequently have received relatively little study by the same micro-meteorological community. However, despite this shortcoming, snowmelt models are often applied to complex areas. The turbulent heat fluxes are usually modeled for selected environments which exhibit some degree of local homogeneity. This usually is

an open environment where micro-meteorological siting guidelines (such as those discussed by Gash (1986) or Garratt (1990)) are usually prescribed. In most cases, the estimated heat fluxes are not verified against eddy covariance methods.

In this chapter, the turbulence processes responsible for surface fluxes of momentum, heat, and water vapour are investigated with the overarching goal of determining whether the turbulent transfer processes in the open environments examined in this thesis are similar to of the simple homogeneous environments from which much of the flux estimation theory is based upon. The analysis was guided by the following science questions: (1) how do turbulence regimes differ between the selected environments, all of which are open and locally homogeneous, but have differing large-scale heterogeneity?; (2) is the turbulence structure measured in these flat open areas similar to the canonical flat homogeneous case that flux-gradient theory is based upon?; and (3) do these environments pose significant measurement challenges for the eddy covariance technique that might not be present in less complex terrain?.

The rationale for the broad range of sites chosen for this chapter stems from a desire to understand the effect of the wind gusts at the two mountain valley sites (HM and ML). The broad alpine ridge site (WCA) was included to see if there were similar terrain-induced effects on turbulent transfer in this upland mountain environment, or whether this is just something that is only typical of mountain valleys. The prairie site (KF) represents the ideal standard: a site to test how well theoretical surface flux relationships hold true over level snow fields.

## 4.2 Site Characterization

### 4.2.1 Wind Flow Characteristics

The frequency distribution of the mean 30-minute horizontal wind speeds measured close to the ground are plotted in Figure 4.1 for the snow covered record of each experiment. At the two valley sites (ML and HM), lower wind speeds were more prevalent with  $> 75\%$  of the values occurring at wind speeds  $< 2.5 \text{ m s}^{-1}$ . This is presumably due to the sheltered topographical nature of the sites, both located in relatively narrow mountain valleys with steep walls. At the prairie and the alpine ridge sites, more moderate wind speed regimes were observed. The alpine site (WCA) is located atop a broad treeless ridge that was rarely calm, and is presumably located in a zone of wind acceleration as the streamlines converge at the top of the mountain. At the open prairie site (KF), a broad range of wind velocities were observed that were typically as low as  $1\text{-}2 \text{ m s}^{-1}$  during cold, stable, high-pressure systems which were interspersed by frontal systems that resulted in much higher windspeeds

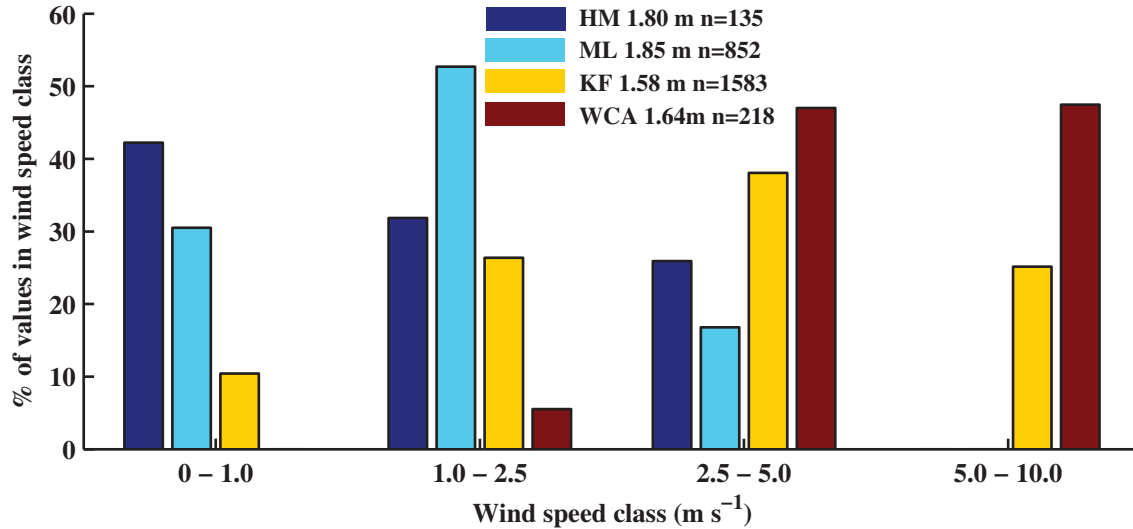


**Figure 4.1:** Frequency distribution of mean 30 min. wind speeds.

for periods usually shorter than a day.

The fluctuations of the wind velocity components are of much greater importance to turbulent processes than the magnitude of the mean wind speed. These are presented as the turbulence intensity (standard deviations of velocity components normalized by the mean horizontal wind speed) in Figure 4.2, for the (a) longitudinal and (b) vertical components. Although the mountain valley sites were shown to be less windy, they are relatively more turbulent. At all sites, the turbulence intensity was largest at low wind speeds owing to the fact that only a few individual large eddies were sampled, which thus exerted a larger influence on the statistic. However, at higher wind speeds the turbulence intensity converged at a near-steady value. In the case of the horizontal turbulence intensity, which can be considered as an indication of the gustiness of the environment, WCA and KF turbulence intensities both appeared to stabilize at around 15%, whereas the HM and ML values were around 32% and 54% respectively. A turbulence intensity of  $> 0.5$  is often cited as the limit for which Taylor’s (1938) frozen turbulence hypothesis can be invoked (*e.g.* Willis and Deardorff 1976, Katul and Parlange 1994). This implies that the conceptual model where turbulent eddies are advected past the sensor at the rate of the mean wind speed is not always applicable in mountain valleys. The vertical turbulence intensity stabilized at around 5% for KF and WCA, but again was larger in the mountain valleys, at around 12-13%. This suggests that the wind field in the valley sites should be more effective at generating turbulent fluxes than KF and WCA. This will be discussed in more detail in section 4.4.2.

The turbulent kinetic energy, as it varied with mean horizontal wind speed is shown in Figure 4.3. Consistent with the turbulence intensity information previously presented, the

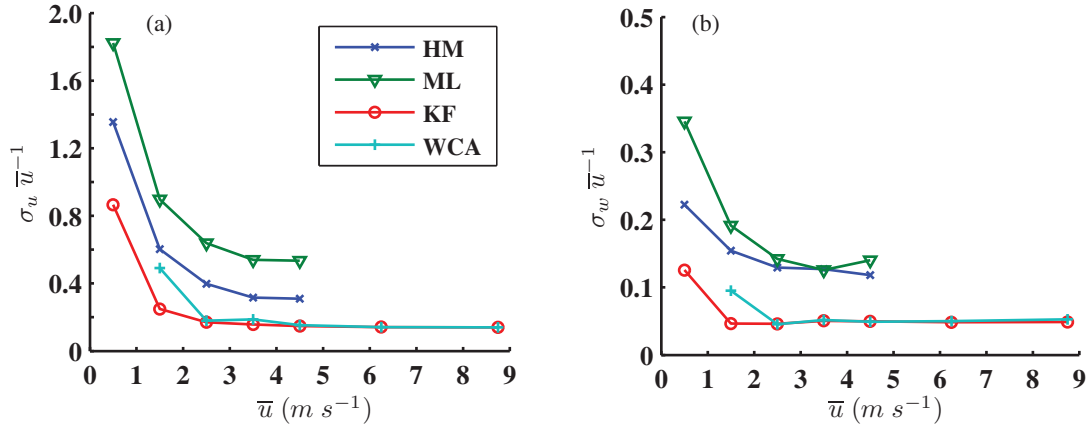


**Figure 4.2:** Variation of mean turbulence intensity with wind speed: (a) longitudinal, (b) vertical. Note the different scales shown on the vertical axes.

mountain valley sites were the most turbulent. Surprisingly, WCA and KF sites exhibited a degree of similarity despite their different environmental attributes.

## 4.2.2 Typical Latent and Sensible Heat Flux Values

The sensible and latent heat fluxes measured during the snow covered record at each site are presented in Figure 4.4. Here, values were filtered to include only good wind directions, and wind speeds  $> 1.0 m s^{-1}$ . At lower wind speeds, the turbulence was poorly defined and the fluxes were inappropriately captured by the EC technique (this will be discussed in more detail in §4.4). In Figure 4.4, all sites are plotted on the same figure for efficient presentation. The differing meteorological conditions during each of the study periods do not permit a direct comparison between sites. However, despite the differing climates, the differences in flux magnitude between the measurement locations were not very remarkable.

Across all measurement locations, the turbulent heat fluxes were relatively small. With respect to sensible heat, at all sites the majority of the energy was directed towards the snowpack, but was typically less than  $30 W m^{-2}$ . Sensible heat fluxes directed towards the atmosphere were most common at WCA, possibly caused by advection of energy from upwind snow-free patches.

At all sites, a large proportion (40-65%) of the latent heat fluxes were near zero ( $\pm 5 W m^{-2}$ ). Otherwise, sublimation was more prevalent than condensation. However, it should be noted that condensation is expected to be underrepresented, due to frost forming on the lenses of the open path hygrometer under condensing conditions.

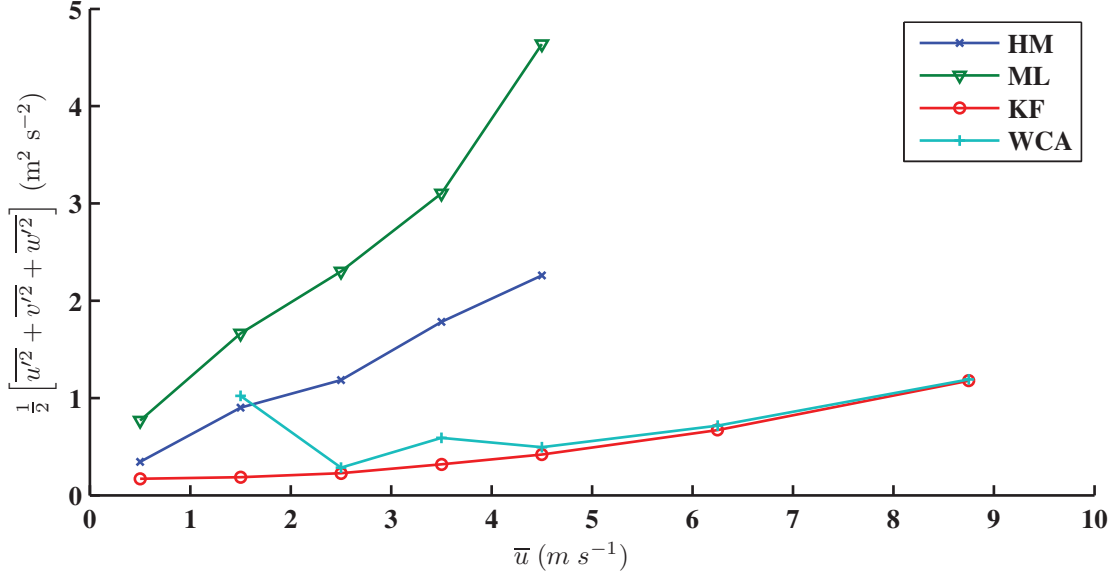


**Figure 4.3:** Variation of the turbulent kinetic energy with mean horizontal wind speed.

### 4.3 Characteristics of the Surface Boundary Layer During Well-Developed Flow Conditions

In order to compare the turbulence properties of each site under strong, well-developed flow conditions, a single event was selected from each site (HM, WCA, and KF) where wind speed and direction were approximately constant and quasi-stationarity could be assumed. This is consistent with the approach of many of the studies reported in the literature where data are handpicked for ideal conditions (*e.g.* Andreas 1987a, Kaimal et al. 1972, Oncley et al. 1996). However, in this case a single event (or continuous portion of) was selected rather than individual 30-60 minute periods so as to better represent the interest of hydrological modeling in which the aggregated results of an event are extremely important. Mud Lake was excluded from this analysis because high frequency data were not available. However, the turbulence characteristics for ML were similar to the other valley site (HM), and the boundary layer structure and turbulence processes are expected to be quite similar. The mean turbulence characteristics for each of the specific events described below are summarized in Table 4.1

#### 4.3.1 Meteorological Conditions of Selected Events

**Kernen Farm (21:30 4 February 2007 to 14:30 5 February 2007):** The wind speeds during this period ranged from 5.5 to 7.5  $m s^{-1}$  and were consistently from the east-southeast ( $114^\circ \pm 5^\circ$ ). The boundary layer appeared to be well developed as both measurement heights

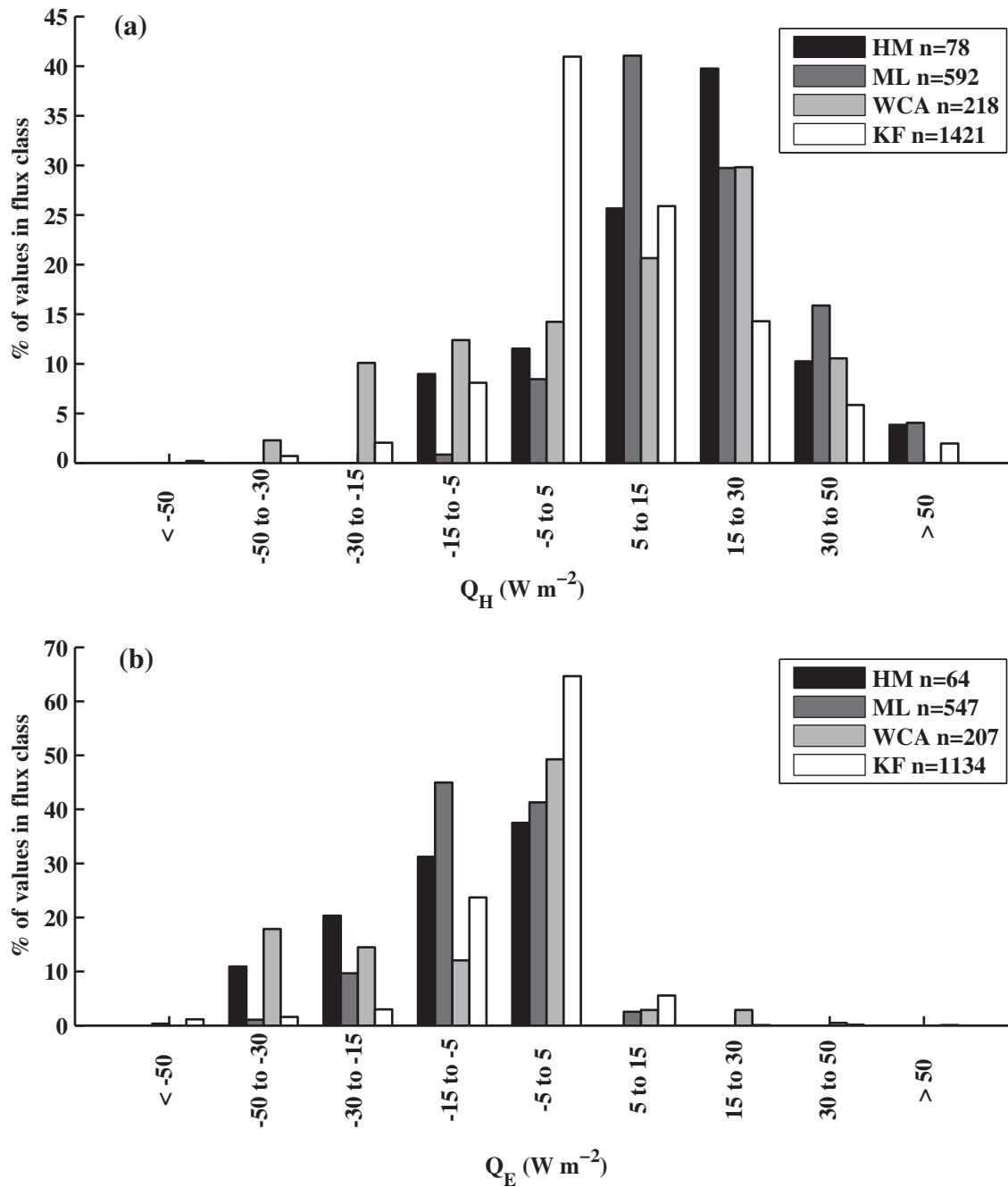


Figure 4.4: Heat flux frequency distribution: (a) sensible heat flux; (b) latent heat flux.

reported very similar fluxes (within 10% of each other for  $u_*$ , and 15% for  $Q_H$  and  $Q_E$ ). Atmospheric conditions were approximately neutral ( $-0.03 > \zeta < 0.02$ ) as the winds were strong and the sensible heat fluxes were small ( $< 35 \text{ W m}^{-2}$ ) and predominantly directed towards the atmosphere. The air temperature was ranged from  $-22^\circ\text{C}$  to  $-18^\circ\text{C}$ . The latent heat fluxes were particularly small ( $< 5 \text{ W m}^{-2}$ ) indicating that only minor sublimation was occurring. Blowing snow was not occurring during the selected period (as indicated by the snow particle detector).

Although the flow conditions were quite strong and the surface exhibited numerous surface roughness features associated with prior blowing snow events, the flow was dynamically quite smooth, with measured  $z_{0m}$  values around  $2\text{-}3 \times 10^{-5} \text{ m}$ . The roughness Reynolds number  $Re_* = u_* z_{0m} \nu^{-1}$  calculated for the selected period reveals that the flow was in the transitional zone between aerodynamically smooth ( $Re_* \leq 0.135$ ) and fully rough ( $Re_* \geq 2.5$ ) conditions. The friction velocity measured by the sonic anemometer was, on average, within 5% of that calculated from the 2-level wind gradient, confirming that the boundary layer was well developed and that the fluxes were related to the mean gradients (at least as far as the momentum flux is concerned). Furthermore, the mean value of the dimensionless wind shear  $\phi_m$ , calculated using (2.28), was exactly 1.0, its expected value at neutral conditions, which confirms this period can be characterized by local scaling variables (M-O theory). The turbulence intensity was relatively low (11%) and was slightly greater in the longitudinal direction than the lateral direction.

**Hay Meadow (9:00 to 17:00 26 February 2006):** This event was characterized by strong westerly flow conditions aloft in which the valley winds were effectively ‘decoupled’ from the overlying flow, as suggested by Figure 4.5 which compares the wind speed and direction measured at the HM site with an upwind ridge location. For the selected period, neutral conditions prevailed (according to  $z/L$  values calculated from the sonic anemometer). Wind speed profiles (Figure 4.6) exhibited logarithmic behaviour throughout the selected period, suggesting that measurements were being made within a developed internal boundary layer. The air temperature during this period warmed from  $-4^\circ\text{C}$  to  $4^\circ\text{C}$ , and sensible heat fluxes directed towards the snowpack averaged  $16 \text{ W m}^{-2}$ , and latent heat fluxes averaged  $24 \text{ W m}^{-2}$  (sublimating).

The flow during this event was dynamically rough, characterized by  $Re_*$  values ranging from 30 to 75. The snow surface was smooth (no dune features) but had a few protruding grass stalks. For the neutral conditions of the selected period, the mean  $z_{0m}$  calculated from the wind speed profile was  $2.1 \times 10^{-3} \text{ m}$ , which is a fairly typical value for snow surfaces (compared to values in Table 2.1). However, the  $z_{0m}$  inferred from the sonic anemometer

**Table 4.1:** Mean turbulence characteristics observed during selected events.

<i>site</i>	(units)	<b>KF</b>		<b>WCA</b>		<b>HM</b>
		1.58	3.24	1.64	3.27	1.80
<i>z</i>	( <i>m</i> )					
$\overline{uu}_*^{-1}$		27.91	30.11	21.01	25.89	11.77
<i>TKE</i>	(m <sup>2</sup> s <sup>-2</sup> )	0.50	0.48	0.67	0.70	2.23
$\sigma_u$	(m s <sup>-1</sup> )	0.76	0.74	0.84	0.85	1.29
$\sigma_v$	(m s <sup>-1</sup> )	0.57	0.55	0.69	0.71	1.56
$\sigma_w$	(m s <sup>-1</sup> )	0.27	0.29	0.29	0.27	0.50
$u_*$	(m s <sup>-1</sup> )	0.23	0.23	0.28	0.26	0.34
$\sigma_u \overline{u}^{-1}$		0.12	0.11	0.15	0.13	0.32
$\sigma_v \overline{u}^{-1}$		0.09	0.08	0.12	0.11	0.39
$\sigma_w \overline{u}^{-1}$		0.04	0.04	0.05	0.04	0.13
$\sigma_u u_*^{-1}$		3.32	3.27	3.09	3.42	3.78
$\sigma_v u_*^{-1}$		2.50	2.42	2.54	2.87	4.55
$\sigma_w u_*^{-1}$		1.17	1.28	1.03	1.09	1.47
$r_{uw}$		-0.26	-0.24	-0.31	-0.27	-0.18
$u'^3 \sigma_u^{-3}$		0.01	-0.01	0.03	-0.07	0.44
$v'^3 \sigma_v^{-3}$		0.01	0.05	-0.07	-0.02	-0.06
$w'^3 \sigma_w^{-3}$		0.15	0.13	0.19	0.34	-0.20
$u'^4 \sigma_u^{-4}$		2.76	2.79	2.89	2.95	3.44
$v'^4 \sigma_v^{-4}$		3.31	3.29	3.40	3.31	3.56
$w'^4 \sigma_w^{-4}$		3.69	3.62	3.62	3.92	4.52

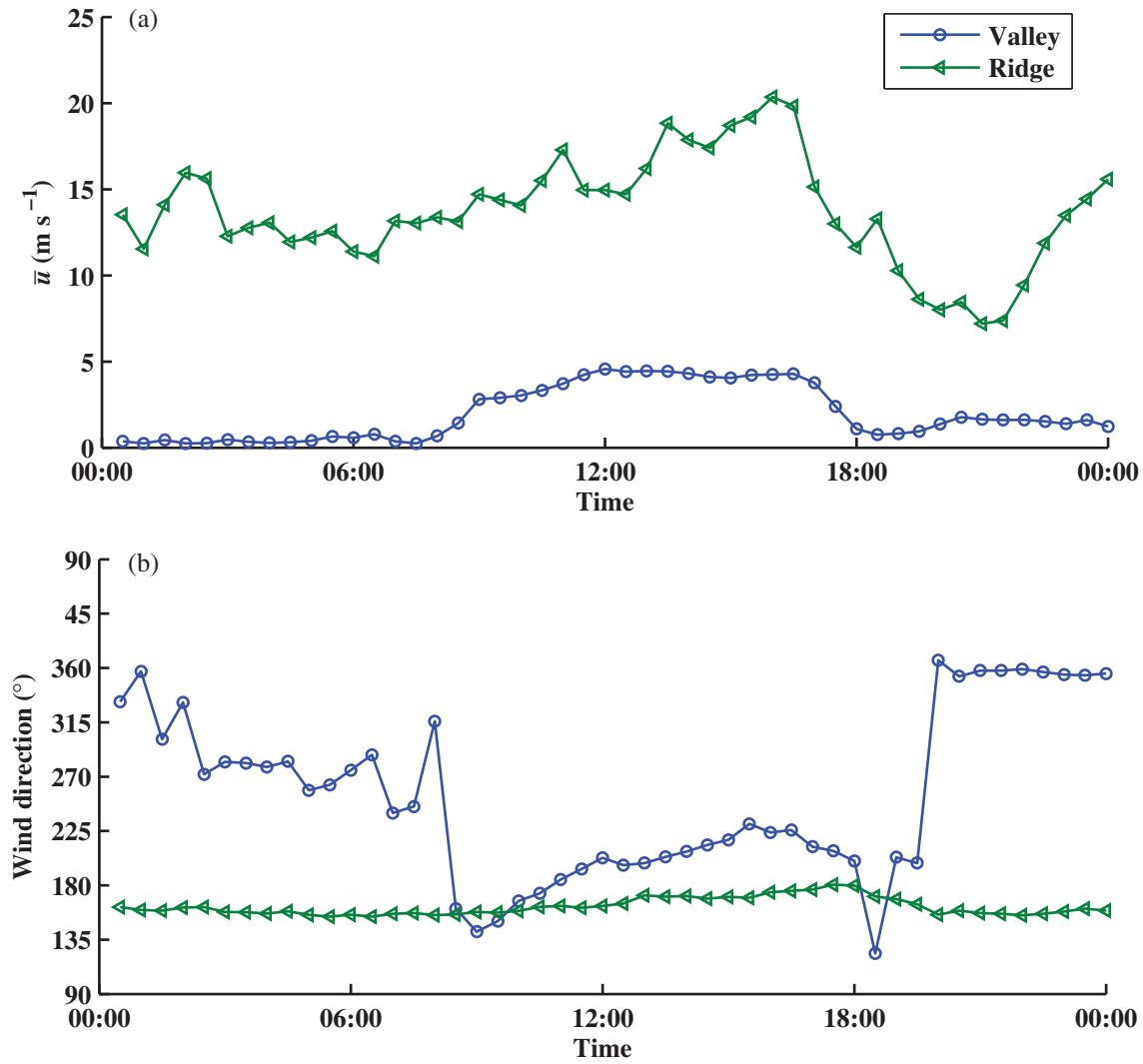


**Figure 4.5:** Comparison of winds at HM valley bottom and upwind ridge top for 26 February, 2006: (a) mean wind speed; (b) mean wind direction.

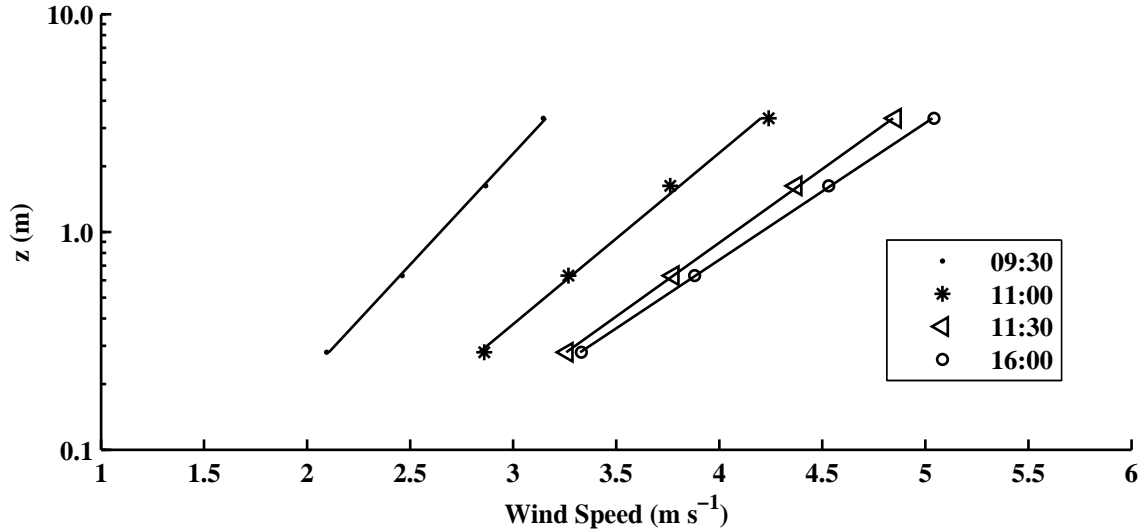


**Figure 4.6:** Selected wind speed profiles measured at HM on 26 February, 2006.

over the same period was  $16.8 \times 10^{-3}$  m. This order of magnitude difference suggests that the actual turbulence, or specifically the momentum transfer to the surface, was much larger than is indicated by the mean wind speed profiles. This is confirmed by the mean value of  $\phi_m$  of 1.7, which also suggests that the turbulence does not scale on local surface variables (for the neutral conditions encountered,  $\phi_m$  was expected to be approximately 1.0). Similar to the results of Figure 4.2, the turbulence intensity was much larger at this location than at WC and KF. Additionally, the lateral variance was larger than the longitudinal variance further suggesting that the wind gusts cannot simply be viewed as larger eddies carried about at the rate of the mean wind speed. Rather, a more complicated boundary layer structure was imposed upon the internal boundary layer that was indicated by the logarithmic wind speed profiles of Figure 4.6. The 3rd and 4th order central moments (skewness and kurtosis respectively) at this site were also markedly different than KF and WCA. Of particular importance, is the vertical velocity distribution that was negatively skewed and has a much larger kurtosis than the other sites. Both of these measures indicate a strong influence of outliers, suggesting that the wind gusts had an effect on the vertical velocity fluctuations, which in turn could be expected to impact the turbulent flux magnitude.

**Wolf Creek (12:00 to 24:00, 14 April 2007):** During the selected period there was strong flow out of the south ( $205^\circ \pm 10^\circ$ ), and the air temperature exhibited a diurnal variation ranging from  $-7^\circ\text{C}$  to  $-3.5^\circ\text{C}$ . The turbulence characteristics in Table 4.1 suggest that the boundary layer was weakly developed, perhaps due to the presence of the ridge. A constant flux layer was not observed, as the momentum flux decreased with height and the heat fluxes increased with height. Vertical variance was higher near the surface, which is in contrast

**Table 4.2:** Example values of the normalized standard deviation of velocity components collected in various environments.

Author(s)	$\sigma_u u_*^{-1}$	$\sigma_v u_*^{-1}$	$\sigma_w u_*^{-1}$	Comments
Panofsky and Dutton (1984)	2.39	1.92	1.25	Flat terrain aggregate
Panofsky and Dutton (1984)	3.45	2.90	1.23	Rolling terrain aggregate
Smeets et al. (1998)	2.4	2.1	1.4	Pasterze glacier; high-pass filtered
Hicks (1981)	-	-	1.25	Kansas Experiment (flat)
King (1990)	-	-	1.42	Antarctic ice shelf (5 m)
Smedman (1988)	-	-	1.28	Gently rolling (2 m)
Wilson (2008)	-	-	1.0	Utah salt flats

to what was observed at KF. It is difficult to assess whether the lower measurement height was in the surface equilibrium boundary layer or not. Sensible heat fluctuated by  $\pm 30$   $\text{W m}^{-2}$  and was initially directed towards atmosphere, and then later towards the snow. This resulted in atmospheric stability ranging from unstable to mildly stable. However, the local bulk temperature gradient suggested that heat should have been directed towards the snowpack for the entire period. This discrepancy was possibly due to advected energy from up-wind snow-free patches (*e.g.* Granger et al. 2006) combined with a very shallow boundary layer due to the pressure-gradient caused by the presence of the ridge. The snowpack was sublimating and latent heat fluxes ranged from 0 to 40  $\text{W m}^{-2}$ . For the period selected,  $z_{0m}$  inferred from the sonic anemometer was  $3.1 \times 10^{-4}$  m and  $Re_* \approx 10$ . The turbulence intensity values were quite similar to those observed at KF.

### 4.3.2 Boundary Layer Structure

The standard deviations of the wind velocity components normalized by the friction velocity, *i.e.*  $\sigma_u u_*^{-1}$ ;  $\sigma_v u_*^{-1}$ ; and  $\sigma_w u_*^{-1}$ , which are sometimes referred to as Integral Turbulence Characteristics (Foken and Wichura 1996) or as the turbulent energy-flux ratio (King 1990), reveal the contribution of each fluctuating velocity component towards the momentum flux. As such, they provide insight into the turbulence mechanisms of a particular environment. In pure mechanical turbulence, the standard deviations of the velocity components are expected to be linear functions of  $u_*$  (Panofsky and Dutton 1984). Thus, in neutral conditions, the normalized standard deviations often take on constant values (which have been summarized in Table 4.2). Furthermore, in stratified flow, M-O theory states that the normalized standard deviations should be functions only of  $\zeta$  when measured in the surface layer. Here, since it is primarily near-neutral atmospheric conditions encountered in these events, the discussion will be similarly restricted.

Owing to non-local turbulence dynamics there are numerous documented cases of larger

normalized variances that do not necessarily scale with  $\zeta$ , and do not necessarily converge at a constant value when  $\zeta = 0$ , particularly for the horizontal variances (*e.g.* McNaughton and Brunet 2002). This has been observed primarily for the horizontal variances in complex terrain (*e.g.* Panofsky and Dutton 1984). However, in many of these cases the vertical ratio is unaffected. This result can be considered in terms of Townsend’s (1961) proposed concept of an equilibrium boundary layer in which turbulence production roughly equals turbulence dissipation. Motions within this layer have been classified by Bradshaw (1967) as either (1) small scale *active* motions that contribute to the shear stress and scale with  $u_*$  and  $z$ , or (2) larger *inactive* motions that are determined by turbulence in the outer region of the boundary layer. The inactive motions are thought to be primarily irrotational eddies which have their centers far from the wall. As such, they contribute to the horizontal variances but not to the vertical variance or to momentum transfer. These motions have much larger length scales and accordingly exhibit a ‘turbulence memory’ due to slow adjustment to the local surface (Beljaars 1987). On the other hand, the motions contributing to the vertical variance must have vertical length scales equal or less than the measurement height; so accordingly the vertical variance usually reaches a more rapid equilibrium with the local surface. Accordingly, the vertical standard deviation rarely deviates from the equilibrium conditions, even in more complex terrain. In general, eddies with vertical length scales larger than the measurement height will not contribute appreciably to the vertical variance due to blocking at the surface.

The horizontal ratios  $\sigma_u u_*^{-1}$  and  $\sigma_v u_*^{-1}$  for all measured sites (Table 4.1) were larger than the values reported in Table 4.2. The values at HM were largest; an anticipated result due to the gusty nature of the site and the complex surrounding topography. In terms of the vertical velocity component,  $\sigma_w u_*^{-1}$ , the value at KF was within the expected range, whereas WCA values were much lower and HM values were much larger. The  $\sigma_w$  values at KF displayed an increase with height, presumably due to a reduction in the effect of blocking at the surface (Högström et al. 2002). At WCA an opposite effect was present, where  $\sigma_w$  was larger at the lower measurement height. This is attributed to changes in the mean flow and turbulence as the flow accelerates over the ridge top and suggests that the equilibrium layer at this site was likely very thin. At both heights,  $\sigma_w$  was normalized by the local value of  $u_*$  (*e.g.* Nieuwstadt 1984) since neither height was within a constant flux layer. The main anomalous result was that  $\sigma_w u_*^{-1}$  at HM was much larger than the other sites, which suggests that the wind gusts were perhaps not inactive, but also contributed to momentum transfer. In a recent study, Wilson (2008) reports data from measurements over a uniform salt flat in Utah (a highly ideal boundary layer) where neutral values of  $\sigma_w u_*^{-1}$  that were around 1.0, and makes the argument that M-O similarity theory is not adequate to describe the velocity variances and reminds the reader of its empirical nature. Rather than

deliberating over the expected value of this ratio, there is more merit in considering what it indicates about boundary layer processes.

The normalized standard deviations are closely related to the linear correlation coefficients (4.1). In homogeneous shear flow in a wind tunnel boundary layer,  $r_{uw}$  is approx -0.5, whereas for atmospheric flows it is commonly reported as -0.3 (Kaimal and Finnigan 1994). This reduction is reportedly due to inactive motions that contribute to horizontal motions but not vertical motions (Smeets et al. 2000). The correlation coefficient is largest at WCA, and slightly smaller at KF, but is appreciably smaller for HM at -0.18.

$$r_{uw} = \frac{\overline{uw}}{\sigma_u \sigma_w} = -\frac{u_*}{\sigma_u} \frac{u_*}{\sigma_w} \quad (4.1)$$

Clearly, due to the blocking effect at the surface, an increase in wind gustiness will act to decrease the correlation coefficient. If  $\sigma_w$  is limited due to blocking by the surface, any contribution from the gusts will decrease the correlation between the horizontal and vertical components and not contribute much to the fluxes. This would explain the low correlation coefficient for HM and also the increased value of  $\sigma_w u_*^{-1}$ .

### 4.3.3 Turbulence Spectra and Cospectra

The Fourier spectra and cospectra reveal important details about the frequency distribution of the energy scales that contribute to the velocity variances and the momentum and heat fluxes. The data collected during the well known Kansas study (*cf.* Kaimal and Wyngaard 1990) has led to the adoption of the spectral and cospectral forms presented by Kaimal et al. (1972) as the canonical curves for the surface boundary layer. In this thesis, the spectral and cospectral measurements made at each study location are compared to the Kansas results, which are considered as the pinnacle of the well-understood homogeneous boundary layer.

The velocity spectra were first plotted in log-log form to ensure that they exhibited the appropriate -5/3 slope in the inertial subrange (Appendix B). Presented in Figures 4.7 to 4.12 are composite frequency-weighted spectra and cospectra that have been normalized by the friction velocity (in the case of the velocity components) or the kinematic flux (in the case of the flux cospectra). In all cases the non-dimensional frequency is used to scale the data, permitting all sites to be presented on the same figure along with the Kansas curves (Kaimal and Finnigan 1994, pg. 47 & 55).

The horizontal spectra (Figures 4.7 and 4.8) indicate that all sites contained significant energy at low frequencies. When normalized by  $u_*$  the effect of inactive motions can be seen quite clearly in that all of the horizontal variances deviated significantly from the Kansas forms at lower frequencies, and distinctions can be made between sites and measurement

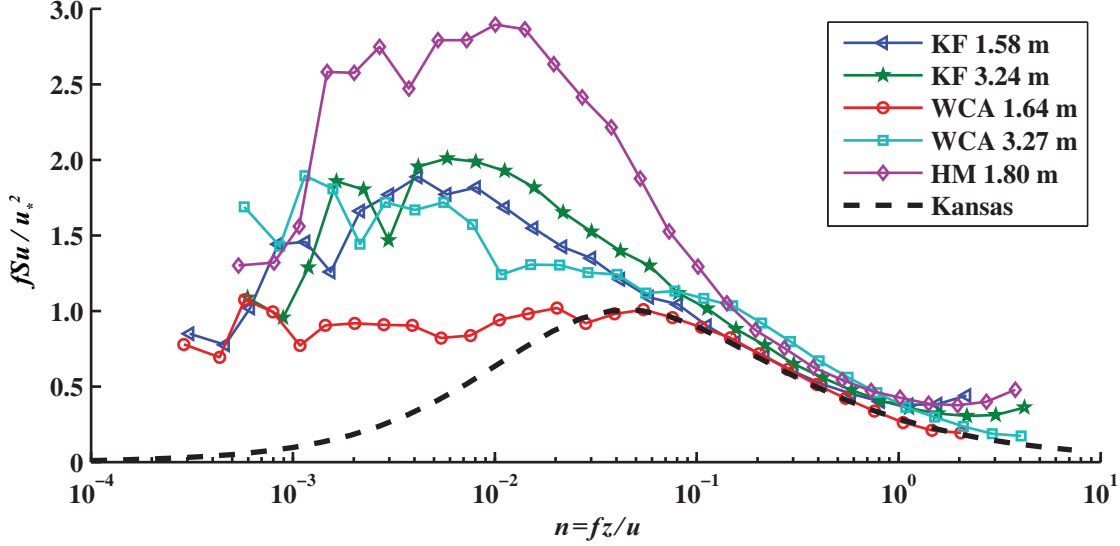


**Figure 4.7:** Frequency weighted, normalized longitudinal velocity spectra.

heights. Further away from the ground the values were larger. In every case, HM exhibited the most excess energy at lower frequencies, but this was particularly so for  $fS_v u_*^{-2}$ . Also worthy of note is that the energy at HM was increased at higher non-dimensional frequencies relative to other sites, perhaps indicating some interaction between the gusts occurring at larger scales and the smaller scale turbulent motions. At KF and HM, some high frequency noise was present in the spectra that did not appear at WCA. This may be related to aliasing, as data at KF and HM were collected at 20  $Hz$ , whereas WCA was similarly collected at 20  $Hz$ , but oversampled at 60  $Hz$ .

The spectra of vertical velocity (Figure 4.9) exhibited a higher degree of organization and similarity among sites. At most sites, the maximum energy occurred at approximately  $n = 0.5$ , but again HM was anomalous, having its maximum closer to  $n = 0.2$ . This is further evidence that the wind gusts were influencing the vertical velocity variance. In this figure the varying magnitude (power) of the curves is related to the degree of correlation between  $w$  and  $u$ , being lowest at HM and highest at WCA (1.64 m height).

The momentum cospectra, presented in Figure 4.10, were quite dissimilar from the Kansas form. The cospectra at both HM and KF sites peaked at lower frequencies than the Kansas cospectrum, whereas the WCA cospectra peaked at slightly higher frequencies. After comparison with Figures 4.9 and 4.7, it can be argued that the larger horizontal motions still maintain some degree of correlation with the vertical components and serve to generate momentum at lower frequencies. This again supports the notion that the wind gusts at HM were not entirely inactive. At KF there was a positive covariance between  $u$  and  $w$  at high frequencies that can not be related to the momentum flux. This may have been due to

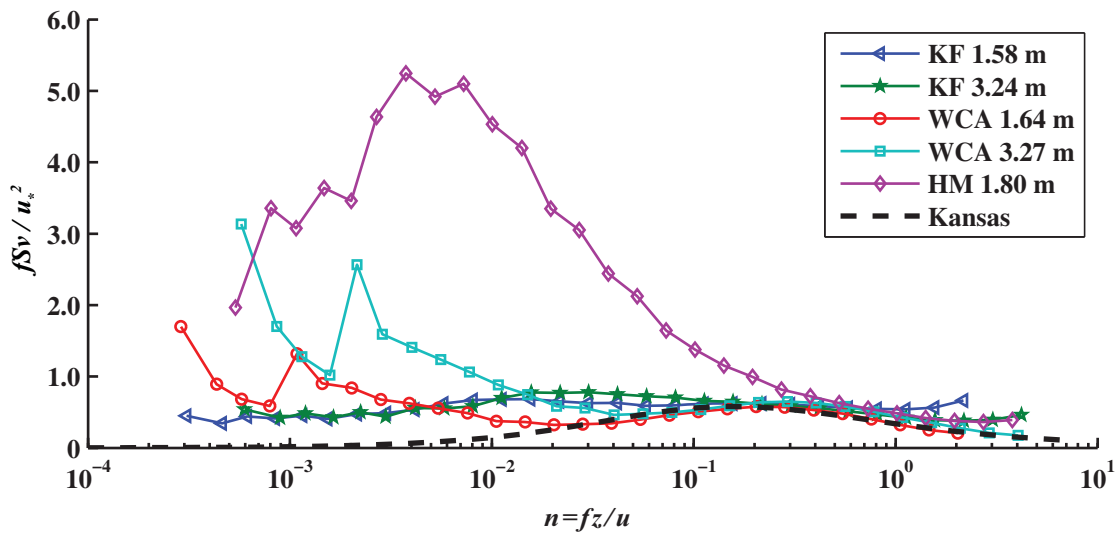


Figure 4.8: Frequency weighted, normalized lateral velocity spectra.

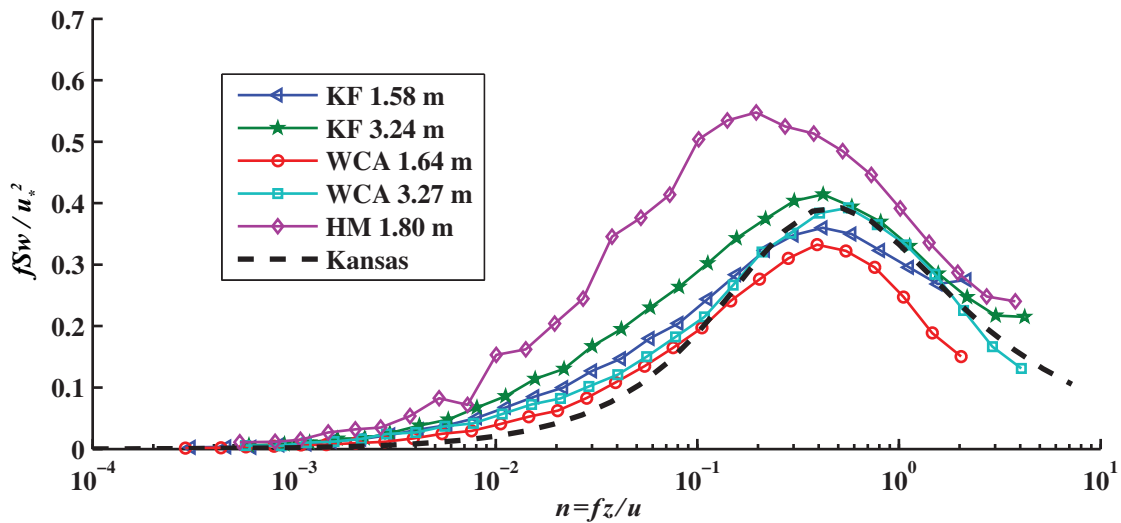
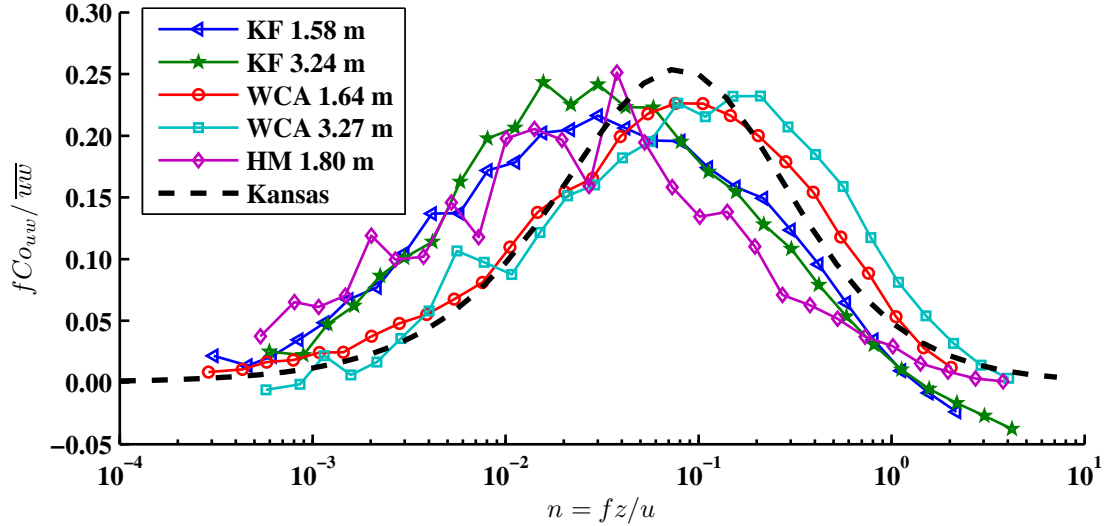


Figure 4.9: Frequency weighted, normalized vertical velocity spectra.



**Figure 4.10:** Frequency weighted, normalized momentum cospectra.

some correlated noise of unknown origin or perhaps from high frequency tower vibrations.

The kinematic sensible heat flux cospectra are shown in Figure 4.11. Again there were considerable departures from the Kansas model. The cospectrum at WCA and KF peaked earlier than the Kansas model, and exhibited a broad flat stretch around  $n = 0.01$  to  $0.2$ . The curve for HM peaked at much lower frequencies, and is more peaked than the other sites. For the kinematic latent heat flux cospectra (Figure 4.12), all sites had a broader shape and more energy at lower non-dimensional frequencies.

Overall, the most significant difference between the measured spectra (cospectra) from all sites and the Kansas curves was the additional energy at lower frequencies. Apparently, this is commonly observed in complex terrain. For example the spectra and cospectra collected by Andreas (1987a) in a locally homogeneous field show a similar difference which was attributed to the effect of perturbations to the boundary layer that were introduced by surrounding hills. Above-canopy measurements made by Turnipseed et al. (2004) at Niwot Ridge, Colorado, also displayed enhanced low frequency spectral energy. During a selected period where wave motions were present, these authors discovered that 25-50 % of the scalar covariance was attributed to large-scale motions present in the boundary layer. The spectra and cospectra collected by Smeets et al. (1998, 2000) also exhibited topographically-generated energy at low frequencies, which were shown to interact with the turbulent scales and similarly contribute to the variances and to the fluxes. For the valley site (HM), the low frequency energy can be attributed to the gusts (which were likely caused by wind flow interactions with the surrounding terrain). Although the significant wind gusts were not observed at WCA or KF, there are similar boundary layer processes that were generating energy at lower frequencies. At WCA large-scale topographical features are inherent in the surroundings, while at KF the

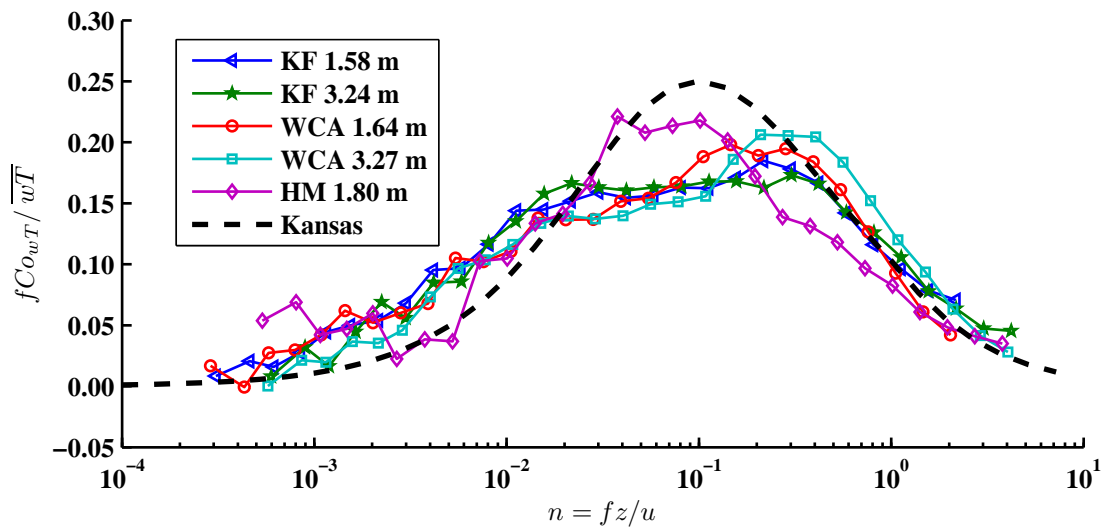


Figure 4.11: Frequency weighted, normalized kinematic heat flux cospectra.

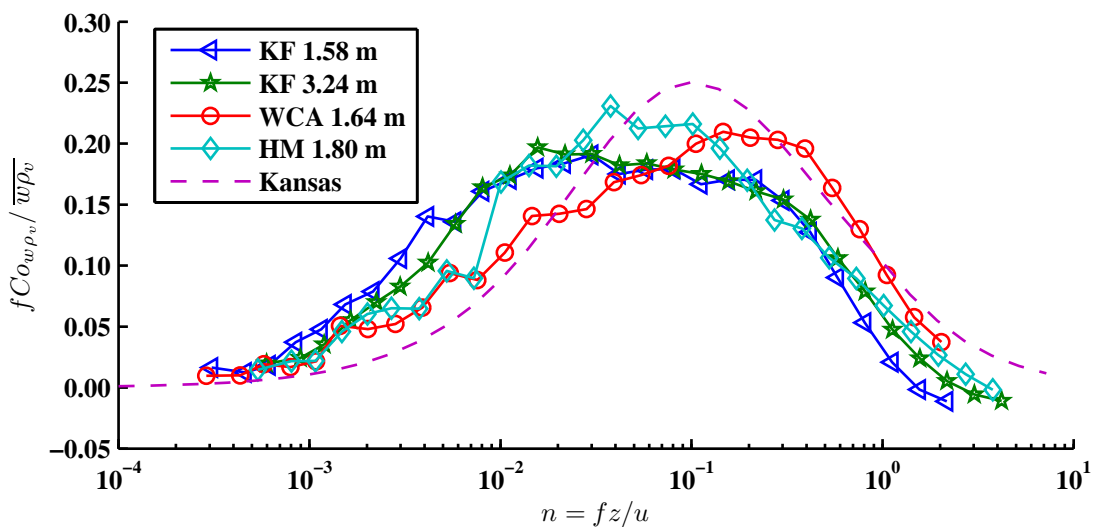


Figure 4.12: Frequency weighted, normalized kinematic water vapour flux cospectra.

source of the perturbations is less clear.

## 4.4 Turbulent Flux Characterization

### 4.4.1 Turbulence Scales and Flux Calculation

#### Flux Decomposition and Turbulence Gap Scales

The energy present at low frequencies in the spectra and cospectra collected at HM suggest that the prevalent wind gusts were influencing the variances and fluxes at lower frequencies than the expected turbulence scales. In order to obtain an indication of how significant the contribution of topographically forced motions were relative to turbulent scales, the covariances were decomposed using the Haar wavelet transform (Howell and Mahrt 1997), referred to by these authors as multi-resolution decomposition (MRFD). The gap detection algorithm of Vickers and Mahrt (2003, 2006) was then employed on the scale dependent Haar wavelet cospectral coefficients. The total covariance for each record (32,768 data points, 27.3 min.) was divided into (i) the turbulent scales which were calculated as those occurring prior to the gap scale, and (ii) the meso-scale contributions that occurred at longer scales. Defined in this manner, the meso-scale contribution for each site is presented in Table 4.3. This was calculated as the summation of the meso-scale fluxes (for all records) divided by the summation of the record-length fluxes. The heat fluxes used in this analysis were restricted to positive (towards the snowpack) sensible heat fluxes and negative (sublimating) latent heat. Both KF and WCA had relatively small amounts of flux occurring due to larger scale motions as compared to HM where the presence of wind gusts resulted in 18-25 % of the flux occurring at larger scales. From the inspection of individual multi-resolution spectra, there was a marked difference between HM and the other sites. Three examples are included to illustrate this. Figure 4.13 demonstrates this approach applied to momentum and sensible heat fluxes collected at KF for the record of 12:00 5 February 2007 where the wind was quite strong (approx.  $7 \text{ m s}^{-1}$ ). Here the peak and the gap scales can both be easily identified, and the accumulation of flux (Figure 4.13 (b) and (d)) had leveled off as the 30-min. averaging time was approached. In this example, meso-scale motions are not identifiable in the spectra and do not appear to have influenced the calculated flux value. However, this was not always the case at lower wind speeds. Figure 4.14, collected at 23:00 7 February 2007 when the windspeed was around  $1 \text{ m s}^{-1}$ , indicates that very little flux was occurring at turbulent scales. Again, the peak and gap scales can be identified, however beyond the gap scale were meso-scale motions that were actually of opposite sign to the turbulent fluxes and were largely responsible for the magnitude and direction of the calculated flux. These two examples

are fairly typical for this site where fluxes were well defined by a turbulence gap at higher wind speeds, but there was clearly a meso-scale influence at lower wind speeds. However, as indicated in Table 4.3, the overall effect of the inclusion of meso-scale motions in the flux calculation was not large.

**Table 4.3:** Total contribution to flux from scales beyond the turbulence gap.

Site	$\overline{uw}$	n	$\overline{wT}$	n	$\overline{wq}$	n
HM	26%	(109)	18%	(105)	20%	(73)
WCA	3%	(172)	8%	(111)	3%	(94)
KF	3%	(796)	4%	(514)	9%	(495)

At Hay Meadow, the multi-resolution spectra do not clearly separate the turbulent scales from the meso-scales. Figure 4.15 was prepared from data collected from 12:30 26 February 2006, when the wind speed was  $4.4 \text{ m s}^{-1}$ . Here, the peak and gap scales could be identified after applying a smoothing filter to the coefficients, however the gap scale did not appear when the cospectral coefficients were near zero. In this example, and in many of the spectra collected at HM, there was significant energy at larger scales that was not clearly separated by a turbulence gap which suggests that the prevalent wind gusts tended to overlap the turbulent scales.

Although no specific examples are presented for WCA, the multi-resolution cospectra appear very similar to those collected at KF, and meso-scale motions do not appear to significantly affect the measured fluxes.

## Stationarity

Non-stationarity is a systematic error that can result when statistics (means, variances, etc.) are calculated over a period which includes larger scale motions that are changing with time. Since the meteorological properties of the atmosphere are constantly changing, atmospheric flows are inherently non-stationary. Standard practice is to select a suitable averaging time which effectively separates turbulent motions, which occur on shorter time scales, from the meso-scale and synoptic scales that change as the meteorology changes. As revealed from the gap scale analysis just presented, at HM there was a large portion of the flux generated by larger-scale motions, whereas at WCA and KF these larger scale motions were only effective when wind speeds were low. The inclusion of the low frequency component often increases the random error associated with the flux calculation simply because there are few eddies sampled during the selected period. While these low frequency motions may be important carriers of flux, lengthening of the averaging period risks incorporating the effects of non-stationarity. Therefore, in selecting a suitable averaging period, there is often a trade off

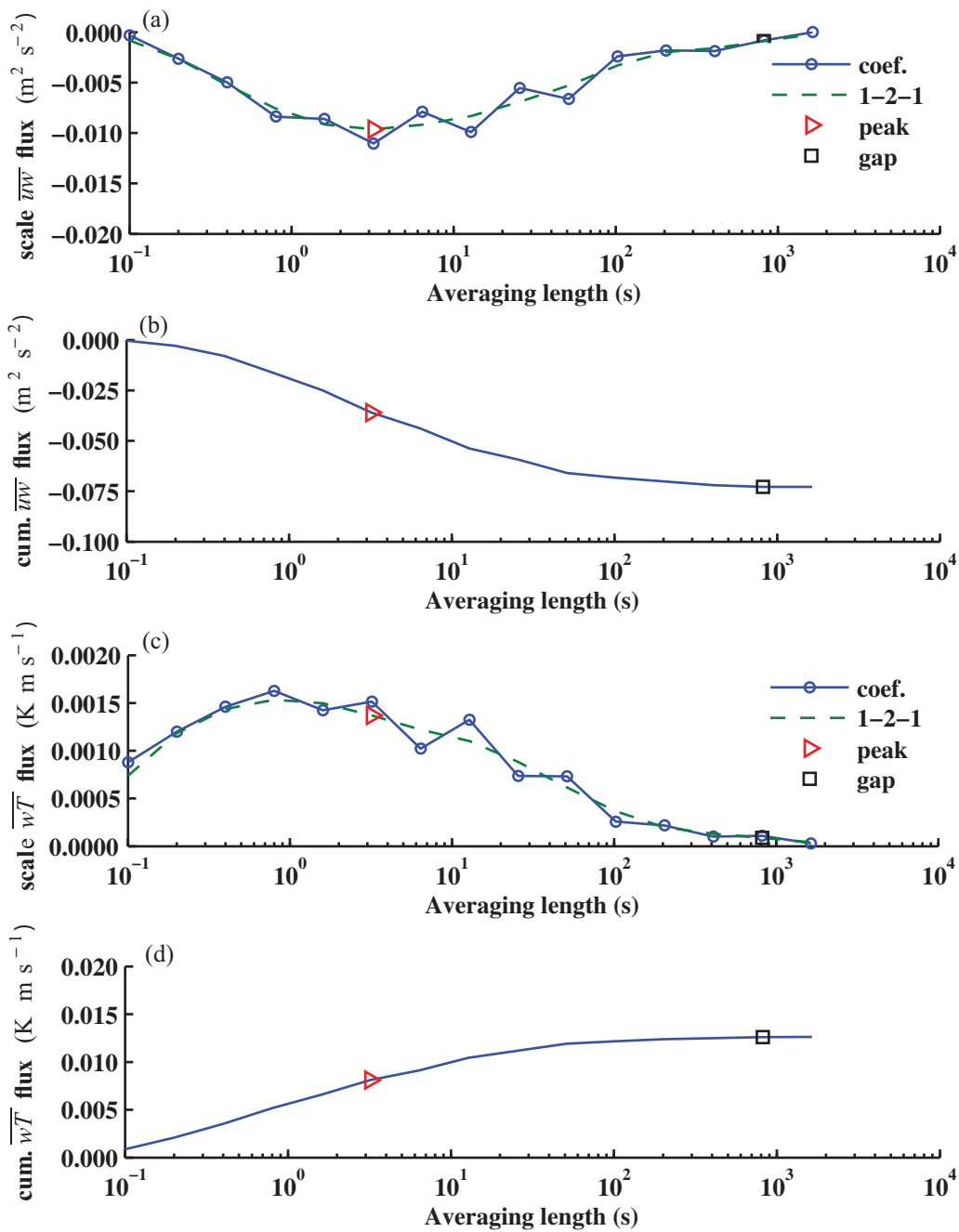


**Figure 4.13:** Example of MRFD applied to Kernen Farm (wind speed  $\approx 7 \text{ m s}^{-1}$ ). Note: dashed line in panels (a) and (c) are the coefficients smoothed using a 1-2-1 filter.

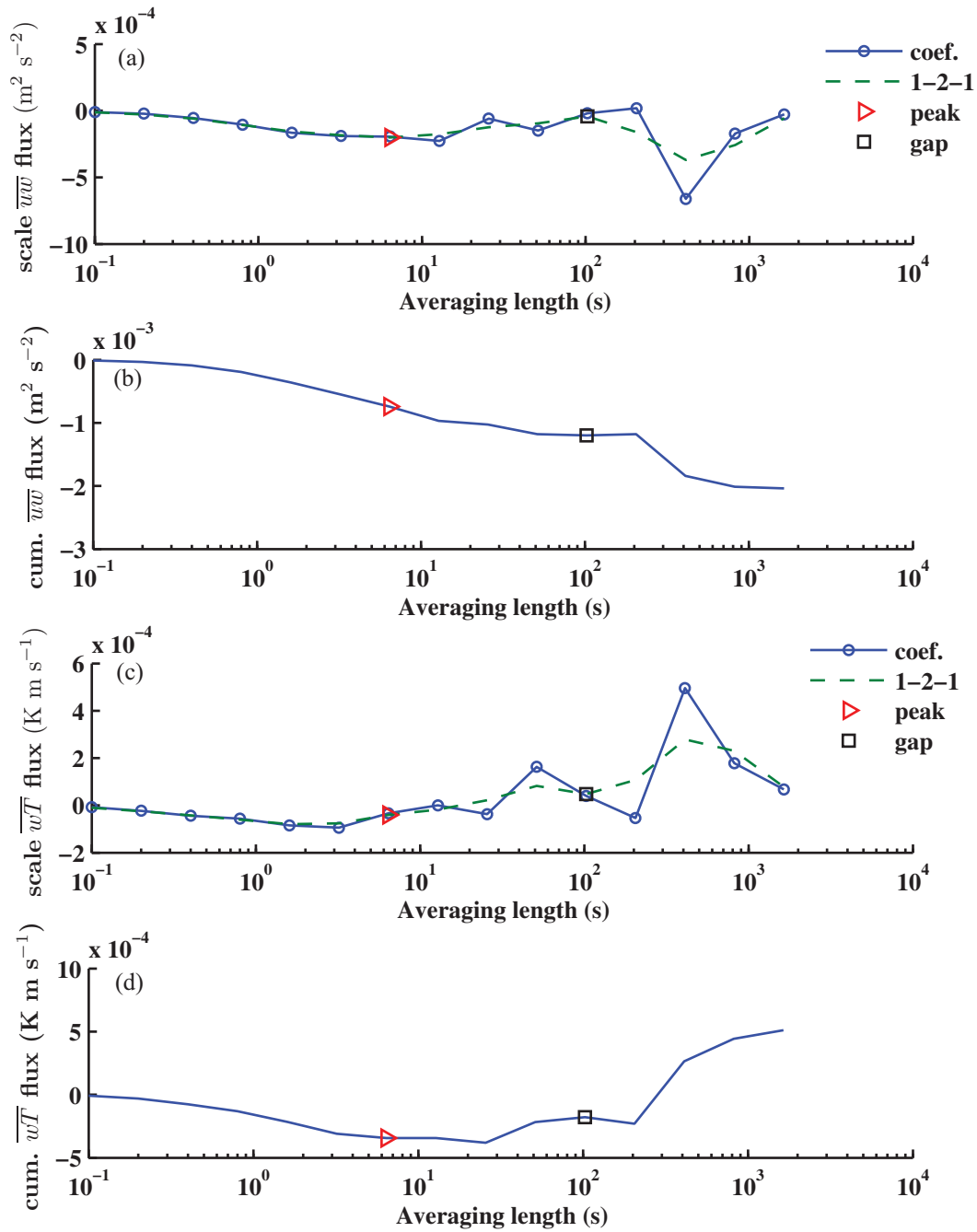


**Figure 4.14:** Example of MRFD applied to Kernen Farm (wind speed  $\approx 1 \text{ m s}^{-1}$ ). Note: dashed line in panels (a) and (c) are the coefficients smoothed using a 1-2-1 filter.

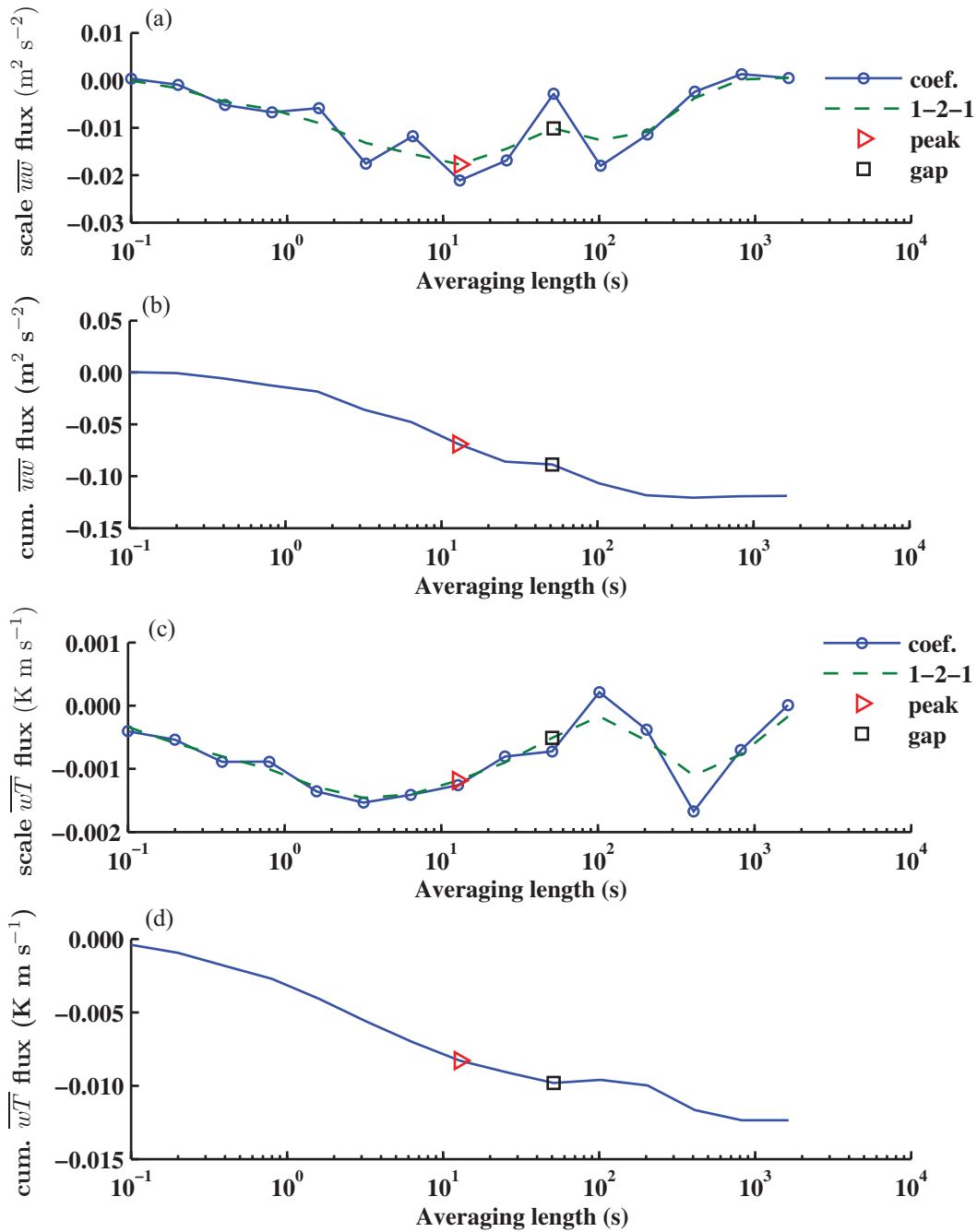


**Figure 4.15:** Example of MRFD applied to HM (wind speed  $\approx 4.5 \text{ m s}^{-1}$ ). Note: dashed line in panels (a) and (c) are the coefficients smoothed using a 1-2-1 filter.

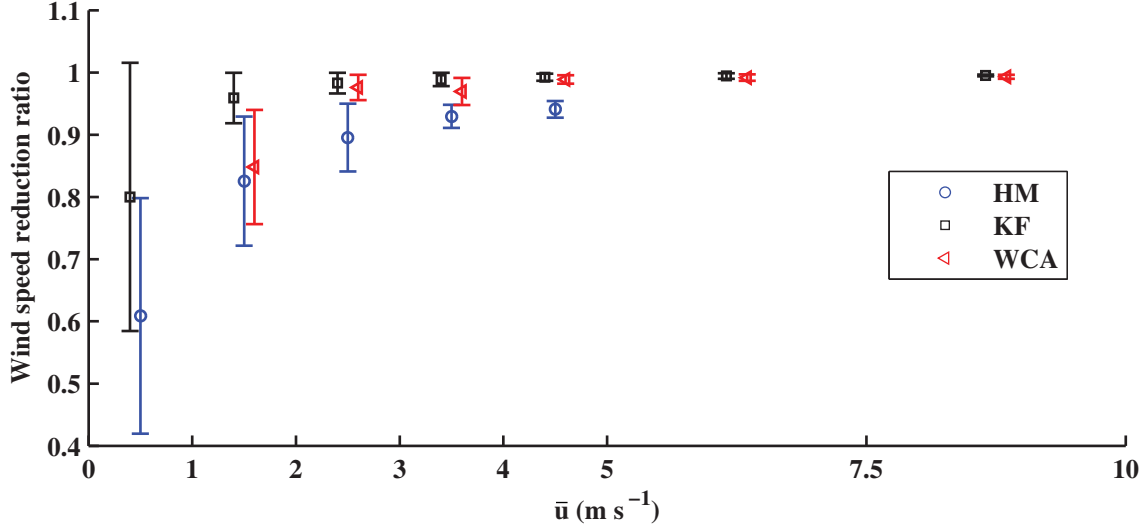


**Figure 4.16:** Ratio of vector averaged wind speed to the average instantaneous wind speed.

between maximizing the number of data points included in the statistic, thereby reducing the random error, while keeping the record short enough to minimize systematic flux errors due to non-stationarity.

There are numerous definitions of non-stationarity that have emerged in the literature. Some common stationarity classifications can be grouped as (1) those that classify the stationarity of the wind, or some other scalar; and (2) those that classify the stationarity of the flux. In this thesis, both are considered. The classification of the mean wind that is adopted for this study is the wind speed reduction test, (Vickers and Mahrt 1997) which calculates the horizontal wind vector calculated over a 30 minute period, as a ratio of the averaged instantaneous horizontal wind speed (Figure 4.16). A reduction of this ratio indicates non-stationarity of the wind direction and results in cancellation of the wind vector. This is an important statistic, as many models use the wind vector, and it is the quantity used throughout this thesis. At low wind speeds, a meandering wind direction caused significant cancellation of the wind vector at both KF and HM. Due to the gustiness of the HM site, the ratio was always less than unity and remained lower than the other sites. A related statistic that is more relevant to turbulent processes is the difference between the mean horizontal wind vector and the mean kinematic momentum flux vector, *i.e.*  $\arctan(\bar{u}/\bar{v}) - \arctan(\overline{u'w'}/\overline{v'w'})$ , which is shown in Figure 4.17. An angle near zero suggests that the main contributions to the momentum flux come from wind motions that are advected by the mean wind and represent a more ideal boundary layer. As expected for the simple terrain at KF, the difference was minimal most of the time, however both mountain sites had a much larger difference; which is presumably a consequence of the complex terrain and non-ideal flow conditions.

The stationarity test recommended by Foken and Wichura (1996) was used to provide a

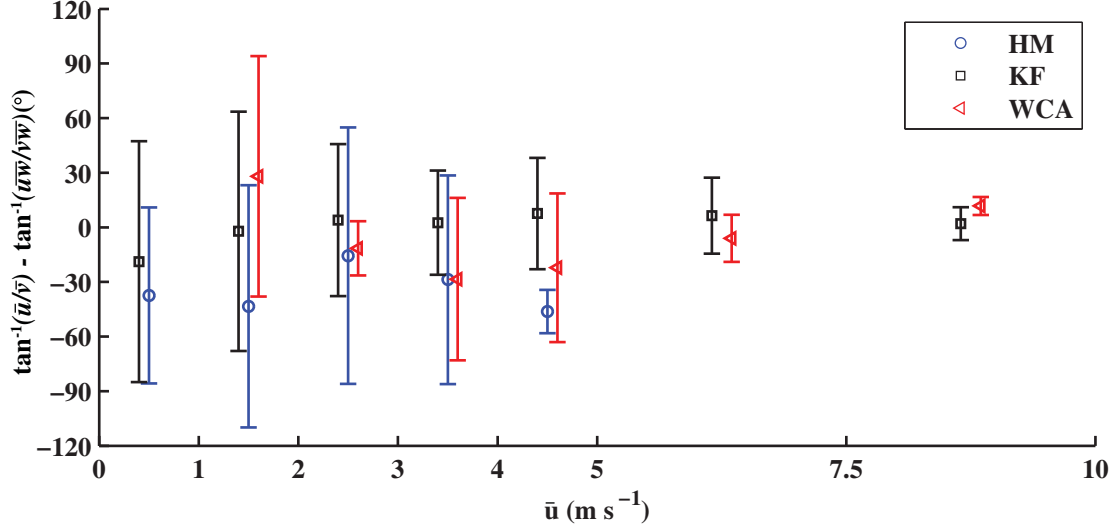


**Figure 4.17:** Offset angle between horizontal wind speed vector and kinematic momentum flux vector.

**Table 4.4:** Percentage of records that are classified as non-stationary.

Site	$\overline{uw}$	$\overline{wT}$	$\overline{w\rho_v}$
HM	43%	9%	11%
KF	29%	9%	13%
WCA	6%	0%	9%

relative comparison of the non stationarity of the fluxes (the authors refer to this as instationarity). In this test the mean value of fluxes calculated over six non-overlapping 5-minute periods were compared to the flux value calculated over a 30 minute averaging period. When the absolute difference was less than 30%, the fluxes were considered to be approximately stationary. Table 4.4 provides the percentage of records (30-min.) that are classified as non-stationary according to this criteria. When supported by Figure 4.18, which illustrates how non-stationarity ratio for the momentum flux depends on mean wind speed, it is revealed that this is primarily a problem at low wind speeds. Thus, the percentages in Table 4.4 largely reflect the wind regime at the site. Since the wind speeds are typically low at HM, the recorded momentum fluxes were quite sensitive to averaging length. Fortunately, the sensible and latent heat fluxes (which are more important for hydrological applications) were less sensitive to the larger scale boundary layer processes and can be considered more stationary.

With respect to the gap-scale analysis of the previous section, where a turbulence gap can be clearly identified, it would be possible to shorten averaging period to exclude larger scales. Calculating the fluxes using an adaptive averaging period, as proposed by Vickers

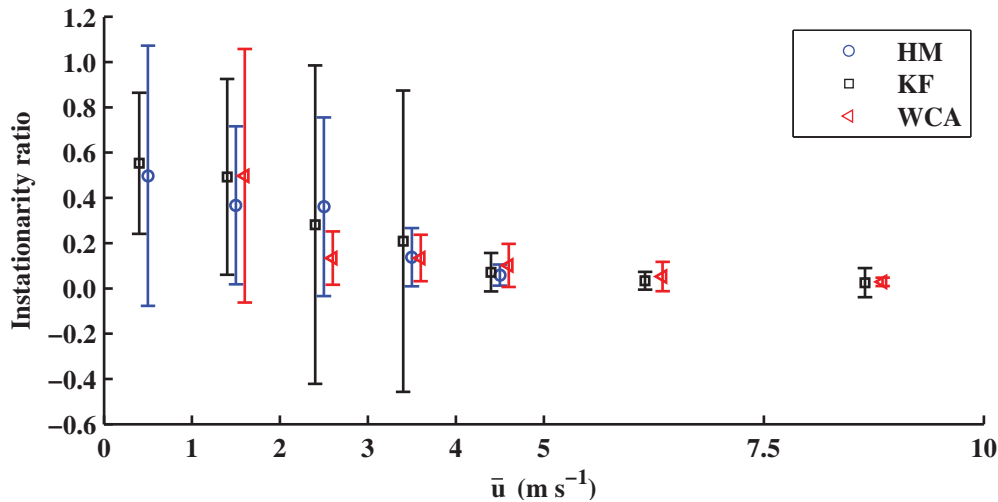


**Figure 4.18:** Momentum non-stationarity vs. mean wind speed (bin averaged).

and Mahrt (2006), would likely reduce the random errors present during calm conditions. Vickers and Mahrt (2006) and Reba et al. (2009) suggest that this approach is necessary to compare measured fluxes with those estimated using the flux-gradient approach. However, these recommendations should be heeded with consideration of the amount of energy that could potentially be excluded. It has been remarked by numerous authors (*e.g.* Finnigan 1999, Cheng et al. 2005, Grachev et al. 2005) that wave-like motions are responsible for significant energy transfer during calm stable conditions. Furthermore, in complex terrain such as at HM or ML, significant energy is present at larger scales. Since the objective of making turbulent flux measurements over snow is to account for all of the energy transfer, a more sensible approach would be to investigate techniques to increase the averaging period to include more of the larger scale motions. The effects of longer averaging periods and approaches for dealing with non-stationarity were not investigated in this thesis, but are deserving of future study.

## 4.4.2 Turbulent Transfer Processes

### Momentum Transfer

As previously discussed, the winds in the mountain valley sites were more effective at transferring momentum than at WCA or KF. Figure 4.19 illustrates the 1st order relationship between friction velocity and wind speed (corrected to 2 m height) for all of the near neutral conditions where  $\bar{u} > 1.0$  m s<sup>-1</sup>. Although there is considerable scatter for all sites, the mountain valley sites clearly exhibited larger momentum fluxes at lower wind speeds. The

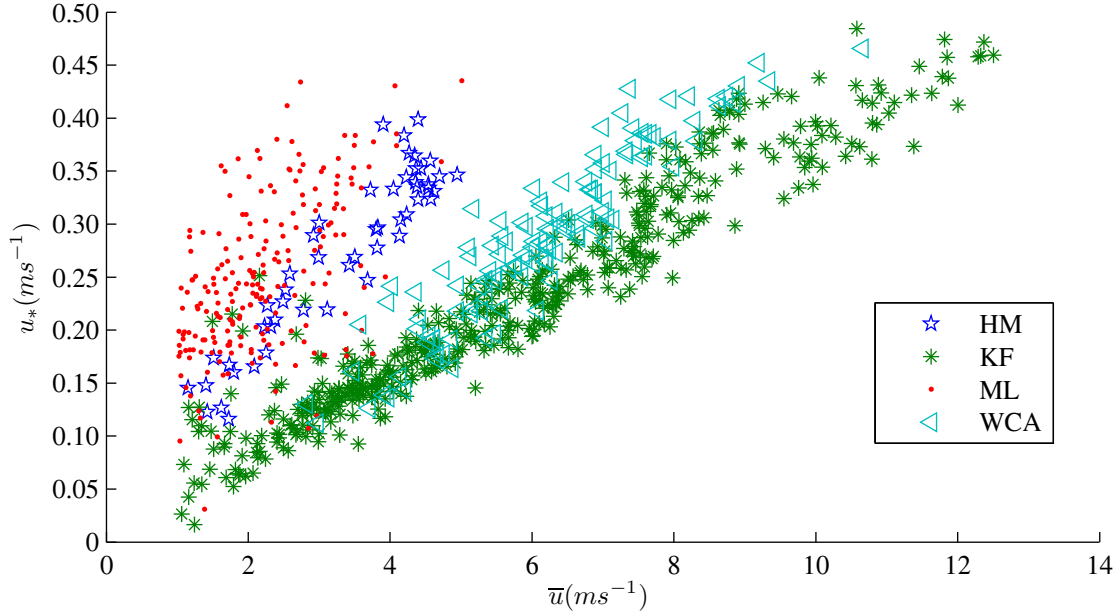


**Figure 4.19:** Friction velocity as a function of wind speed for near-neutral conditions ( $\bar{u} > 1.0 \text{ m s}^{-1}$ ).

effective  $z_{0m}$  values for these sites were  $1.75 \times 10^{-2} \text{ m}$  and  $5.54 \times 10^{-2} \text{ m}$  for HM and ML, respectively. The values corresponding to KF and WCA were  $3.60 \times 10^{-4} \text{ m}$  and  $5.25 \times 10^{-4} \text{ m}$ , respectively. Typical snow values are usually in the range of  $1.0 \times 10^{-4} \text{ m}$  to  $1.0 \times 10^{-3} \text{ m}$  (refer to Table 2.1). In the case of HM and ML, even though these sites have the smoothest snow surfaces, the turbulent momentum flux was influenced by non-local processes (*i.e.* it was not solely due to shear created by the local surface roughness), and accordingly the effective values for the roughness length were 2 orders of magnitude larger than their alpine and prairie counterparts. The noise in the relationship (Figure 4.19) is likely due to the fact that the gusts, which are poorly sampled (in a statistical sense), do not scale with locally measured variables such as the mean wind speed. At WCA, there was much less scatter in the relationship, and it appeared to be a slightly rougher flow than KF (which was consistent with the local surface roughness features). At KF, part of the scatter can likely be attributed to the fact that sastrugi formed at different locations throughout the measurement period, and therefore the actual surface roughness did change at this site. Furthermore, at friction velocities greater than 0.3 some blowing snow could likely be expected (Pomeroy 1988), which would increase the friction velocity.

Figure 4.20 provides a more statistical perspective into the momentum flux relationships by illustrating how the  $u-w$  correlation varies with  $\overline{uw}$  covariance. The lowest correlation is in the mountain valleys (ML and HM) which is consistent with the results presented in

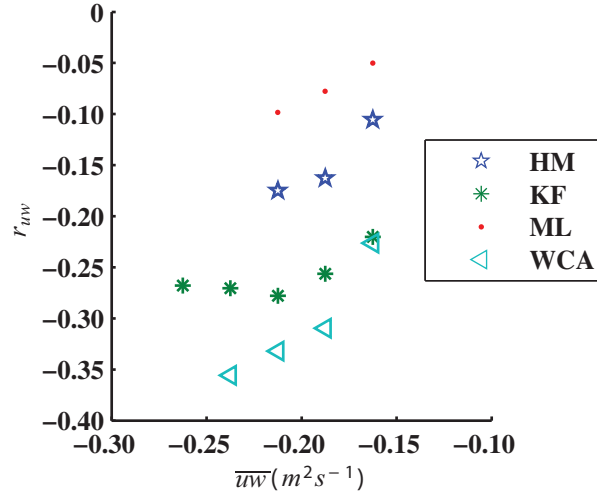


**Figure 4.20:** Linear correlation coefficients for u-w velocity components.

§4.3.2, where it was shown that blocking of large eddies at the surface reduces the correlation coefficient. Although the wind gusts associated with the valley environment tend to lower the overall correlation, they still result in increased momentum flux relative to more homogeneous sites. At WCA and KF for larger values of  $\overline{uw}$ ,  $r_{uw}$  tends towards its expected value of -0.3.

Despite the near-ideal attributes of the prairie environment for examining the boundary layer over snow, an unexpected result was discovered while comparing the friction velocity measured by the sonic anemometer with that inferred from the 2-level gradient technique (Figure 4.21). Here, data collected during February are filtered to include only those conditions where  $\overline{u} > 3 \text{ m s}^{-1}$ ,  $|\zeta| < 0.1$ , and the variation in  $u_*$  between the 2 measurements heights is less than 20%. An approximate agreement between these 2 techniques can be taken as confirmation that the boundary layer is well developed and that the flux is related to the gradients. This is the case in when the heat flux is towards the atmosphere (as it was in the example of well developed flow event presented in §4.3.1). However, when the sensible heat flux is directed towards the snow (the usual case for snow surfaces during mid-winter) the agreement between these 2 methods is quite poor. This is attributed to the active role of the heat flux in boundary layer dynamics and will be investigated in Chapter 5.

## Sensible Heat Transfer

The mechanisms responsible for sensible heat transfer are of particular interest to understanding snowmelt processes. The fact that the mountain valley sites exhibit additional momentum-generating processes makes them interesting cases, particularly if the heat fluxes are also augmented by these non-local turbulence processes (*i.e.* not related to local shear generation). WCA was excluded from this analysis since upwind heat advection was having

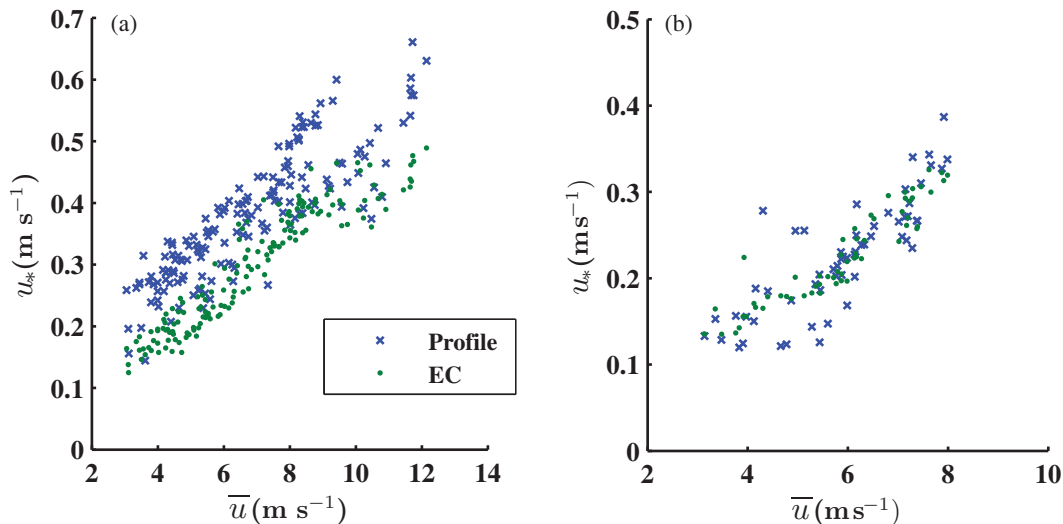


**Figure 4.21:** Friction velocity vs. mean wind speed: (a) heat flux directed towards snowpack ( $n = 165$ ); (b) sensible heat flux directed towards the atmosphere ( $n = 59$ ).

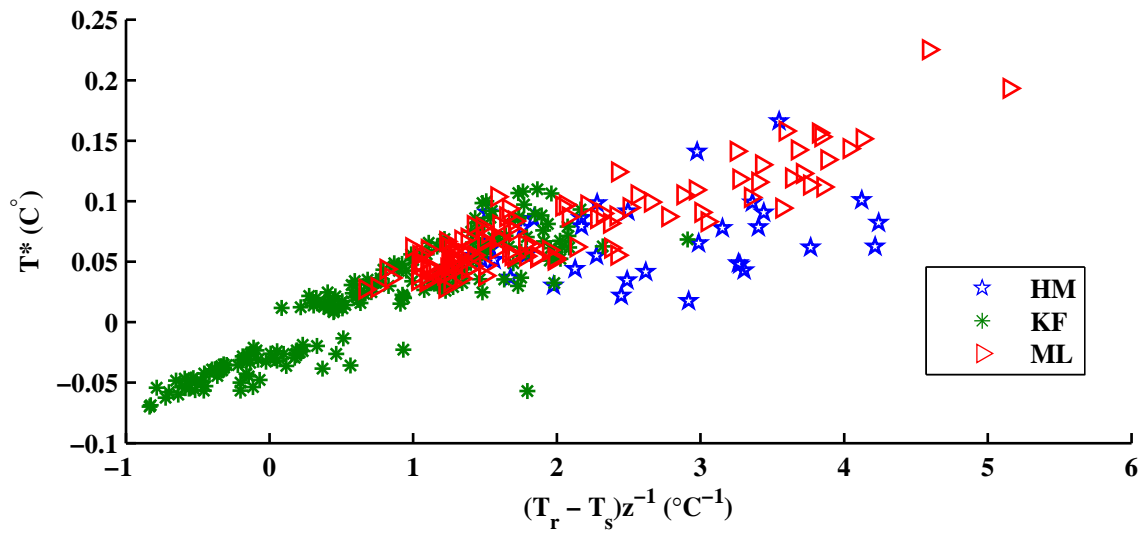
a pronounced effect on the local heat fluxes.

Figure 4.22 shows the temperature scale  $T^* = \frac{w'T'}{u_*}$  as a function of the bulk temperature gradient. Again there is plenty of scatter in the relationship, however the mountain valley sites have larger temperature gradients, but not proportionally larger  $T^*$  values. This suggests that momentum was more readily transported than heat, *i.e.* the friction velocity was increased due to the wind gusts, however the heat transfer was not influenced to the same degree. The reason that mountain valley sites had larger gradients (when compared to other sites under near neutral conditions) is that the larger measured  $u_*$  resulted in a  $\zeta$  value that was closer to neutral.

Figure 4.23 provides the  $w$ - $T$  correlation as it varies with  $Q_H$ . All of the sites exhibited fairly similar correlation values, or at least the differences were not nearly as large as those observed for  $r_{uw}$ . Thus, given that the mountain valleys exhibit larger vertical wind fluctuations as a result of the gustiness while the correlation coefficient is not decreased (relative to other sites), the ability to transfer heat must also be increased by these processes (even if the gusts do not directly transport heat from aloft).

## Latent Heat Flux

The latent heat flux was measured at all four sites, but a reference relative humidity was not available for ML. Owing to the heat advection effects observed at WCA, these data are also excluded from further discussion. In Figure 4.24 the water vapour density scale is plotted against the bulk specific humidity gradient. In order to increase the number of data points



**Figure 4.22:** Temperature scale as a function of the bulk temperature gradient for near-neutral conditions ( $U > 1.0 \text{ m s}^{-1}$ ).

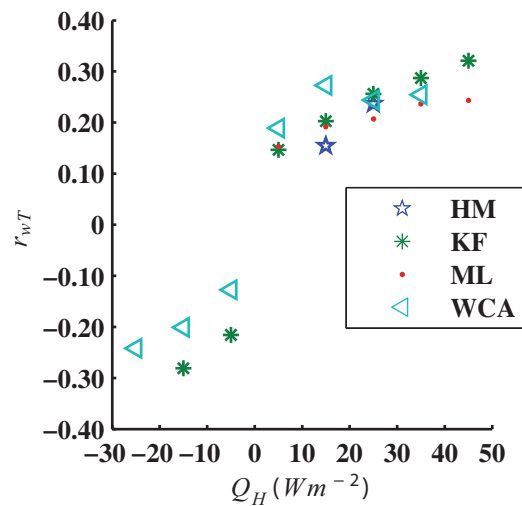


**Figure 4.23:** Linear correlation coefficients of kinematic heat flux components ( $w$ - $T$ ).

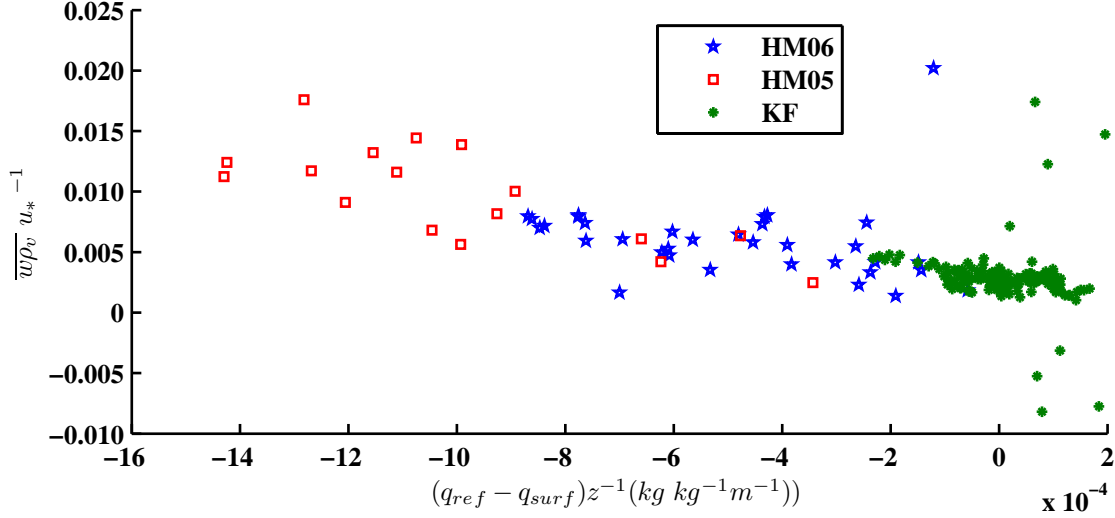


**Figure 4.24:** Vapour density scale as a function of the bulk specific humidity gradient for neutral conditions ( $U > 1.0 \text{ m s}^{-1}$ ).

available, data collected at HM during 2005 were also included in the figure. Although the datasets from each site do not overlap much with respect to the humidity gradient, the vapour density scale seems to be quite similar between sites. Owing to the small measured latent heat flux, the turbulent statistics have a very large degree of uncertainty. With reference to Figure 4.4, the measured latent heat fluxes for all sites were typically less than  $20 \text{ W m}^{-2}$ . At these low values, the correlation coefficient between  $w$  and  $\rho_v$  did not seem to reach any consistent value. The average correlation coefficient for sublimation fluxes larger than  $-5 \text{ W m}^{-2}$  were: HM =  $0.19 \pm 0.09$ ; KF =  $0.23 \pm 0.07$ ; ML =  $0.17 \pm 0.06$  and WCA =  $0.27 \pm 0.07$ .

## 4.5 Summary of Turbulence Generation Mechanisms

**Hay Meadow (HM)** The Hay Meadow, and also the Mud Lake site, is characterized by low wind speeds but dominant wind gusts. Although the origin of these gusts cannot be confirmed, it is hypothesized that they could originate as vortices that are shed as the overlying flow separates over the upwind mountain ridge. Measurements and modelling by Revell et al. (1996) within a valley in the southern Alps of New Zealand revealed that large eddies were shed at the upwind ridge (due to separating flow) and were felt at the valley floor. Vortical features have also been observed to originate at zones of strong shear. Smedman et al. (1994) report the occurrence of large motions originating at a strong shear zone at 1000 m height, which are brought down into the surface layer. Weigel et al. (2007) made extensive turbulence measurements within the Riviera Valley in southern Switzerland and discovered

that strong shear zones aloft were created as a result of the interactions between the valley flow, the katabatic flow from the valley slopes, and cross-valley circulations. The striking differences highlighted by Figure 4.5 suggest that strong shear zones and separating flow are quite likely. This behaviour was also noticed by the author during site visits and related field work throughout the surrounding basin where wind gusts were observed to create wide swaths in which fresh snowfall was unloaded from the canopy of conifers. The structure of large scale features has similarly been observed over water surfaces (for example the cats paws discussed by Hunt and Morrison (2000)), or in wheat fields (Finnigan 1979).

The boundary layer structure observed at this site, despite appearing normal (as suggested by the logarithmic wind profile (Figure 4.6)), was strongly influenced by the wind gusts. Since the origin of these motions was non-local, they advected turbulent energy into the surface layer which then had to be locally dissipated, explaining the large TKE at the mountain valley sites, and also the discrepancies between the measured turbulence and the wind profiles. The advection of energy into the surface layer from aloft necessarily negates the possibility of this site being considered an equilibrium boundary layer. Although it was locally homogeneous, the turbulence structure was quite dissimilar to the homogeneous terrain from which flux gradient and M-O theory were intended. Since the gusts do not scale with the local wind speed, the parameter set which is obtainable from typical weather station data is insufficient to describe the turbulence. Measurements by Smeets et al. (1998, 2000) on the Pasterze Glacier in Austria reveal large scale (low frequency) motions that interact with motions on turbulent-scales and increase the momentum and sensible heat transfer. These authors similarly hypothesized that these boundary layer perturbations were a result of large eddies shed by adjacent mountain ridges.

With respect to the generation of turbulent fluxes, the advected energy exerted the most influence upon the momentum flux, while the heat and vapour fluxes were impacted to a lesser degree. If the origin of the large eddies responsible for the advected turbulence was known, along with the vertical profiles of temperature and vapour, it would be possible to suggest whether this was a general condition for this site. It is conceivable that scalars could be advected from aloft, as in Smeets et al. (1998).

The interpretation of the eddy covariance measurements in the mountain valley environment must be approached with some caution. Since the wind gusts are the dominant flux-enhancing feature, it is important to capture enough individual gusts in the averaging period so their effect can be adequately represented in the calculated fluxes. However, the presence of these larger scale motions also increases the number of non-stationary records (largely because of increased random error), particularly for the momentum flux. The trade off between longer averaging periods and stationarity should be investigated in future studies.

The preferential advection of momentum over heat tends to ensure that the surface layer remains well mixed and tends towards neutral conditions. This also creates some uncertainty in applying a measure of stability. The M-O parameter  $\zeta$  tends to neutral due to the appearance of  $u_*^3$  in the numerator. However this is likely not the appropriate measure since M-O could not be expected to apply at this location. The use of the bulk Richardson number is likely to have the opposite effect since the mean wind speed gradient is not in equilibrium with the turbulence, and does not adequately relate the amount of turbulent mixing that is actually occurring. Similarly, the flux Richardson number expresses the ratio of the shear generation of turbulence to the buoyant destruction of turbulence and does not consider advected turbulence. Empirical relationships derived using these estimates of stability are therefore not likely to apply to these environments.

The relevance to mountain hydrology and meteorology is that the valley sites selected are anomalously homogeneous for the mountain environment in which they are found. If these techniques fail at these sites, then these results are likely to be valid in other mountain valley locations. It is important to realize that meteorological instrumentation installed for routine monitoring of mountain weather (and commonly used by practitioners for flux prediction) are often located in forest openings in mountain valleys, largely due to logistical considerations.

**Wolf Creek Alpine Ridge** The broad ridge (WCA) was included in this study to contrast the mountain valley sites, which it does in practically every way. The site was typically windy (at least for the measurement period), but was not gusty like the valleys. Rather, it shares many characteristics of turbulence with the prairie site. However, some important distinctions must be made. The presence of the ridge suggests that a pressure-gradient boundary layer was formed. This was confirmed by the separation zone (snow drift) that occurred on the lee side of the measurement location. As a result of the accelerating flow, the boundary layer was observed to be very thin, or at least any portion of the boundary layer that could be considered an equilibrium layer only occurred close to the ground. This was confirmed by the markedly different fluxes and turbulence properties measured at the two heights. As a result of the thin boundary layer the measured fluxes could not be considered representative of the local surface. This was indicated by the measured sensible heat fluxes that were often of inconsistent direction when compared to the local bulk temperature gradient. This was presumably caused by advected energy from the bare (snow-free) patches upwind of the station (on the windward slope of the ridge).

Although the ridge is quite broad, and there is a generous uniform upwind fetch (considering the typical mountain environment) an equilibrium boundary layer was not observed at the measurement height. Therefore it was not possible to employ 1st order techniques that

use a local parameter set to describe the turbulence. The main hydrological interest of mountain ridge-tops is that they form the boundary between water supply basins. Consequently, the transport of blowing snow over ridges is of primary concern rather than the estimation of turbulence heat fluxes. Nonetheless, the data collected here demonstrate the requirement for higher order turbulence modeling in mountain environments.

**Kernen Farm** The prairie site was included as the ideal reference location. However, despite the homogeneous nature of the site, the conditions for measuring fluxes with the eddy covariance technique were not always ideal. The wind speeds were often low, and the skies were often clear resulting in cold, stable conditions for long periods at a time. Turbulent fluxes measured during these low-wind conditions were very small. However, multi-resolution decomposition of the time series suggests that there were meso-scale motions that were poorly sampled by the fixed averaging period, but which could be responsible for transferring heat during these conditions. When wind speeds were higher, the turbulence characteristics compare favourably with other homogeneous sites, and the spectra are similar to the Kansas forms, with the exception of containing greater energy at lower frequencies. Overall, the sensible and latent heat fluxes were typically quite small. The main anomalous feature of the collected data was that the friction velocity measured from the sonic anemometer compared very well with that predicted from the mean wind speed gradient for mildly unstable conditions, however smaller values were measured by the sonic anemometer for mildly stable conditions (Figure 4.21). This suggests that the boundary layer structure at this site was more complex than suggested by its simple homogeneous nature. The accuracy of the turbulent heat flux measurements will be further assessed against measurements of the other energy balance components in the following chapter.

# CHAPTER 5

## THE SNOW ENERGY BALANCE

### 5.1 Chapter Overview

The snowpack is a layered, multiphase, permeable, porous medium, in which multiple modes of heat and mass transfer occur, driven by strong energy gradients. Accordingly, spatially and temporally detailed accounting of internal energy is often required. Not only are the complex physical processes imperfectly understood and difficult to capture within a model, but they are also very difficult to measure. Owing to this, rarely are all of the terms in (2.1) actually measured together in the same experiment. In particular, the turbulent heat fluxes are often modeled and the internal energy is often taken as the residual of the other measured terms. As an example, the snowmelt model inter-comparison summarized in Etchevers et al. (2004) was conducted on data where turbulent fluxes were not directly measured due to the difficulty in obtaining reliable flux measurements. However, the use of the eddy correlation technique to measure the turbulent fluxes is now relatively common in hydrological investigations (*e.g.* Shook and Gray 1997, Sauer et al. 1998, Pomeroy and Essery 1999, Hayashi et al. 2005, Pomeroy et al. 2006). The ability to close the energy balance from measurements is an excellent indicator of the uncertainty in the measurements and forms a valuable tool in understanding the limitations of certain parameterizations. The degree of energy balance closure that is obtainable using the eddy covariance technique has been often studied during summertime periods by investigators of land surface energy and gas fluxes (*e.g.* Aubinet et al. 2000, Wilson et al. 2002, Barr et al. 2006), however there are very few estimates of the energy balance closure obtained over snow-covered land.

This chapter reports direct measurements of all of the energy balance components in a homogeneous prairie snowpack during a mid-winter period with the intention of quantifying the uncertainty in the measurements of the energy balance terms. Potential shortcomings of the measurement techniques will be investigated. The following science questions are addressed: (1) what is the energy balance residual (*i.e.* how close can we come to closing the energy balance over snow surfaces?); and (2) what is the significance of energy terms not

usually considered?

All of the measurements reported in this chapter were collected at KF from 1-28 February 2007. Throughout this period, the depth of snow near the instrument site was consistently around 42.5 cm. Deposition of new snow, which amounted to 19 cm (measured at a nearby station), was approximately equal to erosion by blowing snow processes. Due to snow drifting, the snow surface exhibited gentle undulations at scales on the order of 10-20 m with sastrugi occasionally developing at shorter scales (1-2 m). For the data period presented, no snow melt occurred as air temperatures were quite cold for the first half of February, with temperatures ranging from daily highs of  $-15^{\circ}\text{C}$  to lows near  $-35^{\circ}\text{C}$ , followed by a period of more moderate  $-5^{\circ}\text{C}$  to  $-15^{\circ}\text{C}$  temperatures. The wind speeds during the same month exhibited 5 events with wind speeds greater than  $8\text{ m s}^{-1}$  (measured at 1.75 m height) interspersed with calmer periods. A particularly calm period occurred between February 6th and 14th, which in combination with the low temperatures and clear skies, caused significant stable stratification of the atmosphere during this period. The description of the experimental setup and the meteorological conditions can be found in §3.2.2. The sign convention followed throughout this chapter (and throughout the thesis) is that fluxes directed towards the snowpack are considered positive, and those directed away from the snowpack are considered to be negative.

## 5.2 Energy Balance Closure

The degree of energy balance closure is often used as a method of assessing the suitability of the eddy covariance method for determining the turbulent sensible and latent heat fluxes (*e.g.* Barr et al. 2006, Turnipseed et al. 2002, Wilson et al. 2002). In Figure 5.1, the sum of the turbulent fluxes is plotted against the change in internal energy with the net radiation and ground heat flux subtracted. Here, only data from good wind directions, and having friction velocities greater than  $0.1\text{ m s}^{-1}$ , were selected. The last criterion ensured that the flow was well developed, the turbulence was continuous, and the assumptions necessary for invoking the eddy covariance technique were more likely to be valid. The data were further sorted according to whether they were from evening periods ( $Q_{S^*} = 0$ ) or daytime periods when  $Q_{S_i} > 200\text{ W m}^{-2}$ . Data points lying close to the 1:1 line would suggest that the energy balance was being closed by measurements. Unfortunately, overall there are very few such points which suggests that the eddy covariance measurements were under-representing the energy that was required to meet the needs imposed by the radiation. The energy imbalance during nocturnal periods appeared to be less severe than that during the day. When the internal energy change and non-turbulent fluxes were small, the nocturnal turbulent fluxes were similarly scattered about the origin. As the non-turbulent fluxes increased the turbulent

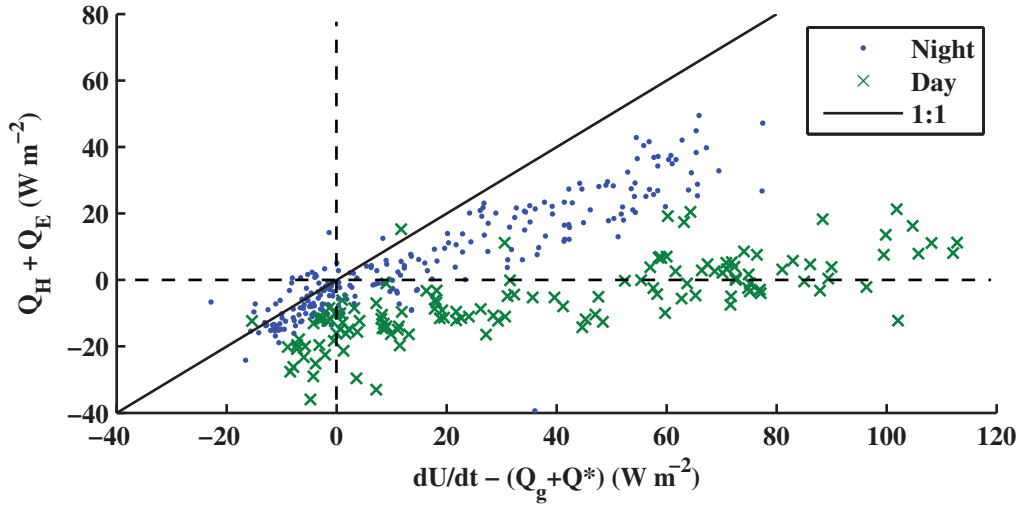


**Figure 5.1:** Energy balance closure: measured turbulent heat fluxes vs. the internal energy change with the net radiation ground heat fluxes subtracted. Note: the dashed lines indicate the zero-flux origin.

fluxes remained smaller, increasing at a lesser slope than the 1:1 line (always remaining at less than 75% closure). However, during the daytime periods, the measured turbulent flux was often of opposite sign to the non-turbulent terms suggesting a more serious non-closure problem.

Before investigating the causes for the noted energy imbalance, it is useful to consider the significance of the energy balance terms and the context of the closure problem. The total energy content of the snowpack, as it varied over the entire month of February, is shown in Figure 5.2 along with the cumulative surface fluxes. Here the turbulent heat fluxes (*i.e.* sensible and latent heat fluxes) were estimated as the residual of the other energy terms. This residual term represents the sum of the sensible and latent heat, as well as any other unmeasured energy terms and any measurement errors in the net radiation flux, ground heat flux and internal energy. This presentation was necessary due to difficulties with obtaining continuous eddy covariance measurements in this environment. In this study, of the 1344 30-minute periods in the month of February, 612 of these were deemed unsuitable to calculate the turbulent heat fluxes due to the occurrence of one or more of the following conditions: (1) condensation (frost) on the lens of the open-path Krypton Hygrometer; (2) unsuitable wind directions (blowing through the frame of the instrument or obstructed by the tower); or (3) a quality flag set high by the sonic anemometer internal processor (usually indicating snow or rime blocking the sensor transducer). The energy status of the snowpack did not change appreciably over the month suggesting that the cumulative sum of the surface fluxes over the same period must approximately balance. The snowpack lost a considerable amount of

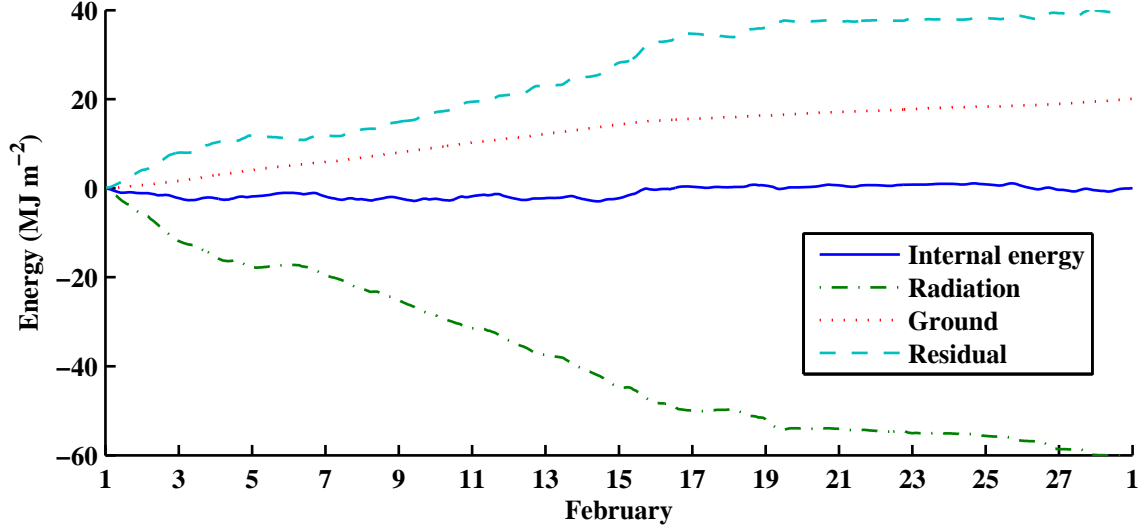


**Figure 5.2:** Cumulative energy fluxes measured over the month of February.

energy ( $60 \text{ MJ m}^{-2}$ ) due to radiation losses which were a result of the low incoming thermal radiation from the atmosphere during the prevailing clear-sky conditions while there was little solar radiation input due to the low sun angles and high albedo of the clean snow surface. The underlying soil, being warmer than the snow, typically provided a heat flux of around  $10 \text{ W m}^{-2}$  which resulted in a cumulative energy transfer of  $20 \text{ MJ m}^{-2}$  over the month. The remaining  $40 \text{ MJ m}^{-2}$  is assumed to have been transferred from the atmosphere, presumably through the turbulent transfer of sensible and latent heat. The residual term is significantly larger than the actual measured turbulent fluxes (as supported by Figure 5.1), but serves to illustrate the temporal distribution and the magnitude of the energy required to offset the dominant thermal radiation losses. Of particular interest is the fact that the largest radiation losses occurred during the first half of the month when winds were light and the atmosphere was very stable with  $Ri_b$  values that were often greater than 0.2 (Appendix A), which is suggestive of significant dampening of turbulent transfer. This result, combined with the fact that snow temperatures did not continue to cool during this period indicates that there is an unmeasured mechanism of heat transfer that is capable of balancing the radiation losses even though turbulent mechanisms are expected to be suppressed.

### 5.2.1 Energy Partitioning for Selected Events

Ideally, it would be desirable to evaluate the degree of energy balance closure over a period of a month or longer using continuous data. However, due to the aforementioned difficulties obtaining high quality eddy covariance data during the winter, this is not possible without resorting to data filling procedures that use modeled data. For these reasons, a more detailed

examination of the apparent lack of energy balance closure is presented for specific shorter events with verifiable data quality. These include two periods with high wind speeds and steady wind direction (quasi-stationary conditions), as well as a stable period with low wind speeds.

During the first example period (Figure 5.3; 4-5 February 2007), the skies were mainly cloudy, with the exception of two clear-sky periods that occurred on 4 February which are indicated by the two periods of strongly negative long-wave radiation fluxes (Figure 5.3c). These periods coincided with the snowpack temperatures cooling and the largest departures between the radiometric surface temperature and the near surface thermocouple (Figure 5.3b). These periods also resulted in the largest energy imbalance, where surface fluxes were under-measured by 20 to 50  $\text{W m}^{-2}$  (Figure 5.3d). During the cloudy periods (when the net long-wave was near zero or slightly positive) the snowpack warmed and caused a reversal in the gradient between the snow surface and the atmosphere, resulting in a sensible heat transfer from the snow to the atmosphere. Due to the partly cloudy conditions, low sun angles, and high albedo, the peak flux of net short-wave radiation was less than 25  $\text{W m}^{-2}$  on both days. The energy balance was most completely closed when the internal energy of snow was not rapidly changing, which incidentally was when all of the fluxes were small. Over the two-day period, the snowpack temperatures increased by an amount that is inconsistent with the measured flux of energy entering the snowpack at the atmosphere and ground surfaces, which suggests that the surface fluxes were being under-measured. In this example, the increase in snow temperature must be attributed primarily to the radiation flux, since the direction of the turbulent fluxes were most often directed toward the atmosphere.

The second example period (Figure 5.4; 7-8 February 2007) was captured during a period of very stable, cold conditions. The wind speeds were very low (Figure 5.4a) and the air to surface temperature gradients were quite large (Figure 5.4b). The net long-wave radiation flux was predominantly negative, and was partially offset by the positive ground heat flux and solar radiation flux. The sensible heat flux was typically near zero, except for a few sporadic fluxes of  $\pm 40 \text{ W m}^{-2}$  that are due to random error that is characteristic of calculating fluxes in stable conditions caused by the inclusion of non-turbulent motions into the covariance calculation (see discussion in §4.4.1). The latent heat flux proved difficult to determine due to frost developing on the lens of the open-path hygrometer. However, when measurements were possible the latent heat flux was very small. It should be noted that the radiation sensor is not expected to suffer from these condensing periods as the on-board heater was used to keep the body temperature above the frost point. When possible to obtain all of the surface fluxes, the residual flux was observed to be quite large around midday of both days examined (Figure 5.4b). In this example, the long-wave radiation losses were consistently large, and

the sum of the surface fluxes was typically negative. However, the snowpack temperatures did not exhibit significant cooling (except for the surface temperature) in response to the negative surface energy balance. The low-wind, stable conditions pose serious difficulties for using the eddy covariance technique to accurately describe the turbulent fluxes, however given the low degree of turbulent mixing and the strength of the inversion, turbulent fluxes could be expected to be small.

The third example period (Figure 5.5; 13 - 15 February 2007) presents a change in weather where cold stable conditions were replaced with warmer windy conditions. Throughout the three-day period, the skies were primarily clear (as indicated by the negative long-wave radiation fluxes in Figure 5.5c). A significant cooling period occurred during the clear sky evening of 13 February where the surface temperature dropped to below  $-35^{\circ}\text{C}$  and established a strongly stable atmospheric stratification. The snowpack temperatures (Figure 5.5b) exhibited three small diurnal increases that coincide with the input of solar radiation, which were superimposed upon a larger warming trend that occurred as the wind speed increased (Figure 5.5a) during the latter part of 14 February through 15 February. Despite the large increase in energy status of the snowpack, the sum of all of the measured fluxes remained negative except for a four-hour period on the morning of 15 February. The largest residual (missing) energy flux was observed during sunny mid-day periods, and can be attributed to the absorption of solar radiation at the snow surface which caused an increase in the outgoing long-wave radiation and ultimately caused the snowpack to lose more energy. The energy imbalance during these periods ranged from 70 to  $90\text{ W m}^{-2}$ . During this event, the air remained warmer than the snowpack surface, and there was a small sensitive heat flux ( $\leq 30\text{ W m}^{-2}$ ) directed toward the snow surface. Of particular interest is the large increase in the snowpack temperature beginning midday 14 February. During this period, the measured surface fluxes were negative except for about 5 hours on February 15. The wind was blowing strongly, yet long-wave losses were large which suggests that the increase in snow temperature may be due to sensible heat transfer.

In all of the above examples, the dynamics of the snowpack temperature (and associated energy change) were inconsistent with the sum of the measured energy fluxes. This is a troubling result, as snow melt rates are often calculated by summing the measured or modeled external fluxes. The observed residual (unmeasured flux) was largest for clear sky conditions when the net long-wave radiation flux was the most negative. This effect was augmented when solar radiation warms the snow, causing a further increase in the outgoing long-wave radiation flux. This result appears to be similar for stable and neutral flows. In order for the energy balance to close during these periods, a heat flux which is of similar magnitude as the net long-wave radiation flux, and is directed toward the snowpack, would be required.

### 5.2.2 Snow Temperature Profiles

Since the residual energy term was largest during clear, sunny, midday periods it is useful to specifically examine these periods in more detail to help understand how energy is being transferred to the snowpack. To this end, the data collected between 10:30 and 18:30 for each day of 13-15 February were examined in closer detail since this event contains both stable and near neutral periods. Table 5.1 provides the mean wind speed, bulk Richardson number, and the cumulative energy change / transfer for each of these periods. Snow temperature profiles for the same periods are given in Figure 5.6a-c. In these figures, the thermocouple at 45 cm height was exposed (above the snow surface) and permits examination of the continuity of temperature across the air-snow interface.

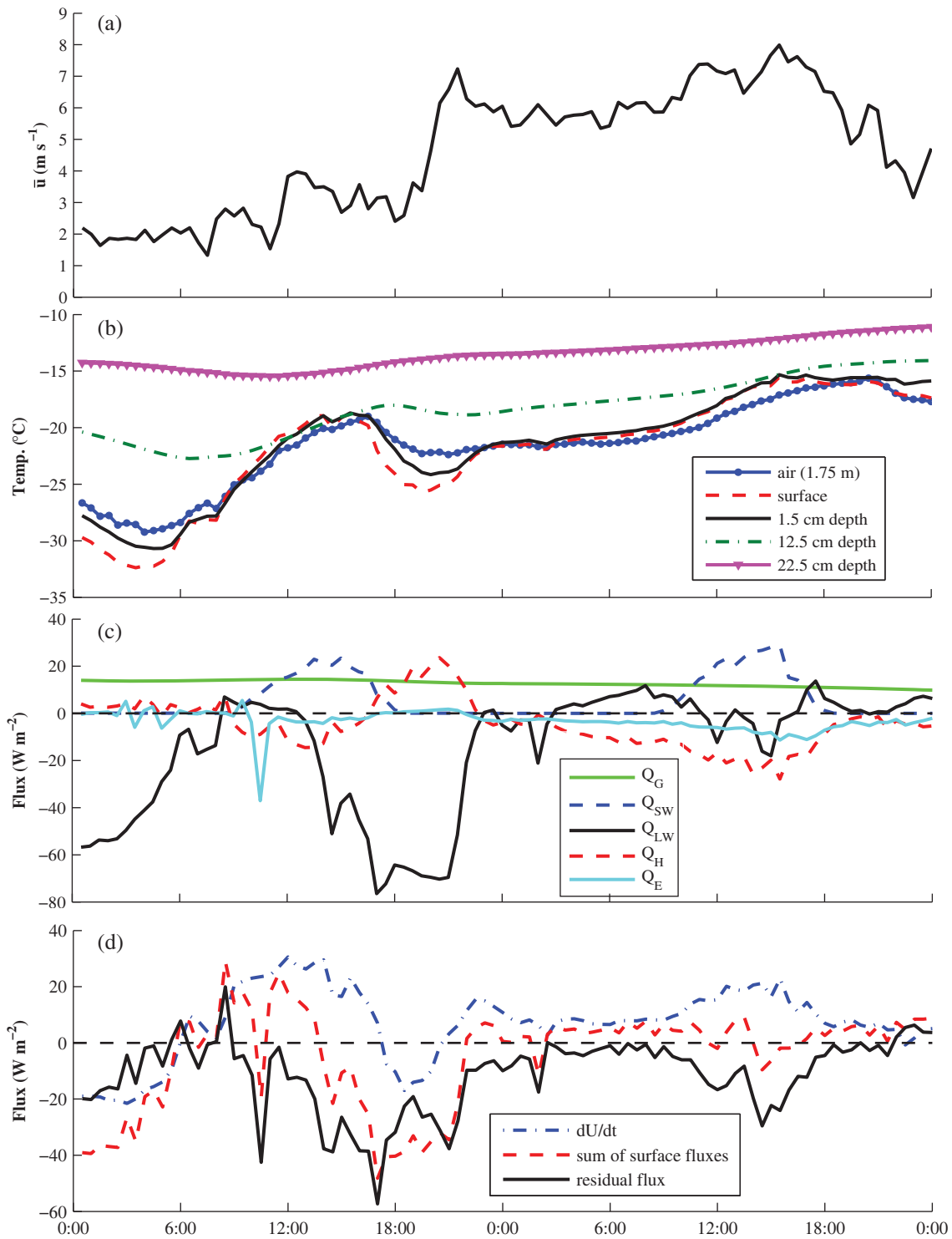


**Figure 5.3:** 4-5 Feb. event: (a) wind speed (1.75 m); (b) air and snow temperatures; (c) measured surface fluxes; (d) comparison of surface fluxes with internal energy changes.

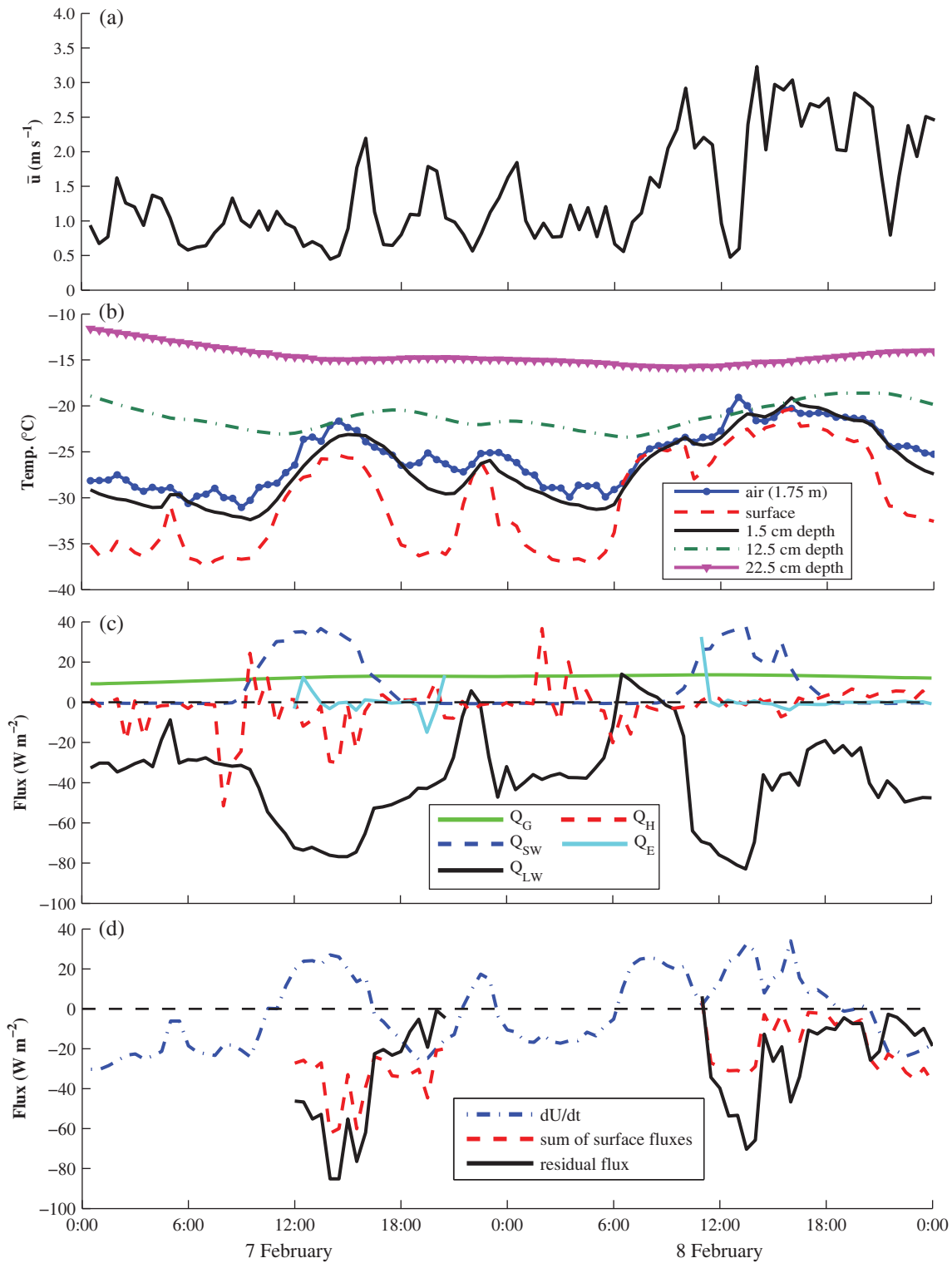


**Figure 5.4:** 7-8 Feb. event: (a) wind speed (1.75 m); (b) air and snow temperatures; (c) measured surface fluxes; (d) comparison of surface fluxes with internal energy changes.

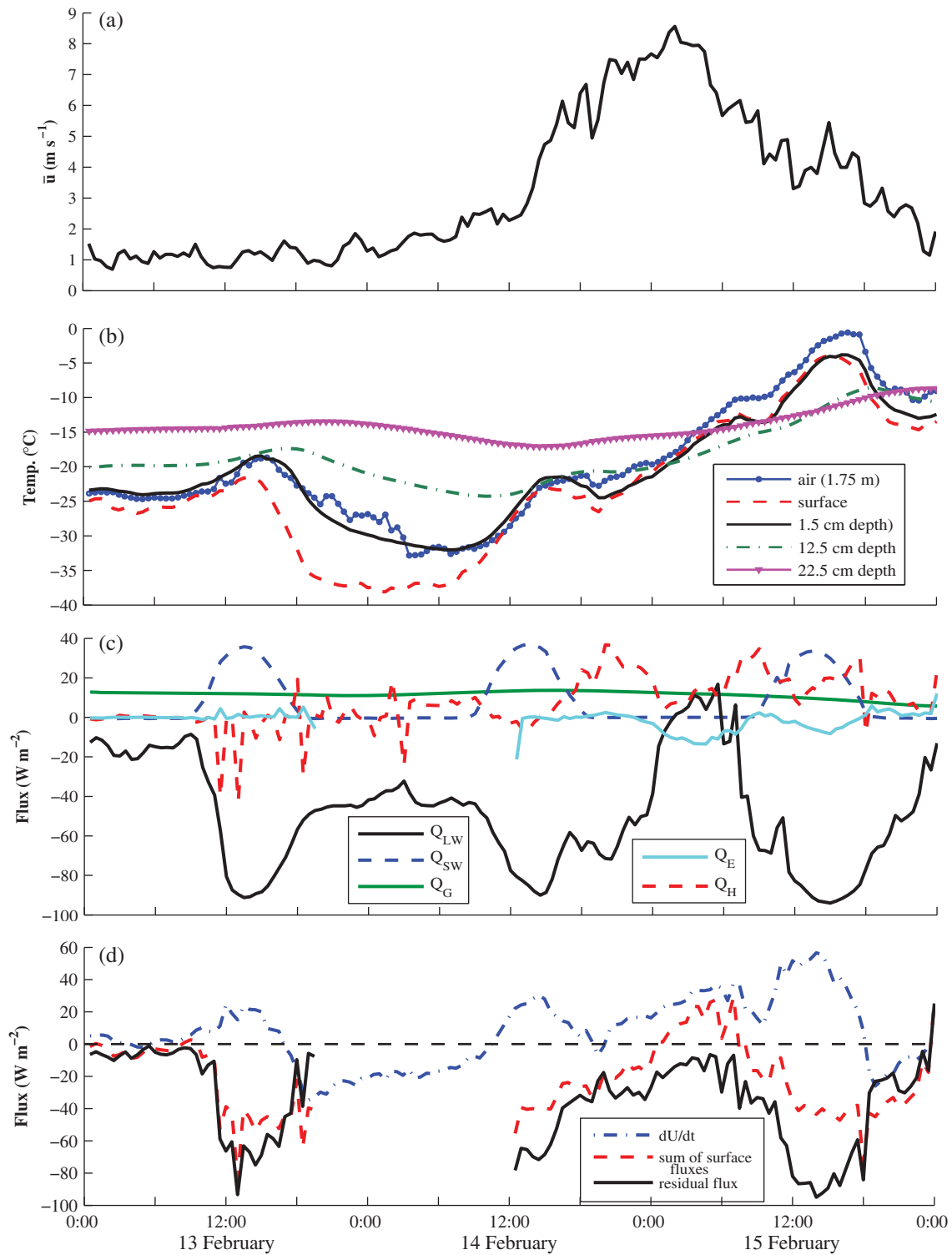


**Figure 5.5:** 13-15 Feb. event: (a) wind speed (1.75 m); (b) air and snow temperatures; (c) measured surface fluxes; (d) comparison of surface fluxes with internal energy changes.

**Table 5.1:** Summary of conditions pertaining to temperature profiles in Figure 5.6.

Date	$\bar{u}$ m s <sup>-1</sup>	Ri <sub>b</sub>	Q <sub>Li</sub> (MJ)	Q <sub>DWo</sub> (MJ)	Q <sub>L*</sub> (MJ)	Q <sub>S*</sub> (MJ)	Q <sub>H</sub> (MJ)	Q <sub>E</sub> (MJ)	Q <sub>G</sub> (MJ)	U (MJ)	residual (MJ)
13 Feb. 11:00 to 18:00	1.13	0.471	3.99	-6.15	-2.16	0.68	-0.21	0.03	0.34	0.25	-1.58
14 Feb. 11:00 to 18:00	4.19	0.009	4.00	-6.15	-2.15	0.69	0.13	-0.10	0.39	0.50	-1.55
15 Feb. 11:00 to 18:00	4.06	0.017	5.81	-8.24	-2.43	0.65	0.46	-0.10	0.26	1.10	-2.21

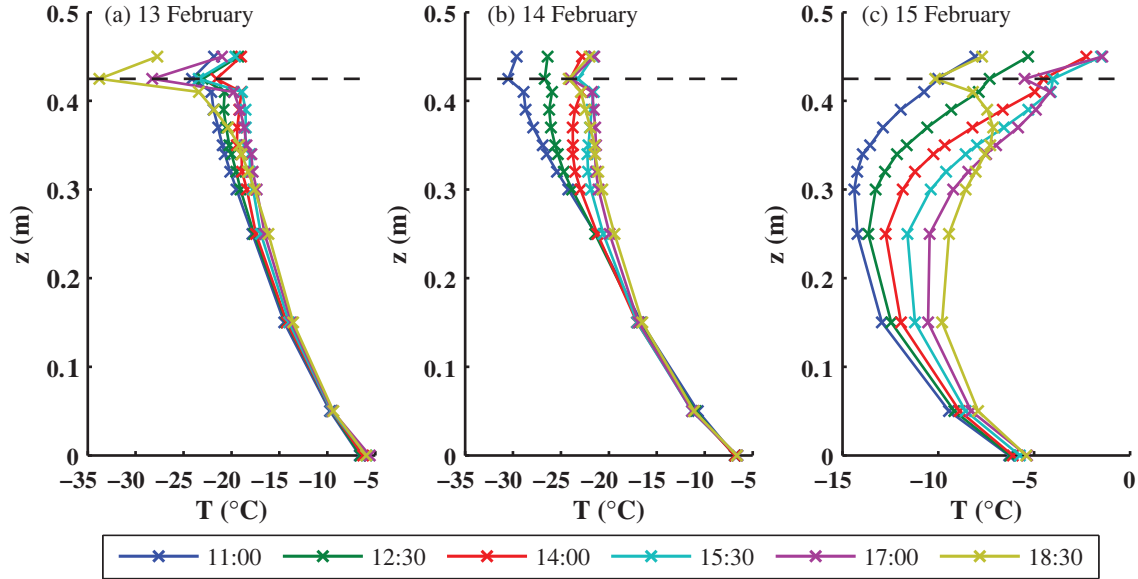


**Figure 5.6:** Snow temperature profiles 13-15 February: 11:30-18:30 daily. Note: dashed horizontal line denotes the snow surface.

During each of the selected periods, the snowpack warmed up during the day and then cooled off again around sunset. The total increase in the energy content of the snowpack approximately doubled during each of selected periods between the 13th to the 15th (Table 5.1). This was related to the warming trend that was observed to occur between 14th to the 15th (Figure 5.5). However, the energy fluxes that could have caused these increases to occur are not consistent with the measurements. The total input of short-wave radiation was similar on each day, and the net radiation losses for the three days were 1.45 MJ, 1.48 MJ, and 1.78 MJ respectively. This suggests that fairly large fluxes of opposing sign (ranging from 1.55 to 2.21 MJ m<sup>-2</sup>) would be required to increase the snowpack as measured. It should be noted that these additional energy requirements were surplus to the turbulent flux values measured, which were reported here to be of a smaller magnitude than the ground heat flux. The turbulence fluxes were either being under-measured or other energy transfer mechanisms were at work.

The surface temperature, which was derived from the outgoing long-wave radiation, often formed a temperature minimum. This was observed in each of the selected periods, but was most prevalent under the light wind conditions experienced on 13 February. This situation resulted in large energy gradients towards the snow surface from both the atmosphere and also from the near surface layers of the snowpack. This phenomenon was also observed by Andreas and Jordan (2004) over snow-covered ice on the Weddell Sea who suggest that this may be indicative of thermal non-equilibrium between the air and ice phases of the snow. The observed temperature depression often diminished as the wind speed increased. In each

example presented in Figure 5.6a-c, the strongest depression was observed at 18:30 after the sun had set. Therefore, it must be assumed that absorption of solar radiation was partially compensating for the long-wave loss (and associated temperature depression).

The temperature gradient of the profiles should be suggestive of the heat transfer mechanism involved. On 13 and 14 February, the temperature gradients remained negative (heat flow directed toward surface) throughout the profile. Therefore, the warming that was observed (to a depth of approx. 20 cm below the snow surface), does not seem to be caused by steady heat conduction of energy entering at the snow-atmosphere interface. This observation is contrasted on 15 February where a larger positive energy gradient was established, which resulted in more energy being moved downwards into the profile, presumably by conduction and possibly aided by convection (wind pumping) and vapour diffusion. The counter-gradient warming observed on the 13th and 14th seems anomalous. Horizontal temperature gradients within the snowpack are not available from measurements, but would be useful in future investigations.

It is well documented that short-wave radiation can penetrate the snow surface, and is often modeled using Beers law (exponential decay). A rough calculation using an extinction coefficient parameterization given by Lehning et al. (2002), and an incoming short-wave value of  $375 \text{ W m}^{-2}$ , suggests that 95 % of the energy would be absorbed within 2 cm of the snow surface. Therefore, it is likely that only a portion of the observed increase in snowpack temperature was due to solar warming. By virtue of the same argument, heating of the thin thermocouples within the snowpack was expected to be minimal.

### 5.3 Causes of the Energy Imbalance

The measured energy change of the cold, dry snowpack constitutes a robust metric for determining the accuracy of the energy flux measurements. This approach is particularly relevant to snow melt hydrology, as the entire practice is based upon the accounting of measured or parameterized energy fluxes of energy entering and leaving the snowpack. However, the measurements reported in this study revealed that the internal energy changes of the snowpack were not consistent with the summation of all of the bounding energy fluxes. This suggests a considerable deficit in the measurement approach or a gap in our understanding of how the snowpack exchanges energy with the environment. This realization carries a great deal of relevance, as these measurements were made in an environment that is very simple and homogeneous compared to many environments of practical interest to hydrologists.

To summarize the observations reported: the largest energy imbalances occurred when net radiation losses were large, which did occur throughout the winter, but were most prevalent

during cold, calm, clear sky periods, where incoming long-wave radiation was very low (often as low as  $130 \text{ W m}^{-2}$ ). The situation was worsened as the solar radiation flux ( $Q_{S^*}$  values were usually less than  $30 \text{ W m}^{-2}$  during mid-winter periods) was absorbed by the upper few centimetres of the snowpack which in turn caused an increase in the outgoing long-wave radiation. Resultantly, net radiative losses of up to  $90 \text{ W m}^{-2}$  were common. The measured turbulent fluxes were too small to offset the negative radiation balance, yet the snowpack temperature changes were not commensurate with the measured energy losses. The observed energy imbalance most strongly corresponded to large net radiation losses, and less so to variations in other meteorological variables. In fact, large energy deficits were observed to occur during calm and windy periods alike. This is clear from Figure 5.2 where large radiation losses accumulate during the stable period between 7-13 February while snowpack temperatures do not fall to significantly lower values than the air temperature. This is taken as preliminary evidence that some form of heat transfer from the atmosphere must be offsetting the radiation losses. However, the measured turbulent fluxes were usually less than  $10 \text{ W m}^{-2}$  reflecting the fact that wind speeds were often low, the atmosphere was stably stratified, and the snowpack was aerodynamically smooth. The nature of the discrepancy between the measured turbulent fluxes, and the residual required to offset the large radiation losses is the subject of the following discussion.

The energy balance closure problem has received plenty of study (Barr et al. 2006, Foken et al. 2006, Foken 2008, Wilson et al. 2002). From an assessment of the energy balance of the FLUXNET sites, Wilson et al. (2002) suggest that lack of closure is usually due to the following factors: (1) sampling errors due to different measurement source areas, *i.e.* different measurement footprints; (2) systematic bias in instrumentation; (3) loss of low and high frequency information in the turbulent fluxes; and (4) neglected energy sinks or neglected advection of scalars. Each of these is considered within the context of this site.

The instruments do have different measurement source areas, ranging from less than 1 m for the snow temperatures and ground heat flux, to 200-300 m for the eddy covariance fluxes. However, given the homogeneous nature of the site, which exhibits negligible change in surface properties for kilometres surrounding, it is unlikely that the differing footprints would be a major source of error. Energy balance measurements are conducted at point scales in much more heterogeneous landscapes with less than 20% error (*e.g.* Turnipseed et al. (2002)).

Systematic instrumental errors have hopefully been minimized by subjecting the data to rigorous data verification procedures, and correcting data where applicable. Since the energy balance residual is largest when the when radiation losses are large, it is tempting to attribute the residual to a bias in the radiometer, however based on verification of the

data, this cannot be justified. Because it is the largest flux, it is worthwhile to reiterate the quality assurance procedures that were applied to the radiation measurements (refer to §3.2.2 for details): (1) outgoing surface temperatures ( $Q_{Lo}$ ) were bound by near surface thermocouple readings; (2) incoming long-wave radiation was bound by theoretical clear-sky parameterizations (Brutsaert 1975a, Sicart et al. 2006); (3) incoming solar radiation was bound by the calculated extraterrestrial radiation for this location; (4) albedo values were within the expected range for a clean snow surface; (5) sensor heating would have negligible effect on net radiation values; and (6) hoar frost accumulation would produce errors in the other direction. In the absence of any nearby radiation measurements to discredit these data, it is assumed that the radiometer is operating within the manufacturer’s specifications ( $\pm 10\%$  of daily totals).

Errors in  $Q_G$  are not suspected to be the root cause of the noted imbalance. Although this term was not large (generally less than  $15 \text{ W m}^{-2}$ ), it was persistent. Errors in this term would appear as a small offset in the energy balance residual, but cannot be related to the temporal dynamics of the residual. Another small source of bias in  $Q_G$  could be due to the fact that the heat flux plate is not able to measure latent heat transfers from the soil to the snowpack.

Since the internal energy was measured with thermocouples, heating due to solar radiation was a possible source of error. The calculation of solar penetration into the snowpack suggests that much of the energy is extinguished near the surface. However, the best indication that the near-surface thermocouples were not affected to a large degree is that during sunny conditions, the infrared surface temperature responds to solar heating at a similar rate as the near surface thermocouple (as seen in Figures 5.3 -5.5). Fortunately, any error that exists due to solar heating will not be accumulated. When the sun goes down, the snowpack temperature cools and a corresponding decrease in internal energy is recorded.

With respect to the turbulent fluxes, the errors can be classified as being either instrumental or meteorological in nature (Massman and Lee 2002). The instrumental errors are those related to flux attenuation due to path length averaging, sampling frequency limitations,  $\text{O}_2$  absorption by the KH20, etc. Raw data were subject to quality control routines, and data were corrected where applicable. In general, the corrections required for the sensible and latent heat fluxes were negligible. Flux attenuation due to limitations on the sampling frequency are most serious at high wind speeds, of which there were very few periods. Nonetheless, the flux variation between the two sampling heights was minimal suggesting that attenuation was not a significant limitation. Losses in flux due to instrument constraints are inevitable, however there is no compelling evidence to suggest that they are responsible for the large residuals observed here.

Errors related to meteorological issues usually relate to the assumptions involved in the eddy covariance framework. Some of these errors can be detected by examining the turbulence characteristics (Foken and Wichura 1996). These were investigated in Chapter 4, and did not reveal any significant cause for concern. Reba et al. (2009) evaluated eddy covariance collected over three snow-seasons and found no unique issues associated with applying the technique over snow surfaces in winter periods. At moderate to high wind speeds, the turbulent fluxes were well defined by the 30-minute averaging period, the co-spectra were similar to the neutral Kansas data (Kaimal et al. 1972), and there was no obvious reason to consider these fluxes as incorrect. Small sensible heat fluxes (near zero) were noticed to sometimes occur at high wind speeds. This is due to a dampening of the temperature fluctuations which may drop below the resolution of the sonic anemometer ( $0.025^{\circ}\text{C}$ ). Turnipseed et al. (2002) suggest that the noise in the sonic temperature signal may become larger than the signal due to characteristic small temperature fluctuations observed in winter periods. More likely in the observed case is that the temperature fluctuations were small because the atmosphere was near adiabatic at that time due to the high wind speeds. If in fact there was a problem with the structure of the surface boundary layer (such as weakly developed turbulence, flow separation, etc.) it was not readily apparent from the turbulence characteristics alone. However, a check of the wind speed normalized by the friction velocity (Figure 4.21) revealed that there were marked differences in the near neutral turbulence development depending on the direction of the heat flux. When the sensible heat flux was directed towards the atmosphere, the momentum fluxes measured by the sonic anemometers were quite similar to those estimated using the 2 levels of wind profile data. However, when heat fluxes were directed towards the snow, the profile method predicted greater flux than was measured by the sonic anemometers. This is perhaps evidence that the demand of energy required by the snow surface to offset the radiation loss was creating a locally stable layer near the surface, which dampened the turbulence and caused the boundary layer to decouple from the surface. This discrepancy is similarly observed at high wind speeds when adequate mixing would be expected, which may indicate that the surface boundary layer does not extend to the height of measurement.

For the sake of a complete discussion, it must be remembered that the majority of the data periods occurred at low wind speeds. The resulting stable conditions pose unique challenges to the eddy covariance technique as they often include weak turbulence which may be temporally intermittent and the turbulent statistics may become contaminated by non-turbulent meso-scale motions such as waves, etc. (Mahrt 1999). These events lead to non-stationarity and an increase the random error associated with the flux calculations. Fluxes calculated during weak turbulence, although contaminated by non-turbulent motion, are usually quite small (Vickers and Mahrt 2006). These conditions were relatively common at

this site. For example, the period on February 13 had very low wind speeds which resulted in very stable atmospheric conditions where bulk Richardson values were in excess of 0.2, which suggests that turbulence was not being sustained. During conditions of low flow, although turbulent transfer is low, some degree of mixing of the atmosphere is still encouraged by non-turbulent motions (Grachev et al. 2005). However, owing to the difficulties of measuring surface fluxes during these conditions, no estimates of the magnitude of energy exchange that could possibly occur during these conditions are available.

Another possible source of error is radiation divergence, which can be significant during stable nocturnal periods (Garratt and Brost 1981). This would result in cooling of the air above the snow surface, and result in measurements of the upwelling radiation which are not representative of the snow surface. However, given that the radiometer was installed within 2 m of the surface, and air at temperatures colder than  $-20\text{ }^{\circ}\text{C}$  can hold very little water vapour, this does not seem like a plausible mechanism. To the author's knowledge, radiation divergence over very cold snow surfaces has not been examined.

The magnitude of the energy imbalance suggests that it cannot be explained by instrumental or experimental errors alone. As indicated in Figure 5.1, under ideal conditions (strong wind speeds with no solar radiation), the turbulent heat fluxes were generally 50% of the sum of the remaining terms. The magnitude of the internal energy changes and the ground heat flux were not sufficient to account for this difference, even if a large unconsidered error was present in their measurement. Rather, very large biases in the turbulent heat fluxes (of up to 100% at times) or in the net radiation losses (of perhaps 50 %) would be required to account for the missing energy. Certainly some error is present in the measurements, however the strong biases required to explain the energy balance would presumably be discovered in the data verification stems previously described.

### 5.3.1 Consideration of Missing Energy Terms

Accepting the limitations of the measurements, the sheer magnitude of the energy flux residual suggests that there is a significant energy term that is not being measured. Furthermore, this is supported by the realization that in mid winter at northern latitudes the radiation balance is typically negative, continental weather systems are slow to change and long periods of cold stable weather are common yet snow temperatures do not drastically cool in response to the energy loss at the surface. This is a physical constraint that has been realized by numerical modelers which has led to the inclusion of a 'windless exchange coefficient' (*e.g.* Brun et al. 1989, Jordan 1991, Brown et al. 2006), which increases the rate of sensible heat transfer at low wind speeds to prevent the snow temperatures from dropping to unrealistic levels. Although this is a commonly employed modeling strategy, there have not been any

studies where the entire snow energy balance is measured, which would lend support for its use. The observations presented in this chapter suggest that this practice is justified on a physical basis for proving a degree of coupling between the snow and atmosphere. From the observations reported here, the snow temperatures tend to respond to changes in the air temperature rather quickly. This is supported by the observation that the snow temperature dynamics are related to the air temperature dynamics, as demonstrated in Figures 5.3b, 5.4b, and 5.5b. A simple plot of the air temperature measured at 1.58 m against the internal energy calculated for the uppermost 7 cm of the snowpack (Figure 5.7) supports the correlation observed between the atmosphere and snow temperatures. However, the fact that the air and the snow (ice-air composite) are at similar thermodynamic states, does not directly imply a specific flux mechanism. Given the meteorological conditions it is reasonable to suspect that an un-measured sensible heat transfer is taking place. Temperature gradients are usually directed towards the snowpack, owing to the radiative cooling effects. Latent heat transfers are not expected to be a significant energy term since the gradient is usually directed towards the atmosphere, and the vapour pressure is very low at cold temperatures. In the event that the temperature gradient and the humidity gradients are both negative (*i.e.* directed towards the surface), Andreas (1989) shows that the Bowen ratio  $Bo = Q_H/Q_E$  is bound by the relationship (5.1), which is controlled by the dependence of the saturation vapour pressure  $\rho_{vs}$  on the surface temperature. The Bowen limit,  $Bo^*$  for negative temperatures is given in Figure 5.8. For the data periods presented in this chapter, surface temperatures were routinely below  $-20^\circ\text{C}$ , dictating that sensible heat be the dominant turbulent energy term.

$$Bo^* = \frac{\rho c_p}{\lambda_{sub} d\rho_{vs}/dT} \Big|_{z=0} \leq Bo < \infty \quad (5.1)$$

If in fact it is sensible heat that is being under-measured, the exact mechanism responsible for its transport from the atmosphere to the snowpack can not be specified exactly. However, two important characteristics of the energy residual are described below.

**(1) Missing energy scales with radiation** Over cold surfaces the sensible heat and long-wave radiation fluxes should be closely coupled due to the intuitive relationship that when long-wave losses are large, the temperature gradient within the surface layer should also become larger and direct more sensible heat towards the surface (Makshtas et al. 1999). Modeling of the surface energy balance over the Weddell sea ice by Andreas and Jordan (2004) and over sea ice at the North Pole by Jordan et al. (1999) revealed that during mid-winter periods the sensible heat tended to mirror the net long-wave radiation. However, this was not the general case observed in this study, at least not for the measured sensible heat

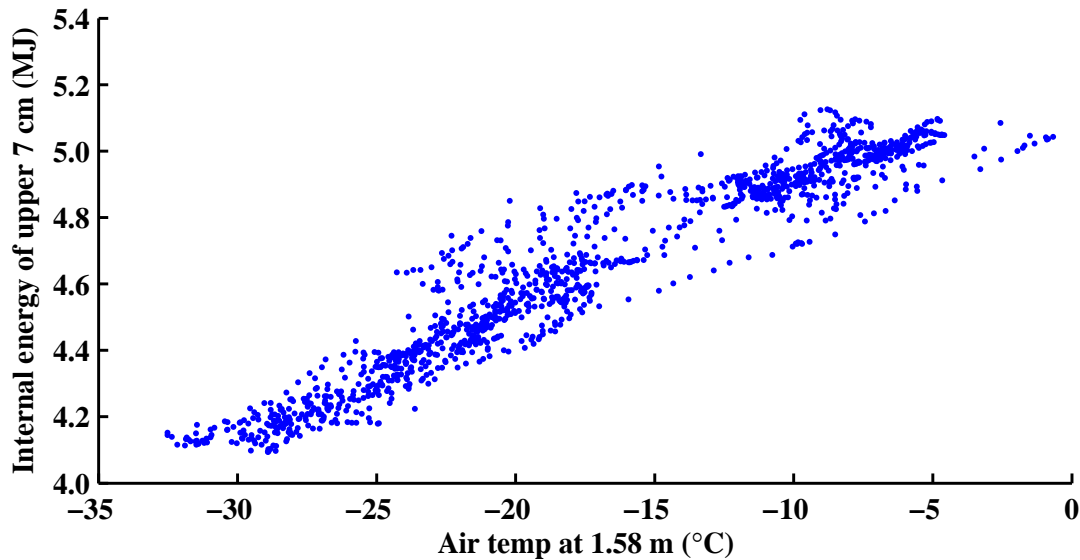


**Figure 5.7:** Internal energy change of near surface snowpack vs. air temperature measured at 1.58 m.

flux. During cold, clear-sky periods ( $Q_{Li} < 180 \text{ W m}^{-2}$ ), the effect of  $Q_{S^*}$  was to increase the surface temperature, thereby increasing the net losses of  $Q_{L^*}$  and decreasing the temperature gradient and fluxes. Otherwise, increasing losses of  $Q_{Lo}$  during nocturnal periods did tend to increase the bulk temperature gradient, however this usually resulted in increased stability and smaller turbulent fluxes. Thus, the observations here do not support that the sensible heat flux is coupled with the long-wave radiation balance through the temperature gradient alone.

**(2) Missing energy is not being captured by eddy covariance measurements** The fact that the eddy covariance measurements did not report larger sensible heat fluxes might suggest that the exchange was occurring at higher or lower frequencies than were being sampled by the sonic anemometer, or that the measurements were being made outside of the surface layer. The turbulence characteristics, which were examined in detail in Chapter 4, did not reveal any deficiencies in the sampling strategies employed. However, the differences noted between the momentum fluxes calculated by the sonic anemometer vs. those calculated with the profile technique (Figure 4.21) strongly indicate that the boundary layer is not as ideal as the turbulence characteristics would suggest. In a recent review paper, Foken (2008) argues that the energy balance residual that is commonly noted is due to large scale exchange processes that go unmeasured with the eddy covariance technique. These are hypothesized to be large-scale circulations that originate from heterogeneities in the landscape, and can be associated with a breakdown of the theoretical framework required for the eddy covariance

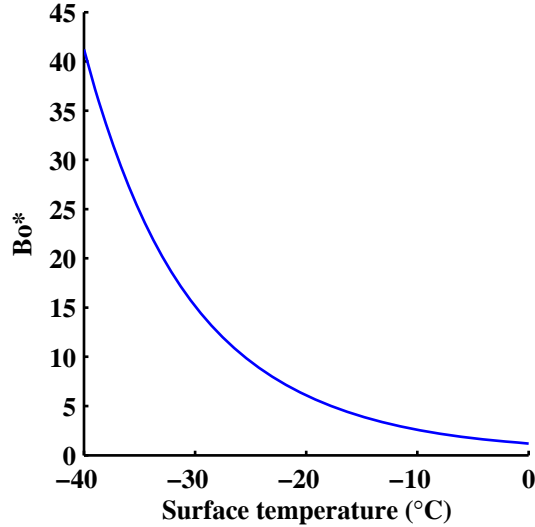


**Figure 5.8:** The limiting Bowen ratio value as a function of surface temperature.

technique. Although the KF prairie is locally flat and homogeneous for the surrounding few kilometres, there are other dissimilar land-cover types nearby, such as the City of Saskatoon (within 5 km). It is difficult to assess the presence or the effectiveness of large scale exchange mechanisms at this site, since neither measurements or modeling of the spatial structure of turbulence are available. The magnitude of the observed imbalance warrants further investigation, particularly to determine whether this is a unique problem associated with snow covered lands.

In all cases, the observed energy imbalance was large whenever the net radiation losses were large. If sensible heat was to replace this energy, with similar temporal dynamics as the thermal radiation balance, it would be necessary to reduce the resistance to convective heat transfer at the snow surface, and also the boundary layer resistance. Possible mechanisms for heat transfer scaling upon the thermal radiation balance will be further investigated in the next chapter. However, the observations indicate that this mechanism alone is not sufficient. If the surface resistance to heat transfer was very low, allowing the snowpack to extract energy from the atmosphere as required to match the thermal radiation loss, this would decrease the temperature of the air near the snow surface. Although this may be sufficient to cause the boundary layer decoupling previously discussed, it would also likely be detectable in the air temperature time series. However, the observed changes in temperature at 1.58 m were usually less than  $1\text{ }^{\circ}\text{C hr}^{-1}$ . All of this suggests that there must have been a mechanism that brought warm air into the surface layer. Thus, an increase in the boundary layer resistance is also required. This mechanism would not necessarily need to be turbulent, and could be due to advective flows, such as cold air drainage or by atmospheric subsidence occurring as a result of the large-scale heterogeneity.

## 5.4 Summary and Conclusions

Detailed energy flux measurements over a homogeneous snowpack revealed a significant inability to close the energy balance. Long-wave radiation losses dominated the energy balance during the mid-winter measurement period while turbulent fluxes remained small. Snowpack temperatures were not observed to cool in response to the predominantly negative radiation balance, suggesting that the sensible heat flux to the snowpack from the atmosphere was actually much larger than was being reported by the eddy covariance measurements. The energy residual was much larger than what could be attributed to experimental errors alone, suggesting that there is an additional energy term present, which is not being measured. Due to the high degree of coupling exhibited between the snow temperatures and the atmospheric temperatures, it is hypothesized that additional sensible heat is being provided by the atmosphere through an unknown mechanism. The exact nature of the mechanism, and the cause of the energy imbalance is unclear.

## CHAPTER 6

# HEAT TRANSFER TO PERMEABLE SNOW SURFACES

### 6.1 Chapter Overview

In the preceding chapter serious problems in closing the energy balance were identified which could not be explained solely on the basis of instrumental errors or experimental bias. Evidence was presented which suggested that the current understanding of how energy is exchanged with the snowpack may be incomplete. This chapter discusses potential mechanisms for exchange between the atmosphere and the snowpack that are not currently considered in snow physics models.

Snow is a porous medium. However, the theories of heat and mass exchange between the snowpack and the atmosphere (as described in Chapter 2) are based on boundary layer flow over an impermeable, rough surface. Furthermore, when modelling snow energetics the turbulent fluxes are considered as boundary conditions, which implies that the input of energy occurs exactly at the snow-air interface. The deficiency of this approach is that the continuity of the air above and within the snowpack and the associated interaction with the ice matrix is not truly considered. Upon consideration of the additional exchange surface of a porous material, larger rates of heat and mass transfer could potentially be expected. For example, Bilger and Atkinson (1992) attempted to model the rate of phosphorus uptake into coral reefs using flat-plate boundary layer correlations, however they were unable to match the large measured transport rates which were attributed to the porous nature of the material.

The flow of a turbulent fluid over a permeable surface is encountered in many engineering and geophysical applications, such as packed bed heat exchangers, porous bearings, fibrous insulation, crude oil extraction, water flow over porous sediments, etc. Accordingly, there have been numerous attempts to model the interactions between the two separate domains (*i.e.* the porous region and the overlying fluid). The crux of the 2-domain approach is to couple the conservation equations for the two domains and to specify appropriate boundary conditions (such as those discussed by Beavers and Joseph (1967), Ochoa-Tapia and Whitaker

(1995, 1997), Alazmi and Vafai (2001)). A few analytical solutions are available for laminar flow with restricted geometric configurations (*e.g.* Kuznetsov 1996, 1997, 1998), but generally a numerical approach is required (*e.g.* Choi and Waller 1997, Silva and de Lemos 2003b, Costa et al. 2004). Within the past decade this approach has been extended to turbulent channel flows (*e.g.* Pedras and de Lemos 2001, Prinos et al. 2003, Silva and de Lemos 2003a, Hahn et al. 2002, Breugem et al. 2006). To date, a situation with as much complexity as turbulent wind flow over snow has not been considered, and to do so would require considerable effort. Unfortunately, despite the abundance of numerical investigations, there are very few experimental observations from which to gain insight from.

This chapter presents some preliminary arguments for a turbulent heat transfer mechanism that is consistent with the results presented in Chapter 5, and considers the effect of the permeable snow surface on heat exchange with the atmosphere.

## 6.2 Conceptual Processes of Heat Exchange with Snow Surfaces

The fundamental requirements for interfacial heat transfer between the atmosphere and the snow surface are: (1) an exchange mechanism (*i.e.* mechanical mixing, molecular diffusion, buoyancy, etc.); (2) surface area for the exchange of energy to occur over; and (3) an energy (temperature) gradient. The application of these essential properties, as they relate to the snow-atmosphere interface, is discussed below.

### 6.2.1 Transfer Mechanisms

The notion of air flow occurring within the snowpack has been broadly considered. Theoretical accounts of air flow in homogeneous and layered snowpacks have been made by Colbeck (1989, 1997), Clarke et al. (1987), Clarke and Waddington (1991), Waddington et al. (1996) and Massman (2006). Extensive modelling of air flow has been conducted by Albert and McGilvary (1992), Albert (1993, 1996, 2002); and measurements of air flow in snow have been made in the field (Albert and Hardy 1995, Albert and Schultz 2002), and within a wind tunnel (Sokratov and Sato 2000, 2001). From these efforts, it is known that air flow in snow can be caused by: (1) slow pressure changes due to changes in barometric pressure; (2) static pressure differences created when wind encounters roughness elements on the snow surface; and (3) rapid pressure changes due to turbulent winds over the snow surface. Of these mechanisms, the most significant cause of air movement within the snowpack is believed to be due to static pressure differences that develop as air moves over topographic obstacles such as

snow drifts (*e.g.* Colbeck 1989, Albert 1996, Albert and Hawley 2002). While this mechanism may be able to induce airflow to significant depths within a snowpack, it is unlikely that it would contribute significantly to heat exchange with the atmosphere. Due to the relatively long flow paths, and the large surface-area to air-volume (see discussion to follow), a thermal equilibrium between the air and ice phases would be reached quite rapidly. It is important to consider that a large part of the motivation for studying wind flow into snow has been for paleo-climate reconstruction, where it is hoped that a better understanding of chemical deposition processes will aid in interpretation of polar ice cores. Few of the aforementioned studies specifically examine the role of air moving through snow from the perspective of energy exchange and snowmelt.

In order for high rates of snow-atmosphere heat exchange to occur, a short flow path with rapid exchange of air would be required. For this reason, it is hypothesized that most of the heat exchange occurs in the thin interfacial region that defines the boundary between the snowpack and the atmosphere. The analysis of Colbeck (1989) suggests that fast pressure fluctuations caused by turbulent eddies cause small changes in pressure at the snow surface but generally result in a very small ( $< 1.0$  mm) displacement of air within the snow (Waddington et al. 1996). While this depth may not be significant when considering the filtering ability of the snowpack, it may in fact exert significant influence on the heat and mass transfer rates between the snow and the atmosphere. Beavers and Joseph (1967) examined the case of Poiseuille flow over a permeable block and discovered that a velocity boundary layer was induced within the permeable material. To account for this, they proposed a slip-velocity boundary condition (6.1) to account for the tangential velocity at the interface. Figure 6.1 depicts how this condition would be applied to a snow surface, where  $u_s$  is the slip velocity, and  $u_p$  is the filter velocity which is the pressure driven flow within the snowpack. Note that this is the area-averaged air flux through the snow rather than the local pore velocity. Equation (6.1) states that the slip velocity depends on the permeability  $K$  of the porous material and a dimensionless variable  $\alpha$  that depends on the structure of the permeable material near the interface. Beavers and Joseph (1967) used various foam metals and found that the value of  $\alpha$  depended on the average pore diameter, and ranged from 0.1 for a pore diameter of  $3 \times 10^{-4}$ m to 4.0 for a pore diameter of  $1 \times 10^{-3}$ m. Since the parameters in (6.1) depend on the porous medium rather than the fluid, this boundary condition is also appropriate for turbulent flow (Hahn et al. 2002).

$$\left. \frac{du}{dz} \right|_{z=0} = \frac{\alpha}{\sqrt{K}}(u_s - u_p) \quad (6.1)$$

The slip velocity boundary condition (6.1) was applied to snow by Bergen (1980) where

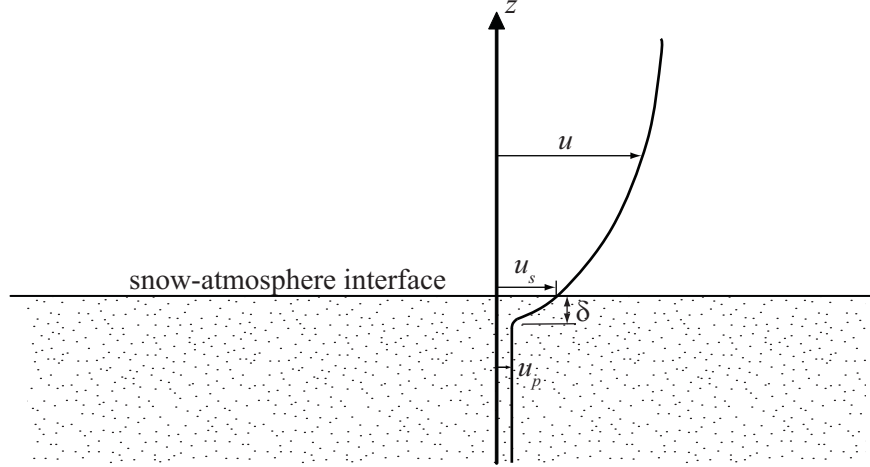


**Figure 6.1:** Conceptual wind velocity profile over a permeable snow surface.

he attempted to indirectly estimate the slip velocity from measured wind velocity profiles and snow permeability, through (6.2). Although only five datum points were collected, they did indicate an increase in the ratio of  $u_s/u_*^2$  with  $\sqrt{K}$ . Unfortunately, these results are insufficient to reveal suitable values of the parameter  $\alpha$  for snow.

$$\frac{u}{u_*} = \frac{1}{\kappa} \ln \left( \frac{z}{z_{0m}} \right) + \frac{u_s}{u_*} \quad (6.2)$$

Within the interfacial sublayer, the velocity profile (6.3) at the boundary scales with the momentum flux  $\tau$ , which allows for a convenient expression for the slip velocity to be developed (6.4).

$$\nu \frac{du}{dz} = \frac{\tau}{\rho} = u_*^2 \quad (6.3)$$

$$u_s = \frac{u_*^2 \sqrt{K}}{\alpha \nu} \quad (6.4)$$

Example slip velocities calculated using (6.4) are given in Figure 6.2 for typical snow permeabilities  $K = 1 - 10 \times 10^{-10}$  and  $\alpha$  values of 1 and 4 (loosely based on the values in Beavers and Joseph (1967)). This suggests that interfacial velocities are likely less than  $0.1 \text{ m s}^{-1}$ .

The depth of penetration of air motion that is induced within the snowpack will be quite important for calculating the ‘wetted’ surface area. Goharzadeh et al. (2005) used particle image velocimetry and refractive index matching to study the velocity with the interface region of flow over a bed of glass beads. They found that the depth of the interface region

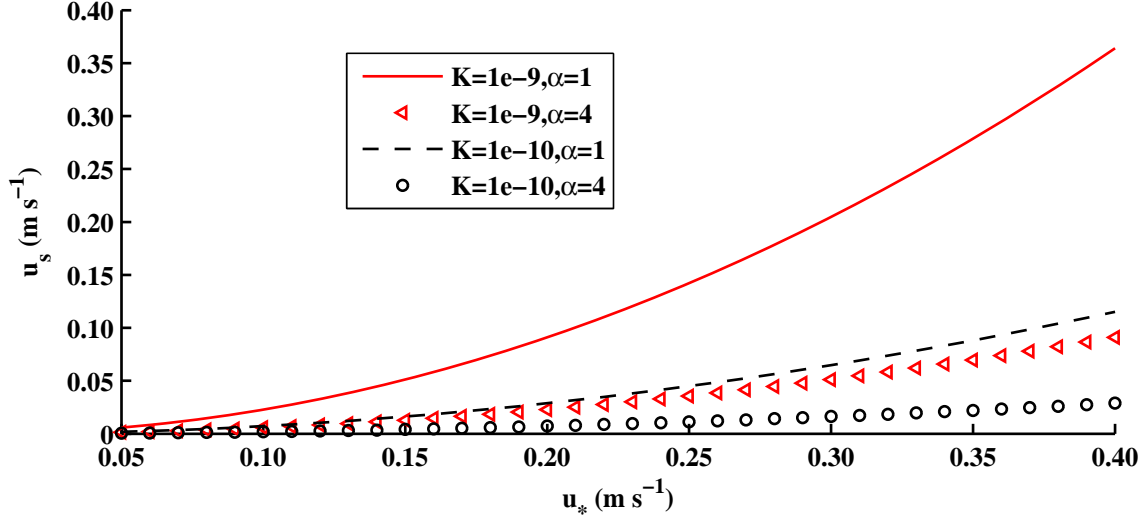


**Figure 6.2:** Slip velocities estimated for the snow-air interface.

is on the order of the grain size, and the depth was not sensitive to the Reynolds number. Similarly, Choi and Waller (1997) state that the depth of penetration is primarily dependent on the Darcy number of the porous medium. Both of these studies suggest that the interface (slip) velocity does not affect the depth of penetration, but does affect the velocity profile. For snow, this implies that the depth of the interfacial region is likely on the order of  $10^{-4}$  to  $10^{-3}$  m.

The actual transfer mechanism is expected to largely depend on the turbulence characteristics of the flow, and how they are influenced by the underlying porous material. Direct numerical simulations of turbulent fluid flow over a packed bed of spheres were performed by Breugem et al. (2006). They found that that the permeability Reynolds number (6.5) describes the behaviour of the permeable region in permitting the effects of turbulence into the snowpack.

$$Re_K = \frac{\sqrt{K}u_*}{\nu} \quad (6.5)$$

For  $Re_K \ll 1$  it was confirmed that a porous wall behaves essentially as a solid wall. This is due to the viscous sublayer that forms over all of the individual solid elements coalescing to form a single viscous layer which blocks penetration of eddies into the porous layer. At  $Re_K \gg 1$ , the viscous effects were less important, and eddies were able to influence air movement within the porous structure. Given the low permeability of snow,  $Re_K$  will be much less than 1 which suggests that the turbulent interaction between the overlying fluid and the pore fluid will be limited. This implies that flow within the interface region can be adequately

described by Darcy’s law (*i.e.* inertial effects will not be present). However, it should be noted that the permeability measurements available from the literature are presumably collected from within the porous medium where the porosity is relatively constant. At the interface, the porosity increases as the atmosphere domain is encountered, so it is also likely that the permeability of the interfacial layer also increases.

An important consequence of the introduction of a slip velocity is the reduction of the depth of the viscous sublayer (Breugem et al. 2006). The logarithmic law of the wall is still formed, but is usually shifted downwards (Schetz 1993). For highly permeable walls, the turbulence structure above the wall is modified due to a reduction in viscous layer (Breugem et al. 2006), resulting in an increase in momentum transfer. Most investigators note an increase in skin friction for turbulent flow over porous walls (*e.g.* Zippe and Graf 1983, Breugem et al. 2006).

Given that the snow layer usually makes up a very small portion of the atmospheric boundary layer, it is probable that the small induction of velocity (and consequent extraction of momentum) would not be detectable from measurements above the surface (say at a height of 2 m). However, from the perspective of the snowpack, the mechanisms described above are likely significant enough to play a role in exchange of heat and water vapour with the atmosphere.

## 6.2.2 Exchange Area

Given the porous nature of snow, it inherently exhibits a larger surface area than the planar area of an impermeable wall. Legagneaux et al. (2002) report specific surface area (SSA) values of snow which are between 100-1600 cm<sup>2</sup> g<sup>-1</sup>. In consideration of the interfacial region as the predominant zone of heat exchange, any estimate of the surface area must take into account how the porosity varies at the interface. Over the length of one particle, the porosity must vary from  $n = 1$  above the interface to  $n_s = 1 - \rho_s/\rho_i$ . Breugem et al. (2006) suggest a 5th order polynomial (6.6).

$$n(z) = -6(n_s - 1) \left(\frac{z}{\delta}\right)^5 - 15(n_s - 1) \left(\frac{z}{\delta}\right)^4 - 10(n_s - 1) \left(\frac{z}{\delta}\right)^3 + 1 \quad (6.6)$$

Using this approximation (6.6), assuming that the specific surface area of snow is 30 m<sup>2</sup> kg<sup>-1</sup>, the average snow density is 300 kg m<sup>-3</sup>, and the interface region is approximately 1 mm, the wetted surface area per unit planar area is approx. 4.72 m<sup>2</sup>m<sup>-2</sup>. Meanwhile, the pore volume within this region is 7.78x10<sup>-4</sup> m<sup>3</sup>m<sup>-2</sup>. From this simple analysis, clearly any air that happens to penetrate the interface would surrender its energy to the snowpack quite quickly.

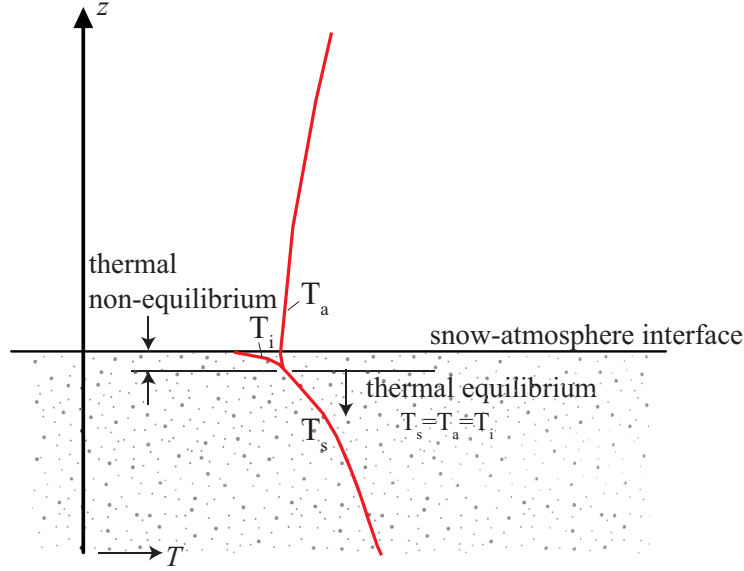


**Figure 6.3:** Conceptual temperature profile at the air-snow interface.

### 6.2.3 Energy Gradient

Although it is plausible that wind does penetrate into the snowpack to some depth, creating a large wetted surface area for which exchange is possible, it is the interfacial temperature difference that will ultimately control the heat flux. Within the snowpack, thermal equilibrium (*i.e.*  $T_s = T_a = T_i$ ) is usually assumed. However, at the interface this does not hold, as only the air phase can exhibit a continuous temperature profile, and a temperature difference will exist between the ice and air phases. The heat transfer potential is therefore characterized by the effective area of ice surface which is at a different temperature than the air phase. A sketch of a conceptual temperature profile exhibiting thermal non-equilibrium conditions at the snow-air interface is provided as Figure 6.3. Note that this discussion is restricted to a cold, dry snowpack with negligible water content.

The energy equations for the air and ice constituents of an elemental volume that are under thermal non-equilibrium conditions are given as (6.7-6.8), where conduction, radiation, and convection heat transfer mechanisms are presented as the first three terms on the right hand side. The terms  $k_a$  and  $k_i$ , are the thermal conductivities of the air and ice respectively,  $q_r'''$  represents a volumetric energy conversion due to radiation, and  $h_v$  is a interfacial volumetric convective heat transfer coefficient. The energy equation for the ice phase also has an energy term associated with latent heat change, however these effects are excluded from the present analysis.

$$n(\rho c_p)_a \frac{\partial T_a}{\partial t} + (\rho c_p)_a \mathbf{v} \cdot \nabla T_a = nk_a \nabla^2 T_a + nq_{r,a}''' + h_v(T_i - T_a) \quad (6.7)$$

$$(1 - n)(\rho c_p)_i \frac{\partial T_i}{\partial t} = (1 - n)k_i \nabla^2 T_i + (1 - n)q_{r,i}''' + h_v(T_i - T_a) + L_{sub} \quad (6.8)$$

The dominant energy forcing in the mid winter period is thermal radiation exchange with the atmosphere, which is often very cold. Radiation transfer to the atmosphere is presumed to occur at the outermost tips of those snow crystals which have a view to the atmosphere. Since the ice has high emissivity ( $\epsilon \approx 0.99$ ) and a relatively low thermal capacity, as the outer surface of the ice matrix cools, a temperature gradient will form within the interfacial region. Depending on the magnitude of the long wave radiation losses, it is possible that the area of snow that is experiencing local thermal non-equilibrium may increase. Equation (6.8) states that thermal radiation is balanced by conduction from within the solid matrix, as well as by forced convective heat transfer. Figure 6.4 compares the temperature difference observed at KF between the surface and thermocouples located  $\pm 2$  cm from the interface as affected by the long wave radiation balance for calm and windy periods. Only nocturnal periods are considered, as to exclude any effects of solar heating on thermocouple readings. During the calm periods, the temperature gradients near the surface become quite large, reflecting the absence of thermal convection in the energy balance. Conduction alone cannot maintain the equilibrium condition, and the temperature of the ice layer decreases. It is conjectured that the degree of non-equilibrium increases and the effective area also increases, permitting diffusive and convective exchange to the snow. During windy periods, the gradients are much smaller, but are still noted to exhibit a dependence on  $Q_{L^*}$ . Note that during the calm periods, very large temperature gradients of up to  $200^\circ\text{C m}^{-1}$  can result, making natural convection processes likely also important. Bartelt et al. (2004) provide a non-equilibrium treatment of heat and mass transfer within a snowpack, in which their model predicted the occurrence of non-equilibrium conditions in near-surface snow layers. However, the non-equilibrium conditions reported in their study were caused by the large differences in thermal diffusivity between the air and ice phases, not from advection. Nonetheless, their study demonstrates the possibility for occurrence of non-equilibrium conditions.

The interfacial heat transfer coefficient,  $h_{a \rightarrow i}$  for snow has not previously been specified. In lieu of a snow-specific value, a correlation obtained for a packed bed heat exchanger (p. 739 Kaviany 2002) is considered:

$$Nu = h_{a \rightarrow i} L / k_a = 2 + (0.4 Re_D^{1/2} + 0.2 Re_D^{2/3}) Pr^{0.4} \quad (6.9)$$

where the particle diameter Reynolds number  $Re_D = \frac{D_p \langle u \rangle}{\nu(1-n)}$ , which is based on the area-averaged velocity  $\langle u \rangle$  and an effective particle diameter  $D_p = \frac{6V_i}{A_i}$ . Since  $\langle u \rangle > u_s$ , which is likely around  $0.05 \text{ m s}^{-1}$ , a maximum value of  $h_{a \rightarrow i}$  for the example snow parameters

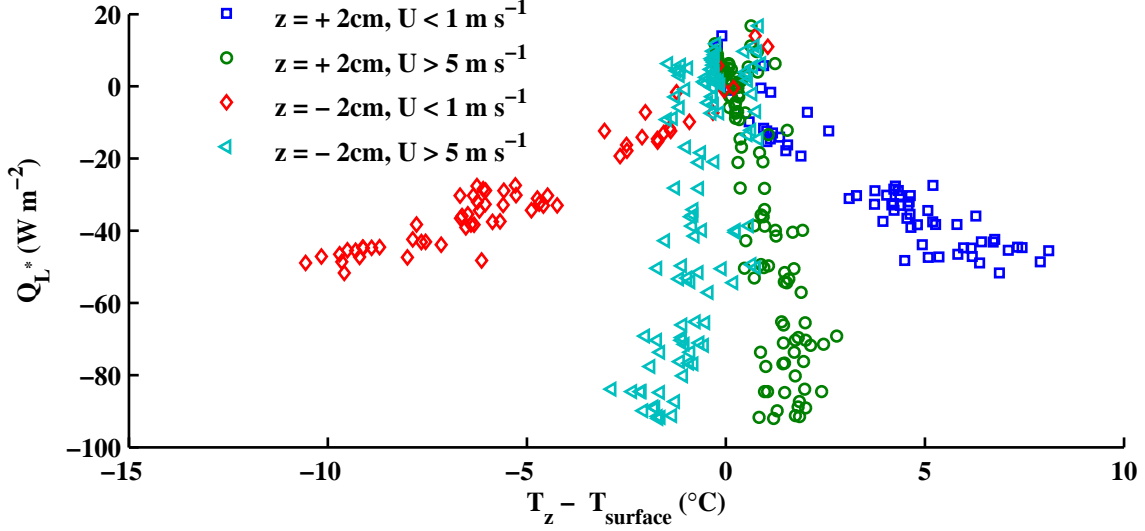


**Figure 6.4:** Surface temperature depression dependency on  $Q_{LW}$  and  $\bar{u}$ .

previously specified is approximately  $63 \text{ W m}^{-2}\text{K}^{-1}$ . Although this is a sizable heat transfer coefficient, it suggests that it is ultimately the depth of the non-equilibrium layer which controls the role of convection heat transfer. The Peclet number  $Pe$  represents that ratio of conduction to convection. Since the resistance to convective heat transfer depends on the effective wetted area, and the resistance to conduction heat transfer depends on the fraction of area that is ice (*i.e.*  $1 - n$ )  $Pe$  can be expressed as:

$$Pe = \frac{A_{wet} N u k_a}{(1 - n) k_i} \quad (6.10)$$

For a fixed porosity, the wetted area for convection increases as the effective depth of the non-equilibrium layer increases. For example, for an effective interfacial region depth of  $0.5 \times 10^{-4} \text{ m}$ ,  $Pe$  is around 0.2, which suggests that conduction is the dominant mechanism, however for a interfacial depth of  $2.0 \times 10^{-3} \text{ m}$ ,  $Pe$  increases to 0.8. These calculations are dependent on the physical nature of the snow crystals that make up the interfacial region, not only in terms of the porosity variation and surface area, but also on the degree of metamorphism. Presumably, the nature of the bonding between snow crystals would introduce another conduction resistance term not considered.

Ultimately, a numerical approach is warranted to determine the nature of the non-equilibrium conditions. However, since the exact physical nature and dimensions of the snow crystals in the interface are not known, numerical analysis should be preceded by microstructural observations.

## 6.3 Discussion

Although the ideas presented thus far are primarily qualitative, they are consistent with the observations noted in the previous chapters. Essentially, the concepts presented permit sensible heat exchange to scale on long-wave radiation instead of just the bulk temperature gradient and turbulence mechanism. This provides a mechanism for the coupling between the sensible heat flux and long wave radiation that was observed in the previous chapter, and also noted by workers in polar regions (*e.g.* King et al. 1996, Jordan et al. 1999, Andreas and Jordan 2004).

These ideas may also be consistent with the boundary layer decoupling that was observed during periods of strong heat requirement (such as in Figure 4.21). When air flows over any surface that is colder, a stable boundary layer results. However, the porous snowpack may be a unique case. Given that snowpacks are typically quite smooth, mechanical mixing due to shear production is small and the turbulent heat flux is limited. If the radiation-imposed demand is larger than can be supplied by turbulence, and conduction alone cannot transfer enough energy to meet the demand, the surface temperature is expected to drop (*cf.* Derbyshire 1999). This is likely accompanied by an increase in the degree of thermal non-equilibrium, which in turn allows convective heat transfer from the atmosphere to occur. As energy is extracted from the atmosphere, the atmosphere near the interface would cool and a local stable layer would develop that could potentially suppress turbulent production and cause the boundary layer to become decoupled from the surface. From the observations in Chapter 5, the near snowpack layers rarely cool below that of the atmosphere, which supports that the energy to meet the radiative demand is extracted from the atmosphere, rather than from within deeper snowpack layers. More detailed measurements of the temperature and wind speed profiles would be required to verify this. However, there are numerous references within the literature to a temperature minimum that is observed just over a snow surface (*e.g.* Nyberg 1938, Fleagle 1956, Oke 1970).

The mechanisms presented here also provide some insight into the physical basis of a windless exchange coefficient. Energy balance models have been noted to exhibit a cold bias during mid-winter periods where the wind speed is very low, radiation losses are large, and the modeled turbulent fluxes are small. The modeled turbulent transfer to the surface is insufficient to meet the radiation losses and the surface temperature drops, thereby increasing the stability (and further reducing the turbulent fluxes), resulting in a temperature crash and boundary layer decoupling (Derbyshire 1999, Slater et al. 2001). Jordan (1991) introduced a windless exchange coefficient to prevent unrealistic cooling of the boundary layer, hypothesizing that gravity waves are responsible for supplying energy to the surface when turbulence

is negligible (Jordan et al. 1999). These authors find that the additional energy added by this empirical coefficient (which is typically on the order of  $1\text{-}2\text{ Wm}^{-2}\text{K}^{-1}$ ) is sufficient to prevent boundary layer decoupling. It is possible that these non-turbulent processes are aided by an increase in the effective area that is at a thermal non-equilibrium as described above.

## 6.4 Chapter Summary

A new conceptual model of how the porous nature of the snowpack affects exchange energy with the atmosphere was presented. It is hypothesized that, due to a slip velocity at the air-snow interface, air flow is induced within a thin interfacial layer creating an enlarged surface area for heat exchange. Within this region, the effective area of ice that is at a different temperature than the air within the pores (*i.e.* thermal non-equilibrium) controls the potential for heat transfer. It is suggested that the effective area scales upon the thermal radiation balance, and enables convective heat transfer to play a larger role in the surface energy balance. This mechanism is particularly prevalent during periods where the thermal radiation balance is strongly negative, and the turbulent fluxes towards the snowpack are limited due to the low mechanical mixing over the smooth snow surface. The proposed framework permits the sensible heat to be coupled with the thermal radiation balance, allowing the necessary transfer of energy to balance the large radiation losses observed in mid-winter periods. Further development of these ideas will require a physical analysis of the structure of snow crystals at the snow-atmosphere interface, along with coupled atmosphere-snowpack numerical modeling which permits an analysis of how the air above the snowpack influences air movement within the snowpack.

# CHAPTER 7

## PARAMETERIZING TURBULENT FLUXES OVER SNOW SURFACES

### 7.1 Chapter Overview

From the information presented in the previous chapters, it is readily apparent that the processes of turbulent flux generation can challenge our measurement techniques and our understanding of the stable boundary layer. In the context of this thesis, the reason for making these measurements was to obtain a better understanding of the turbulence processes in open snow-covered environments - from which to guide model development and improve parameterization techniques. Accordingly, the specific objective of this chapter is to *assess the limitations of the currently employed flux-gradient estimation techniques in each of the studied environments and to make recommendations for future parameterization strategies for snow surfaces*. The two environments that will be addressed in this chapter are the homogeneous prairie environment (KF) and the mountain valley environment (HM). These sites have the necessary data and meteorological conditions to adequately assess the modelling issues, and they also serve to address the key findings in the previous chapters: (1) poor energy balance closure; and (2) non-local turbulence sources.

### 7.2 Homogeneous Prairie - Kernen Farm

The results presented in Chapter 5 revealed a significant energy imbalance, which was attributed to under-measured sensible heat. In this section, the ability of flux-gradient approaches to close the energy balance were tested, using the following science questions to guide the analysis: (1) how can the energy balance deficit (and associated energy terms be properly parameterized)?; and (2) how well do two relevant snow melt models (SNTHERM and CLASS) handle these conditions?

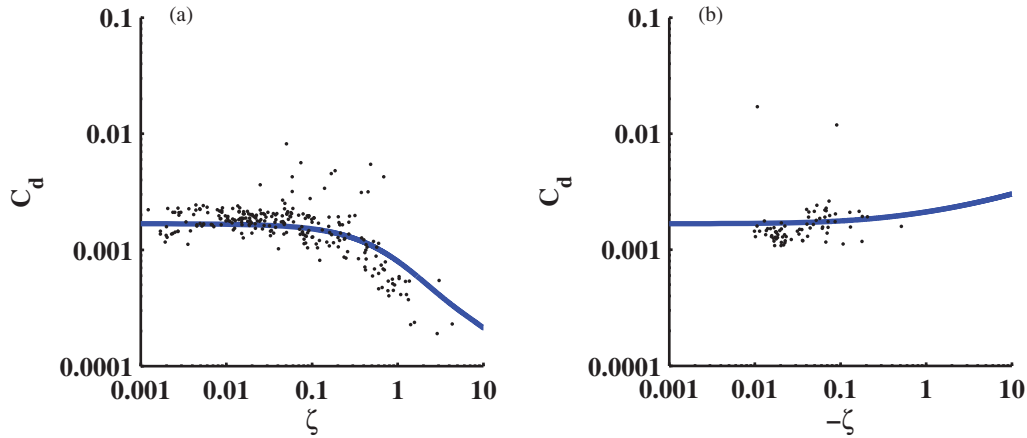


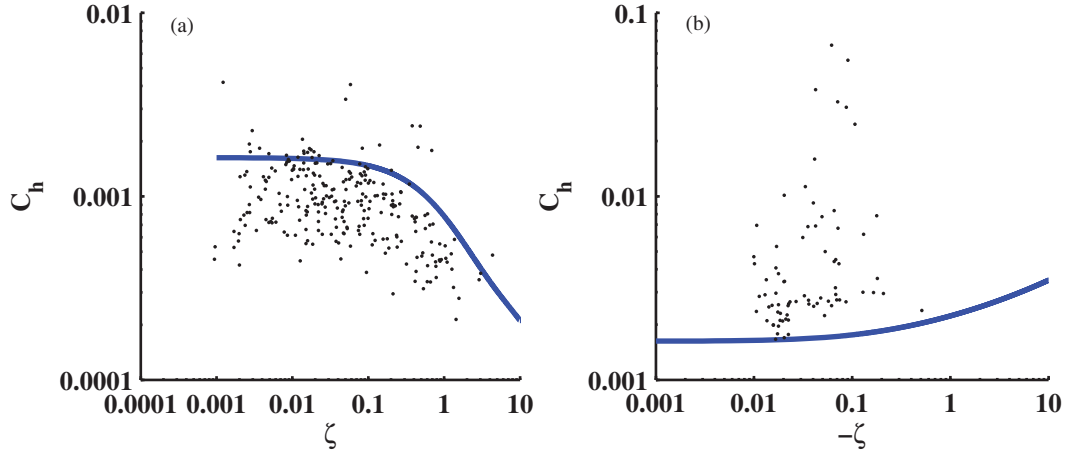
**Figure 7.1:** Inferred drag coefficient ( $C_d$ ) for KF filtered data: (a) stable conditions; (b) unstable conditions.

### 7.2.1 Measured Turbulent Exchange Coefficients

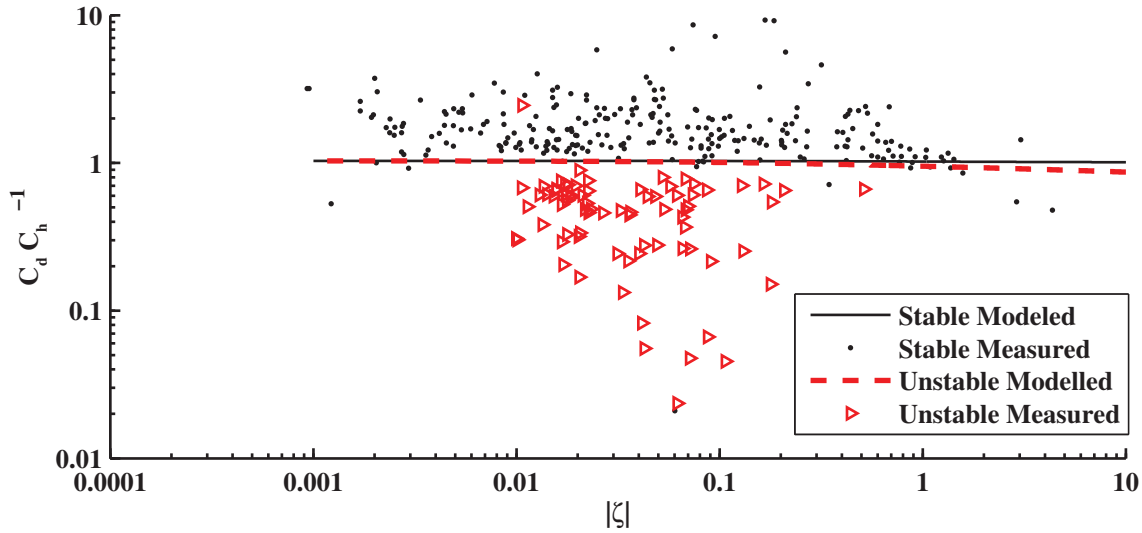
Since the majority of snowmelt models use the bulk transfer approach for calculating turbulent fluxes, the following presentation considers bulk transfer coefficients rather than their profile (gradient) counterparts.

Figure 7.1 presents the drag coefficient ( $C_d$ ) inferred from the sonic anemometer under stable and unstable conditions as it varies with  $\zeta$ . The modeled line is the value predicted by M-O theory using the profile function of Holtslag and De Bruin (1988) using an average  $z_{0m}$  value of  $0.9 \times 10^{-4} \text{m}$ . The values were filtered to include only good-quality flux data where the measured wind speeds were greater than  $1.0 \text{ m s}^{-1}$  and the sensible heat flux was greater than  $\pm 5 \text{ W m}^{-2}$  (necessary to ensure meaningful values of  $\zeta$ ). The values in Figure 7.1 fall on either side of the predicted line depending on the direction of the sensible heat flux. This observation was previously noted in §4.4.2 (see Figure 4.21) where the momentum roughness length measured by the gradient method or inferred from the sonic anemometer measurements were different depending whether the heat flux was towards the snow or the atmosphere. The gradient values more closely match the sonic anemometer values when the heat flux is directed towards the atmosphere.

For the sensible heat transfer coefficients  $C_h$  presented in Figure 7.2 the modeled value is prescribed from the surface renewal theory of Andreas (1987b). The ratio  $C_d C_h^{-1}$ , which can be considered as a type of bulk turbulent Prandtl number that depends slightly on measurement height and is important in invoking an extension of the Reynolds analogy, is presented in Figure 7.3. Here it can be seen that for the stable conditions, heat was transported less effectively than momentum, whereas in the unstable case it was actually more effectively transported. It must be kept in mind that the observed heat transfer was



**Figure 7.2:** Inferred bulk heat transfer coefficient ( $C_h$ ) for KF filtered data: (a) stable conditions; (b) unstable conditions.



**Figure 7.3:** Ratio of turbulent transfer coefficients for KF ( $C_d C_h^{-1}$ ) for KF filtered data.

much smaller than what was predicted by the energy balance residual (as discussed in Chapter 5). The relatively narrow range of  $\zeta$  values reported in the figures are reflective of the low rates of measured sensible heat transfer (i.e. small buoyancy forces).

The inferred latent heat transfer coefficients are given in Figure 7.4 but are misleadingly large. This occurred due to the presumed inability to accurately measure very small specific humidity differences (often less than  $1 \times 10^{-4} \text{ kg kg}^{-1}$ ). As a result of these small gradients a very wide range of transfer coefficients were measured which do not provide much certain information about actual vapour transfer processes.

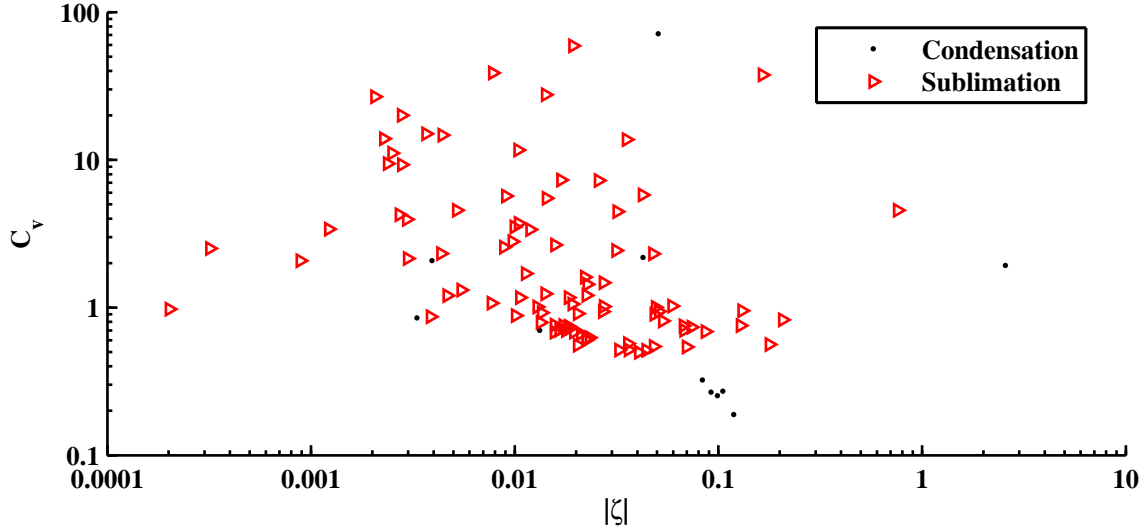


Figure 7.4: Inferred bulk vapour transfer coefficient ( $C_v$ ) for KF filtered data.

## 7.2.2 Strategies for Parameterization

Given the amount of scatter in the log-log plots in Figures 7.1 and 7.2, which were essentially derived by inverting the bulk transfer equations, it should be anticipated that flux estimates using the bulk transfer approach will differ from the measured turbulent fluxes. Nonetheless, it is useful to examine the magnitude of the differences and discern which conditions pose the largest challenges. Data from 7-15 February 2007 were used to examine the performance of a few bulk transfer parameterizations. This period was chosen to coincide with the detailed energy balance measurements in the previous chapter, and also because it contains a long stable period (7-13 February) which is followed by higher wind speeds associated with a frontal system (14-15 February). With the understanding that measured turbulent heat transfer was under-predicted relative to the amount of energy required to actually close the energy balance, a few different parameterization options are demonstrated at their effectiveness at minimizing this discrepancy. This is essentially referring to different effective parameterization schemes, which are discussed separately below:

**Case 1: *Assumed state of practice*** The model of Andreas (1987b) is used here as the standard approach for parameterizing the bulk transfer equations. A fixed value of  $z_{0m} = 2 \times 10^{-4}$  was used while the Andreas model provides an estimate of the heat transfer coefficient based upon model  $Re_*$ . For the chosen value of  $z_{0m}$  the modeled value of  $C_d C_h^{-1}$  is approximately 1.

**Case 2: *Increased roughness length*** One way to increase the amount of turbulent energy is to simply increase the momentum roughness length, which will in turn increase the

heat transfer coefficient. Here the effect of increasing the  $z_{0m}$  value to  $1 \times 10^{-3}$  m is demonstrated.

**Case 3: *Decrease bulk Prandtl number*** In situations where an effective parameterization scheme is warranted, it may prove advantageous to be able to specify a fixed value for the momentum roughness length as well as a fixed ratio of  $C_d C_h^{-1}$ . Here,  $z_{0m}$  was set to  $2 \times 10^{-4}$  m and the value of  $C_d C_h^{-1}$  was set at 0.65 in order to increase the heat transfer rate. The value of  $C_d$  and  $C_h$  therefore do not depend on flow roughness in this case.

**Case 4: *Windless exchange coefficient*** Numerous authors have noted that at low wind speeds numerical surface energy balance models report an unrealistically low surface temperature due to the lack of heat transfer from the atmosphere that is required to balance the radiation energy loss (*e.g.* Jordan 1991, Slater et al. 2001, Brown et al. 2006). A modelling tactic for this problem is to add a windless exchange coefficient, which is simply proportional to the temperature gradient. Here, a value of  $2 \text{ W m}^{-2} \text{ K}^{-1}$  (which is consistent with values reported in the literature), is added to the scheme described in Case 3.

**Case 5: *Empirical heat transfer*** The more ‘effective’ that the parameterization strategy becomes, the less sensible it is to hang on to the physical origins of a particular approach. The intent of this work is not to develop an empirical technique from the data, but to demonstrate just one available technique that has been used in snowmelt applications. This is the Kuz’min method described in Gelfan et al. (2004). It has no provisions for atmospheric stability, and is simply just a function of wind speed and the temperature gradient (or vapour pressure gradient).

## Performance of effective parameterization strategies

The accumulated daily turbulent heat flux ( $Q_H + Q_E$ ) estimated by these parameterization approaches are presented in Figure 7.5. The total cumulative turbulent energy, as well as the daily and 30-minute root mean squared errors (R.M.S.E.), are provided in Table 7.1. The performance of each approach is discussed relative to their ability to match the turbulent heat that is estimated from the measured energy balance residual.

**Case 1:** This approach is essentially the inverse of the results highlighted in Figures 7.1 - 7.2, so given the amount of scatter in the previous figures it is not surprising to see that the estimated fluxes poorly match the measured results. Furthermore, as discussed in the Chapter 5, the measured turbulent energy exchange is much lower than would be

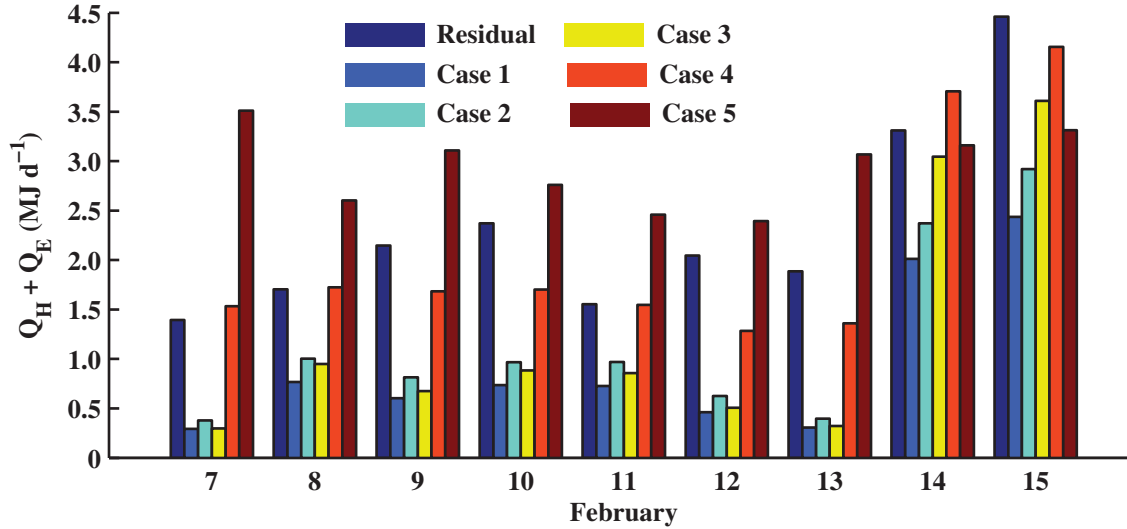


**Figure 7.5:** Cumulative daily turbulent heat fluxes as measured as the energy balance residual and calculated by various bulk transfer parameterization scenarios: (Case 1) Andreas model  $z_{0m} = 2 \times 10^{-4}$ ; (Case 2) Andreas model  $z_{0m} = 1 \times 10^{-3}$ ; (Case 3)  $z_{0m} = 2 \times 10^{-4}$ ,  $C_d C_h^{-1} = 0.65$ ; (Case 4) same as Case 3 with additional windless exchange coefficient =  $2 \text{ W m}^{-2} \text{ K}^{-1}$ ; (Case 5) Kuz'min empirical method.

**Table 7.1:** Performance of bulk transfer parameterization schemes.

	$\sum(Q_H + Q_E)$ (MJ m <sup>-2</sup> )	R.M.S.E (daily) (MJ m <sup>-2</sup> )	R.M.S.E (30-min.) (W m <sup>-2</sup> )
Case 1	8.34	1.44	28.1
Case 2	10.44	1.21	27.1
Case 3	11.15	1.17	26.8
Case 4	18.70	0.45	25.0
Case 5	26.38	1.06	33.3
Measured (residual)	20.87		

required to close the energy balance so consequently flux-gradient parameters based on the measured turbulent fluxes are less than 50% of the energy balance residual.

**Case 2:** The effect of increasing the momentum roughness length by an order of magnitude was minimal. This was primarily related to the prevalent low winds, but was also due to an increase in  $C_d C_h^{-1}$ , thereby canceling some of the effectiveness of increasing  $z_{0m}$ . As illustrated in Figure 7.6, increasing the momentum roughness length also increases the ratio  $C_d C_h^{-1}$  so the effect on turbulent heat transfer is more limited than is first apparent (*i.e.* for rougher flows momentum is transported more effectively than heat). Furthermore, from the perspective of estimating the momentum transfer, there was no justification for increasing the momentum roughness length so rather this approach becomes an indirect attempt to increase the heat transfer coefficient (thereby losing the ability to accurately predict  $u_*$ ). The effectiveness of this strategy relies on knowledge of the heat transfer relationships modeled by the surface renewal theory of Andreas (1987b), which scales the heat and vapour transfer on the Reynolds roughness number. For 14-15 February, this strategy was more effective since the wind speeds were larger.

**Case 3:** Moving away from the Andreas (1987b) theoretical relationship between momentum and heat allows the transfer coefficients to be calibrated individually. In this example, the decreased value for  $C_d C_h^{-1}$  was only shown to be effective during windy conditions (14-15 February). During calm periods, the additional energy added was minimal.

**Case 4:** Adding a windless exchange coefficient of  $2 \text{ W m}^{-2} \text{ K}^{-1}$  had a marked impact on the energy of this dataset because the wind speed was low during the first 6 days considered. As noted in Table 7.1, this option most closely matched the required sensible heat transfer and also had the lowest R.M.S.E. of all of the options demonstrated. Thus, it was an effective way to increase the amount of energy available during low wind periods without unnecessarily modifying the momentum transfer rate.

**Case 5:** The empirical formula of Kuz'min adds the most energy of the options demonstrated. At high wind speeds it was comparable to the other bulk transfer methods, however at lower wind speeds when conditions were stable the model greatly over predicted the available energy since the effects of thermal stratification were not considered.

In most of the demonstrated cases, the energy estimated differed significantly from the residual amount. Given the temporal distribution of the energy balance residual, which was demonstrated in Chapter 5 to correspond to net radiation, and not with the temperature gradient or wind speed, it is not entirely surprising to determine that the bulk transfer cannot be parameterized to match this amount of energy. Some were more effective during

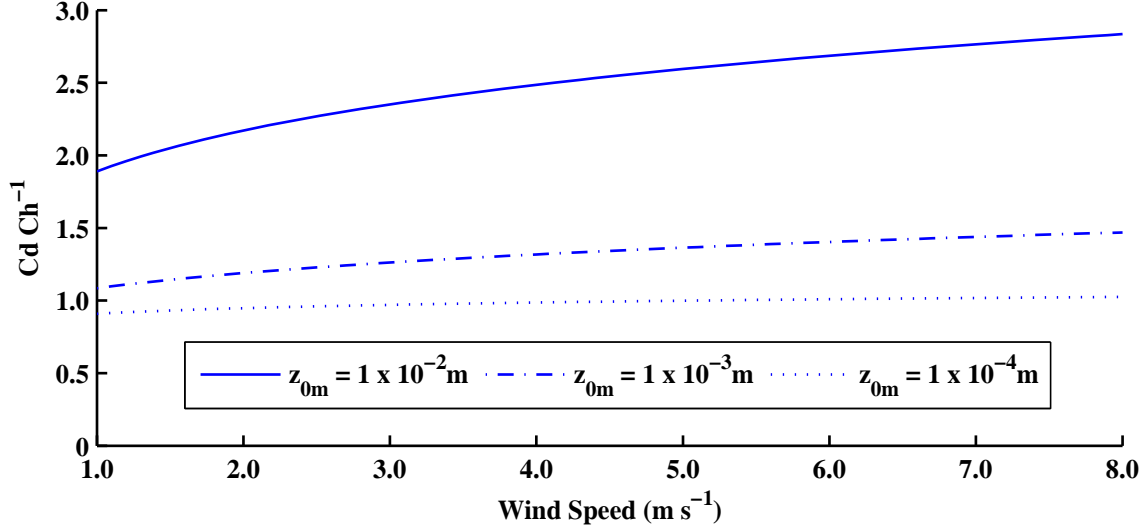


**Figure 7.6:** The ratio of transfer coefficients,  $C_d C_h^{-1}$ , predicted by Andreas (1987b) at increasing wind speeds under neutral conditions for various  $z_{0m}$  values.

calm periods, while others during windy periods. The most successful simulation (Case 4) occurred through a combination of calibrated transfer coefficient, along with the use of a windless exchange coefficient. However, due to the empirical nature of this approach, data from additional sites are required to present any general recommendations for their use. Although the cumulative estimated energy matched the measured energy reasonably well, and the R.M.S.E. of the daily energy transfer was small, the R.M.S.E. for the 30-minute periods was quite large ( $\approx 27 \text{ W m}^{-2}$ ), indicating that the physics of the energy residual are not truly being captured by this effective parameterization scheme.

### 7.2.3 Numerical Snow Modelling

The off-line bulk transfer modelling that was applied in the last section considers the turbulent transfer mechanisms independent of other processes in the energy balance. If the mechanisms are accurately parameterized and the forcing data are free from uncertainty then this approach should yield good estimates of the turbulent transfer. However, when dealing with real data and uncertain processes, a more conservative approach would be to employ a numerical energy balance model that considers all of the energy balance terms and consequently bounds the solution within a framework of energy conservation. To evaluate this, two numerical models are considered. The first model, SNTHERM.89.rev4 (Jordan 1991), is representative of a detailed multi-layer snow physics model. The second model considered, CLASS v.3.4 (Verseghy 1991, 2000), is a land surface scheme that is typically used to provide the surface boundary conditions for numerical weather prediction models or global

**Table 7.2:** Performance of simulated turbulent fluxes.

	$\sum(Q_H + Q_E)$ (MJ m <sup>-2</sup> )	R.M.S.E (daily) (MJ m <sup>-2</sup> )	R.M.S.E (30-min.) (W m <sup>-2</sup> )
SNTHERM-1	17.02	0.49	16.70
SNTHERM-2	13.89	0.81	19.16
CLASS	10.24	1.40	30.37
Measured (residual)	20.87		

circulation models. Accordingly, the physical representation of the snowpack within CLASS is considerably more simple, only considering a single layer. Nonetheless, it is representative of the numerical approach that is used to estimate the effect of snow cover on the atmosphere at large scales.

For this analysis, three simulations are considered: (1) *SNTHERM-1* [ $z_{0m} = 1 \times 10^{-3}$ m]; (2) *SNTHERM-2* [ $z_{0m} = 1 \times 10^{-4}$ m (approximately representative of measured turbulent conditions, and typical of smooth snow surface)]; and (3) *CLASS* [ $z_{0m} = 1 \times 10^{-3}$ m (this parameter is not actually adjustable within the model)].

Figure 7.7 illustrates the partitioning of the simulated energy for each of these 3 cases along with the measured partitioning (assuming that the turbulent fluxes make up the energy balance residual). In order to contrast the modelling approaches with the measurements, the energy balance terms are compared in Figure 7.8. The cumulative flux estimates and the R.M.S.E. values are provided in Table 7.2.

With respect to the SNTHERM simulations, although neither of the runs matched the turbulent energy exactly (Figure 7.8c), the dynamics of the estimated turbulent flux were quite similar to those of the measured energy residual. SNTHERM-1, with the larger  $z_{0m}$  value ( $1 \times 10^{-3}$ m), most closely matched the accumulated energy and had the lowest R.M.S.E.. In comparison to the off-line bulk transfer approach with the same value of  $z_{0m}$  (Case 2), the performance of the full energy balance implementation was much better. This is somewhat surprising, as SNTHERM uses the surface renewal model of Andreas (1987b) which is presumably parameterized in the same manner as Case 2, along with the profile functions of Holtslag and De Bruin (1988) with a windless exchange coefficient of  $1 \text{ W m}^{-2}$ . A time-series comparison between the SNTHERM-1 and the off-line implementation (Case 2) of the bulk transfer approach is given in Figure 7.9. The estimated flux was much larger than predicted by a similar off-line approach because of differences in the surface temperature which the model iteratively solved for. SNTHERM predicted a warmer surface temperature, which resulted in a smaller gradient, and presumably less stable conditions which permitted larger fluxes to occur. Since the version of SNTHERM employed in this study did not output a stability measure as a diagnostic variable this could not be confirmed. The SNTHERM-2

simulation, with a  $z_{0m}$  value that is more suitable, for the smooth snow surface predicted turbulent fluxes that were too small.

With respect to snow melt modelling, the surface fluxes are estimated in order to quantify the change in internal energy so that the occurrence of melt can be predicted. In that regard, the two SNTHERM simulations were remarkably similar. The change in internal energy predicted by SNTHERM-1 was  $-2.6 \text{ MJ m}^{-2}$ , whereas SNTHERM-2 was  $-2.4 \text{ MJ m}^{-2}$ , as compared to the measured change of  $-1.5 \text{ MJ m}^{-2}$ . Most of the discrepancy between the measured and modeled occurred on a few specific days (Figure 7.8). Although the turbulent heat fluxes were slightly larger for SNTHERM-1, this resulted in higher surface temperatures, and larger thermal radiation losses which resulted in a similar internal energy change within the snow. The largest difference between the SNTHERM simulations and the measured fluxes occurred with the ground heat flux, which was predicted to be much larger than measured.

The CLASS model, having a simple structure and rigid parameterization did not compare well to the measured energy fluxes. The turbulent fluxes were predicted to be much smaller than the energy residual and the SNTHERM simulations. The additional energy was made up by extra incoming shortwave radiation (due to an overactive albedo decay routine) and significantly larger than measured ground heat flux. As a result, the internal energy changes differed substantially from the measured case, and were occasionally of opposite sign (Figure 7.8d).

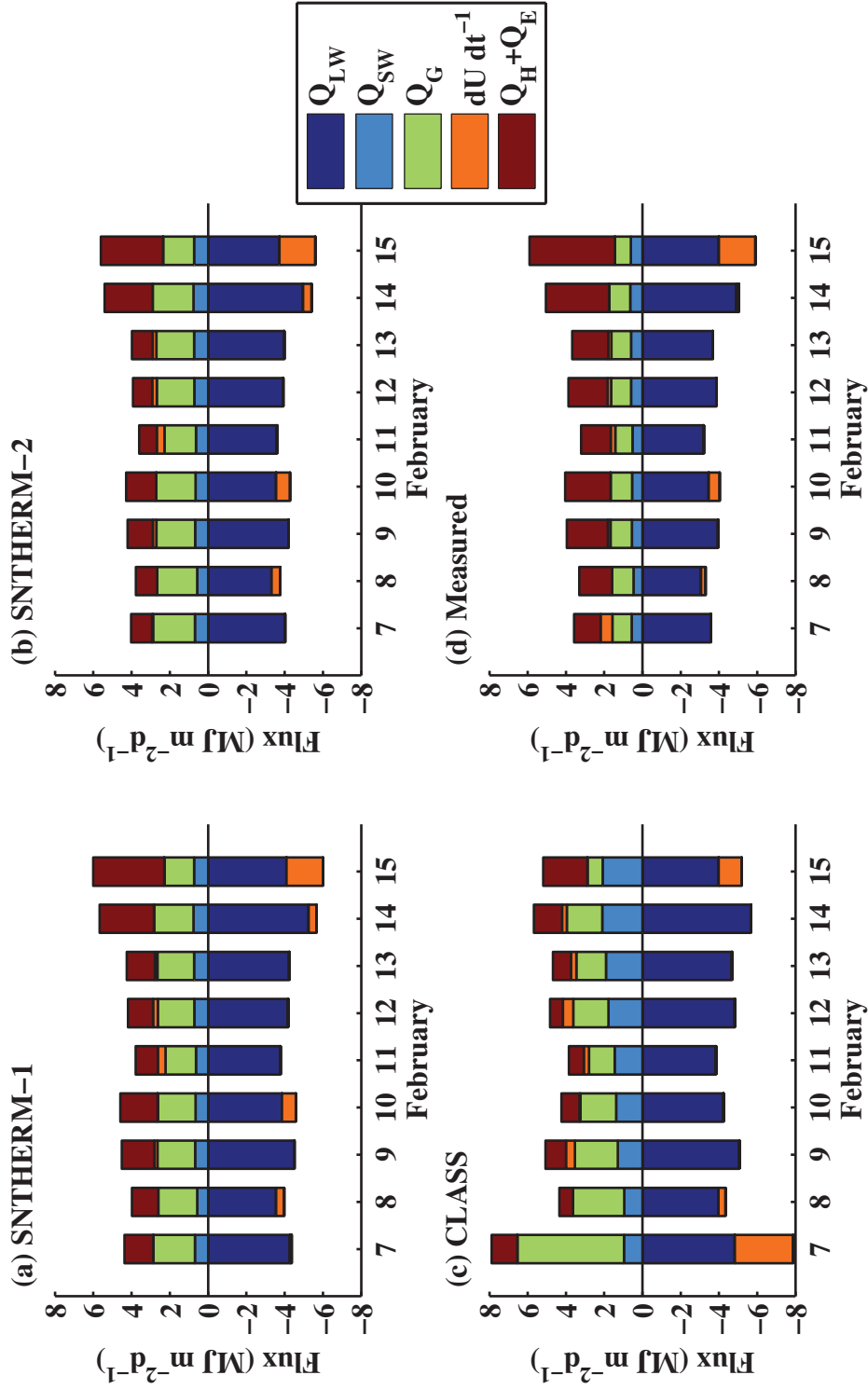


**Figure 7.7:** KF numerical modelling - energy partitioning. Note that  $Q_H + Q_E$  for the measured case (d) is estimated from the energy balance residual.

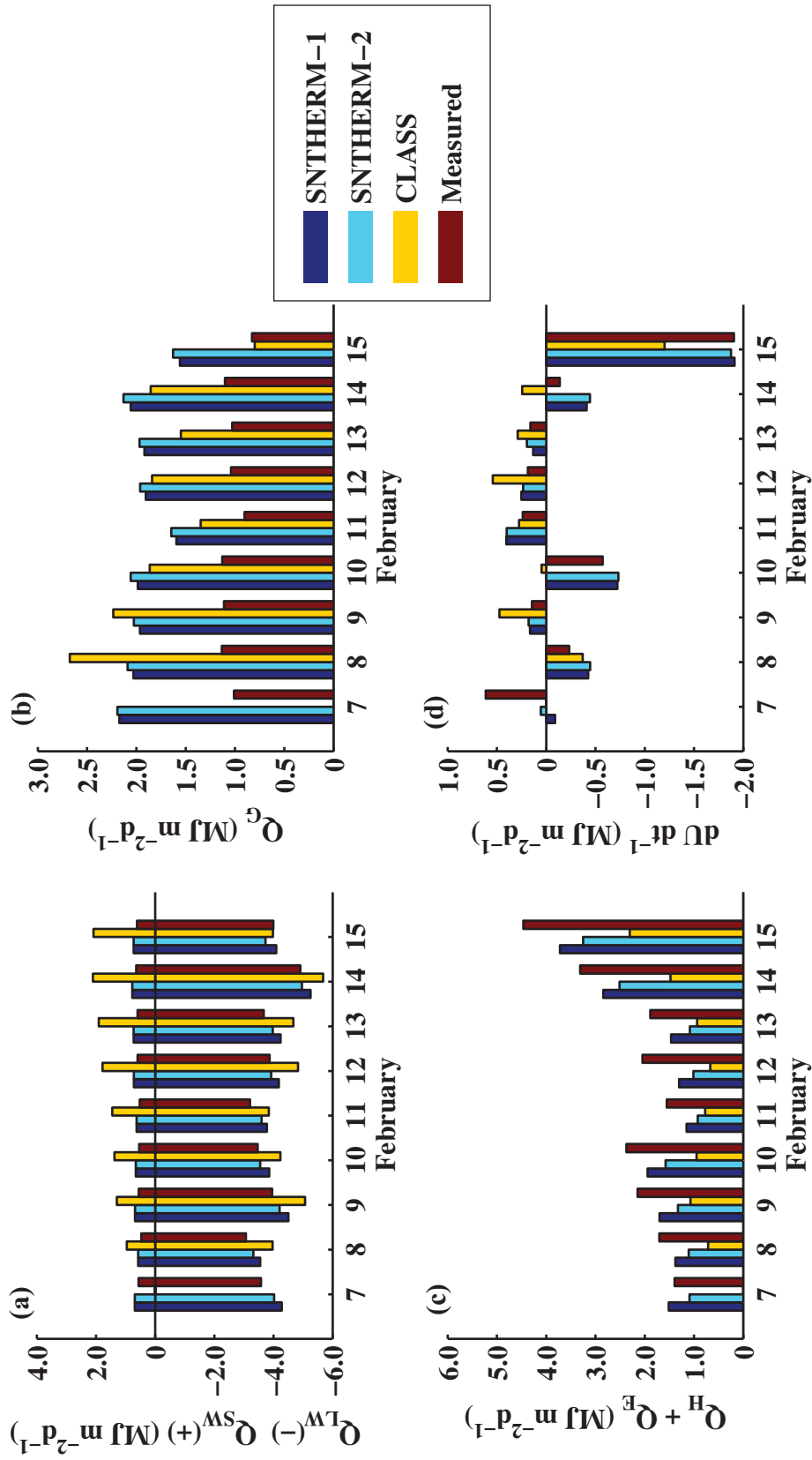


**Figure 7.8:** KF numerical modelling - energy flux comparison. Note that  $Q_H + Q_E$  for the measured case (d) is estimated from the energy balance residual.

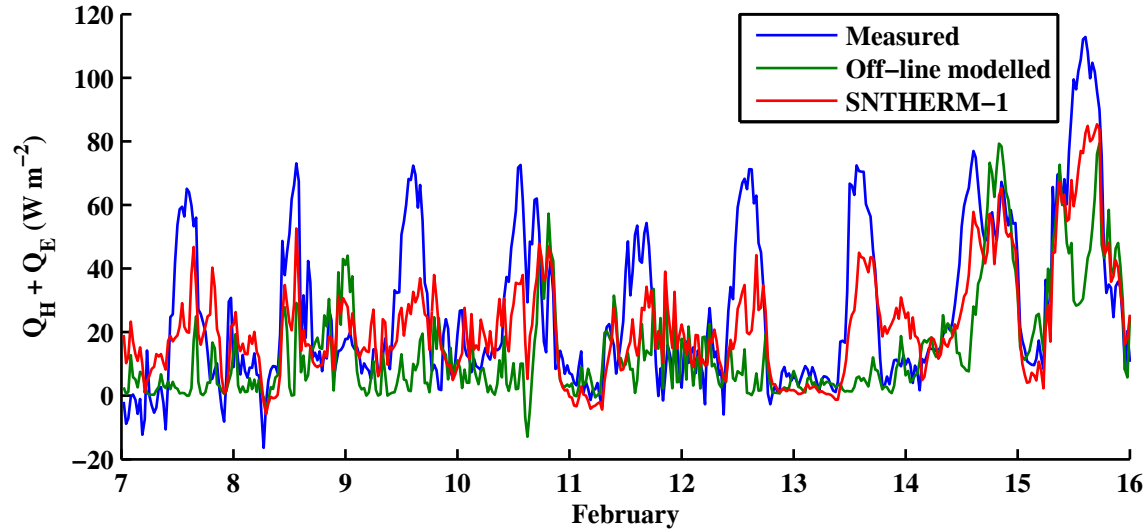


**Figure 7.9:** Comparison of off-line modelling approach (surface renewal model;  $z_{0m} = 1.0 \times 10^{-3}$ ) with SNTHERM-1.

## 7.3 Mountain Valley (Hay Meadow)

In the two mountain valley sites (HM and ML) discussed in Chapter 4, it was discovered that an equilibrium boundary layer did not exist at these sites. The prevalent wind gusts, which were described as being non-local in origin, bring additional turbulent energy into the surface layer, which then must be dissipated locally. As a result, the measured momentum flux was much larger than would be predicted from the local wind speed gradient. This has important consequences for modeling, since the heat and vapour flux parameterizations are usually scaled upon  $u^*$ . In this section, parameterization strategies to deal with the non-local turbulence generation mechanisms are considered.

### 7.3.1 Measured Turbulent Exchange Coefficients

The drag coefficients,  $C_d$ , inferred from sonic anemometer data from 2005 and 2006 are presented in Figure 7.10. Here they are compared to the theoretical variation with stability for a  $z_{0m} = 1.7 \times 10^{-2}$  m, which was reported in §4.3.1. Although the values measured during 2005 appear to be larger (i.e. rougher flow), the entire group of values is grouped about the theoretical curve. Similar to previous discussions of turbulence processes at HM, there is a considerable amount of variability within the measured data (especially considering the log-log presentation in Figure 7.10).

The inferred heat and vapour transfer coefficients are presented in Figure 7.11. Again there is considerable scatter, however the data points are not described by the theoretical

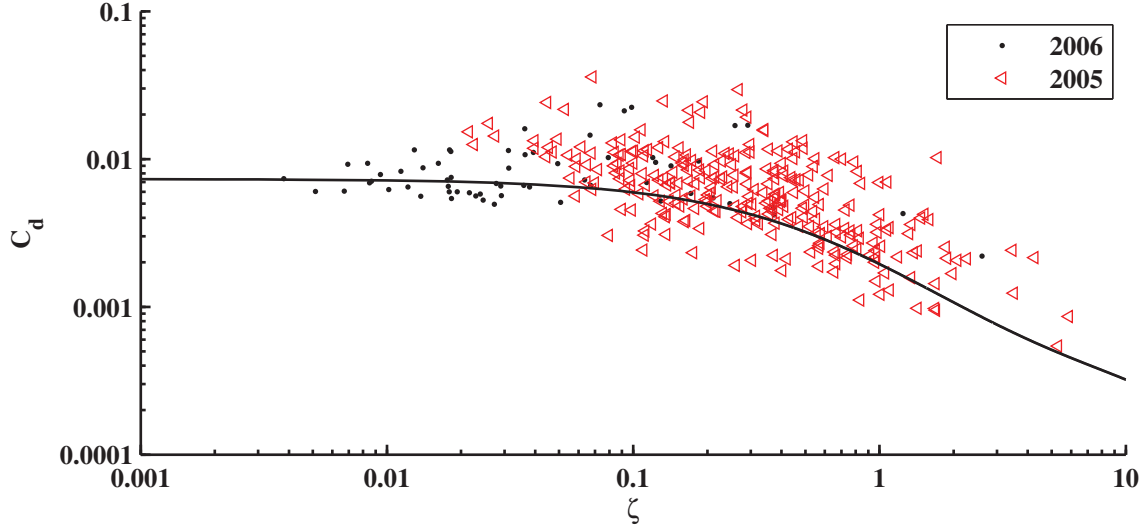


**Figure 7.10:** HM bulk transfer drag coefficient  $C_d$ , as it varies with stability. The solid line is the drag coefficient predicted by the model of Andreas (1987b) for  $z_{0m} = 1.7 \times 10^{-2}$  m.

relationship (which was modeled using the surface renewal theory of Andreas (1987b)). There does not appear to be any organization of the values with increasing stability. Also, the heat and vapour coefficients are much smaller than the  $C_d$  values in Figure 7.10, which reaffirms that the wind gusts are more effective at transporting momentum than heat or vapour. This is explicitly presented in Figure 7.12 where the ratios  $C_d C_h^{-1}$  and  $C_d C_v^{-1}$  are seen to be much larger than 1 (particularly for near neutral conditions). From Figures 7.11-7.12 it appears that, on average,  $C_v$  is slightly larger than  $C_h$ .

### 7.3.2 Strategies for Parameterization

In this environment, the primary challenge to estimating the turbulent fluxes using a bulk transfer approach is that the turbulence does not scale with local parameters. To demonstrate some different parameterization options, three strategies are demonstrated. The results of the predictions for  $Q_H$  and  $Q_E$  compared to measured values (eddy covariance) collected from 24 February through 3 March 2005 are provided in Figures 7.13-7.14. Each option is discussed separately below.

**Option a:** [ $z_{0m} = 1.7 \times 10^{-2}$ ;  $C_d C_h^{-1}$  modeled;  $C_d C_v^{-1}$  modeled] Figures 7.13a and 7.14a demonstrate the use of the Andreas (1987b) model with a fixed  $z_{0m} = 1.7 \times 10^{-2}$ , which was calibrated to the measured momentum flux. For this method  $Q_H$  values were over predicted, but  $Q_E$  values were actually predicted fairly well. The modeled ratio of  $C_d C_h^{-1} = C_d C_v^{-1}$  for this value of  $z_{0m}$  was around 2 (as described in Figure 7.6).

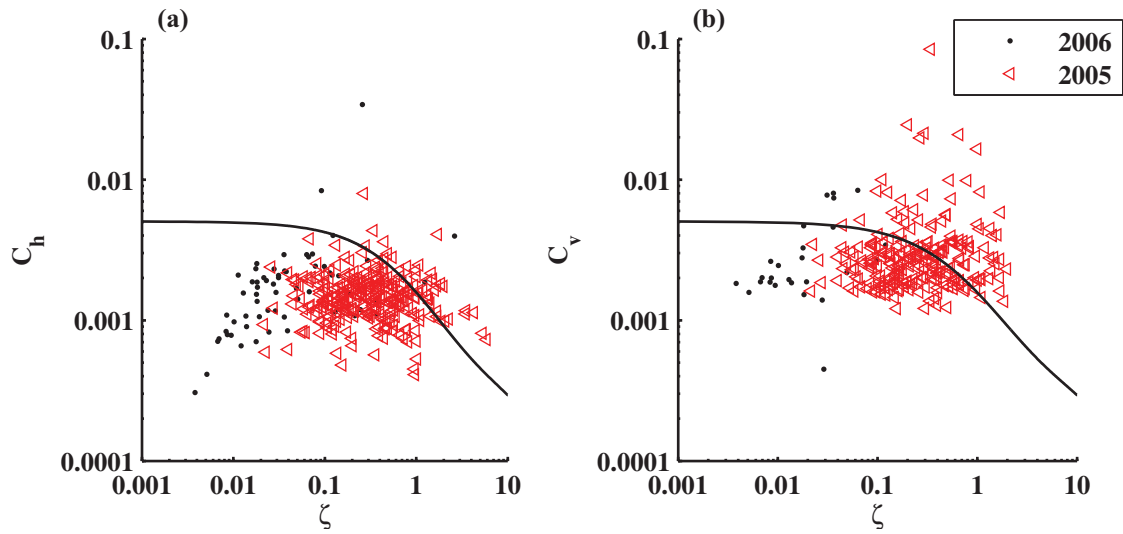


Figure 7.11: HM bulk transfer (a) heat coefficient ( $C_h$ ), and (b) vapour transfer coefficient ( $C_v$ ), as they vary with stability.

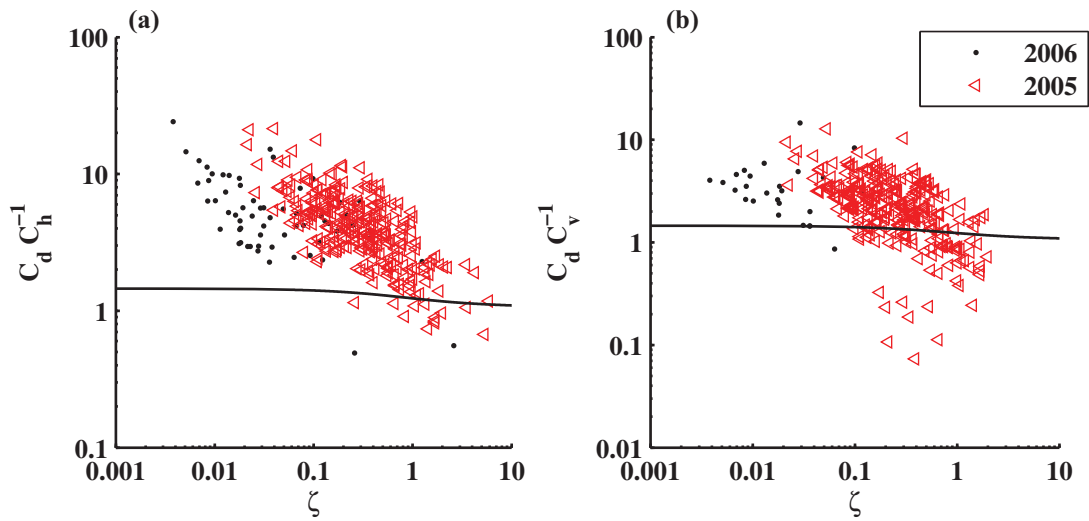
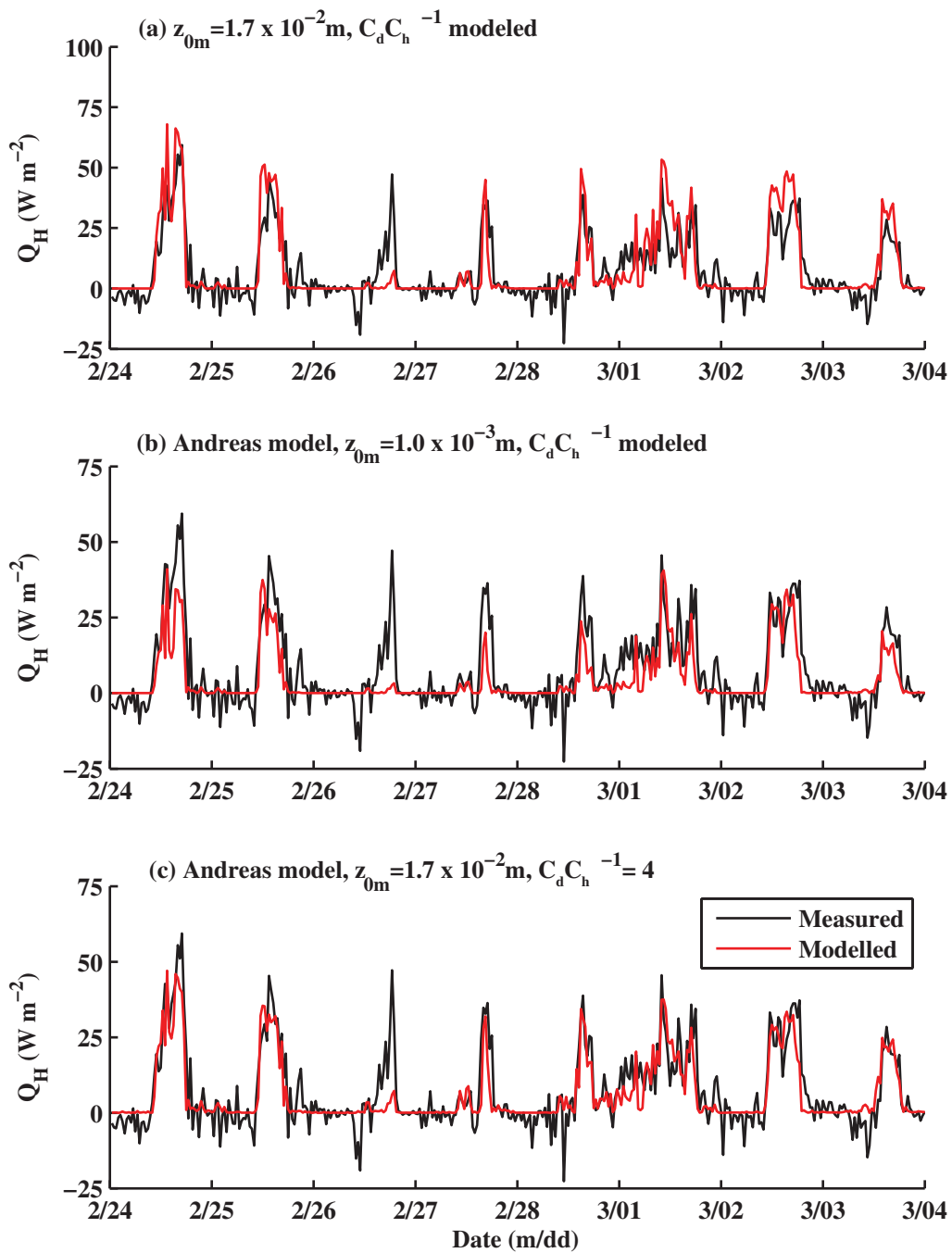


Figure 7.12: HM bulk transfer coefficient ratios as they vary with stability.

**Option b:** [ $z_{0m} = 1.0 \times 10^{-3}$ ;  $C_d C_h^{-1}$  modeled;  $C_d C_v^{-1}$  modeled] Without prior knowledge of the effect of the wind gusts, it is unlikely that one would select such a large value for  $z_{0m}$  for a smooth snow surface. To demonstrate the effect of a more typical value, the Andreas (1987b) model was run with a value of  $z_{0m} = 1.0 \times 10^{-3}$ . Figures 7.13b and 7.14b show that the magnitude of  $Q_H$  is approximately correct, but  $Q_E$  is under-predicted. In this case it is entirely coincidental that the heat transfer was accurately predicted.

**Option c:** [ $z_{0m} = 1.7 \times 10^{-2}$ ;  $C_d C_h^{-1} = 4$ ;  $C_d C_v^{-1} = 2$ ] From the two examples just presented, it is apparent that the temporal dynamics of the heat and vapour fluxes were captured by the bulk transfer approach, however the magnitude was not well predicted by the surface renewal method. By specifying a fixed value of  $z_{0m} = 1.7 \times 10^{-2}$  and a fixed value of  $C_d C_h^{-1} = 4$  and  $C_d C_v^{-1} = 2$  (Figures 7.13c and 7.14c) it is demonstrated that the bulk transfer method can be made to work in this environment if prior information regarding the heat transfer processes is available.

In Figure 7.15 the turbulent sensible and latent heat fluxes are added together to illustrate that, under these conditions, the net contribution from these heat fluxes is often small due to their opposing sign. Not surprisingly the model with the calibrated heat transfer coefficients (option c) most closely matches the measured net turbulent heat flux. Owing to the inherent variability in the measured fluxes, particularly at small values, the R.M.S.E. of modeled vs. measured was not calculated. However, the cumulative turbulent heat flux as modeled and measured is provided in Table 7.3, where it can be seen that, although option c was the most similar to the measured flux in terms of the magnitude and timing, when summed over the measurement period all of parameterization strategies resulted in a total energy transfer that was of opposite sign to the measured. In any case, both the modeled and measured fluxes were very small, and it would seem that the turbulent fluxes contribute little to the snow energy balance. However, when compared to the cumulative radiative fluxes which were  $31.7 \text{ MJ m}^{-2}$  for  $Q_{S^*}$  and  $-46.4 \text{ MJ m}^{-2}$  for  $Q_{L^*}$ , resulting in a  $Q^*$  transfer of  $-14.7 \text{ MJ m}^{-2}$  as recorded during the period where a 10 cm snowpack was ablated leads to suspicion that the turbulent fluxes are being grossly under-measured, as noted at KF (reported in Chapter 5). Unfortunately, the internal energy of the snowpack was not measured, so it is not possible to examine the energy balance closure.



**Figure 7.13:** Estimation of sensible heat fluxes using bulk transfer formulae, Hay Meadow 2005.

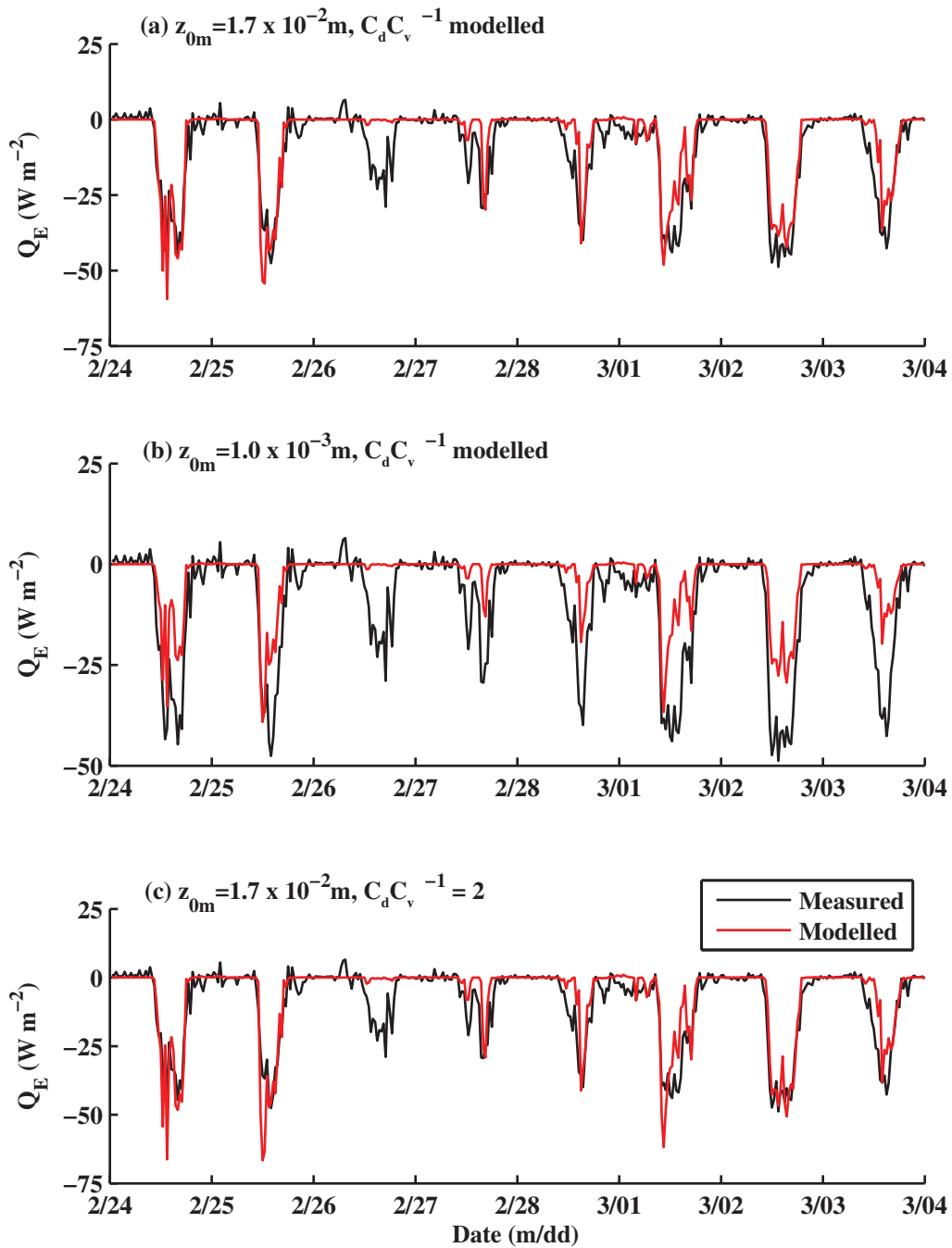


**Figure 7.14:** Estimation of latent heat fluxes using bulk transfer formulae, Hay Meadow 2005.

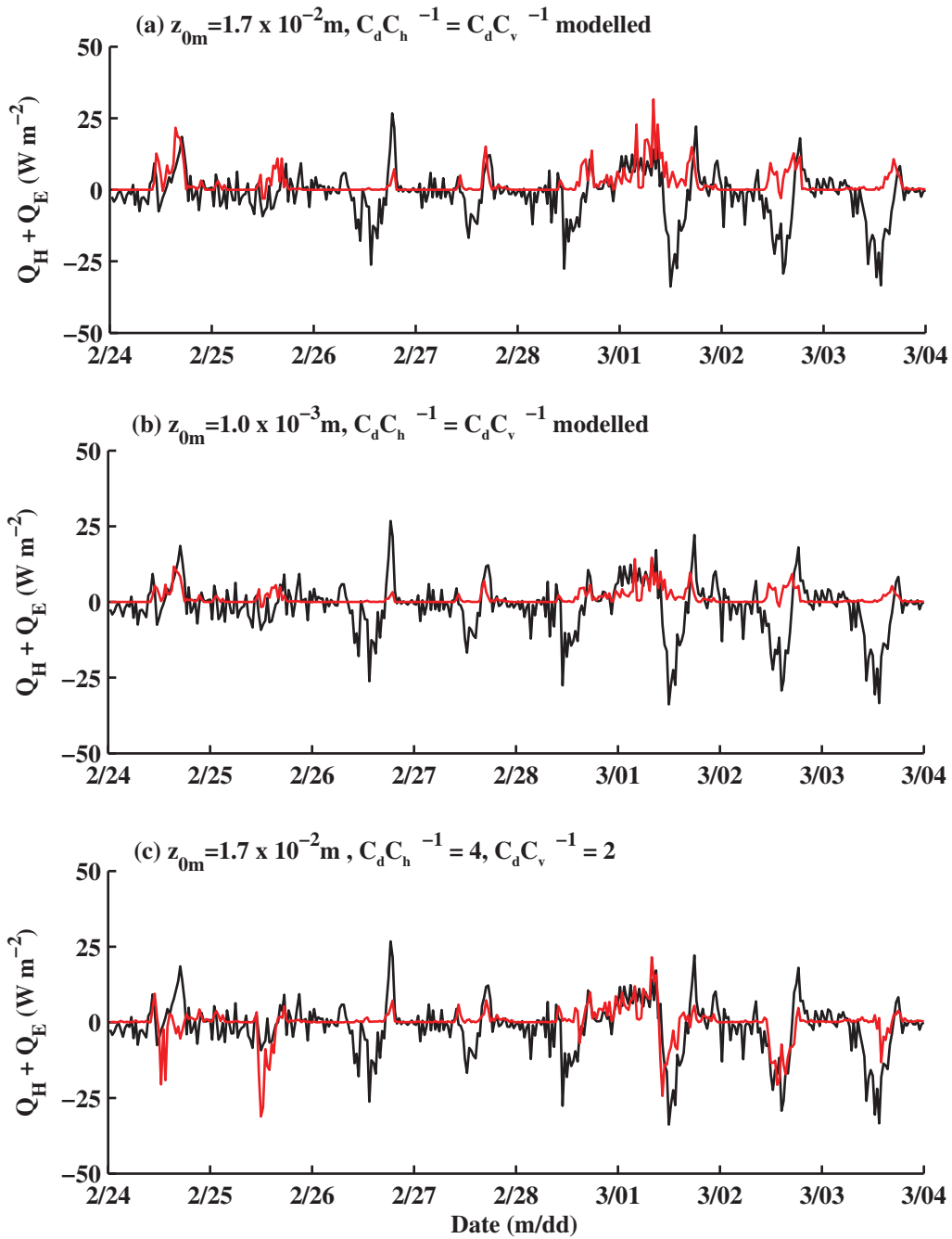


Figure 7.15: Sum of the estimated turbulent heat fluxes, Hay Meadow 2005.

**Table 7.3:** Accumulated turbulent fluxes (Hay Meadow 2005).

	$\sum(Q_H)$ (MJ m <sup>-2</sup> )	$\sum(Q_E)$ (MJ m <sup>-2</sup> )	$\sum(Q_H + Q_E)$ (MJ m <sup>-2</sup> )
Option (a)	5.7	-4.1	1.6
Option (b)	3.1	-2.3	0.8
Option (c)	4.4	-4.5	0.1
Measured	4.9	-6.0	-1.1

## 7.4 Summary and Conclusions

### 7.4.1 Summary and Recommendations for the Prairie Environment

At KF, the mid-winter conditions presented significant difficulties for measurement and modelling of the turbulent fluxes. Low wind speeds often resulted in highly stable conditions with very little turbulent mixing. At the same time, radiation fluxes were quite large and were consistently directed toward the atmosphere. Through examination of the changes in the internal energy status of the snowpack and the other surface fluxes it was confirmed that the heat flux from the atmosphere was being under-measured by the eddy covariance technique. Accordingly, various bulk transfer parameterization schemes were tested for their ability to simulate a transfer of energy from the atmosphere that was consistent with the energy required to close the energy balance. The best results were achieved when the bulk transfer equation had the most free parameters. That is, when site specific values could be set for the momentum transfer coefficient,  $C_d$  (set via appropriate selection of  $z_{0m}$ ), the heat transfer coefficient,  $C_h$  (set by specifying the ratio for  $C_d C_h^{-1}$ ), and also a windless exchange coefficient. The transfer coefficients specified by the commonly used model of Andreas (1987b) resulted in fluxes that were too small to adequately match the required energy.

Two numerical snow models (SNTHERM and CLASS) were also tested. Overall, the performance of the bulk transfer approach implemented within a complete energy balance model was better than similar techniques used in off-line mode. This was attributed to the inherent coupling between the turbulent fluxes and the outgoing thermal radiation via the surface temperature which is iteratively solved. When small turbulent heat fluxes were predicted by the model, a lower surface temperature resulted, which reduced the outgoing radiation loss from the snowpack. In this manner, estimating the fluxes within a full energy balance model was demonstrated to be a much more conservative approach.

In all of the estimation techniques examined, it was apparent that these are simply effective parameterization approaches. The 30-minute fluxes exhibited large R.M.S.E. (when

compared to the measured energy residual) which suggest that the true physics of the energy exchange is not being captured. Thus, further development of the ideas presented in the previous chapter is warranted. Estimation techniques would greatly benefit from a more thorough understanding of energy exchange mechanisms during calm mid-winter periods, and also from a recognition of the role that the porous nature of the snowpack has on heat exchange.

### 7.4.2 Recommendations for Mountain Valleys

The mountain valley in which the HM site is located is characterized by calm periods interspersed with large wind gusts, which have an overbearing effect on the turbulence processes. Accordingly, difficulties arise when attempting to relate the surface fluxes to the wind gusts which do not scale upon locally measured variables. The turbulent processes as measured at the HM site similarly requires that the surface renewal approach is abandoned in favour of site-specific transfer coefficients. Given the amount of scatter present in Figure 7.11 it is not anticipated that the demonstrated values of  $CdCh^{-1} = 4$  and  $CdCv^{-1} = 2$  will become universal values in this type of environment. However, considering the uncertainty involved in the measurements, site-specific parameters will have to be employed until a theory relating the fluxes to the large scale boundary layer processes is developed. Given the difficulties in closing the energy balance that were reported in Chapter 5, there are certainly questions if similar processes affect the turbulence measures in this site as well. It was not possible to evaluate the energy balance closure since the internal energy of the snowpack was not measured.

# CHAPTER 8

## SUMMARY AND CONCLUSIONS

In order to understand the processes responsible for turbulent heat and mass fluxes over snow surfaces in complex mountain terrain, eddy covariance measurements were made in two mountain valleys in Kananaskis, AB, which were contrasted with data collected on a broad alpine ridge, near Whitehorse, YT, and also those collected at a flat homogeneous prairie site near Saskatoon, SK. The prairie site was used as an experimental control, since its characteristics were ideally suited for micro-meteorological measurements. At this site, measurements of all of the terms in the snow energy balance were used to verify the quality of the eddy covariance measurements.

The mountain valley sites (HM and ML) were characterized as having low wind speeds with predominant gusts. As a consequence, the turbulence characteristics varied significantly from the other sites considered. The wind gusts, which are presumed to be vortical motions shed at the surrounding ridges as the flow separates, were responsible for advecting turbulent energy into the surface layer. As a result, the momentum flux measured with the sonic anemometer was greater than that predicted from the slope of the wind speed profile under neutral conditions. The additional mixing provided by the wind gusts increased the transfer rates of heat or water vapour, although to a lesser extent than the momentum flux. Multi-resolution flux decomposition (Howell and Mahrt 1997) was used to evaluate the contribution of these large-scale motions, revealing that approximately 25% of the momentum flux was generated at scales larger than the turbulent gap scale. Since the gusts have a non-local origin, the resulting turbulence was not well described by the local parameter set of M-O similarity theory. Various effective parameterization schemes for the bulk transfer technique were evaluated to determine what modifications to this first order approach would be necessary for this environment. It was determined that the surface renewal model of Andreas (1987b) was not appropriate for these conditions, and that the modeled fluxes were most similar to the measured fluxes when  $z_{0m}$  and  $z_{0T}$  were set individually using site-specific parameters.

The alpine mountain ridge site (WCA) was included in this study in order to contrast the

turbulence processes that were observed at the valley sites. During the campaign, moderate wind speeds ( $5\text{-}10\text{ m s}^{-1}$ ) were frequently observed, and many of the turbulence characteristics were similar to a flat site. The gusty conditions that were effective flux generating mechanisms at the valley sites were not a factor at the ridge top. The flow was strongly affected by the presence of the ridge, and the resulting boundary layer on the top of the ridge was very thin. The momentum and heat fluxes often differed between the two measurement heights (1.63 m and 3.26 m), and the local temperature gradient was often of different direction than the sensible heat flux. For this reason, it was believed that the fluxes measured were above the surface layer. Efforts to validate the bulk transfer technique at this site were not undertaken.

At the prairie site (KF), the turbulence characteristics appeared to be typical of smooth sites when wind speeds were steady. In order to confirm the accuracy of the turbulent flux measurements, all of the components of the snow energy balance were directly measured. It was observed that the turbulent fluxes measured by the eddy covariance technique were much too small (usually  $< 30\text{ W m}^{-2}$ ) to effectively close the energy balance. The noted imbalance was larger than could be explained by experimental errors alone. It was argued that the transfer of sensible heat to the snow surface was being under-measured. Throughout the period of interest (February) the thermal radiation balance was predominantly negative. However, the snow temperatures were not observed to cool in response to this persistent loss of energy. Rather, the snowpack exhibited a degree of coupling to the atmosphere, where the near surface snowpack temperatures were closely correlated with the above-snow air temperatures. The exact cause of the energy imbalance is not known. There was some indication that the boundary layer became periodically decoupled from the surface. The friction velocity measured by the sonic anemometer was closely matched by that estimated by the wind speed gradient when the heat flux was directed towards the atmosphere and the environment was mildly unstable. However, when the heat flux was directed towards the snowpack, the friction velocity measured by the sonic anemometers was less than that suggested by the wind speed gradient. It was hypothesized that the boundary layer could become decoupled if the rate of turbulent heat transfer from the atmosphere was insufficient to meet the demand imposed by radiation loss and a near surface stable layer could develop.

In order to explain the degree of coupling that necessarily must occur between the thermal radiation flux and the sensible heat flux during cold mid-winter periods, a conceptual hypothesis was developed. Since snow is a permeable medium, when air flows over the snowpack, a slip velocity occurs at the air-snow interface, potentially exposing a very large surface area for heat exchange. It is hypothesized that the effective area of the interfacial region which is experiencing thermal non-equilibrium conditions scales with the long-wave radiation balance. Since the resistance to radiative heat transfer to the atmosphere, which occurs

from the outer-most surfaces of exposed snow crystals, is much lower than the resistance of heat conduction through the ice matrix to supply the necessary amount of energy, a micro-temperature gradient results and the effective area for heat exchange grows. In this manner, the long-wave radiation flux can be coupled with the sensible heat flux, not only through changes in the bulk temperature gradient, but more importantly through an increase in the effective surface area over which heat can be exchanged. Further development of these ideas through numerical modeling and detailed observations are recommended for future study.

In order to test the ability of the parameterization schemes to match the amount of energy required to close the energy-balance at the prairie location, the bulk transfer technique was implemented ‘off-line’, and also within two numerical snow models, SNTHERM and CLASS. It was found that the appropriate amount of energy transfer could be simulated if  $z_{0m}$  and  $z_{0T}$  were set individually and a windless exchange coefficient was included. The implementation of the bulk transfer routine with the full energy balance model SNTHERM produced the best results with minimal adjustment of parameters.

The most significant findings of this thesis are:

1. Within the mountain valley sites considered, the turbulent fluxes were significantly influenced by the inherently gusty conditions. As a result, the bulk transfer approach using the existing parameterizations for snow were found to be unsuitable. However, by using environment-specific transfer coefficient relationships, such as increasing the roughness length for momentum to account for topographically generated turbulence, while reducing the ratio between the momentum and heat transfer coefficients, the turbulent fluxes can be adequately represented in snow melt models.
2. Measurement of all of the energy balance terms of a homogeneous snowpack at a level prairie site revealed that the actual sensible heat transfer to the snowpack from the atmosphere was grossly under-measured by the eddy covariance technique. The exact cause of the imbalance could not be determined exactly, but was perhaps related to the low degree of turbulent mixing that occurs over smooth snow surfaces. Future study of this problem is warranted.
3. During cold mid-winter periods, the sensible heat flux (measured as the residual of the energy balance) was observed to offset long-wave radiation losses from snow. In order to improve efforts of estimating sensible heat transfer, a conceptual hypothesis was developed in which the effective area for heat transfer scales upon the thermal radiation balance, and enables penetrative convective heat transfer to play a dominant role in the surface energy balance. It is recommended that this model be further developed through numerical analysis and detailed micro-structural measurements.

## BIBLIOGRAPHY

- Acton, D. F. and Ellis, J. G.: 1978, The soils of the Saskatoon map area 73-B Saskatchewan, *Technical Report Publication S4*, Saskatchewan Institute of Pedology.
- Alazmi, B. and Vafai, K.: 2001, Analysis of fluid flow and heat transfer interfacial conditions between a porous medium and a fluid layer, *International Journal of Heat and Mass Transfer* **44**, 1735–1749.
- Albert, M. and Krajewski, G.: 1998, A fast, physically based point snowmelt model for use in distributed applications, *Hydrological Processes* **12**, 1809–1824.
- Albert, M. R.: 1993, Some numerical experiments on firn ventilation with heat transfer, *Annals of Glaciology* **18**, 161–165.
- Albert, M. R.: 1996, Modeling heat, mass, and species transport in polar firn, *Annals of Glaciology* **23**, 138–143.
- Albert, M. R.: 2002, Effects of snow and firn ventilation on sublimation rates, *Annals of Glaciology* **35**, 52–55.
- Albert, M. R. and Hardy, J. P.: 1995, Ventilation experiments in a seasonal snow cover, in K. A. Tonneson, M. W. Williams and M. Tranter (eds), *Biogeochemistry of Seasonally Snow-Covered Catchments*, IAHS Publ. no, 228, IAHS, pp. 41–49.
- Albert, M. R. and Hawley, R. L.: 2002, Seasonal changes in snow surface roughness characteristics at Summit, Greenland: implications for snow and firn ventilation, *Annals of Glaciology* **35**, 510–514.
- Albert, M. R. and McGilvary, W. R.: 1992, Thermal effects due to air flow and vapour transport in dry snow, *Journal of Glaciology* **38**(129), 273–281.
- Albert, M. R. and Schultz, E. F.: 2002, Snow and firn properties and air-snow transport processes at Summit, Greenland, *Atmospheric Environment* **36**, 2789–2797.
- Anderson, D. E.: 1968, Development and testing of snowpack energy balance equations, *Water Resources Research* **4**(1), 19–37.

- Andreas, E. L.: 1987a, Spectral measurements in a disturbed boundary layer over snow, *Journal of the Atmospheric Sciences* **44**(15), 1912–1939.
- Andreas, E. L.: 1987b, A theory for the scalar roughness and the scalar transfer coefficients over snow and sea ice, *Boundary-Layer Meteorology* **38**, 159–184.
- Andreas, E. L.: 1989, Comments on “A physical bound on the Bowen ratio”, *Journal of Applied Meteorology* **28**, 1252–1254.
- Andreas, E. L.: 2002, Parameterizing scalar transfer over snow and ice: a review, *Journal of Hydrometeorology* **3**, 417–432.
- Andreas, E. L. and Jordan, R. E.: 2004, Simulations of snow, ice, and near-surface atmospheric processes on Ice Station Weddell, *Journal of Hydrometeorology* **5**, 611–624.
- Andreas, E. L., Jordan, R. E. and Makshtas, A. P.: 2005, Parameterizing turbulent exchange over sea ice: the Ice Station Waddell results, *Boundary-Layer Meteorology* **114**, 439–460.
- Arck, M. and Scherer, D.: 2002, Problems in the determination of sensible heat flux over snow, *Geografiska Annaler: Series A, Physical Geography* **84**(3-4), 157–169.
- Armstrong, R. and Brown, R.: 2008, Introduction, in R. Armstrong and E. Brun (eds), *Snow and Climate: Physical Processes, Surface Energy Exchange and Modeling*, Cambridge University Press, pp. 1–11.
- Arons, E. M. and Colbeck, S. C.: 1998, Effective medium approximation for the conductivity of sensible heat in dry snow, *International Journal of Heat and Mass Transfer* **41**(17), 2653–2666.
- Aubinet, M., Grelle, A., Ibrom, A., Rannik, U., Moncrieff, J., Foken, T., Kowalski, A. S., Martin, P. H., Berbigier, P., Bernhofer, C., Clement, R., Elbers, J., Granier, A., Grünwald, T., Morgenstern, K., Pilegaard, K., Rebmann, C., Snijders, W., Valentini, R. and Vesala, T.: 2000, Estimates of the Annual net carbon and water exchange of forests: The EUROFLUX methodology, *Advances in Ecological Research* **30**, 113–175.
- Barr, A. G., Morgenstern, K., Black, T. A., McCaughey, J. H. and Nesic, Z.: 2006, Surface energy balance closure by the eddy-covariance method above three boreal forest stands and implications for the measurement of CO<sub>2</sub> flux, *Agricultural and Forest Meteorology* **140**, 322–337.
- Barry, R.: 2002, The role of snow and ice in the global climate system: a review, *Polar Geography* **26**(3), 235–246.

- Bartelt, P., Buser, O. and Sokratov, S. A.: 2004, A nonequilibrium treatment of heat and mass transfer in snowcovers, *Cold Regions Science and Technology* **39**, 219–242.
- Bartelt, P. and Lehning, M.: 2002, A physical SNOWPACK model for the Swiss avalanche warning Part I: numerical model, *Cold Regions Science and Technology* **35**, 123–145.
- Beavers, G. S. and Joseph, D. D.: 1967, Boundary conditions at a naturally permeable wall, *Journal of Fluid Mechanics* **30**(1), 197–207.
- Beljaars, A. C. M.: 1987, On the memory of wind standard deviation for upstream roughness, *Boundary-Layer Meteorology* **38**, 95–101.
- Bengtsson, L.: 1980, Evaporation from a snow cover: Review and discussion of measurements, *Nordic Hydrology* **11**, 221–234.
- Bergen, J. D.: 1980, A slip-velocity hypothesis applied to hydraulically smooth wind flow over a snow cover, *Journal of Glaciology* **26**(94), 447–452.
- Berger, R. H.: 1979, Snowpack optical properties in the infrared, *Technical Report 79-11*, CRREL.
- Bernier, P. Y. and Swanson, R. H.: 1993, The influence of opening size on snow evaporation in the forests of the Alberta Foothills, *Canadian Journal of Forest Research* **23**, 239–244.
- Bilger, R. W. and Atkinson, M. J.: 1992, Anomalous mass transfer of phosphate on coral reef flats, *Limnology and Oceanography* **37**(2), 261–272.
- Bintanja, R.: 1995, The local surface energy balance of the Ecology Glacier, King George Island, Antarctica: measurements and modelling, *Antarctic Science* **7**(3), 315–325.
- Bintanja, R. and van den Broeke, M. R.: 1995a, Momentum and scalar transfer coefficients over aerodynamically smooth Antarctic surfaces, *Boundary-Layer Meteorology* **74**, 89–111.
- Bintanja, R. and van den Broeke, M. R.: 1995b, The surface energy balance of Antarctic snow and blue ice, *Journal of Applied Meteorology* **34**, 902–926.
- Bougeault, P., Binder, P., Buzzi, A., Dirks, R., Houze, R., Kuettner, J., Smith, R. B., Steinacker, R. and Volkert, H.: 2001, The MAP special observing period, *Bulletin of the American Meteorological Society* **82**, 433–462.
- Box, J. E. and Steffen, K.: 2001, Sublimation on the Greenland ice sheet from automated weather station observations, *Journal of Geophysical Research* **106**(D24), 33965–33981.

- Bradshaw, P.: 1967, 'Inactive' motion and pressure fluctuations in turbulent boundary layers, *Journal of Fluid Mechanics* **30**(2), 241–258.
- Breugem, W. P., Boersma, B. J. and Uittenbogaard, R. E.: 2006, The influence of wall permeability on turbulent channel flow, *Journal of Fluid Mechanics* **562**, 35–72.
- Brown, R., Bartlett, P., MacKay, M. and Verseghy, D.: 2006, Evaluation of snow cover in CLASS for SnowMIP, *ATMOSPHERE-OCEAN* **44**(3), 223–238.
- Brown, T. and Pomeroy, J. W.: 1989, A blowing snow particle detector, *Cold Regions Science and Technology* **16**(2), 167–174.
- Brun, E., Martin, E., Simon, V., Gendre, C. and Coleau, C.: 1989, An energy and mass balance model of snow cover suitable for operational avalanche forecasting, *Journal of Glaciology* **35**(121), 333–342.
- Brutsaert, W.: 1975a, On a derivable formula for long-wave radiation from clear skies, *Water Resources Research* **11**(5), 742–744.
- Brutsaert, W.: 1975b, A theory for local evaporation (or heat transfer) from rough and smooth surfaces at ground level, *Water Resources Research* **11**(4), 543–550.
- Brutsaert, W.: 1979, Heat and mass transfer to and from surfaces with dense vegetation or similar permeable roughness, *Boundary-Layer Meteorology* **16**, 365–388.
- Brutsaert, W.: 1982, *Evaporation into the Atmosphere: Theory, History, and Applications*, D. Reidel Publishing Company, Boston.
- Calanca, P.: 2001, A note on the roughness length for temperature over melting snow and ice, *Quarterly Journal of the Royal Meteorological Society* **127**, 255–260.
- Campbell, J. L., Mitchell, M. J., Groffman, P. M., Christenson, L. M. and Hardy, J. P.: 2005, Winter in northeastern North America: a critical period for ecological processes, *Frontiers in Ecology and the Environment* **3**(6), 314–322.
- Cava, D., Giostra, U. and Tagliazucca, M.: 2001, Spectral maxima in a perturbed stable boundary layer, *Boundary-Layer Meteorology* **100**, 421–437.
- Cheng, Y., Parlange, M. B. and Brutsaert, W.: 2005, Pathology of Monin-Obukhov similarity theory in the stable boundary layer, *Journal of Geophysical Research* **110**, D06101.
- Choi, C. Y. and Waller, P. M.: 1997, Momentum transport mechanism for water flow over porous media, *Journal of Environmental Engineering* **123**(8), 792–799.

- Clarke, G. K. C., Fisher, D. A. and Waddington, E. D.: 1987, Wind pumping: a potentially significant heat source in ice sheets, *Proceeding of the Vancouver Symposium*, Vancouver, BC.
- Clarke, G. K. C. and Waddington, E. D.: 1991, A three-dimensional theory of wind pumping, *Journal of Glaciology* **37**(125), 89–96.
- Cline, D.: 1995, Snow surface energy exchanges and snowmelt at a continental alpine site, *Biogeochemistry of Seasonally Snow-Covered Catchments*, IAHS Publ. no. 228, IAHS, pp. 157–166.
- Colbeck, S. C.: 1982, An overview of seasonal snow metamorphism, *Reviews of Geophysics and Space Physics* **20**(1), 45–61.
- Colbeck, S. C.: 1988, On the micrometeorology of surface hoar growth in mountainous area, *Boundary-Layer Meteorology* **44**, 1–12.
- Colbeck, S. C.: 1989, Air movement in snow due to windpumping, *Journal of Glaciology* **35**(120), 209–213.
- Colbeck, S. C.: 1997, Model of wind pumping for layered snow, *Journal of Glaciology* **43**(143), 60–65.
- Costa, V. A. F., Oliviera, L. A., Baliga, B. R. and Sousa, A. C. M.: 2004, Simulation of coupled flows in adjacent porous and open domains using a control-volume finite-element method, *Numerical Heat Transfer, Part A*. **45**, 675–697.
- Cullen, N. J., Mölg, T., Kaser, G., Steffen, K. and Hardy, D. R.: 2007, Energy-balance model validation on the top of Kilimanjaro, Tanzania, using eddy covariance data, *Annals of Glaciology* **46**, 227–233.
- Danckwerts, P. V.: 1951, Significance of liquid-film coefficients in gas adsorption, *Industrial and Chemical Engineering* **43**(6), 1460–1467.
- Davis, R. E., Dozier, J., LaChapelle, E. R. and Perla, R.: 1985, Field and laboratory measurements of snow liquid water content by dilution, *Water Resources Research* **21**(9), 1415–1420.
- Denby, B. and Snellen, H.: 2002, A comparison of surface renewal theory with the observed roughness length for temperature on a melting glacier surface, *Boundary-Layer Meteorology* **103**, 459–468.

- Denoth, A., Foglar, A., Weiland, P., Mätzler, C., Aebischer, H., Tiuri, M. and Sihvola, A.: 1984, A comparative study of instruments for measuring the liquid water content of snow, *Journal of Applied Physics* **56**(7), 2154–2160.
- Derbyshire, S. H.: 1999, Boundary-layer decoupling over cold surfaces as a physical boundary-instability, *Boundary-Layer Meteorology* **90**, 297–325.
- Doran, J. C., Wesely, M. L., McMillen, R. T. and Neff, W. D.: 1989, Measurements of turbulent heat and momentum fluxes in a mountain valley, *Journal of Applied Meteorology* **28**, 438–444.
- Dozier, J. and Warren, S. G.: 1982, Effect of viewing angle on the infrared brightness temperature, *Water Resources Research* **18**(5), 1424–1434.
- Etchevers, P., Martin, E., Brown, R., Fierz, C., Lejeune, Y., Bazile, E., Boone, A., Dai, Y.-J., Essery, R., Fernandez, A., Gusev, Y., Jordan, R., Koren, V., Kowalczyk, E., Nasonova, N. O., Pyles, R. D., Schlosser, A., Shmakin, A. B., Smirnova, T. G., Strasser, U., Verseghy, D., Yamazaki, T. and Yang, Z.-L.: 2004, Validation of the energy-budget of an alpine snowpack simulated by several snow models (SnowMIP project), *Annals of Glaciology* **38**, 150–158.
- Finnigan, J.: 1999, A note on wave-turbulence interaction and the possibility of scaling the very stable boundary layer, *Boundary-Layer Meteorology* **90**, 529–539.
- Finnigan, J. J.: 1979, Turbulence in waving wheat. I. Mean statistics and honami, *Boundary-Layer Meteorology* **16**, 181–211.
- Fleagle, R. G.: 1956, The temperature distribution near a cold surface, *Journal of Meteorology* **13**, 160–165.
- Foken, T.: 2008, The energy balance closure problem: an overview, *Ecological Applications* **18**(6), 1351–1367.
- Foken, T. and Wichura, B.: 1996, Tools for quality assessment of surface-based flux measurements, *Agricultural and Forest Meteorology* **78**, 83–105.
- Foken, T., Wimmer, F., Mauder, M., Thomas, C. and Liebethal, C.: 2006, Some aspects of the energy balance closure problem, *Atmospheric Chemistry and Physics* **6**, 4395–4402.
- Garratt, J. R.: 1990, The internal boundary layer - a review, *Boundary-Layer Meteorology* **50**, 171–203.

- Garratt, J. R. and Brost, R. A.: 1981, Radiative cooling effects within and above the nocturnal boundary layer, *Journal of Atmospheric Sciences* **38**, 2730–2746.
- Gash, J. H. C.: 1986, A note on estimating the effect of a limited fetch on micrometeorological evaporation measurements, *Boundary-Layer Meteorology* **35**, 409–413.
- Gelfan, A. N., Pomeroy, J. W. and Kuchment, L. S.: 2004, Modeling forest cover influences on snow accumulation, sublimation, and melt, *Journal of Hydrometeorology* **5**, 785–803.
- Goharzadeh, A., Khalili, A. and Jörgensen, B. B.: 2005, Transition layer thickness at a fluid-porous interface, *Physics of Fluids* **17**, 057102.
- Golding, D. L.: 1978, Calculated snowpack evaporation during chinooks along the eastern slopes of the Rocky Mountains in Alberta, *Journal of Applied Meteorology* **17**, 1647–1651.
- Grace, B.: 1990, Some observations on the effect of chinooks on field microclimates and soil moisture status in southern Alberta, *Climatological Bulletin* **24**(2), 67–83.
- Grachev, A. A., Fairall, C. W., Persson, P. O. G., Andreas, E. L. and Guest, P. S.: 2005, Stable boundary layer scaling regimes: the Sheba data, *Boundary-Layer Meteorology* **116**, 201–235.
- Granger, R. J., Chanasyk, D. S., Male, D. H. and Norum, D. I.: 1977, Thermal regime of a prairie snowcover, *Soil Science Society of America Journal* **41**, 839–842.
- Granger, R. J., Essery, R. and Pomeroy, J. W.: 2006, Boundary-layer growth over snow and soil patches: field observations, *Hydrological Processes* **20**, 943–951.
- Granger, R. J., Pomeroy, J. and Parviainen, J.: 2002, Boundary-layer integration approach to advection of sensible heat to a patchy snow cover, *Hydrological Processes* **16**, 3559–3569.
- Gray, D. M. and Landine, P. G.: 1988, An energy-budget snowmelt model for the Canadian Prairies, *Canadian Journal of Earth Sciences* **25**, 1292–1303.
- Hahn, S., Je, J. and Choi, H.: 2002, Direct numerical simulation of turbulent channel flow with permeable walls, *Journal of Fluid Mechanics* **450**, 259–285.
- Hayashi, M., Hirota, T., Iwata, Y. and Takayabu, I.: 2005, Snowmelt energy balance and its relation to foehn events in Tokachi, Japan, *Journal of the Meteorological Society of Japan* **83**(5), 783–798.
- Hayashi, M., van der Kamp, G. and Schmidt, R.: 2003, Focused infiltration of snowmelt water in partially frozen soil under small depressions, *Journal of Hydrology* **270**, 214–229.

- Hicks, B. B.: 1981, An examination of turbulence statistics in the surface boundary layer, *Boundary-Layer Meteorology* **21**, 389–402.
- Hiller, R., Zeeman, M. J. and Eugster, W.: 2008, Eddy-covariance flux measurements in the complex terrain of an alpine valley in Switzerland, *Boundary-Layer Meteorology* **127**, 449–467.
- Hock, R.: 2003, Temperature index modeling in mountain areas, *Journal of Hydrology* **282**, 104–115.
- Högström, U., Hunt, J. C. R. and Smedman, A.-S.: 2002, Theory and measurements for turbulence spectra and variances in the atmospheric neutral surface layer, *Boundary-Layer Meteorology* **103**, 101–124.
- Holtslag, A. A. M. and De Bruin, H. A. R.: 1988, Applied modeling of the nighttime surface energy balance over land, *Journal of Applied Meteorology* **27**, 689–704.
- Hood, E., Williams, M. and Cline, D.: 1999, Sublimation from a seasonal snowpack at a continental, mid-latitude alpine site, *Hydrological Processes* **13**, 1781–1797.
- Horst, T. W. and Oncley, S.: 2006, Corrections to inertial-range power spectra measured by CSAT3 and Solent sonic anemometers, 1. Path-averaging errors, *Boundary-Layer Meteorology* **119**, 375–395.
- Howell, J. and Mahrt, L.: 1997, Multiresolution flux decomposition, *Boundary-Layer Meteorology* **83**, 117–137.
- Hug, C., Faure, F., Lehning, M., Mobbs, S., Raderschall, N. and Hertig, J.-A.: 2005, Small scale wind field simulations for the steep Gaudergrat Ridge using CFX-4 and ARPS; influence of the boundary conditions and comparison with measurements, *27th International Conference on Alpine Meteorology*, Zadar, Croatia.
- Hunt, J. C. R. and Morrison, J. F.: 2000, Eddy structure in turbulent boundary layers, *European Journal of Mechanics B/Fluids* **19**, 673–694.
- Jensen, N. O. and Busch, N. E.: 1982, Atmospheric turbulence, in E. J. Plate (ed.), *Engineering Meteorology: Fundamentals of Meteorology and their Applications to Problems in Environmental and Civil Engineering*, Studies in Wind Engineering and Industrial Aerodynamics, Elsevier Scientific Publishing Company, New York.
- Jones, E. B., Rango, A. and Howell, S. M.: 1983, Snowpack liquid water determinations using freezing calorimetry, *Nordic Hydrology* **14**(3), 113–123.

- Jones, H. G. and Pomeroy, J. W.: 1998, The ecology of snow and snow-covered systems: summary and relevance to Wolf Creek, Yukon, *in* J. W. Pomeroy and R. J. Granger (eds), *Wolf Creek Research Basin: Hydrology, Ecology, Environment*, Environment Canada, Whitehorse, Yukon, pp. 1–13.
- Jordan, R. E.: 1991, A one-dimensional temperature model for a snow cover, *Technical Report Special Report 91-16*, U.S. Army Cold Regions Research and Engineering Laboratory.
- Jordan, R. E., Andreas, E. L. and Makshtas, A. P.: 1999, Heat Budget of snow-covered sea ice at North Pole 4, *Journal of Geophysical Research* **104**(C4), 7785–7806.
- Kaimal, J. C. and Finnigan, J. J.: 1994, *Atmospheric Boundary Layer Flows: Their Structure and Measurement*, Oxford University Press, New York.
- Kaimal, J. C. and Wyngaard, J. C.: 1990, The Kansas and Minnesota Experiments, *Boundary-Layer Meteorology* **50**, 31–47.
- Kaimal, J. C., Wyngaard, J. C., Izumi, Y. and Cotè, O. R.: 1972, Spectral characteristics of surface layer turbulence, *Quarterly Journal of the Royal Meteorological Society* **98**, 563–589.
- Katul, G., Cava, D., D., P., Albertson, J. and Mahrt, L.: 2004, Stationarity, homogeneity, and ergodicity in canopy turbulence, *in* X. Lee, W. Massman and B. Law (eds), *Handbook of Micrometeorology: A Guide for Surface Flux Measurement and Analysis*, Kluwer Academic Publisher, Boston, pp. 161–180.
- Katul, G. G. and Parlange, M. B.: 1994, On the active role of temperature in surface-layer turbulence, *Journal of the Atmospheric Sciences* **51**(15), 2181–2195.
- Kaviany, M.: 2002, *Principles of Heat Transfer*, John Wiley and Sons, Inc., Toronto, ON.
- King, J. C.: 1990, Some measurements of turbulence over an antarctic ice shelf, *Quarterly Journal of the Royal Meteorological Society* **116**, 379–400.
- King, J. C. and Anderson, P. S.: 1994, Heat and water vapour fluxes and scalar roughness lengths over an Antarctic ice shelf, *Boundary-Layer Meteorology* **69**, 101–121.
- King, J. C., Anderson, P. S. and Mann, G. W.: 2001, The seasonal cycle of sublimation at Halley, Antarctica, *Journal of Glaciology* **47**(156), 1–8.
- King, J. C., Anderson, P. S., Smith, M. C. and Mobbs, S. D.: 1996, The surface energy and mass balance at Halley, Antarctica during winter, *Journal of Geophysical Research* **101**(D14), 19119–19128.

- Kohsiek, W., Liebenthal, C., Foken, T., Vogt, R., Oncley, S., Bernhofer, C. and Debruin, H.: 2007, The Energy Balance Experiment EBEX-2000. Part III: Behaviour and quality of the radiation measurements, *Boundary-Layer Meteorology* **123**, 55–75.
- Kuchment, L. S. and Gelfan, A. N.: 1996, The determination of the snowmelt rate and the meltwater outflow from a snowpack for modelling river runoff generation, *Journal of Hydrology* **179**, 23–36.
- Kuznetsov, A. V.: 1996, Analytical investigation of the fluid flow in the interface region between a porous medium and a clear fluid in channels partially filled with a porous medium, *Applied Scientific Research* **56**, 53–67.
- Kuznetsov, A. V.: 1997, Influence of the stress jump condition at the porous-medium/clear-fluid interface on a flow at a porous wall, *International Communications in Heat and Mass Transfer* **24**(3), 401–410.
- Kuznetsov, A. V.: 1998, Analytical study of fluid flow and heat transfer during forced convection in a composite channel partly filled with a Brinkman-Forchheimer porous medium, *Flow, Turbulence and Combustion* **60**, 173–192.
- Legagneaux, L., Carbanes, A. and Dominé, F.: 2002, Measurement of the specific surface area of 176 snow samples using methane adsorption at 77 K, *Journal of Geophysical Research* **107**(D17), 4335.
- Lehning, M., Bartelt, P., Brown, B. and Fierz, C.: 2002, A physical SNOWPACK model for the Swiss avalanche warning Part III: meteorological forcing, thin layer formation and evaluation, *Cold Regions Science and Technology* **35**, 169–184.
- Lehning, M., Völksch, I., Gustafsson, D., Nguyen, T. A., Stähli, M. and Zappa, M.: 2006, ALPINE3D: a detailed model of mountain surface processes and its application to snow hydrology, *Hydrological Processes* **20**, 2111–2128.
- Mahrt, L.: 1998, Stratified atmospheric boundary layers and breakdown of models, *Theoretical and Computational Fluid Dynamics* **11**, 263–279.
- Mahrt, L.: 1999, Stratified atmospheric boundary layers, *Boundary-Layer Meteorology* **90**, 375–396.
- Mahrt, L.: 2007, The influence of nonstationarity on the turbulent flux-gradient relationship for stable stratification, *Boundary-Layer Meteorology* .

- Makshtas, A. P., Andreas, E. L., Svyashchennikov, P. N. and Timachev, V. F.: 1999, Accounting for clouds in sea ice models, *Atmospheric Research* **52**, 77–113.
- Male, D. H. and Gray, D. M.: 1981, Snowcover ablation and runoff, in D. M. Gray and D. H. Male (eds), *Handbook of Snow: Principles, Processes, Management & Use*, Pergamon Press, Toronto, pp. 360–436.
- Marks, D., Domingo, J., Suson, D., Link, T. and Garen, D.: 1999, A spatially distributed energy balance snowmelt model for application in mountain basins, *Hydrological Processes* **13**, 1935–1959.
- Marks, D. and Dozier, J.: 1992, Climate and energy exchange at the snow surface in the alpine region of the Sierra Nevada 2. Snow cover energy balance, *Water Resources Research* **28**(11), 3043–3054.
- Marks, D., Kimball, J., Tingey, D. and Link, T.: 1998, The sensitivity of snowmelt processes to climate conditions and forest cover during rain-on-snow: a case study of the 1996 Pacific Northwest flood., *Hydrological Processes* **12**, 1569–1587.
- Marks, D., Reba, M., Pomeroy, J., Link, T., Winstral, A., Flerchinger, G. and Elder, K.: 2008, Comparing simulated and measured sensible and latent heat fluxes over snow under a pine canopy to improve and energy balance snowmelt model, *Journal of Hydrometeorology* **9**, 1506–1522.
- Massman, W. J.: 2006, Advective transport of CO<sub>2</sub> in permeable media induced by atmospheric pressure fluctuations: 1. An analytical model, *Journal of Geophysical Research* **111**, G03004.
- Massman, W. J. and Lee, X.: 2002, Eddy covariance flux corrections and uncertainties in long-term studies of carbon and energy exchanges, *Agricultural and Forest Meteorology* **113**, 121–144.
- McNaughton, K. G. and Brunet, Y.: 2002, Tonwsend’s hypothesis, coherent structures and Monin-Obukhov similarity, *Boundary-Layer Meteorology* **102**, 161–175.
- Monin, A.: 1970, The atmospheric boundary layer, *Annual Review of Fluid Mechanics* **2**, 225–250.
- Munro, D. S.: 1989, Surface roughness and bulk heat transfer on a glacier: Comparison with eddy correlation, *Journal of Glaciology* **35**(121), 343–348.

- Munro, D. S. and Davies, J. A.: 1977, An experimental study of the glacier boundary layer over melting ice, *Journal of Glaciology* **18**(80), 425–436.
- Nakamura, R. and Mahrt, L.: 2005, A study of intermittent turbulence with CASES-99 tower measurements, *Boundary-Layer Meteorology* **114**, 367–387.
- Nieuwstadt, F. T. M.: 1984, The turbulent structure of the stable, nocturnal boundary layer, *Journal of the Atmospheric Sciences* **41**(14), 2202–2216.
- Nyberg, A.: 1938, Temperature measurements in an air layer very close to the snow surface, *Geografiska Annaler* **20**, 234–275.
- Ochoa-Tapia, J. A. and Whitaker, S.: 1995, Momentum transfer at the boundary between a porous medium and homogenous fluid - I. Theoretical development, *International Journal of Heat and Mass Transfer* **38**(14), 2635–2646.
- Ochoa-Tapia, J. A. and Whitaker, S.: 1997, Heat transfer at the boundary between a porous medium and a homogeneous fluid, *International Journal of Heat and Mass Transfer* **40**(11), 2691–2707.
- Ohmura, A.: 2001, Physical basis for the temperature-based melt-index method, *Journal of Applied Meteorology* **40**, 753–761.
- Oke, T. R.: 1970, The temperature profile near the ground on calm clear nights, *Quarterly Journal of the Royal Meteorological Society* **96**(407), 14–23.
- Oncley, S. P., Friehe, C. A., Larue, J. C., Businger, J. A., Itsweire, E. C. and Chang, S. S.: 1996, Surface-layer fluxes, profiles, and turbulence measurements over uniform terrain under near-neutral conditions, *Journal of the Atmospheric Sciences* **53**(7), 1029–1044.
- Panofsky, H. A. and Dutton, J. A.: 1984, *Atmospheric Turbulence: Models and Methods for Engineering Applications*, John Wiley and Sons, Toronto.
- Paulson, C. A.: 1970, The mathematical representation of wind speed and temperature profiles in the unstable atmospheric surface layer, *Journal of Applied Meteorology* **9**, 857–861.
- Pedras, M. H. J. and de Lemos, M. J. S.: 2001, Simulation of turbulent flow in porous media using a spatially periodic array and a low Re two-equation model, *Numerical Heat Transfer, Part A*. **39**, 35–59.
- Pomeroy, J. W.: 1988, *Wind Transport of Snow*, PhD thesis, University of Saskatchewan.

- Pomeroy, J. W., Bewley, D. S., Essery, R. L. H., Hedstrom, N. R., Link, T., Granger, R. J., Sicart, J. E., Ellis, C. R. and Janowicz, J. R.: 2006, Shrub tundra snowmelt, *Hydrological Processes* **20**, 923–941.
- Pomeroy, J. W. and Essery, R. L. H.: 1999, Turbulent fluxes during blowing snow: field tests of model sublimation predictions, *Hydrological Processes* **13**, 2963–2975.
- Pomeroy, J. W. and Gray, D. M.: 1995, Snowcover: Accumulation, relocation and management, *Technical report*, Environment Canada.
- Pomeroy, J. W., Gray, D. M., Shook, K. R., Toth, B., Essery, R. L. H., Pietroniro, A. and Hedstrom, N.: 1998, An evaluation of snow accumulation and ablation processes for land surface modelling, *Hydrological Processes* **12**, 2339–2367.
- Pomeroy, J. W., Toth, B., Granger, R. J., Hedstrom, N. R. and Essery, R. L. H.: 2003, Variation in surface energetics during snowmelt in a subarctic mountain catchment, *Journal of Hydrometeorology* **4**, 702–719.
- Prinos, P., Sofialidis, D. and Keramaris, E.: 2003, Turbulent flow over and within a porous bed, *Journal of Hydraulic Engineering* **129**(9), 720–733.
- Raderschall, N., Lehning, M. and Doorschot, J.: 2002, Boundary layer wind field over steep, snow covered, high alpine topography, *10th Conference on Mountain Meteorology*, American Meteorological Society, Park City, Utah, pp. 303–306.
- Raupach, M. R., Antonia, R. A. and Rajogopalan, S.: 1991, Rough-wall turbulent boundary layers, *Applied Mechanics Reviews* **44**(1), 1–25.
- Reba, M. L., Link, T. E., Marks, D. and Pomeroy, J.: 2009, An assessment of corrections for eddy covariance measured turbulent fluxes over snow in mountain environments, *Water Resources Research* **45**, W000D38.
- Revell, M. J., Purnall, D. and Lauren, M. K.: 1996, Requirements for large-eddy simulation of surface wind gusts in a mountain valley, *Boundary-Layer Meteorology* **80**, 333–353.
- Rotach, M. W., Andretta, M., Calanca, P., Weigel, A. P. and Weiss, A.: 2008, Boundary layer characteristics and turbulent exchange mechanisms in highly complex terrain, *Acta Geophysica* **56**(1), 194–219.
- Rotach, M. W. and Zardi, D.: 2007, On the boundary-layer structure over highly complex terrain: Key findings from MAP, *Quarterly Journal of the Royal Meteorological Society* **133**, 937–948.

- Rutter, N., Essery, R., Pomeroy, J., Altimir, N., Andreadis, K., Baker, I., Barr, A., Bartlett, P., Boone, A., Deng, H., Douville, H., Dutra, E., Elder, K., Ellis, C., Feng, X., Gelfan, A., Goodbody, A., Gusev, Y., Gustafsson, D., Hellström, R., Hirabayashi, Y., Hirota, T., Jonas, T., Koren, V., Kuragina, A., Lettenmaier, D., Li, W., Luce, C., Martin, E., Nasonova, O., Pumpanen, J., Pyles, R., Samuelsson, P., Sandells, M., Schädler, G., Shmakin, A., Smirnova, T., Stähli, M., Stöckli, R., Strasser, U., Su, H., Suzuki, K., Takata, K., Tanaka, K., Thompson, E., Vesala, T., Viterbo, P., Wiltshire, A., Xia, K., Xue, Y. and Yamazaki, T.: 2009, Evaluation of forest snow processes models SnowMIP2, *Journal of Geophysical Research* **114**, D06111.
- Sauer, T. J., Hatfield, J. L., Prueger, J. H. and Logsdon, S. D.: 1998, Energy balance of a corn residue-covered field during snowmelt, *Journal of the American Water Resources Association* **34**(6), 1401–1414.
- Schetz, J. A.: 1993, *Boundary Layer Analysis*, Prentice Hall, Toronto.
- Shook, K. and Gray, D. M.: 1997, Snowmelt resulting from advection, *Hydrological Processes* **11**, 1725–1736.
- Sicart, J. E., Hock, R. and Six, D.: 2008, Glacier melt, air temperature, and energy balance in different climates: The Bolivian Tropics, the French Alps, and northern Sweden, *Journal of Geophysical Research* **113**, D24113.
- Sicart, J. E., Pomeroy, J. W., Essery, R. L. H. and Bewley, D.: 2006, Incoming longwave radiation to melting snow: observations, sensitivity and estimation in northern environments, *Hydrological Processes* **20**, 3697–3708.
- Sicart, J. E., Wagnon, P. and Ribstein, P.: 2005, Atmospheric controls of the heat balance of Zongo Glacier (16S, Bolivia), *Journal of Geophysical Research* **110**, D12106.
- Silva, R. A. and de Lemos, J. S.: 2003a, Turbulent flow in a channel occupied by a porous layer considering the stress jump at the interface, *International Journal of Heat and Mass Transfer* **46**, 5113–5121.
- Silva, R. A. and de Lemos, M. J. S.: 2003b, Numerical analysis of the stress jump interface condition for laminar flow over a porous layer, *Numerical Heat Transfer, Part A*. **43**, 603–617.
- Slater, A. G., Schlosser, C. A., Desborough, C. E., Pitman, A. J., Henderson-Sellers, A., Robock, A., Vinnikov, K. Y., Mitchell, K., Boone, A., Braden, H., Chen, F., Cox, P. M.,

- de Rosnay, P., Dickinson, R. E., Dai, Y.-J., Duan, Q., Entin, J., Etchevers, P., Gedney, N., Gusev, Y. M., Habets, F., Kim, J., Koren, V., Kowalczyk, E. A., Nasonova, O. N., Noilhan, J., Schaake, S., Shmakin, A. B., Smirnova, T. G., Verseghy, D., Wetzel, P., Xue, Y., Yang, Z.-L. and Zeng, Q.: 2001, The representation of snow in land surface schemes: results from PILPS 2(d), *Journal of Hydrometeorology* **2**, 7–25.
- Smedman, A.-S.: 1988, Observations of a multilevel turbulence structure in a very stable boundary layer, *Boundary-Layer Meteorology* **44**, 231–253.
- Smedman, A.-S., Tjernström, M. and Högström, U.: 1994, The near-neutral marine atmospheric boundary layer with no surface shearing stress: A case study, *Journal of the Atmospheric Sciences* **51**(23), 3399–3411.
- Smeets, C. J. P. P., Duynkerke, P. G. and Vugts, H. F.: 1998, Turbulence characteristics of the stable boundary layer over a mid-latitude glacier. Part I: A combination of katabatic and large scale forcing, *Boundary-Layer Meteorology* **87**, 117–145.
- Smeets, C. J. P. P., Duynkerke, P. G. and Vugts, H. F.: 1999, Observed wind profiles and turbulence fluxes over an ice surface with changing surface roughness, *Boundary-Layer Meteorology* **92**, 101–123.
- Smeets, C. J. P. P., Duynkerke, P. G. and Vugts, H. F.: 2000, Turbulence characteristics of the stable boundary layer over a mid-latitude glacier. Part II: Pure katabatic forcing conditions, *Boundary-Layer Meteorology* **97**, 73–107.
- Smeets, C. J. P. P. and van den Broeke, M. R.: 2008, The parameterisation of scalar transfer over rough ice, *Boundary-Layer Meteorology* **128**, 339–355.
- Sokratov, S. A. and Sato, A.: 2000, Wind propagation to snow observed in laboratory, *Annals of Glaciology* **31**, 427–433.
- Sokratov, S. A. and Sato, A.: 2001, The effect of wind on the snow cover, *Annals of Glaciology* **32**, 116–120.
- Stull, R. B.: 1988, *An Introduction to Boundary Layer Meteorology*, Kluwer Academic Publishers, Boston.
- Sturm, M.: 1991, The role of thermal convection in heat and mass transport in the subarctic snow cover, *Technical Report CRELL Report 91-19*, U.S. Army Corps of Engineers, Cold Regions Research and Engineering Laboratory.

- Sturm, M. and Benson, C. B.: 1997, Vapor transport, grain growth and depth-hoar development in the subarctic snow, *Journal of Glaciology* **43**(143), 42–59.
- Sturm, M., Holmgren, J., König, M. and Morris, K.: 1997, The thermal conductivity of seasonal snow, *Journal of Glaciology* **43**(143), 26–41.
- Tarbotan, D. G. and Luce, C. H.: 1996, Utah Energy Balance Snow Accumulation and Melt Model (UEB) Computer Model Technical Description and Users Guide, *Technical report*, Utah State University.
- Taylor, G. I.: 1938, The spectrum of turbulence, *Proceedings of the Royal Society of London. A.* **164**(919), 476–490.
- Townsend, A. A.: 1961, Equilibrium layers and wall turbulence, *Journal of Fluid Mechanics* **11**, 97–120.
- Townsend, A. A.: 1976, *The Structure of Turbulent Shear Flow*, 2nd edn, Cambridge University Press, New York.
- Turnipseed, A. A., Anderson, D. E., Blanken, P. D., Baugh, W. W. and Monson, R. K.: 2003, Airflows and turbulent flux measurements in mountainous terrain Part 1: Canopy and local effects, *Agricultural and Forest Meteorology* **119**, 1–21.
- Turnipseed, A. A., Anderson, D. E., Burns, S., Blanken, P. D. and Monson, R. K.: 2004, Airflows and turbulent flux measurements in mountainous terrain Part 2: mesoscale effects, *Agricultural and Forest Meteorology* **125**, 187–205.
- Turnipseed, A. A., Blanken, P. D., Andersen, D. E. and Monson, R. K.: 2002, Energy budget above a high-elevation subalpine forest in complex topography, *Agricultural and Forest Meteorology* **110**, 177–201.
- van den Broeke, M., van As, D., Reijmer, C. and van de Wal, R.: 2004, Assessing and improving the quality of unattended radiation observations in Antarctica, *Journal of Atmospheric and Oceanic Technology* **21**, 1417–1431.
- van Dijk, A.: 2002, Extension to 3D of "The effect of line averaging on scalar flux measurements with a sonic anemometer near the surface" by Kristensen and Fitzjarrald, *Journal of Atmospheric and Oceanic Technology* **19**, 80–82.
- Verseghy, D.: 1991, CLASS - A Canadian land surface scheme for CGMS. I: Soil model, *International Journal of Climatology* **11**, 111–133.

- Verseghy, D.: 2000, The Canadian Land Surface Scheme (CLASS); Its history and future, *ATMOSPHERE-OCEAN* **38**, 1–13.
- Vickers, D. and Mahrt, L.: 1997, Quality control and flux sampling problems for tower and aircraft data, *Journal of Atmospheric and Oceanic Technology* **14**, 512–526.
- Vickers, D. and Mahrt, L.: 2003, The cospectral gap and turbulent flux calculations, *Journal of Atmospheric and Oceanic Technology* **20**, 660–672.
- Vickers, D. and Mahrt, L.: 2006, A solution for flux contamination by mesoscale motions with very weak turbulence, *Boundary-Layer Meteorology* **118**, 431–447.
- Waddington, E. D., Cunningham, J. and Harder, S. L.: 1996, The effects of snow ventilation on chemical concentrations, in E. W. Wolff and R. C. Bales (eds), *Chemical Exchange Between the Atmosphere and Polar Snow*, Vol. 143 of *NATO ASI Series*, Springer-Verlag, Berlin, pp. 403–451.
- Warren, S. G.: 1982, Optical properties of snow, *Reviews of Geophysics and Space Physics* **20**(1), 67–89.
- Warren, S. G. and Wiscombe, W. J.: 1980, A model for the spectral albedo of snow. II: Snow containing atmospheric aerosols, *Journal of the Atmospheric Sciences* **37**, 2734–2745.
- Webb, E. K., Pearman, G. I. and Leuning, R.: 1980, Correction of flux measurements for density effects due to heat and water vapour transfer, *Quarterly Journal of the Royal Meteorological Society* **106**, 85–100.
- Weigel, A. P., Chow, F. K. and Rotach, M. W.: 2007, On the nature of turbulent kinetic energy in a steep narrow alpine valley, *Boundary-Layer Meteorology* **123**, 177–199.
- Wilczak, J. M., Oncley, S. P. and Stage, S. A.: 2001, Sonic anemometer tilt correction algorithms, *Boundary-Layer Meteorology* **99**, 127–150.
- Willis, G. E. and Deardorff, J. W.: 1976, On the use of Taylor’s translation hypothesis for diffusion in the mixed layer, *Quarterly Journal of the Royal Meteorological Society* **102**, 817–822.
- Wilson, J. D.: 2008, Monin-Obukhov functions for standard deviations of velocity, *Boundary-Layer Meteorology* **129**, 353–369.
- Wilson, K., Goldstein, A., Falge, E., Aubinet, M., Baldocchi, D., Berbigier, P., Bernhofer, C., Ceulemans, R., Dolman, H., Field, C., Grelle, A., Ibrom, A., Law, B. E., Kowalski, A.,

- Meyers, T., Moncrieff, J., Monson, R., Oechel, W., Tenhunen, J., Valentini, R. and Verma, S.: 2002, Energy balance closure at FLUXNET sites, *Agricultural and Forest Meteorology* **113**, 223–243.
- Wiscombe, W. J. and Warren, S. G.: 1980, A model for the spectral albedo of snow. I: Pure snow, *Journal of the Atmospheric Sciences* **37**, 2712–2733.
- World Meteorological Organization: 1986, Results of an intercomparison of models on snowmelt runoff, *Modelling Snowmelt-Induced Processes*, IAHS Publ. no. 155, IAHS, Budapest.
- Zippe, H. J. and Graf, W. H.: 1983, Turbulent boundary-layer flow over permeable and non-permeable rough surfaces, *Journal of Hydraulic Research* **21**(1), 51–65.

APPENDIX A  
BACKGROUND METEOROLOGICAL CONDITIONS

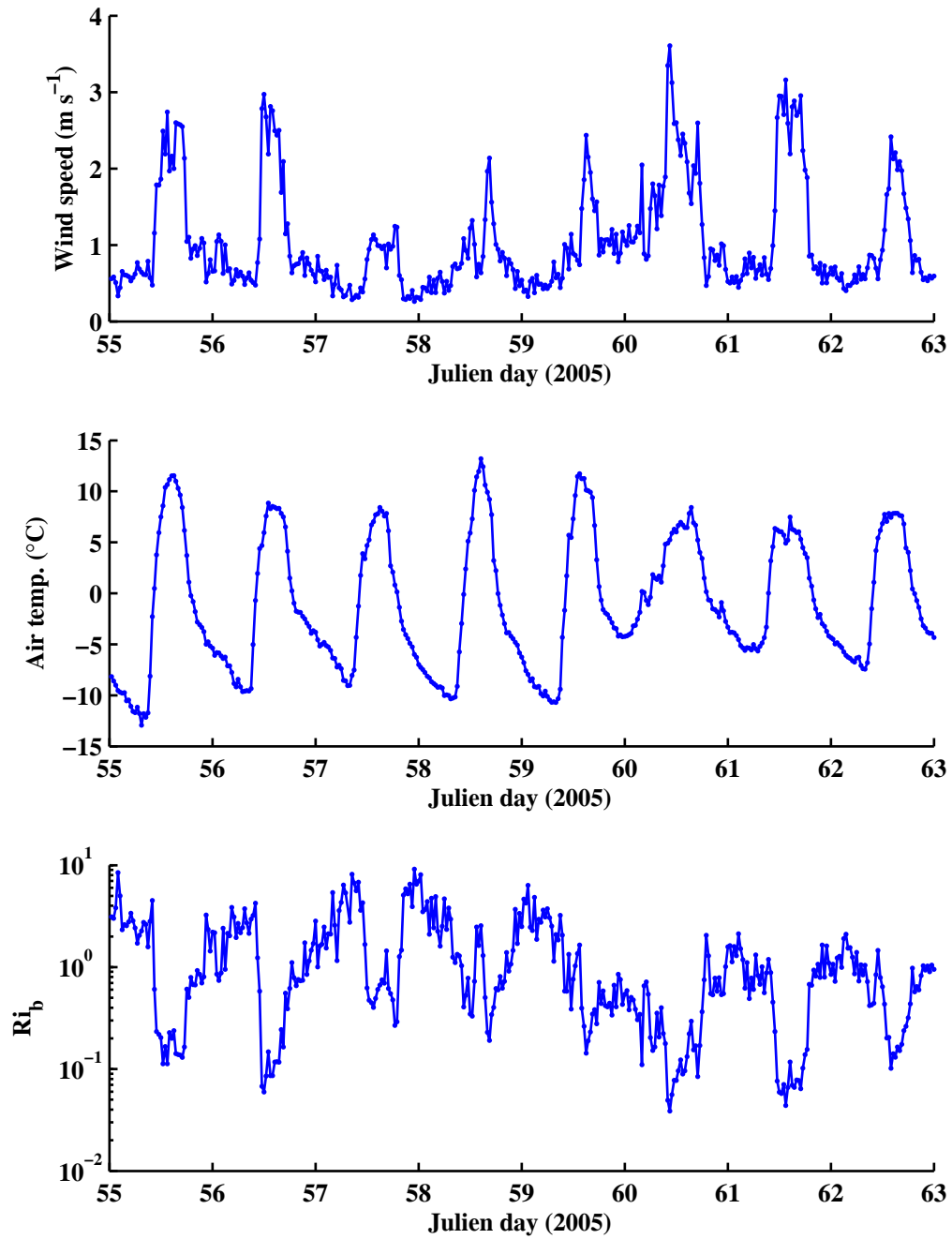


Figure A.1: Background meteorological conditions of data collection period of HM site A.

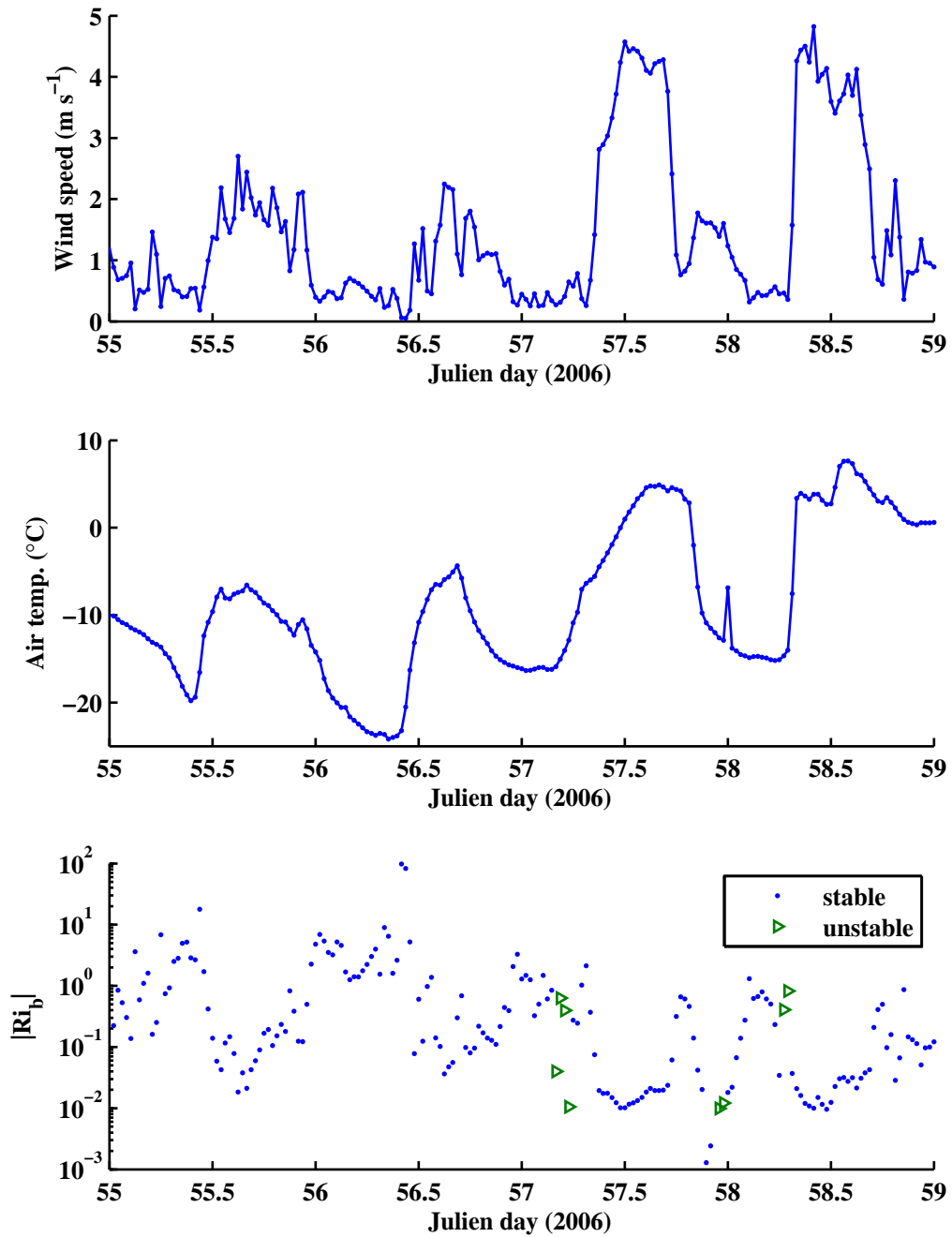


Figure A.2: Background meteorological conditions of data collection period of HM site B.

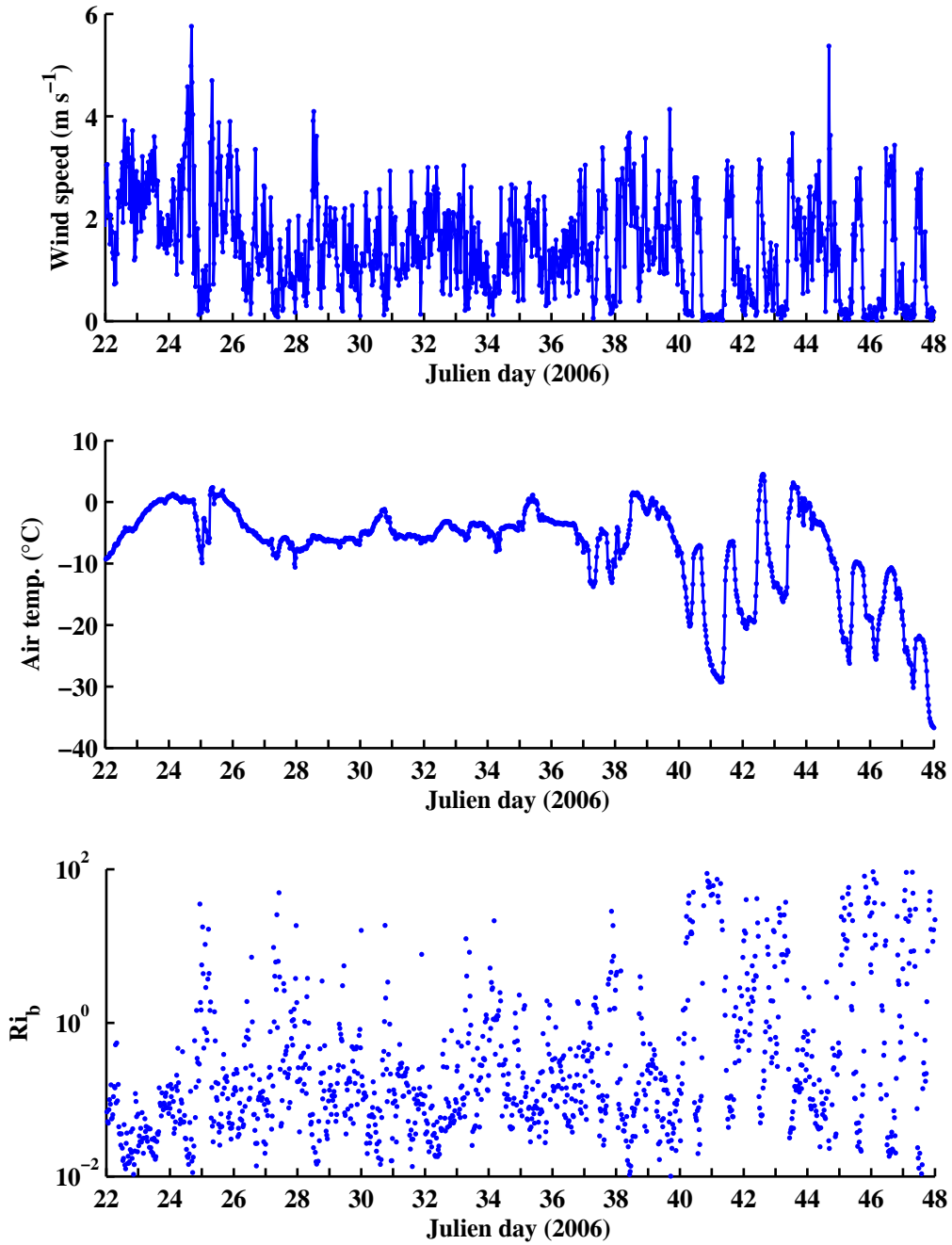


Figure A.3: Background meteorological conditions of data collection period of ML.

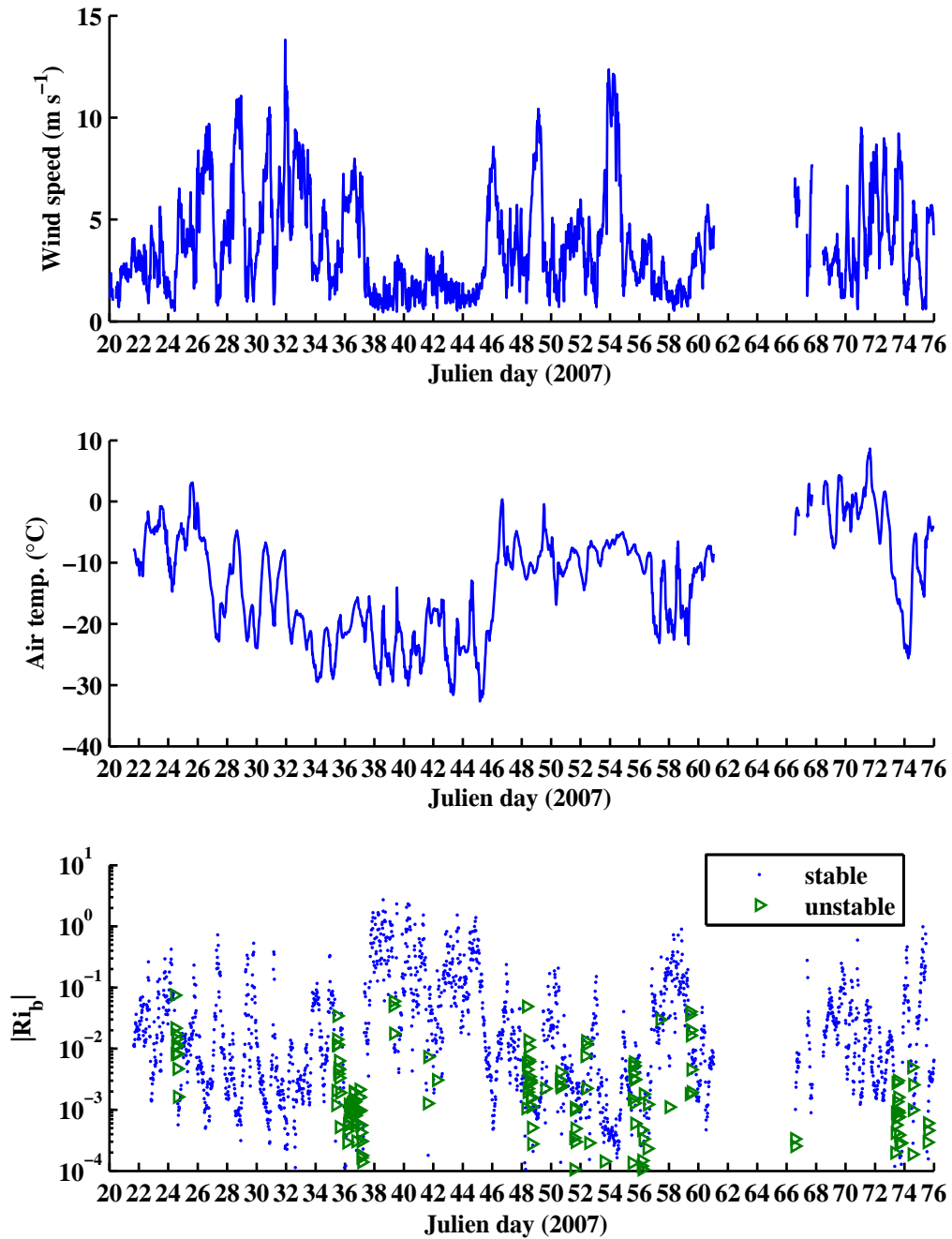


Figure A.4: Background meteorological conditions of data collection period of KF.

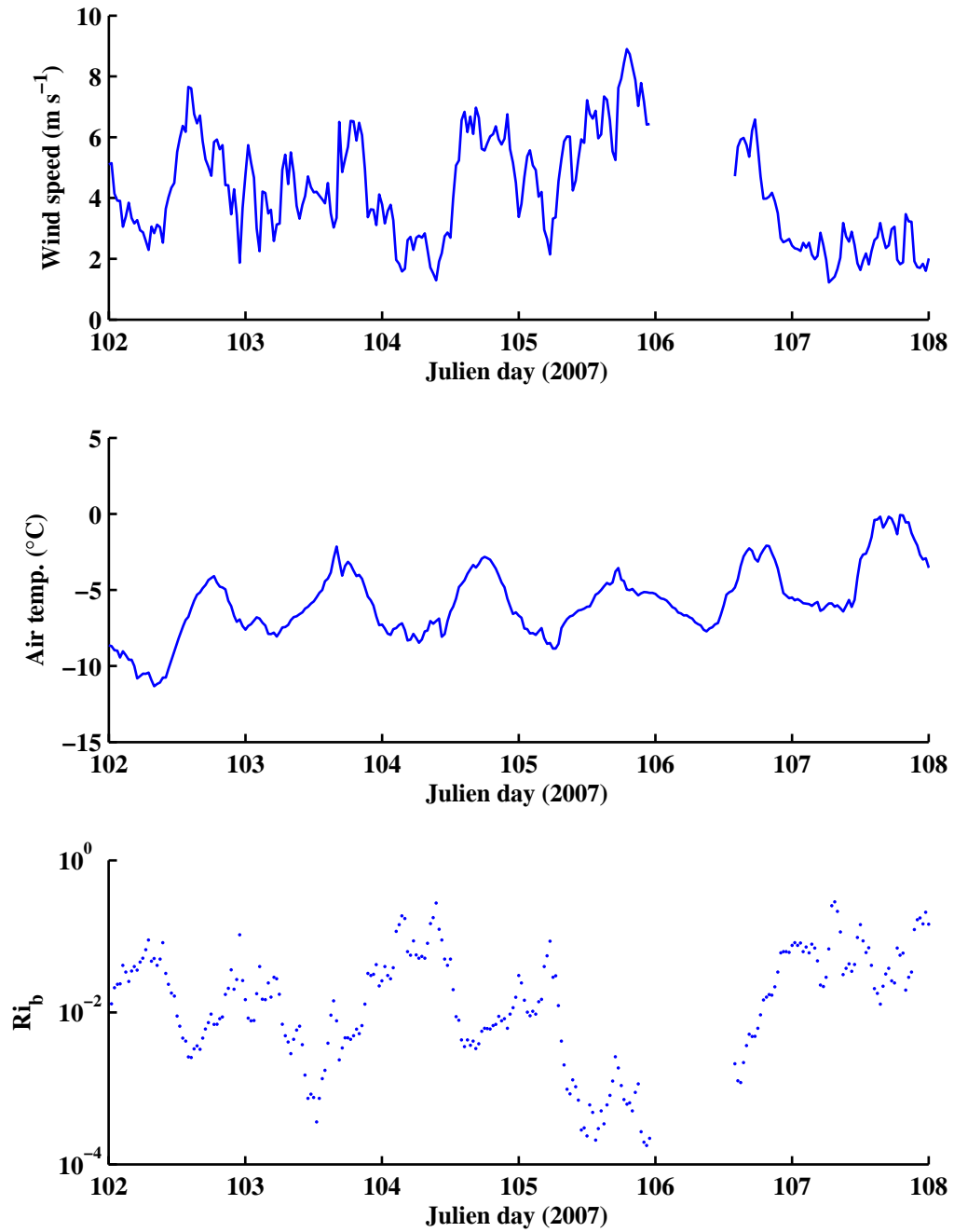


Figure A.5: Background meteorological conditions of data collection period of WCA.

APPENDIX B  
SPECTRA AND COSPECTRA

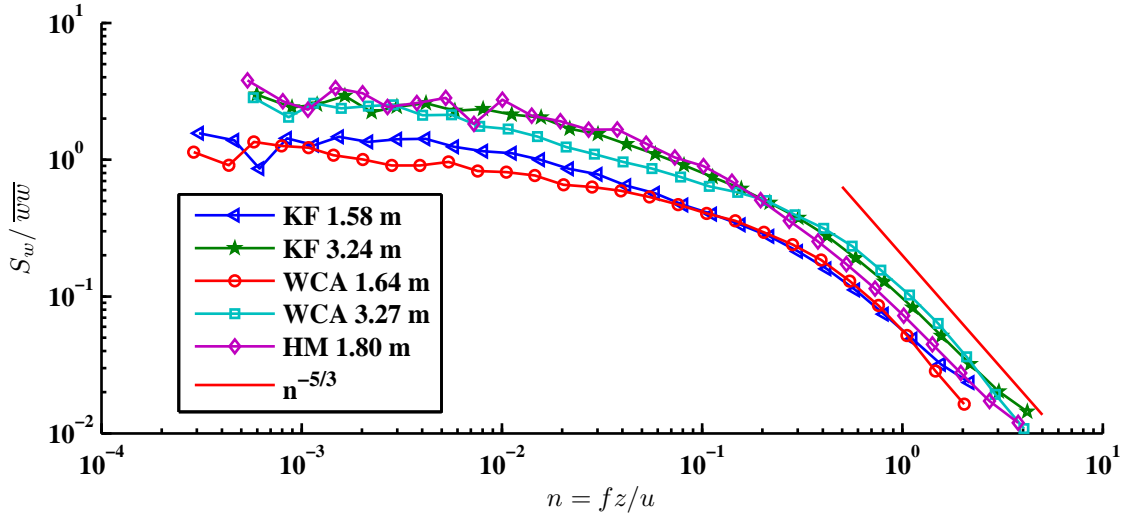


Figure B.1: Composite  $w$  spectra for sites and events considered in Chapter 4.

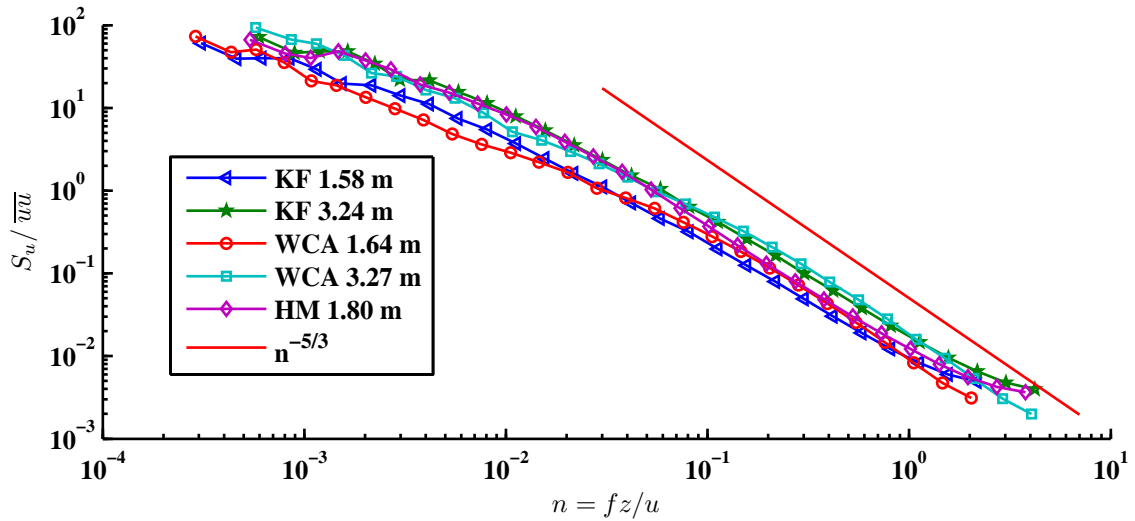


Figure B.2: Composite  $u$  spectra for sites and events considered in Chapter 4.

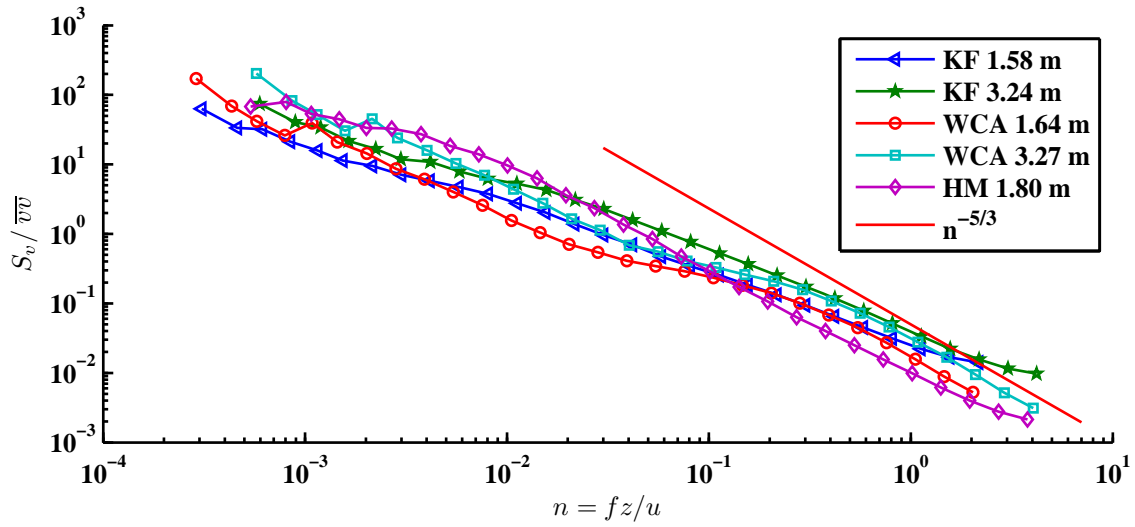


Figure B.3: Composite  $v$  spectra for sites and events considered in Chapter 4.

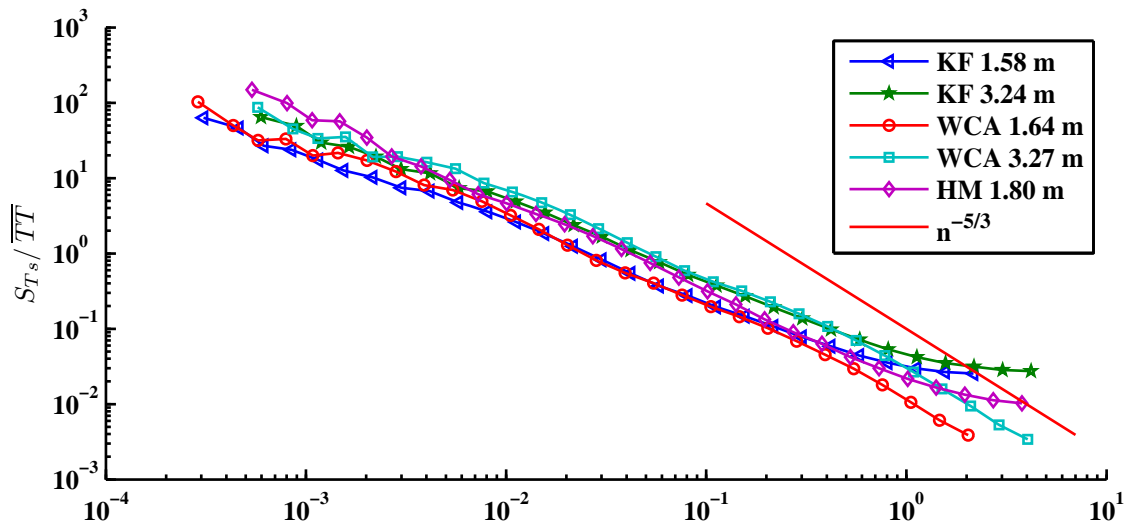


Figure B.4: Composite  $T_s$  spectra for sites and events considered in Chapter 4.

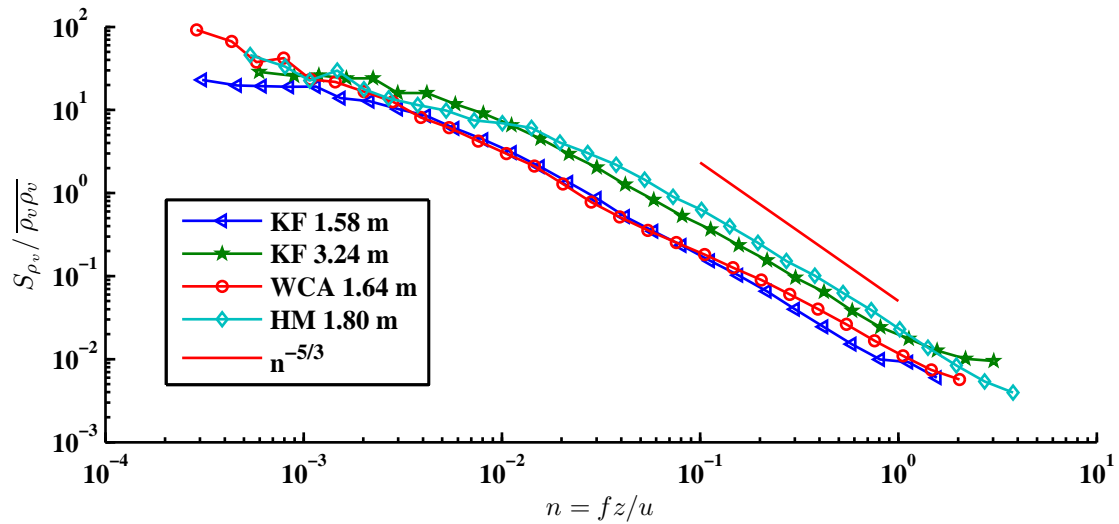


Figure B.5: Composite  $\rho_v$  spectra for sites and events considered in Chapter 4.

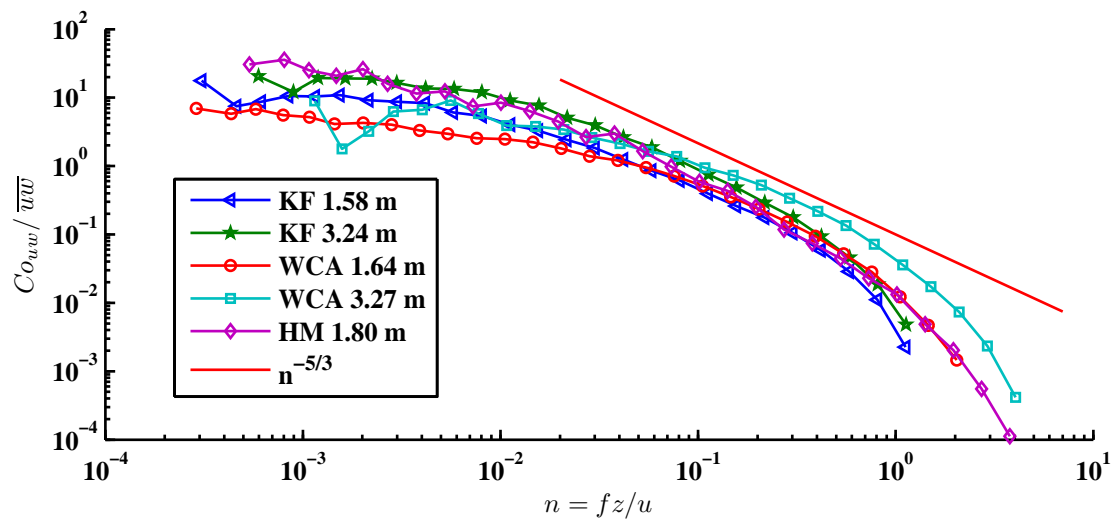


Figure B.6: Composite  $uw$  cospectra for sites and events considered in Chapter 4.

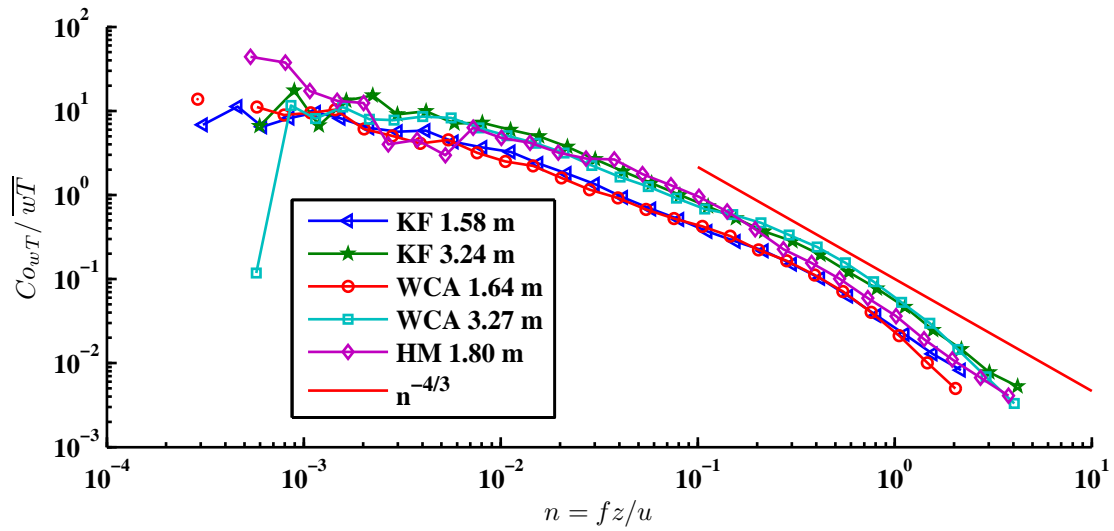


Figure B.7: Composite  $wT$  cospectra for sites and events considered in Chapter 4.

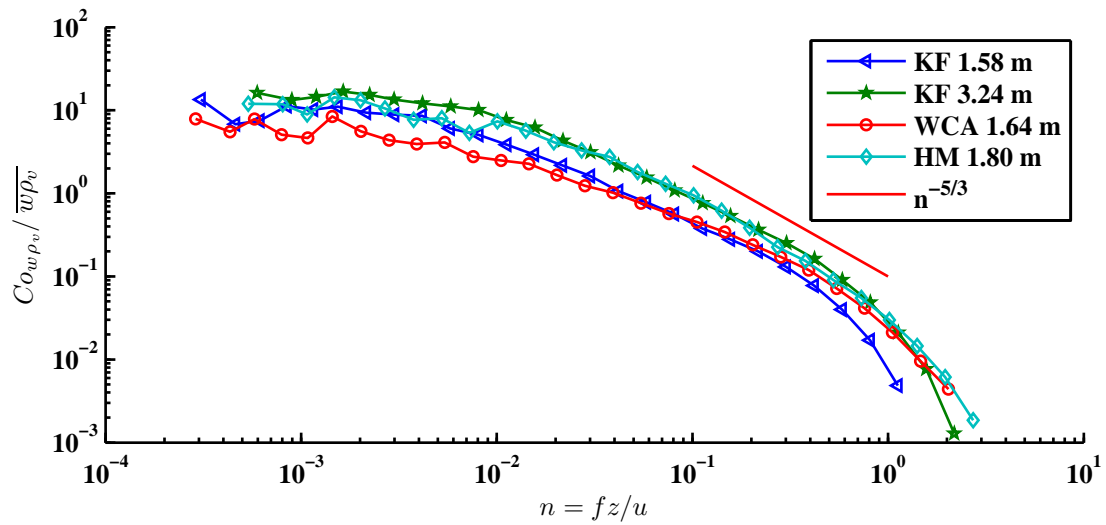


Figure B.8: Composite  $w\rho_v$  cospectra for sites and events considered in Chapter 4.